Journal of Applied Mechanics

(Contributions of the ASME Applied Mechanics Division)

Singular Yield Conditions and Associated Flow Rules . . . . . *William Prager* 317
Graphical-Numerical Solution of Problems of Saint-Venant Torsion and Bending . *B. A. Boley* 321
Elastic Spheres in Contact Under Varying Oblique Forces . . *R. D. Mindlin and H. Deresiewicz* 327
Combined Bending and Twisting of Thin Tubes in the Plastic Range . *E. T. Onat and R. T. Shield* 345
Improved Electrical Analogy for Analysis of Beams in Bending . . . . . *W. T. Russell and R. H. MacNeal* 349
Determination of Stresses in Cemented Lap Joints. . . . . *R. W. Cornell* 355
Effect of Range of Stress on Fatigue of 76S-T61 Aluminum Alloy . . . . . *W. N. Findley* 365
Calculation of Elastic Displacements From Photoelastic Curves . . *H. Poritsky and R. P. Jerrard* 375
The Vibration of Rotating, Tapered-Twisted Beams . . . . . *G. W. Jarrett and P. C. Warner* 381
Two-Dimensional Diffuser Flow . . . . . *K. R. Galle and R. C. Binder* 390
Axisymmetric Flow of Ideal Incompressible Fluid About a Solid Torus . . . . . *E. Sternberg and M. A. Sadowsky* 393
Viscous Flow Through Axial Turbomachines . . . . *T. P. Torda, H. H. Hilton, and F. C. Hall* 401
Temperature Distribution in the Wake of a Heated Sphere . . . . . *D. H. Baer, W. G. Schlinger, V. J. Berry, and B. H. Sage* 407
Laminar Boundary-Layer Flow With Variable Properties . . . . . *S. Levy and R. A. Seban* 415
Measurement of Acceleration Pulses . . . . . *Henry Shapiro and D. E. Hudson* 422
Transient Deformations in Elastoplastic Media. . . . . *E. J. Sternglass and D. A. Stuart* 427
Design Data and Methods
Design of Helical and Leaf Springs for Minimum Weight. . . . . *M. F. Spotts* 435
Discussion on previously published papers by *H. H. Bleich; E. H. Kennard; A. K. Oppenheim; D. S. Carter; W. R. Sears; Samuel Levy; W. Wright; T. P. Torda, W. O. Ackermann, and H. R. Burnett; S. I. Pai; and H. D. Conway* 438
Brief Notes
A Strain-Energy Expression for Thin Cylindrical Shells . . . *H. H. Bleich and F. Dimaggio* 448
Angle and Strain Relations in Flat-Plate Lüders' Bands . . . . . *G. R. Irwin* 449
Note on Oil Whip . . . . . *Oscar Pinkus* 450
Book Reviews 451

SEPTEMBER, 1953

VOL. 20, NO. 3

Transactions of The American Society of Mechanical Engineers

Journal of Applied Mechanics

Papers Contributed to the Transactions by the ASME Applied Mechanics Division

EXECUTIVE COMMITTEE OF THE APPLIED MECHANICS DIVISION

DANA YOUNG, *Chairman* N. M. NEWMARK, *Secretary*

JOHN M. LESSELLS, *Technical Editor*

Published Quarterly by

The American Society of Mechanical Engineers

Publication Office, 20th and Northampton Streets, Easton, Pa.
Editorial Department at the Headquarters of the Society, 29 West Thirty-Ninth Street, New York 18, N. Y.

OFFICERS OF THE SOCIETY

FREDERICK S. BLACKALL, JR., *President*

JAMES L. KOPP, *Treasurer* C. E. DAVIES, *Secretary*
E. J. KATES, *Assistant Treasurer*

PUBLICATIONS COMMITTEE

GEORGE R. RICH, *Chairman* GEORGE A. STETSON, *Editor*
K. W. CLEMENTSON, *Mgr. Editor*

By-Law: The Society shall not be responsible for statements or opinions advanced in papers or . . . printed in its publications (B13, Par. 4).

Published quarterly by The American Society of Mechanical Engineers. Publication office at 20th and Northampton Streets, Easton, Pa. The editorial department is located at the headquarters of the Society, 29 West Thirty-Ninth Street, New York 18, N. Y. Cable address, "Dynamic," New York. Price $1.25 a copy; $5.00 a year; to members $2.50 a year, single copy price to members, $1.00. Changes of address must be received at Society headquarters four weeks before they are to be effective on the mailing list. Please send old as well as new address. . . . By-Law: The Society shall not be responsible for statements or opinions advanced in papers or . . . printed in its publications (B13, Par. 4). . . . Entered as second-class matter March 14, 1929, at the Post Office at Easton, Pa., under the Act of August 24, 1912. . . . Copyright, 1958, by The American Society of Mechanical Engineers. Reprints from this publication may be made on condition that full credit be given the JOURNAL OF APPLIED MECHANICS and the author, and that date of publication be stated.

On the Use of Singular Yield Conditions and Associated Flow Rules[1]

By WILLIAM PRAGER,[2] PROVIDENCE, R. I.

It is well known that the use of Tresca's yield condition frequently leads to a simpler system of equations for the stresses in a plastic solid than the use of the yield condition of Mises. However, in most cases where Tresca's yield condition has been used, the flow rule associated with the Mises condition has been retained. Following Koiter,[3] it is shown that further simplification results from the use of the flow rule associated with the Tresca condition. The reason for this is discussed in connection with two examples concerning the finite enlargement of a circular hole in an infinite sheet of perfectly plastic or work-hardening material. The second example is probably the first nontrivial case in which a problem of finite plastic deformation of a work-hardening material has been treated in closed form by the use of incremental stress-strain relations.

Introduction

THE mechanical behavior of a perfectly plastic solid is defined by the yield condition and the flow rule. The yield condition specifies the states of stress under which plastic flow will occur. For each of these states of stress, the flow rule specifies the components of the plastic-strain rate to within an arbitrary common factor. This positive factor is required by the assumption that the solid is inviscid; i.e., the state of stress necessary to cause a certain type of plastic flow does not depend on the speed of deformation. In the following, a set of strain-rate components that are defined only to within a common positive factor will be said to specify a "flow mechanism."

For an isotropic perfectly plastic solid, the orientation of the principal axes of stress does not enter into the yield condition. This condition, therefore, assumes the form

$$f(\sigma_1, \sigma_2, \sigma_3) = 0 \quad \ldots\ldots\ldots\ldots\ldots\ldots [1]$$

where the function f must be symmetric in the principal stresses σ_1, σ_2, σ_3. If the solid retains its isotropy during plastic flow, the principal axes of the strain rate must coincide with those of the stress. The flow rule, therefore, reduces to a relation between the principal stresses σ_1, σ_2, σ_3 and the principal strain rates e_1, e_2, e_3.

It is convenient to represent the yield condition in Equation [1] geometrically by considering σ_1, σ_2, and σ_3 as the rectangular co-ordinates of a point on the "yield surface." The flow rule then may be taken to specify a direction at each point of the yield surface, the three direction cosines being proportional to e_1, e_2, e_3.

Mises[4] proposed the flow rule that associates with each point of the yield surface the direction of the exterior normal of this surface at this point

$$e_1 : e_2 : e_3 = \frac{\partial f}{\partial \sigma_1} : \frac{\partial f}{\partial \sigma_2} : \frac{\partial f}{\partial \sigma_3} \quad \ldots\ldots\ldots\ldots\ldots\ldots [2]$$

In Equation [2] it has been assumed that the sign of the yield function f has been chosen so that the exterior normal of the yield surface indicates the direction of increasing values of f.

The idea of using the yield function f as the "plastic potential" proved useful for the formulation of flow rules for crystals and other anisotropic solids. In recent years the concept of the plastic potential has gained added importance because the theory of limit analysis is based on this relation between the yield condition and the flow rule.[5, 6]

The flow rule in Equation [2] presupposes that there is a uniquely determined exterior normal at each point of the yield surface. Not all yield conditions used in the mathematical theory of plasticity satisfy this regularity requirement. For example, the yield surface corresponding to Tresca's condition of constant maximum shearing stress is a regular hexagonal prism. At a point on an edge of this prism, the exterior normal is not defined; this raises the question of how the flow rule in Equation [2] should be modified at such a singular point.

Consider first a point P on the edge formed by two adjacent flat or curved faces of a yield surface. Each of these faces has a unique exterior normal at P, and each of these normals may be considered as representing a flow mechanism that is possible under the state of stress represented by P. It is natural then to assume that other possible flow mechanisms can be obtained by combining these two fundamental mechanisms in a linear fashion and with positive coefficients.

In the case of Tresca's yield condition, for instance, the faces of the prismatic yield surface lie in the planes

$$\sigma_1 - \sigma_2 = \pm\sigma, \quad \sigma_1 - \sigma_3 = \pm\sigma, \quad \sigma_2 - \sigma_3 = \pm\sigma \ldots [3]$$

where σ is the yield stress in simple tension. For points on one of the adjacent faces $\sigma_1 - \sigma_2 = \sigma$ and $\sigma_1 - \sigma_3 = \sigma_3$, the flow rule of Equation [2] furnishes

$$e_1 : e_2 : e_3 = 1 : -1 : 0 \quad \ldots\ldots\ldots\ldots\ldots\ldots [4]$$

and

$$e_1 : e_2 : e_3 = 1 : 0 : -1 \quad \ldots\ldots\ldots\ldots\ldots\ldots [5]$$

---

[1] The results presented in this paper were obtained in the course of research sponsored by the Office of Naval Research under Contract N7onr-35801 with Brown University.

[2] Professor of Applied Mechanics, Brown University. Mem. ASME.

[3] "On Partially Plastic Thick-Walled Tubes," by W. T. Koiter, Biezeno Anniversary Volume, Haarlem, Holland, 1953, p. 232.

Presented at the National Conference of the Applied Mechanics Division, Minneapolis, Minn., June 18–20, 1953, of THE AMERICAN SOCIETY OF MECHANICAL ENGINEERS.

Discussion of this paper should be addressed to the Secretary, ASME, 29 West 39th Street, New York, N. Y., and will be accepted until October 10, 1953, for publication at a later date. Discussion received after the closing date will be returned.

NOTE: Statements and opinions advanced in papers are to be understood as individual expressions of their authors and not those of the Society. Manuscript received by ASME Applied Mechanics Division, January 2, 1953. Paper No. 53—APM-23.

[4] "Mechanik der platischen Formaenderung von Kristallen," by R. von Mises, *Zeitschrift für angewandte Mathematik und Mechanik*, vol. 8, 1928, pp. 161–185.

[5] "Extended Limit Design Theorems for Continuous Media," by D. C. Drucker, W. Prager, and H. J. Greenberg, *Quarterly of Applied Mathematics*, vol. 9, 1952, pp. 381–389.

[6] "The General Theory of Limit Design," by W. Prager, sectional address presented at the Eighth International Congress of Applied Mechanics, Istanbul, Turkey, 1952, to appear in the Congress Proceedings.

respectively. The first flow mechanism represents pure shear in the σ_1, σ_2 plane; the second mechanism, pure shear in the σ_1, σ_3 plane. The point representing the state of simple tension $\sigma_1 = \sigma$ lies on the common edge of these two faces. According to the flow rule proposed, the flow mechanisms possible under this state of simple tension are characterized by

$$e_1 : e_2 : e_3 = 1 : -\lambda : -(1 - \lambda) \quad [6]$$

where $0 \leq \lambda \leq 1$. The three terms on the right-hand side of Equation [6] are obtained by multiplying the corresponding terms of Equations [4] and [5] by λ and $1 - \lambda$, respectively, and adding the products.

Although the type of singular point just discussed is the only one occurring in connection with Tresca's yield condition, other types, such as a vertex of a polyhedron or a cone, can be treated in a similar manner.

At first glance it might seem that this modification of the flow rule in Equation [2], at singular points of the yield surface, would complicate greatly the mathematical treatment of problems of plastic flow. As was pointed out by Koiter,[8] however, the contrary is true, i.e., a considerable simplification results from the joint use of Tresca's yield condition and the associated flow rule. The reason for this will be explained in connection with examples which also will demonstrate that the simplification by no means is restricted to the case of small plastic deformations considered by Koiter.

Tresca's Yield Condition in Problems of Plane Stress

In problems of plane stress, one of the principal stresses, say σ_3, vanishes, and the yield condition can be represented by a curve or polygon in the σ_1, σ_2 plane. If Tresca's yield condition is used, the yield polygon is formed by the lines with the equations

$$\sigma_1 - \sigma_2 = \pm\sigma, \quad \sigma_1 = \pm\sigma, \quad \sigma_2 = \pm\sigma \quad [7]$$

obtained from Equation [3] by setting $\sigma_3 = 0$. Fig. 1 shows this hexagon, which is an oblique section of the afore-mentioned hexagonal prism. The axis of this prism passes through the origin O and forms equal angles with the positive axes of σ_1, σ_2, and σ_3 (the latter being normal to the plane of Fig. 1).

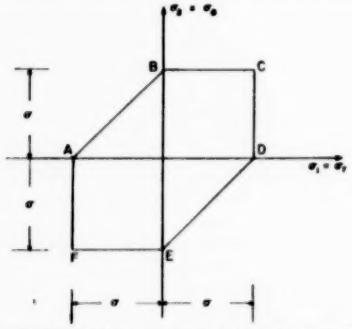

Fig. 1 Tresca Hexagon for Plane Plastic Stress

Consider a generic point P on one side of the yield hexagon, for instance, on A-B. The exterior normal of the three-dimensional yield surface at P is not contained in the plane of the figure. The projection of this normal on the plane of the figure is normal to A-B, however. Thus the ratio $e_1 : e_2$ for the state of stress represented by P may be obtained as the ratio between the direction cosines of the normal to the yield hexagon at P. Once the ratio $e_1 : e_2$ is known, the condition of incompressibility

$$e_1 + e_2 + e_3 = 0 \quad [8]$$

yields the ratios $e_1 : e_2 : e_3$.

All states of stress occurring in the following examples will turn out to be represented by points on the side A-B of the yield hexagon. With $0 \leq \lambda \leq 1$, the modified flow rule then furnishes the following information:

1 State of stress represented by point A

$$\sigma_1 = -\sigma, \quad \sigma_2 = \sigma_3 = 0, \quad e_1 : e_2 : e_3 = -1 : \lambda : (1 - \lambda) \quad [9]$$

2 State of stress represented by interior point of segment A-B

$$\sigma_1 - \sigma_2 = -\sigma, \quad \sigma_3 = 0, \quad e_1 : e_2 : e_3 = -1 : 1 : 0 \quad [10]$$

3 State of stress represented by point B

$$\sigma_2 = \sigma, \quad \sigma_1 = \sigma_3 = 0, \quad e_1 : e_2 : e_3 = -\lambda : 1 : -(1 - \lambda) \quad [11]$$

If the yield stress σ remains constant during plastic flow, the solid is called perfectly plastic; if the yield stress increases during plastic flow, the solid is called work-hardening. For the most general type of work-hardening solid, the form of the yield condition also could change during plastic flow. For example, the hexagon in Fig. 1 could change gradually into an ellipse. This would correspond to a gradual transition from the yield condition of Tresca to that of Mises. This case will not be considered in this paper, however. It will be assumed that during plastic flow the yield hexagon remains centered at the origin and merely increases in size. In the following, the yield stress of the virgin material will be denoted by σ_0 and it will be assumed that the rate of hardening $\dot{\sigma}$ is proportional to the rate D at which mechanical energy is dissipated during plastic flow

$$\dot{\sigma} = \alpha D \quad [12]$$

where α is a constant.

For the three cases being considered, $D = \sigma_1 e_1 + \sigma_2 e_2 + \sigma_3 e_3$ has the following values

$$D = -\sigma e_1 \quad [13]$$

$$D = (\sigma_1 - \sigma_2) e_1 = -\sigma e_1 \quad [14]$$

$$D = \sigma e_3 \quad [15]$$

Finite Enlargement of a Circular Hole

As the first example, consider the finite enlargement of a circular hole in a sheet of a perfectly plastic material. This problem has been treated by Taylor[7] who used Tresca's yield condition but with the flow rule associated with Mises' yield condition. The comparison of Taylor's work with the following analysis reveals the great simplification achieved by the use of the appropriate flow rule.

A circular hole of radius a_0 in an infinite plate of uniform thickness h_0 is to be enlarged to the radius $a = 1.4\, a_0$ by application of a gradually increasing uniform pressure to the edge of the hole. Since finite plastic deformations will be considered, elastic deformations will be neglected. The material at a sufficiently large distance from the hole then must be treated as rigid, because it will not reach the yield limit. Under these circumstances, radial displacement of the material near the hole is made possible only by a thickening of the sheet.

In the elastic part of the sheet the radial stress σ_r and the hoop stress σ_θ are inversely proportional to the square of the radius r, and $\sigma_\theta = -\sigma_r > 0$. Thus the state of stress at the elastic-plastic interface is represented by the center of the segment A-B

[7] "The Formation and Enlargement of a Circular Hole in a Thin Plastic Sheet," by G. I. Taylor, *Quarterly Journal of Mechanics and Applied Mathematics*, vol. 1, 1948, pp. 103–124. See also, "The Mathematical Theory of Plasticity," by R. Hill, Oxford, England, 1950, pp. 307–313.

in Fig. 1. Just inside this interface the yield condition and flow rule are given by Equations [10] with the subscripts 1, 2, and 3 standing for r, θ, and z, respectively. Since $\epsilon_z = 0$, there is no thickening of the sheet and radial displacement is therefore impossible. The material just inside the elastic-plastic interface accordingly remains rigid, even though the stresses σ_r and σ_θ satisfy the yield condition

$$\sigma_r - \sigma_\theta = -\sigma_0 \qquad [16]$$

The condition of radial equilibrium in this rigid plastic zone is

$$\frac{\partial \sigma_r}{\partial r} + \frac{\sigma_r - \sigma_\theta}{r} = 0 \qquad [17]$$

From Equations [16] and [17] and the boundary condition $\sigma_r = -\sigma_\theta = -\sigma_0/2$ at the elastic plastic interface ($r = \rho_0$), it follows that

$$\left.\begin{aligned} \sigma_r &= -\sigma_0 \left(\frac{1}{2} + \log \frac{\rho_0}{r} \right) \\ \sigma_\theta &= \sigma_0 \left(\frac{1}{2} - \log \frac{\rho_0}{r} \right) \end{aligned}\right\} \qquad [18]$$

in the rigid plastic zone. The hoop stress, therefore, is decreasing as one progresses from the elastic-plastic interface into the rigid plastic zone. It follows from the second Equation [18] that the hoop stress vanishes for

$$r = \rho_0/\sqrt{e} = 0.606\rho_0 \qquad [19]$$

This radius, which occurs frequently in the following work, is denoted by ρ. The state of stress at $r = \rho$ is represented by point A in Fig. 1.

Just inside the circle $r = \rho$, the circumferential strain rate ϵ_θ must vanish on account of the rigidity of the surrounding material. The radial strain rate ϵ_r need not vanish, however. The flow mechanism, therefore, is represented by the normal to the side A-F of the yield hexagon.

There are two possibilities regarding the variation of stress and flow mechanism inside the circle $r = \rho$. If the point representing the state of stress moves from A toward F, the flow rule requires that $\epsilon_\theta = 0$. This means that the radial velocity v must remain zero inside the circle $r = \rho$, because $\epsilon_\theta = v/r$. The sheet, therefore, would remain rigid even inside the circle $r = \rho$. If, on the other hand, the point representing the state of stress remains at A, the greater degree of freedom in the choice of the flow mechanism at this singular point allows a plastic deformation of the sheet inside the circle $r = \rho$.

Since the sheet thickness h will not remain constant inside the circle $r = \rho$, the equation of radial equilibrium has the form

$$\frac{\partial (h\sigma_r)}{\partial r} + \frac{h(\sigma_r - \sigma_\theta)}{r} = 0 \qquad [20]$$

Since $\sigma_r = -\sigma_0$, $\sigma_\theta = 0$ when the state of stress is represented by the point A, this equilibrium condition may be written as follows

$$\frac{\partial}{\partial r}(rh) = 0 \qquad [21]$$

While it is convenient to use the terms "velocity," "strain rate," and "rate of dissipation of mechanical energy," it must be remembered that the plastic solids considered here are inviscid. Consequently, the flow process is independent of the time scale, and any variable that increases monotonically during the flow process may be used as a measure of "time." In the following, the radius ρ will be used in this manner.

If the radial velocity is denoted by v, the radial and circumferential strain rates are $\epsilon_r = \partial v/\partial r$ and $\epsilon_\theta = v/r$. The strain rate in the direction normal to the sheet is $(1/h)Dh/D\rho$ where $Dh/D\rho = \partial h/\partial \rho + v\,\partial h/\partial r$ denotes the "material" derivative of h. The condition of incompressibility requires that the sum of the three strain rates vanish

$$\frac{1}{h}\frac{\partial h}{\partial \rho} + \frac{v}{h}\frac{\partial h}{\partial r} + \frac{\partial v}{\partial r} + \frac{v}{r} = 0 \qquad [22]$$

Equations [21] and [22] and the boundary conditions

$$h = h_0, \quad v = 0 \text{ at } r = \rho \qquad [23]$$

define the functions $h = h(r, \rho)$, $v = v(r, \rho)$. From Equation [21] and the first boundary condition given in Equation [23], it follows that

$$h = h_0 \frac{\rho}{r} \qquad [24]$$

With this expression for h, Equation [22] reduces to a differential equation for v. The solution satisfying the second boundary condition given in Equation [23] is

$$v = 1 - \frac{r}{\rho} \qquad [25]$$

(Since the radius ρ is used as a measure of time, the velocity must be dimensionless.) From Equation [25] the strain rates are obtained as follows

$$\epsilon_r = \frac{\partial v}{\partial r} = -\frac{1}{\rho}, \qquad \epsilon_\theta = \frac{v}{r} = \frac{1}{r} - \frac{1}{\rho} \qquad [26]$$

If the material that at time ρ is at the radius r was initially at the radius r_0, conservation of mass requires

$$2\pi \int_r^\rho hr\,dr = \pi h_0(\rho^2 - r_0^2) \qquad [27]$$

Substitution of Equation [24] into Equation [27] yields

$$r = \frac{\rho^2 + r_0^2}{2\rho} \qquad [28]$$

Equation [24] therefore can be written in the form

$$h = 2h_0 \frac{\rho^2}{\rho^2 + r_0^2} \qquad [29]$$

According to Equation [9], the solution just obtained will be valid only if $\epsilon_1 : \epsilon_2$ lies between $-1:0$ and $-1:1$. The first of these bounds is attained at $r = \rho$ where $\epsilon_\theta = 0$ as shown by Equation [26]. The other bound is attained at $r = \rho/2$ where Equation [26] furnishes $\epsilon_r = 1/\rho$, $\epsilon_\theta = 1/\rho$. Equation [28] shows that $r = \rho/2$ corresponds to $r_0 = 0$. Thus the solution remains valid even in the case where a pinhole is enlarged to some finite radius.

Formally, the results obtained in the foregoing agree with those furnished by the "simplified analysis" which Taylor[7] attributes to Bethe. Taylor rejects this analysis because the ratios of the principal strain rates vary although the ratios of the principal stresses are constant. As was shown in this section, Bethe's results can be obtained from a consistent theory, and only experiment can decide whether a given material agrees better with the formulas of Taylor or Bethe.

Influence of Strain-Hardening

The second example differs from the first only in so far as the sheet material is supposed to be work-hardening in accordance with Equation [12]. Since no hardening takes place where the material remains rigid, the stresses outside the circle $r = \rho$ are

the same as in the previous example. To keep track of the progressive hardening of the material inside the circle $r = \rho$, it is necessary to use the Lagrangian co-ordinate r_0 as one of the independent variables, the other independent variable being ρ as before.

Again, $\sigma_\theta = 0$ inside the circle $r = \rho$. Since $\sigma_r = -\sigma$ is no longer constant, the condition of equilibrium, shown in Equation [21], now must be replaced by

$$\frac{\partial}{\partial r}(rh\sigma) = \frac{1}{(\partial r/\partial r_0)} \frac{\partial}{\partial r_0}(rh\sigma) = 0 \quad [30]$$

The solution of this equation that satisfies the boundary conditions $h = h_0$, $\sigma = \sigma_0$ for $r = \rho$ is

$$rh\sigma = \rho h_0 \sigma_0 \quad [31]$$

In accordance with Equations [12] and [13], the rate of strain-hardening is

$$\frac{\partial \sigma}{\partial \rho} = \alpha D = -\alpha \sigma \epsilon_r \quad [32]$$

where

$$\epsilon_r = \frac{\partial v}{\partial r} = \frac{1}{(\partial r/\partial r_0)} \frac{\partial v}{\partial r_0} = \frac{1}{(\partial r/\partial r_0)} \frac{\partial^2 r}{\partial r_0 \partial \rho} = \frac{\partial}{\partial \rho} \log \left| \frac{\partial r}{\partial r_0} \right| \quad [33]$$

With the use of this expression for ϵ_r, Equation [32] can be written as follows

$$\frac{\partial}{\partial \rho}\left(\sigma^{1/\alpha} \left| \frac{\partial r}{\partial r_0} \right|\right) = 0 \quad [34]$$

The circumferential strain rate is

$$\epsilon_\theta = \frac{v}{r} = \frac{1}{r} \frac{\partial r}{\partial \rho} = \frac{\partial}{\partial \rho} \log r \quad [35]$$

and the strain rate, in the direction normal to the plane of the sheet is

$$\epsilon_z = \frac{1}{h} \frac{\partial h}{\partial \rho} = \frac{\partial}{\partial \rho} \log h \quad [36]$$

The condition of incompressibility, therefore, can be written in the form

$$\frac{\partial}{\partial \rho}\left(hr \left| \frac{\partial r}{\partial r_0} \right|\right) = 0 \quad [37]$$

Those solutions of the differential Equations [34] and [37] that are compatible with Equation [31] and satisfy the boundary condition $\sigma = \sigma_0$ for $r = \rho$ are

$$\sigma = \sigma_0 \left(\frac{\rho}{r_0}\right)^{\alpha/(1+\alpha)} \quad [38]$$

and

$$r = \frac{\rho}{2+\alpha}\left[1 + (1+\alpha)\left(\frac{r_0}{\rho}\right)^{(2+\alpha)/(1+\alpha)}\right] \quad [39]$$

As before, the solutions represented by Equations [31], [38], and [39] are valid only as long as the ratio $\epsilon_r : \epsilon_\theta$ remains below -1. From Equations [33] and [35] it is found that this is the case when $r > \rho/2$. According to Equation [39] this means that the following inequalities must be fulfilled if this solution is to be valid

$$\frac{a_0}{\rho} > \left(\frac{\alpha}{2}\right)^{\frac{1+\alpha}{2+\alpha}} \quad [40]$$

$$\frac{a}{a_0} < \frac{1}{2+\alpha}\left[1 + (1+\alpha)\frac{\alpha}{2}\right]\left(\frac{\alpha}{2}\right)^{-\frac{1+\alpha}{2+\alpha}} \quad [41]$$

To indicate the manner in which Bethe's solution for a perfectly plastic sheet is modified by work-hardening, assume that $\alpha = 0.5$. For simple tension, this corresponds to 0.5 per cent increase in yield stress for a strain of 1 per cent. Fig. 2 shows the

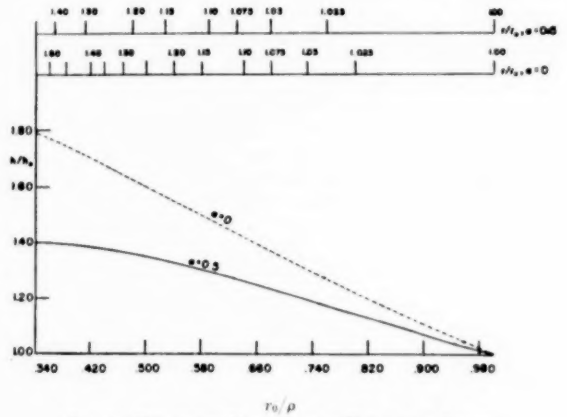

FIG. 2 THICKNESS VARIATION IN DEFORMED SHEET

thickness distribution plotted versus r_0/ρ and r/r_0. The solid curve corresponds to $\alpha = 0.5$ and the dotted curve to $\alpha = 0$. It is seen that even such a small amount of strain-hardening has a significant influence on the thickness distribution. According to Equation [41] the solution represented by the solid curve in Fig. 2 is valid for $a/a_0 < 1.48$.

CONCLUSION

It has been shown that the joint use of Tresca's yield condition and the associated flow rule can lead to a considerable simplification of the mathematical work in problems of plane plastic stress. This is so because corresponding to the sides and the vertexes of the yield polygon, one has either a unique flow mechanism and a one-parameter family of principal stress values, or unique values of the principal stresses and a one-parameter family of flow mechanisms. In either case, considerable simplifications result, and the complete solution is built up of zones in which one or the other type of simplification pertains.

ACKNOWLEDGMENT

The author is indebted to Professor Koiter for the use of an advance copy of his paper.[3]

Graphical-Numerical Solution of Problems of Saint-Venant Torsion and Bending

By B. A. BOLEY[1] NEW YORK, N. Y.

A simple successive-approximations procedure for the solution of the problems of Saint-Venant torsion and bending of beams of arbitrary cross section is presented. The shear stresses in a cross section of the beam are first calculated from the formulas valid for thin-walled sections, on the basis of an assumed set of lines of shearing stress. From these a first approximation to the stress function of either the torsion or the bending problem is found. The second approximation to the stress function is then obtained from the governing equation of the problem, expressed in finite-difference form; this in turn allows the determination of an improved set of lines of shearing stress, and hence of the shearing stress itself. The procedure can be repeated until the results of two successive steps are sufficiently close. Applications are presented for a beam cross section for which the exact solutions are known, and it is shown that no further difficulties arise in applications to more complicated shapes.

Nomenclature

The following nomenclature is used in the paper:

A = mean of areas enclosed by outer and inner boundaries of a thin-walled closed section
C = shearing rigidity of a thin-walled closed section, defined in Equation [3]
G = shear modulus
I = moment of inertia about neutral axis
i, j = subscripts indicating line of shearing stress, or "shell" bounded by two neighboring such lines
Q = static moment of an area
q = shear flow
q' = $(1/2)(qC'/T)$ for torsion problem; $= q(I/V)$ for bending problem
q_i = $\tau_i t_i$
s = distance along median line of thin-walled section
T = torque
t = thickness; direction perpendicular to s
V = shear-force component perpendicular to neutral axis
x, y = axes in cross section of bar
z = axis measuring distance along bar
θ = angle of twist per unit of length
ν = Poisson's ratio
τ = shear stress
$\tau_{zx}, \tau_{yz}, \tau_{zs}$ = shear stress in x, y, s-directions, respectively, acting in cross section of bar
φ = stress function for torsion problem
ψ = stress function for bending problem
ψ' = $\psi(I/V)$

Introduction

The rigorous analytical calculation of the shearing stresses in solid prismatical bars under torsion or bending is difficult to obtain except for particular cross-sectional shapes. On the other hand, the behavior of thin-walled sections is always easily determined with the aid of well-known formulas, some of which are listed in the paper for purposes of reference. These formulas may be used, however, to simplify the analysis of solid bars, since a portion of such a bar bounded by two neighboring lines of shearing stress behaves as a thin-walled section and therefore may be treated as such. A line of shearing stress is a line whose tangent is, at any point, in the direction of the resultant shearing stress at that point. Thus the relation

$$\tau_{zx}dy - \tau_{yz}dx = 0 \qquad [1]$$

holds on any such line, x and y denoting mutually perpendicular directions in the plane of a cross section, z the distance along the longitudinal axis of the bar, and τ_{zx} and τ_{yz} the shear stresses in the x and y-directions, respectively. Use of these lines in the solution of the torsion problem was made by Batho (1),[2] but his method could be applied in a practical way only to sections for which the rigorous solution could be found by the classical methods as well.

It is evident that if the position and shape of the lines of shearing stress were known for a particular bar, the stresses could be found readily. A step-by-step procedure by means of which these lines may be approximated as closely as desired is described in this paper. As examples, the stresses in a bar under either torsion or bending are determined for a cross-sectional shape for which the results of the suggested procedure can be compared with the exact values; however, the method is sufficiently general to be applicable to all cross-sectional shapes without additional difficulties. The problems of torsion and bending are considered in that order.

The formulas needed for the analysis of thin-walled sections are listed here. The shear flow q in a closed thin-walled section under a pure torque T is

$$q = T/(2A) \qquad [2]$$

where A is one half the sum of the areas enclosed by the outer and the inner boundaries of the section. The corresponding angle of twist θ per unit of length is

$$\theta = [T/(4A^2G)]\oint(1/t)ds = T/(GC) \qquad [3]$$

where G is the shear modulus, t the thickness, C the torsional rigidity, and s is the distance along the median line of the section.

The shear flow q in an open thin-walled section bent by a transverse force is

$$q = VQ/I \qquad [4]$$

[1] Associate Professor of Civil Engineering, in charge of Aircraft Structures, Columbia University.

Presented at the National Conference of the Applied Mechanics Division, Minneapolis, Minn., June 18–20, 1953, of The American Society of Mechanical Engineers.

Discussion of this paper should be addressed to the Secretary, ASME, 29 West 39th Street, New York, N. Y., and will be accepted until October 10, 1953, for publication at a later date. Discussion received after the closing date will be returned.

Note: Statements and opinions advanced in papers are to be understood as individual expressions of their authors and not those of the Society. Manuscript received by ASME Applied Mechanics Division, October 14, 1952. Paper No. 53—APM-22.

[2] Numbers in parentheses refer to the Bibliography at the end of the paper.

where I is the moment of inertia of the cross section about the neutral axis, V the component of the shear force perpendicular to that axis, and Q the integral

$$Q = \int_0^{s_1} yt\, ds \quad [4a]$$

where y is the perpendicular distance between the neutral axis and the point s. The point at which the stresses are sought is denoted by $s = s_1$; one of the free edges of the section is denoted by $s = 0$.

The relation between the shear flow and the shear stress is

$$\tau = q/t \quad [5]$$

or, more generally

$$\tau = dq/dt \quad [5a]$$

Derivations of the above formulas may be found, for example, in reference (2).

Torsion

The problem of Saint-Venant torsion requires (3) the solution of the equation

$$\frac{\partial^2 \varphi}{\partial x^2} + \frac{\partial^2 \varphi}{\partial y^2} = -2G\theta \quad [6]$$

where φ is a stress function, under the condition that

$$\varphi = \text{const} \quad [6a]$$

at all points of the boundary. For a solid section this constant is usually taken equal to zero. The shearing stresses τ_{xz}, τ_{yz}, and τ_{sz} in the x, y, and s-directions, respectively, are

$$\tau_{xz} = \frac{\partial \varphi}{\partial y}; \quad \tau_{yz} = -\frac{\partial \varphi}{\partial x}; \quad \tau_{sz} = -\frac{\partial \varphi}{\partial t} \quad [6b]$$

where the t-direction is perpendicular to s. Substitution into Equation [1] shows that along any line of shearing stress φ is constant; hence the boundary of the cross section is one such line. Comparison of the last of Equations [6b] with Equation [5a] shows that the symbols φ and q represent the same quantity, provided that the direction s is taken at any point as that of the line of shearing stress through that point.

The proposed method of solution consists of the following steps:

Step 1. Plot an assumed set of lines of shearing stress, and number them consecutively from the outside proceeding inward. Thus line 1 is the boundary of the beam cross section. Let the "shell" bounded by the ith and the $(i + 1)$th line be known as the ith shell. For each of these calculate the quantity $\Delta q_i'$ defined by the formula

$$\Delta q_i' = \Delta\left(\frac{q_i C}{2T}\right) = A_i/[\oint (1/t_i) ds_i] \quad [7]$$

in which the quantities T and C have been taken from Equations [2] and [3]. For each line of shearing stress calculate the quantity q_i' from the formula

$$q_i' = \sum_{j=1}^{j=i-1} (\Delta q_j'); \quad q_1' = 0 \quad [8]$$

The previous discussion shows that q_i' must also satisfy Equation [6]; since, however, it is only known at a finite number of points, that equation will be rewritten in finite-difference form. Consider two mutually perpendicular axes, intersecting at point O, and denote as A and C two neighboring points on one of these axes, and as B and D two similar points on the other. Let a, b, c, and d be the distances from O to A, B, C, and D, respectively; then the desired equation is (4)

$$\frac{q_a' - q_o'}{a(a + c)} + \frac{q_b' - q_o'}{b(b + d)} + \frac{q_c' - q_o'}{c(c + a)} + \frac{q_d' - q_o'}{d(d + b)} = -(1/2) \quad [9]$$

where q_a', q_b', q_c', q_d', and q_o' are the values of q' at the points indicated by the subscripts. A slightly different form of this equation was given by Southwell (5). For a special case in which some of the distances a, b, c, d are equal it reduces to one given by Salvadori (6); the general case used here is easily derived with the formulas given in this reference. If all the rays are equal, that is, if $a = b = c = d$, Equation [9] reduces to

$$q_a' + q_b' + q_c' + q_d' - 4q_o' = -a^2 \quad [9a]$$

Step 2. Obtain an improved set of lines of shearing stress with the aid of Equation [9], as follows: Equation [9] holds for any pair of mutually perpendicular axes; construct then such a pair, crossing at a point O in the ith shell; let the four intersections of these axes with the ith and the $(i + 1)$th lines of shearing stress be the points A, B, C, and D mentioned previously. The values of q_a', q_b', q_c', and q_d' are then known and q_o' can be determined from Equation [9]. Repeat the entire process for each shell; then interpolate a set of contour lines for the quantity q', that is, lines of constant q'; these are the improved lines of shearing stress. Step 1 may now be repeated on the basis of these new lines, and the whole process used as many times as necessary to give acceptably close results between successive cycles. All that remains then is to calculate the shear stress τ_i at any point in the ith shell from the formula

$$\tau_i = (\Delta q_i)/t_i \quad [10]$$

The quantity (Δq_i) is found from $(\Delta q_i')$ by means of Equation [7] and the relation

$$C = \sum_{i=1}^{n} C_i = 4 \sum_{i=1}^{n} [A_i^2/\oint (1/t_i) ds_i] \quad [11]$$

where C_i is the shearing rigidity of the ith shell and n is the number of shells.

Some of the possible variations of which the foregoing basic procedure admits are illustrated by the following numerical example.

Numerical Example for Torsion Problem

Let it be required to find the shear-stress distribution and the shearing rigidity for a beam with an equilateral-triangular section of height 9 in., subjected to a torque T. One sixth of the triangle only need be considered because of symmetry. Line 1 in Fig. 1(a) represents the boundary of the cross section; there $q_1' = 0$. As a first guess, the lines of shearing stress also were taken to form equilateral triangles; the first of these is indicated by line 2 in Fig. 1(a). Substitution of numerical values into Equations [7] and [8] gives $q_2' = \Delta q_1' = 1.38$ (all values of q_i' are given in square inches). Because of the crudeness of the first guess it was decided to obtain a correction immediately; for this purpose the values of q' were calculated of points A and B, Fig. 1(a). At point A all rays are equal (only two of them are shown because of symmetry; $a = 0.707$ in.) and therefore Equation [9a] applies. At point B the rays were scaled off as follows: $a = 1.042$ in., $b = 0.6$ in. $= d$, $c = 0.372$ in.; hence Equation [9] applies. Substitution gives $q_A' = 0.815$ and $q_B' = 0.68$. Point C in Fig. 1(a) was then determined (by linear interpolation between points B and D) as the point where $q_C' = 0.815$, and therefore lies on the same line of shearing stress as point A. Other such points were

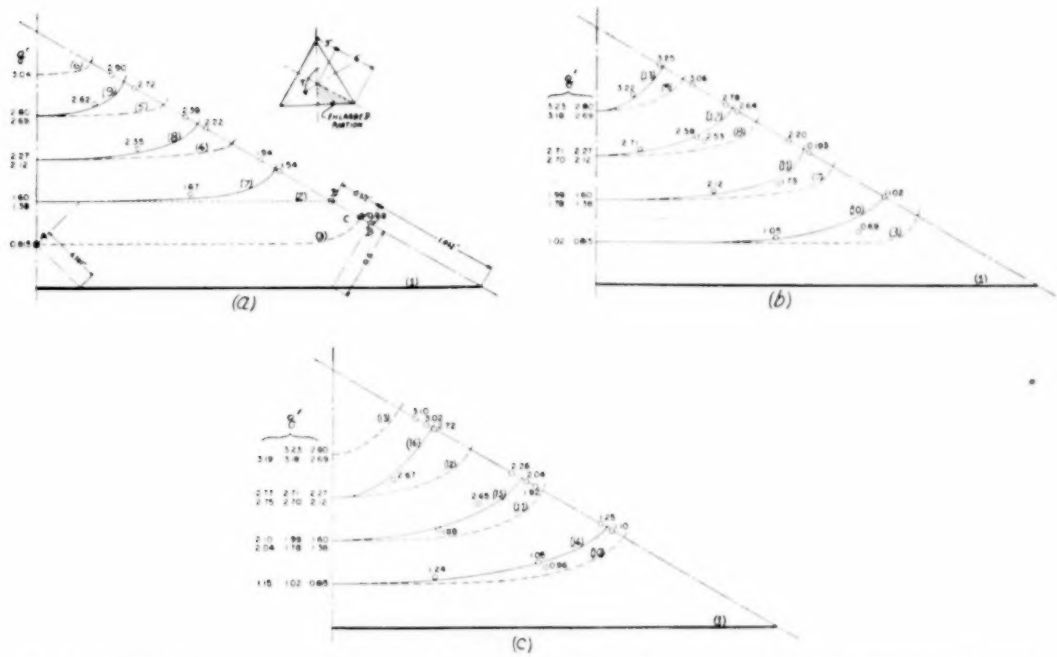

FIG. 1 VARIOUS APPROXIMATIONS FOR LINES OF SHEARING STRESS IN AN EQUILATERAL-TRIANGULAR SECTION IN TORSION
(Numbers in parentheses refer to lines; others are values of q' in square inches.)

found between A and C and then the improved line of shearing stress denoted as line 3 in Fig. 1(a) was plotted.

At this point a complete new set of lines of shearing stress was assumed, consisting of lines 3, 4, 5, and 6 in Fig. 1(a). Equations [7] and [8] led to $q' = 2.12$, 2.69, and 3.04 for lines 4, 5, and 6, respectively; at line 3, as before, $q_3' = 0.815$. Equation [9] was then employed to determine the values of q' shown in Fig. 1(a) next to their corresponding points. From these the next approximation to the lines of shearing stress, shown as lines 7, 8, and 9 in Fig. 1(a), was interpolated, corresponding to $q_7' = 1.60$, $q_8' = 2.27$, $q_9' = 2.80$. The values of q' for the last two cycles are listed on the left-hand side of Fig. 1(a); since there is a large discrepancy between the two results the procedure was repeated.

Lines 7, 8, and 9 are the best approximation thus far available; therefore they were taken as the initial guess in Fig. 1(b). Equations [7] and [8] gave the new values of $q_7' = 1.78$, $q_8' = 2.70$, $q_9' = 3.18$. Use of Equation [9] and the previously discussed interpolation procedure gave the next approximation, shown in Fig. 1(b) as lines 10, 11, 12, and 13, corresponding to $q_{10}' = 1.02$, $q_{11}' = 1.99$, $q_{12}' = 2.71$, $q_{13}' = 3.23$. One more similar repetition was carried out as indicated in Fig. 1(c). The final approximations are the full lines, 14, 15, and 16 of that figure and correspond to $q_{14}' = 1.15$, $q_{15}' = 2.1$, $q_{16}' = 2.77$.

These lines divide the section into four shells with the following shearing rigidities: $C_1 = 158.9$ in^4; $C_2 = 70.5$ in^4; $C_3 = 30.4$ in^4; $C_4 = 11.4$ in^4. The shearing rigidity of the entire cross section is then $C = 271.2$ in^4. The exact value is (7) $C = 252.8$ in^4; the difference between the two is about 7.3 per cent of the exact value. The maximum shear stress given by Equation [10] is $\tau_{max} = 0.017$ psi. The exact value is (7) $\tau_{max} = 0.0178$ psi; the error is about 4.5 per cent of the exact value. Fig. 2 shows the variation of the shear stress along the altitude of the triangular section, as calculated by the present procedure, as well as the exact results. It may be seen that the agreement between the two is good.

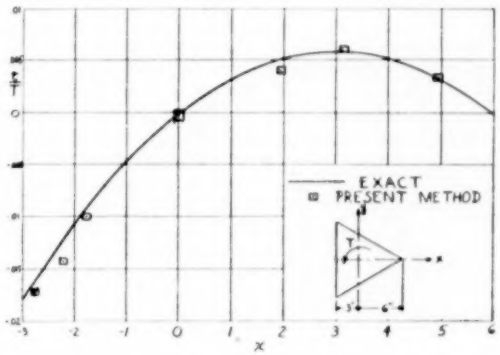

FIG. 2 VARIATION OF SHEAR STRESS ALONG LINE $y = 0$

The following remarks regarding the example may be of some interest. The quantity $[\Sigma(1/t)\Delta s]$ was used in place of the integral $[\oint(1/t)ds]$; the thickness t was measured normal to the median line of the shell in question at the mid-point of the segment Δs. A double-scale drawing of the section was found satisfactory to scale off the required distances and thicknesses. All areas were measured by means of a planimeter, and all calculations were performed with a slide rule.

BENDING

The behavior of a prismatic cantilever beam under the action of a concentrated end load may be described mathematically in a number of slightly different, though equivalent, manners (3, 8). The one chosen here was given by Timoshenko (7) and requires the solution of the equation

$$\frac{\partial^2\psi}{\partial x^2} + \frac{\partial^2\psi}{\partial y^2} = 0 \quad \ldots\ldots\ldots\ldots\ldots\ldots [12]$$

for the stress function ψ under the condition that

$$\psi' = \psi(I/V) = (1/2)\int y^2 dx - [\nu/(1+\nu)](x^3/6) + \text{const.} \ldots [12a]$$

along the boundary of the section. The shearing stresses are

$$(I/V)\tau_{yz} = \frac{\partial\psi'}{\partial x} - (y^2/2) + [\nu/(1+\nu)](x^2/2) \ldots [12b]$$

$$(I/V)\tau_{xz} = -\frac{\partial\psi'}{\partial y} \quad \ldots\ldots\ldots\ldots\ldots\ldots [12c]$$

Substitution of these into Equation [1] shows that Equation [12a] must hold along any line of shearing stress; hence the boundary of the cross section is again one of these lines.

The proposed method of solution for the bending problem consists essentially of the same steps as that for torsion; the main differences arise from the fact that here the shear flow and the stress function are no longer the same quantity. The basic steps are as follows:

Step 1. Plot an assumed set of lines of shearing stress, and let the ith of these be denoted by the subscript i. For each line calculate

$$\Delta q_i' = (\Delta q_i)(I/V) = Q_i \quad \ldots\ldots\ldots\ldots [13]$$

and then q_i' from Equations [8]. Note that $(V_i/I_i) = (V/I)$, where V_i and I_i are, respectively, the load carried and the moment of inertia of the ith shell. Integration of Equation [12b] with respect to x (y being kept constant) leads to the relation

$$[\psi'(x_2, y) - \psi'(x_1, y)] = (I/V)\int_{x_1}^{x_2} \tau_{yz}\, dx + (y^2/2)(x_2 - x_1) - [\nu/(1+\nu)][(x_2^3 - x_1^3)/6] \ldots [14]$$

The term containing the integral may be replaced by the quantity q_i' (see Equations [8]) provided that points x_1 and x_2 lie on the ith and $(i+1)$th lines of shearing stress, respectively. Calculate then from Equation [12a] the values of ψ' along the boundary, choosing a suitable value for the constant appearing in that equation; let these values be $\psi'(x_1, y)$; then ψ' can easily be obtained from Equation [14] along any other line of shearing stress.

Step 2. Improved values of ψ' may now be determined by satisfying Equation [12] in finite difference form, that is

$$\frac{\psi_a' - \psi_o'}{a(a+c)} + \frac{\psi_b' - \psi_o'}{b(b+d)} + \frac{\psi_c' - \psi_o'}{c(c+a)} + \frac{\psi_d' - \psi_o'}{d(d+b)} = 0 \ldots [15]$$

in a notation similar to that employed for Equation [9]. The shear flow and the shear stress may then be solved for from Equations [14] and [10], respectively.

An improved set of lines of shearing stress, which is required to obtain the next approximation, may be found as follows: Consider, for example, the line of shearing stress passing through the point (x_1, y_1), and let it be required to find the point (x_2, y_2) where this line crosses $y = y_2$. Using the best available values of ψ', plot a curve of ψ' against x for $y = y_1$ and a similar curve for $y = y_2$: read from the first of these the value $\psi_1' = \psi'(x_1, y_1)$. Rewrite Equation [12a] as follows

$$\psi_2' - \psi_1' = \Delta Q - [\nu/(1+\nu)][(x_2^3 - x_1^3)/6] \ldots [16]$$

where ΔQ is the static moment about the neutral axis of the area bounded by the lines $x = x_1$, $y = y_1$, $x = x_2$ and the desired line of shearing stress. Approximating the last of these by a straight line, one may write

$$\Delta Q = (1/6)(y_1^2 + y_1 y_2 + y_2^2)(x_2 - x_1) \ldots [17]$$

Since a curve of ψ_2' against x_2 is available, the only unknown remaining in Equation [16] is x_2; it may be solved for by trial and error. Thus the point (x_2, y_2) has been found; by the same process further points along the same line of shearing stress may be calculated, and the entire line constructed.

Numerical Example for Bending Problem

The shear-stress distribution will be calculated in a cantilever beam with an equilateral-triangular section of height 12 in. Only one half the triangle, as shown in Fig. 3, need be considered because of symmetry. Poisson's ratio was taken as 0.5, because for this value the exact results are known (7, 8). The value of ψ' at the point (8, 0) was taken as zero; this determined the constant in Equation [12a] for the boundary of the cross section. The initial guess for the lines of shearing stress is shown in Fig. 3. The values of ψ' at points 1 to 23 were then calculated, and the results collected in Table 1. It may be noticed that for many points ψ' may be obtained by two equivalent methods. Consider, for

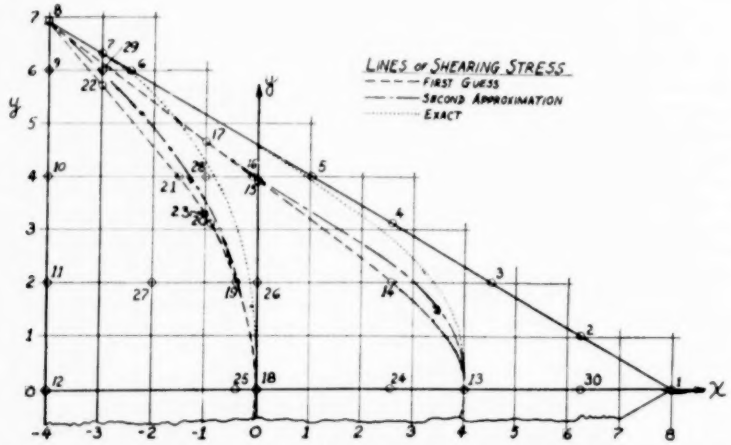

Fig. 3 Various Approximations for Lines of Shearing Stress in an Equilateral-Triangular Section in Bending
(Numbers refer to points in Table 1.)

TABLE 1 VALUES OF ψ'

Point no.	x (in.)	y (in.)	ψ' (in²)	—Points from which ψ' was found— By Eq. [12a]	By Eq. [14]	By Eq. [15]
1	8	0	0	Assumed Value		
2	6.27	1	14.50	1	.....	.....
3	4.52	2	20.95	1	.....	.....
4	2.57	3.12	18.65	1	.....	.....
5	1.02	4	9.50	1	.....	.....
6	−2.47	6	−34.40	1	.....	.....
7	−3	6.31	−44.00	1	.....	.....
8	−4	6.94	−64	1	.....	.....
9	−4	6	−64	8	6	.....
10	−4	4	−64	8	5	.....
11	−4	2	−64	8	3	.....
12	−4	0	−64	8	1	.....
13	4	0	2.90	..	1	.....
14	2.57	2	4.30	13	3	.....
15	0	3.92	−6.50	13	.....	.....
16	−0.09	4	−7.28	13	5	.....
17	−1	4.70	−16.33	13	.....	.....
18	0	0	−22.82	..	1, 12, or 13	.....
19	−0.38	2	−23.20	18	3, 11, or 14	.....
20	−0.90	3.10	−24.78	18	.....	.....
21	−1.50	4	−29.02	18	5, 10, or 16	.....
22	−3	5.76	−46.00	18	.....	.....
23	−1	3.30	−25.41	18	.....	.....
24	2.57	0	0.69	..	.....	13, 14, 18
25	−0.38	0	−24.80	..	.....	12, 18, 19
26	0	2	−17.92	..	.....	14, 15, 18, 19
27	−2	2	−37.75	..	.....	10, 12, 18, 20
28	−1	4	−20.90	..	.....	16, 17, 21, 23
29	−3	6	−45.10	..	.....	6, 7, 9, 22
30	6.27	0	12.60	..	.....	1, 2, 13

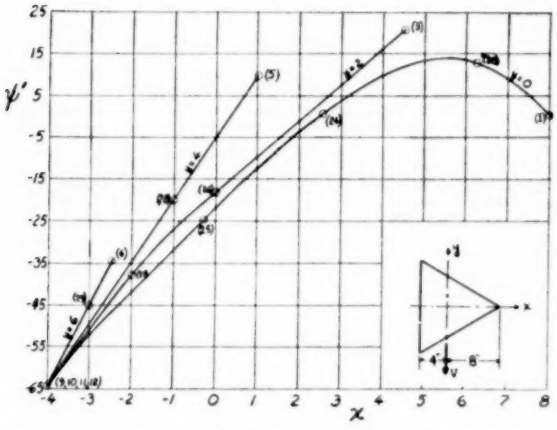

FIG. 4 VARIATION OF STRESS FUNCTION ψ' WITH x, CORRESPONDING TO SECOND APPROXIMATION
(Numbers in parentheses refer to points in Fig. 3.)

example, point 13. At point 1, $\psi_1' = 0$; one may then calculate first ψ_2' from Equation [12a] and then ψ_{13}' from Equation [14], or first calculate ψ_{11}' from Equation [14] and then ψ_{13}' from Equation [12a]. Another check is provided by the fact that, along the line $x = -4$, ψ' must be constant (see Equation [12a]).

Equation [15] was then employed to calculate the remaining values of ψ' given in Table 1. From these the variation of ψ' with x along the lines $y = 0$, $y = 2$, $y = 4$, $y = 6$, was plotted as shown in Fig. 4, noting that the correct value of ψ' is known on the boundary of the cross section. To obtain satisfactory accuracy it was found desirable to employ an enlarged plot of this figure at least 10 in. × 12 in. in size.

The stress τ_{yz} now can be obtained from Equation [12b]. Fig. 5 shows the variation of this stress along the line $x = -4$, corresponding to the initial guess for the lines of shearing stress, the newly found second approximation, and the exact results. The error in the maximum stress corresponding to the initial guess is 18.9 per cent of the exact value, while the error in the second approximation is 7.9 per cent of that value.

These results probably are accurate enough for most practical purposes; in general, however, the exact results would not be

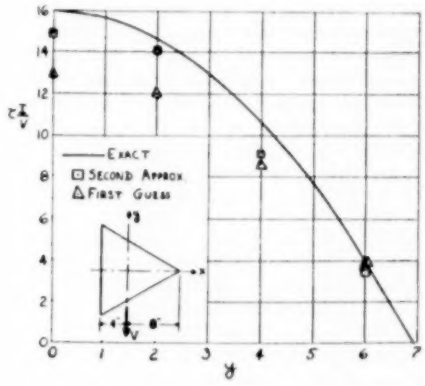

FIG. 5 VARIATION OF SHEAR STRESS ALONG LINE $x = -4$

available for comparison and therefore the next approximation would have to be found. The required improved set of lines of shearing stress was then determined by the method outlined previously. The details of the plotting of the line of shearing stress passing through the origin are described in the following:

Point (x_1, y_1) of Equation [16] was chosen as the origin. Then, from Fig. 4, $\psi_1' = -20.9$. For $y_2 = 2$, a trial-and-error solution of Equation [16] gave $x_2 = -0.40$ and $\psi_2' = -21.2$. Thus the sought line of shearing stress passes through the points (0, 0) and (−0.4, 2). The next point was found by letting $(x_1, y_1) = (-0.4, 0)$ and $\psi_1' = -21.2$ in Equation [16]; calculations showed that $(x_2, y_2) = (-1.3, 4)$ and $\psi_2' = -25.2$. Similarly, the point (−3, 6) was also found to lie on this line of shearing stress, a plot of which is shown in Fig. 3 along with the actual line of shearing stress. The line of shearing stress passing through (4, 0) was corrected in a similar manner and shown in Fig. 3.

An estimate of the importance of the difference between the guessed and corrected positions of the lines of shearing stress may be found as follows: The average stress τ_{avg}, along the line $y = y_0$, in the region $x_1 < x < x_2$, is

$$\tau_{avg} = (I/V)Q_{x_1,x_2} \quad [18]$$

where Q_{x_1,x_2} is the static moment about the neutral axis of the area bounded by the line y_0 and the lines of shearing stress passing through (x_1, y_0) and (x_2, y_0). The results obtained with $y_0 = 0$, collected in Table 2, show that further repetitions of this procedure are necessary to obtain satisfactory results in the region $4 < x < 8$. In the neighborhood of the maximum stress, however, the second approximation gives fairly good results.

TABLE 2 AVERAGE SHEAR STRESS τ_{avg} at $y = 0$

From x =	To x =	$(I/V)\tau_{avg}$ exact	$(I/V)\tau_{avg}$ 2nd approximation
−4	0	13.33	12.0
0	4	8.00	7.0
4	8	2.67	5.0

GENERAL REMARKS

The rapidity of the convergence of the procedures described in the foregoing depends not only on the accuracy of the initial guess for the lines of shearing stress, but also on the details of the calculation. An investigation of some of these was carried out by Merchant (9) whose contributions to the development of these methods are gratefully acknowledged. He showed that in the torsion problem, for example, convergence is improved by choosing the lines of shearing stress close together near the boundary of the cross section, and farther apart away from there.

The methods suggested in this paper can also be applied in cases of combined torsion and bending loadings and to beams with asymmetrical cross sections. Whenever the position of the center of twist is known (as, for example, because of symmetry, in the equilateral-triangular section discussed previously) it is of course possible to break up any combined loading into a twist about the center of twist plus a shear force through that point. If the center of twist is not known, the usual methods (4, 8) can be applied here. For example, one may determine first the position of the center of twist by solving the problem of bending twice on the basis of two assumed neutral axes, in each case determining the line of action of the shear force resultant so as to cause no twisting moment. The intersection of the two lines of action thus determined is the center of twist; once this point is known the solution can be obtained readily.

Accurate drawings, from which the required distances may be scaled off, are of course necessary in any application of these methods. This is especially true in the bending problem, where small differences of large numbers sometimes arise. In the example discussed previously it was noticed that serious errors resulting from this cause could be avoided by the use of carefully plotted curves of ψ' against x, Fig. 4, and by employing all the checks available on the calculations. Some of these have been indicated in the text; others are easily devised if it is remembered that the exact values of the stress functions are always known on the boundary of the cross section. As in most successive approximation methods, however, errors made in any one cycle do not change the final results, but merely retard the convergence.

The results of the torsion example show that fairly rapid convergence may be obtained even when the initial guess is greatly in error. The bending example shows that a crude net of lines of shearing stress sometimes may be sufficient to give satisfactory results. If the calculations have been carried through a large number of cycles, an improved value of the maximum stress sometimes may be obtained by means of one of the graphical extrapolation procedures described in reference (10). The most advantageous details of the procedure, from the standpoints of accuracy and convergence have not, of course, been studied fully in this paper, but the results given seem to indicate that the suggested procedure offers a promising method of analysis of beams of complicated shapes under bending and torsion. It may be of interest to note that the solution of each of the illustrative examples was obtained in approximately $3^1/_2$ hr.

BIBLIOGRAPHY

1 "The Torsion of Solid and Hollow Prisms and Cylinders," by C. Batho, *Engineering*, vol. 102, November 24 and December 1, 1916, pp. 497–498, 521–522.

2 "Strength of Materials," by S. Timoshenko, The Macmillan Company, New York, N. Y., 1938; also Reference (7).

3 "A Mathematical Theory of Elasticity," by A. E. H. Love, Dover Publications, New York, N. Y., fourth edition, 1944.

4 "Analytical Investigations of High-Solidity Thin-Wing Designs," by the Department of Aeronautical Engineering, University of Cincinnati, Air Force Technical Report 5682, February, 1948.

5 "Relaxation Methods in Theoretical Physics," by R. V. Southwell, Clarendon Press, Oxford, England, 1946.

6 "Numerical Computation of Buckling Loads by Finite Differences," by M. G. Salvadori, Paper No. 2441, Trans. ASCE, vol. 116, 1951, p. 590; or "Numerical Methods in Engineering," by M. G. Salvadori and M. L. Baron, Prentice Hall, Inc., New York, N. Y., 1952, p. 213ff.

7 "Theory of Elasticity," by S. Timoshenko, McGraw-Hill Book Company, Inc., New York, N. Y., first edition, 1934.

8 "Mathematical Theory of Elasticity," by I. S. Sokolnikoff, McGraw-Hill Book Company, Inc., New York, N. Y., first edition, 1946.

9 "A Numerical Solution for the Torsion of Bars of Arbitrary Section," by M. K. Merchant, thesis submitted to the Department of Aeronautical Engineering, The Ohio State University, Columbus, Ohio, 1951.

10 Discussion to the first of References (6) by Bruno A. Boley, Trans. ASCE, vol. 116, 1951, p. 627.

Elastic Spheres in Contact Under Varying Oblique Forces[1]

By R. D. MINDLIN[2] and H. DERESIEWICZ,[3] NEW YORK, N. Y.

An investigation is made of the phenomena occurring at the contact surfaces of like elastic spheres subjected to a variety of applied forces. Owing to the presence of slip, with its associated energy dissipation and permanent set, the changes in tractions and displacements depend not only upon the initial state of loading, but upon the entire past history of loading and the instantaneous relative rates of change of the normal and tangential forces. On the basis of three of the simplest cases of varying oblique forces, a set of rules of procedure is assembled and then applied to two types of problems. In the first, the initial tangential compliances are calculated for a variety of past histories and instantaneous rates of loading; in the other, a detailed history of a varying oblique force is investigated.

1 Introduction

THE mathematical study of the effects produced by mutual compression of elastic bodies was initiated by Hertz[4] who considered the case in which the forces between bodies are normal to the contact surfaces. Recent studies[5, 6, 7] of the effects of forces tangential to the contact surfaces have revealed the necessity for taking slip into account. This phenomenon, with its accompanying energy dissipation and permanent set, introduces nonlinearities of a different character than the Hertz nonlinearity. Not only do the changes in stresses and displacements depend upon the initial state of loading, but also upon the entire past history of loading and the instantaneous relative rates of change of the normal and tangential forces. For example, different phenomena are involved and different results obtained depending upon whether the normal or tangential force is held constant, while the other varies; whether they both vary, and whether the sense of the variation is such that one increases while the other decreases, both increase, or both decrease; whether the relative rate of change is greater or less than the coefficient of friction; whether the immediate past history of loading was in the same or opposite sense as the current loading. This situation makes it necessary to study a variety of special cases. The ones selected are those which seem likely to arise in applications and, at the same time, reveal new phenomena or require new techniques. In every case, the elastic bodies considered are identical spheres.

After a brief statement, in Section 2, of the results of the Hertz theory, three of the simplest cases of varying oblique forces are considered in Sections 3 to 5. In these, the normal force is held constant while the tangential force increases, decreases, and oscillates. On the basis of the considerations employed and the results obtained in the preceding cases, a set of rules for further procedure is stated in Section 6. The rules are then applied to two types of problems. In the first (Sections 7 to 13), the initial tangential compliances are calculated for a variety of past histories and instantaneous rates of loading. In the second (Sections 14 to 19), a detailed history of a varying oblique force is investigated. An integral is encountered which necessitates a definite choice of loading history in order to proceed further. The one selected is the case of an initial normal load, followed by an oblique force whose inclination remains constant while its magnitude varies. The force first increases, then decreases, and, finally, oscillates.

2 Normal Force Varying, Tangential Force Zero

This is the case to which the Hertz theory[4] is applicable. The theory predicts a plane, circular contact surface of radius

$$a = (KNR)^{1/3} \qquad [1]$$

where N is the normal force, R is the radius of the spheres, and $K = 3(1 - \nu^2)/4E$, in which ν and E are Poisson's ratio and Young's modulus, respectively, of the material.

The distribution of normal traction on the contact surface is given by

$$\sigma = \frac{3N}{2\pi a^3}(a^2 - \rho^2)^{1/2}, \qquad [2]$$

where ρ is the radial distance from the center of the contact surface.

The theory also gives the relative approach of the spheres

$$\alpha = 2(KN/R^{1/3})^{2/3} \qquad [3]$$

Hence the normal compliance of one sphere is

$$c_n = \frac{1}{2}\frac{d\alpha}{dN} = \frac{2}{3}\left(\frac{K^2}{RN}\right)^{1/3} = \frac{1}{4\mu a}\frac{1-\nu}{} \qquad [4]$$

where μ is the shear modulus of the material.

3 Normal Force Constant, Tangential Force Increasing

This is the case investigated by Cattaneo[5] and Mindlin.[6] The normal force is applied first, following which the tangential force

[1] This investigation was supported by the Office of Naval Research under Contract Nonr-266(09).

[2] Professor of Civil Engineering, Columbia University. Mem. ASME.

[3] Assistant Professor of Civil Engineering, Columbia University. Jun. ASME.

[4] "Theory of Elasticity," by S. Timoshenko and J. N. Goodier, McGraw-Hill Book Company, Inc., New York, N. Y., 1951, p. 372.

[5] "Sul contatto di due Corpi Elastici," by C. Cattaneo, Accademia dei Lincei, Rendiconti, Series 6, vol. 27, 1938, pp. 342–348, 434–436, and 474–478.

[6] "Compliance of Elastic Bodies in Contact," by R. D. Mindlin, Journal of Applied Mechanics, Trans. ASME, vol. 71, 1949, pp. A-259–268.

[7] "Effects of an Oscillating Tangential Force on the Contact Surfaces of Elastic Spheres," by R. D. Mindlin, W. P. Mason, T. F. Osmer, and H. Deresiewicz, Proceedings of the First U. S. National Congress of Applied Mechanics, 1951, pp. 203–208.

Presented at the National Conference of the Applied Mechanics Division, Minneapolis, Minn., June 18–20, 1953, of The American Society of Mechanical Engineers.

Discussion of this paper should be addressed to the Secretary, ASME, 29 West 39th Street, New York, N. Y., and will be accepted until October 10, 1953, for publication at a later date. Discussion received after the closing date will be returned.

Note: Statements and opinions advanced in papers are to be understood as individual expressions of their authors and not those of the Society. Manuscript received by ASME Applied Mechanics Division, November 5, 1952. Paper No. 53—APM-14.

T increases monotonically from zero. Considerations of symmetry show that the distribution of normal traction is not altered during application of T, as long as the two spheres are alike.[5]

If it is assumed that no slip occurs, symmetry considerations lead to the conclusion that the tangential component of displacement at the contact surface is that of a rigid body. The situation is thus reduced to a mixed boundary-value problem in elasticity. On the contact surface, the normal component of traction (zero) and the tangential component of displacement (constant) are given. On the remainder of the surface of the sphere, approximated as plane, the three components of traction are given (all zero). Solution of this problem gives the tangential component of traction τ on the contact surface. This is everywhere parallel to the displacement (and the force T), is axially symmetric in magnitude and increases to infinity at the edge of the contact surface. In addition to yielding the initial tangential compliance, this solution reveals that slip must accompany tangential forces, as infinite tractions are required in the absence of slip.

Slip may be expected to start at the edge of the contact surface, where infinite tangential tractions would occur without slip, and progress radially inward. Since τ, in the absence of slip, is radially symmetric, it is reasonable to suppose that slip occurs on an annulus. Further, as a first approximation, it is assumed that the tangential traction on the annulus of slip is in the direction of the tangential force and has the magnitude $\tau = f\sigma$, where f is a constant coefficient of friction. On account of symmetry, the tangential component of displacement is constant on the portion of the contact surface on which no slip occurs (the "adhered portion"). Thus the situation is reduced to another mixed boundary-value problem in elasticity. The tangential displacement (constant) and the normal traction (zero) are given on the adhered portion and the traction is given over the remainder of the boundary (tangential traction $= f\sigma$, normal traction zero on the annulus of slip and all three components of traction zero outside). Solution of this problem[5,6] yields the inner radius of the annulus of slip

$$c = a\,(1 - T/fN)^{1/3} \qquad [5]$$

the distribution of tangential traction on the contact surface

$$\left.\begin{aligned} \tau &= \frac{3fN}{2\pi a^3}\,(a^2 - \rho^2)^{1/2}, \quad c \leqslant \rho \leqslant a \\ \tau &= \frac{3fN}{2\pi a^3}\,[(a^2 - \rho^2)^{1/2} - (c^2 - \rho^2)^{1/2}], \quad \rho \leqslant c \end{aligned}\right\} \qquad [6]$$

and the displacement of distant points with respect to the uniform displacement of the adhered portion

$$\left.\begin{aligned} \delta &= \frac{3(2-\nu)fN}{16\mu a}\left(1 - \frac{c^2}{a^2}\right) \\ &= \frac{3(2-\nu)fN}{16\mu a}\left[1 - \left(1 - \frac{T}{fN}\right)^{2/3}\right] \end{aligned}\right\} \qquad [7]$$

The distribution of tangential traction on the contact surface and the relation between tangential load and displacement are illustrated in Figs. 1 and 2, respectively. As T approaches fN, point c in Fig. 1 approaches the center of the contact surface (point O) in accordance with Equation [5]. For any $T < fN$ there corresponds a point on the curve in Fig. 2, in accordance with Equation [7]. When $T = fN$, the adhered portion of the contact surface has shrunk to zero and the displacement has reached the abscissa of point F in Fig. 2, at which point the displacement becomes indeterminate, as rigid-body sliding takes place over the whole contact surface. A distinction is thus made between slip and slide. The term slip is used here when there is relative tangential displacement over only a portion of contiguous surfaces. When T reaches the value for which the inner boundary of the slip surface shrinks to zero, there is relative displacement over the whole contact surface; this situation is termed slide.

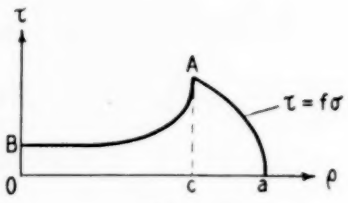

FIG. 1

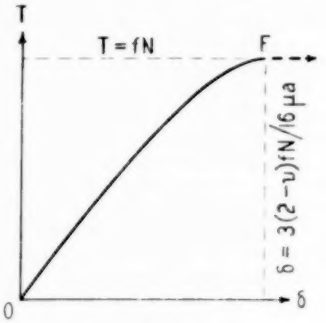

FIG. 2

The tangential compliance for the case of constant normal force and monotonically increasing tangential force is the reciprocal of the slope of the curve in Fig. 2 and is given by the formula

$$c_t = \frac{d\delta}{dT} = \frac{2-\nu}{8\mu a}\left(1 - \frac{T}{fN}\right)^{-1/3} \qquad [8]$$

Thus the tangential compliance is $(2-\nu)/8\mu a$ at $T = 0$ and is infinite at $T = fN$; i.e., free sliding takes place at the latter load.

The ratio of the initial tangential compliance, $(2-\nu)/8\mu a$, to the normal compliance, Equation [4], is $(2-\nu)/2(1-\nu)$. Hence the ratio ranges from unity, for $\nu = 0$, to $3/2$, for $\nu = 1/2$.

4 Normal Force Constant, Tangential Force Decreasing

Suppose, now, that after having reached a value T^*, where $0 < T^* < fN$, the tangential force T is reduced. If slip were prevented, the tangential traction τ would tend to negative infinity on the boundary $\rho = a$. This conclusion is reached from the solution of the appropriate boundary-value problem in elasticity, as described in the preceding section. Hence slip, opposite in sense to the initial slip, is presumed to start at $\rho = a$ and penetrate to a radius b, assumed, temporarily, to lie in the interval $c \leqslant b \leqslant a$. As in the preceding section, the tangential traction on the annulus $b \leqslant \rho \leqslant a$ is equal to $f\sigma$ but its sense is now opposite to that of the initial traction. Hence the change of traction over the annulus $b \leqslant \rho \leqslant a$ is $-2f\sigma$. Since no additional slip occurs on the surface $\rho \leqslant b$, the change of tangential displacement in that region must, from symmetry, be that of a rigid body. Thus the change due to reduction of T presents a boundary-value problem in elasticity identical in form with that

[5] A case in which the normal traction is changed as a result of application of a tangential force is considered by H. Poritsky, JOURNAL OF APPLIED MECHANICS, Trans. ASME, vol. 72, 1950, pp. 191–201.

encountered in the preceding section. Hence the change in tangential traction, by analogy with Equations [6], is

$$\left.\begin{aligned} \tau_c &= -\frac{3fN}{\pi a^3}(a^2-\rho^2)^{1/2}, \quad b \leqslant \rho \leqslant a \\ \tau_c &= -\frac{3fN}{\pi a^3}[(a^2-\rho^2)^{1/2}-(b^2-\rho^2)^{1/2}], \quad \rho \leqslant b \end{aligned}\right\} \quad [9]$$

This distribution is illustrated by curve a-A'-B' in Fig. 3.

The resultant traction accompanying a reduction in T is obtained by adding the initial traction, Equations [6], and the change, Equations [9], with the result

$$\left.\begin{aligned} \tau &= -\frac{3fN}{2\pi a^3}(a^2-\rho^2)^{1/2}, \quad b \leqslant \rho \leqslant a \\ \tau &= -\frac{3fN}{2\pi a^3}[(a^2-\rho^2)^{1/2}-2(b^2-\rho^2)^{1/2}], \quad c \leqslant \rho \leqslant b \\ \tau &= -\frac{3fN}{2\pi a^3}[(a^2-\rho^2)^{1/2}-2(b^2-\rho^2)^{1/2} \\ &\qquad +(c^2-\rho^2)^{1/2}], \quad \rho \leqslant c \end{aligned}\right\} \quad [10]$$

This is illustrated, in Fig. 3, by curve a-D-E-F, which is the sum of a-A-B and a-A'-B'.

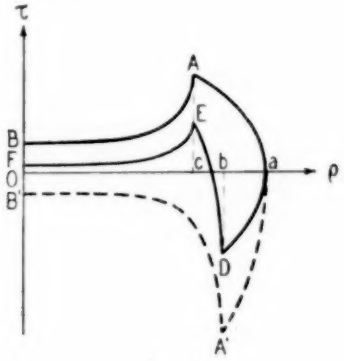

FIG. 3

The equilibrium condition

$$T = \int_0^{2\pi}\int_0^a \tau\,\rho\,d\rho\,d\theta \quad \ldots\ldots [11]$$

yields, upon insertion of τ from Equations [10]

$$T = \frac{fN}{a^3}(a^3-c^3) - \frac{2fN}{a^3}(a^3-b^3) \quad \ldots\ldots [12]$$

Noting, from Equation [5], that the first term on the right of Equation [12] is the initial tangential force T^*, the depth of penetration of counterslip is

$$b = a\left(1-\frac{T^*-T}{2fN}\right)^{1/3} \quad \ldots\ldots [13]$$

Thus the assumption $c \leqslant b \leqslant a$ is valid as long as $-T^* \leqslant T \leqslant T^*$. When $T = -T^*$, i.e., when the tangential load is fully reversed, $b = c$, i.e., counterslip has penetrated to the depth of the initial slip. At the same time, Equations [10] reduce to Equations [6] with signs reversed. The traction is then distributed just as the initial traction at $T = T^*$ was, but with opposite sense. The situation is the same as if no positive T had ever been applied, but only a negative T of magnitude $-T^*$. Upon further decrease of T to $-fN$ the phenomenon is again the same as the one described in the preceding section for a monotonic T.

The associated displacement of the adhered portion is found by a similar process of superposition. The change in displacement is obtained by multiplying the first of Equations [7] by -2 and replacing c by b as given in Equation [13]. The initial displacement is given by the second of Equations [7] with T replaced by T^*. The sum of the two is

$$\begin{aligned} \delta_d &= \frac{3(2-\nu)fN}{16\mu a}\left(2\frac{b^2}{a^2}-\frac{c^2}{a^2}-1\right) \\ &= \frac{3(2-\nu)fN}{16\mu a}\left[2\left(1-\frac{T^*-T}{2fN}\right)^{2/3}-\left(1-\frac{T^*}{fN}\right)^{2/3}-1\right] \end{aligned} \quad \ldots\ldots [14]$$

The tangential load-displacement curve is illustrated by the full lines in Fig. 4.

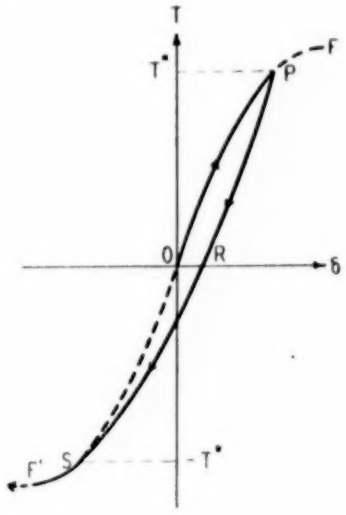

FIG. 4

The compliance for unloading is

$$\frac{d\delta_d}{dT} = \frac{2-\nu}{8\mu a}\left(1-\frac{T^*-T}{2fN}\right)^{-1/3} \quad \ldots\ldots [15]$$

It is interesting to note that the initial compliance on unloading ($T = T^*$ in Equation [15]) is the same as the initial compliance on loading ($T = 0$ in Equation [8]); that is, in Fig. 4, the slope of PR at P is the same as the slope of OP at O.

When T has been reduced from T^* to zero, there is a permanent set given by OR, in Fig. 4, the magnitude of which is obtained by setting $T = 0$ in Equation [14]. The accompanying traction is not zero, but is a self-equilibrating distribution obtained by setting $b = a(1-T^*/2fN)^{1/3}$ in Equations [10].

When T has been reduced to $-T^*$, the displacement has reached the negative of the displacement at $T = T^*$, i.e., the abscissa of S in Fig. 4 is the negative of the abscissa of P, and the compliance is identical with that of curve OP at $T = T^*$. Hence the unloading curve P-R-S is tangent, at S, to the central perversion OS, of the loading curve OP. Upon further decrease of T^* to $-fN$, the unloading curve follows the reflected loading curve SF', in accordance with the results for monotonic T given in Section 3.

5 Normal Force Constant, Tangential Force Oscillating

In the preceding section the entire situation at $T = -T^*$ is identical with that at $T = T^*$, except for reversal of sign. Hence a subsequent increase of T from $-T^*$ to T^* will be accompanied by the same events as occurred during the decrease from T^* to $-T^*$, except for reversal of sign. Thus, in starting along SU, Fig. 5, the compliance at S is the same as the compliance at P of PR. Slip again starts at $\rho = a$ in the same sense as occurred

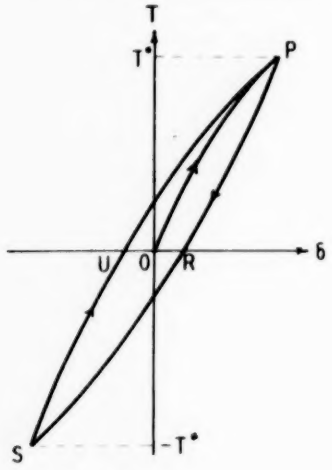

Fig. 5

along path OP. At an intermediate point of SU, the traction will be like a-D-E-F, Fig. 3, with sign reversed. When the tangential force once more reaches T^*, b will again have penetrated to c and the traction will be exactly a-A-B.

The displacement along path S-U-P is

$$\delta_s = -\delta_d(-T) = -\frac{3(2-\nu)fN}{16\mu a}\left[2\left(1-\frac{T^*+T}{2fN}\right)^{2/3} - \left(1-\frac{T^*}{fN}\right)^{2/3} - 1\right] \quad \ldots\ldots [16]$$

Hence, when $T = T^*$, the terminal points P of S-U-P and P of OP, Fig. 5, are identical, as may be seen by comparing Equation [16] with Equation [7] for that value of T.

Subsequent diminution of T will then produce a repetition of the events accompanying the first diminution.

It is now evident that during oscillation of T between $\pm T^*$, with N maintained constant, the load-displacement curve traverses the loop P-R-S-U-P, Fig. 5.

The area enclosed in the loop gives the frictional energy loss per cycle

$$F = \int_{-T^*}^{T^*}(\delta_d - \delta_s)dT = \frac{9(2-\nu)f^2N^2}{10\mu a}\left\{1-\left(1-\frac{T^*}{fN}\right)^{5/3} - \frac{5T^*}{6fN}\left[1+\left(1-\frac{T^*}{fN}\right)^{2/3}\right]\right\} \quad \ldots\ldots [17]$$

For small T^*/fN, Equation [17] reduces to

$$F = \frac{(2-\nu)T^{*3}}{36\mu afN} \quad \ldots\ldots [18]$$

i.e., the energy loss per cycle varies as the cube of the maximum tangential force.

Some of the conclusions reached in this section have been subjected to experimental test.[7] The occurrence of the annulus of slip has been verified, as well as the constancy of the coefficient of friction and the relation between the size of the inner radius of the annulus and the magnitude of T^*. In the tests, the energy dissipation, for magnitudes of T^*/fN close to unity, agreed with the values predicted by the theory; for T^*/fN in the vicinity of zero, however, it appeared to vary more nearly as the square than the cube of the maximum tangential force.

6 Rules of Procedure

The results of the two preceding sections have been obtained by means of extensions of Cattaneo's and Mindlin's solutions for the case of constant N and monotonically increasing T. Before proceeding to cases of greater complexity, it may be helpful to set down, explicitly, the rules upon which the two preceding and the subsequent developments are based:

Rule 1. The radius of the contact surface and the normal component of traction on it are given by the Hertz formulas, Equations [1] and [2].

Rule 2. With every application or change of tangential force, slip will be initiated whenever, in the absence of slip, the solution of the appropriate boundary-value problem in the theory of elasticity yields a tangential traction, at any point, in excess of the product of a constant coefficient of friction and the normal component of traction at that point.

Rule 3. Slip, in the direction of the force causing it,[8] progresses concentrically, radially inward from the boundary of the contact surface, forming an "annulus of slip."

Rule 4. At any point on a contact surface, the magnitude of the tangential component of traction is at most equal to the product of a constant coefficient of friction and the normal component of traction at that point. The equality necessarily holds at a point at which slip has just occurred, in which case the traction has the same sense as the slip.[9]

Rule 5. The adhered portion of the contact surface, i.e., the portion encircled by an annulus on which slip occurs, is subjected to a change of tangential traction and undergoes a rigid-body tangential displacement. The radius of the adhered portion, the distribution of the traction and the magnitude of the displacement are obtained from Cattaneo's and Mindlin's formulas, Equations [5], [6], [7].

Rule 6. Beginning with an equilibrium position, for which the displacement and the distribution of traction have been established in accordance with the preceding rules, the effects of a change in the state of loading are obtained by advancing to the desired state through a sequence of equilibrium positions, each of which is obtained from its predecessor by applying Rules 1 to 5. In particular, the condition of equilibrium, Equation [11], is useful.

In the following sections these rules are applied to the calculation of tangential compliances for a number of past histories, initial states, and variations of both N and T.

7 N Increasing, T Increasing

Suppose that, after an initial state has been reached by first applying a normal force N and then a tangential force T, both N and T are to increase at an arbitrary relative rate.

The initial state is given by Equations [1], [2], [5], [6], and [7]. The distribution of tangential traction is illustrated by

[8] There is a small lateral component of relative tangential displacement which accompanies the major slip in the direction of the applied force. The lateral tangential traction, which accompanies the lateral slip, is neglected.

curve a-A-B in Fig. 6, the tangential load-displacement history by curve OA in Fig. 7.

Now, increase N by an increment ΔN. The radius of the contact surface increases to a value a_1 given by Equation [1] with N replaced by $N + \Delta N$

$$a_1 = [K(N + \Delta N)R]^{1/3} \quad [19]$$

The tangential traction remains unchanged.

With the normal load held constant at $N + \Delta N$, increase the tangential force by an increment $\Delta T < f\Delta N$. In accordance with the rules of Section 6, slip begins at $\rho = a_1$ and progresses inward to a radius c_1 given by Equation [5] with c, a, T, and N replaced by c_1, a_1, ΔT_1, and $N + \Delta N$, respectively

$$c_1 = a_1 [1 - \Delta T_1/f(N + \Delta N)]^{1/3} \quad [20]$$

From Equations [1] and [19]

$$a^3(N + \Delta N) = a_1^3 N \quad [21]$$

Hence

$$c_1 = a(fN)^{-1/3} (fN + f\Delta N - \Delta T)^{1/3} \quad [22]$$

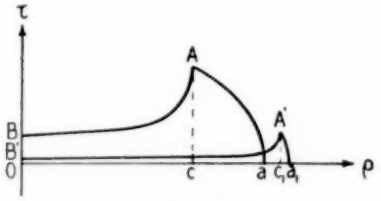

Fig. 6

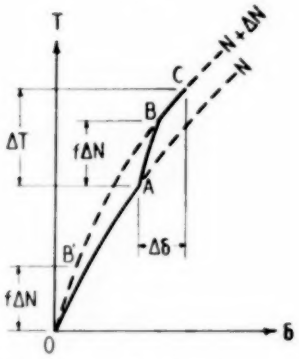

Fig. 7

The same replacements in Equations [6] and [7] give the increments in traction and displacement, the former of which is illustrated by curve a_1-A'-B' in Fig. 6. The load-displacement relation, during the increment, is illustrated by curve AB, in Fig. 7. The slope of AB, at A, is $8\mu a_1/(2 - \nu)$. These conclusions may be ascertained from Equation [7] and its derivative with respect to ΔT, after the appropriate replacements have been made.

Now increase ΔT to $f\Delta N$. From Equation [22], c_1 progresses in to a; i.e., the inner radius of the incremental annulus of slip shrinks to the radius of the initial contact surface. The increment in tangential traction is now given by

$$\left.\begin{aligned} \Delta\tau &= \frac{3f(N + \Delta N)}{2\pi a_1^3} (a_1^2 - \rho^2)^{1/2}, \quad a \leqslant \rho \leqslant a_1 \\ \Delta\tau &= \frac{3f(N + \Delta N)}{2\pi a_1^3} [(a_1^2 - \rho^2)^{1/2} - (a^2 - \rho^2)^{1/2}], \rho \leqslant a \end{aligned}\right\} \quad [23]$$

and is illustrated by curve a_1-A'-B' in Fig. 8. The total tangential traction is the sum of Equations [6] and [23]. Using Equation [21], this becomes

$$\left.\begin{aligned} \tau_R &= \tau + \Delta\tau = \frac{3f(N + \Delta N)}{2\pi a_1^3} (a_1^2 - \rho^2)^{1/2}, c \leqslant \rho \leqslant a_1 \\ \tau_R &= \frac{3f(N + \Delta N)}{2\pi a_1^3} [(a_1^2 - \rho^2)^{1/2} - (c^2 - \rho^2)^{1/2}], \rho \leqslant c \end{aligned}\right\} \quad [24]$$

But this is the distribution that would have been obtained if the entire history had been an initial application of normal force $N + \Delta N$ followed by a single application of tangential force $T + f\Delta N$. Thus the sum of curves a-A-B and a_1-A'-B', in Fig. 8,

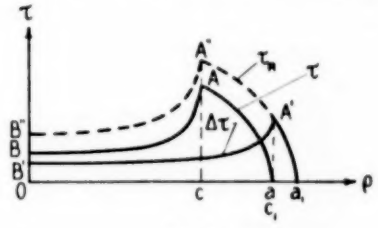

Fig. 8

is a_1-A''-B'', which is the curve corresponding to Equations [24]. Further increase in ΔT will then produce tractions in accordance with the findings in Section 3 for monotonic increase in T.

Further, when $\Delta T = f\Delta N$, the total displacement is the same as would have been obtained if an initial normal force $N + \Delta N$ had been followed by a tangential force $T + f\Delta N$; i.e., point B of AB, in Fig. 7, coincides with point B of the load-displacement curve, O-B'-B, for initial normal force $N + \Delta N$. Upon further increase in T, the load-displacement curve follows path BC.

The compliance at A of curve AB, in Fig. 7, is

$$\frac{2 - \nu}{8\mu a_1}$$

The compliance at B of curve O-B-C is

$$\frac{2 - \nu}{8\mu a_1} \left(1 - \frac{T}{f(N + \Delta N)}\right)^{-1/3}$$

Hence, for small $\Delta T \geqslant f\Delta N$, the increment in displacement is

$$\Delta\delta = \frac{2 - \nu}{8\mu a} \left[f\Delta N + \left(1 - \frac{T}{f(N + \Delta N)}\right)^{-1/3} (\Delta T - f\Delta N)\right]$$

The compliance at (N, T), for N and T increasing, is then

$$c_t = \lim_{\substack{\Delta N \to 0 \\ \Delta T \to 0}} \frac{\Delta\delta}{\Delta T} = \frac{2 - \nu}{8\mu a} \left[f\frac{dN}{dT} + \left(1 - f\frac{dN}{dT}\right)\left(1 - \frac{T}{fN}\right)^{-1/3}\right], 0 \leqslant \frac{dN}{dT} \leqslant \frac{1}{f} \quad [25]$$

If $\Delta T < f\Delta N$, the load-displacement curve does not extend beyond B in Fig. 7. Hence

$$\Delta\delta = \frac{2 - \nu}{8\mu a} \Delta T$$

and the compliance is

$$c_t = \frac{2 - \nu}{8\mu a}, \quad \frac{dN}{dT} \geqslant \frac{1}{f} \quad [26]$$

8 N Decreasing, T Increasing

Starting with the same initial state as in Section 7, it is desired first to decrease N by an amount ΔN, with the tangential load held constant. Such a decrease would reduce the contact radius to a value a_1, given by Equation [1] with N replaced by $N - \Delta N$. However, the portions of the spheres in annulus $a_1 \leqslant \rho \leqslant a$ would no longer be in contact, and would be unable to sustain tangential traction. Consequently, before a reduction of normal load may be effected, it is necessary to remove the existing tangential traction from this region. This removal may be accomplished by means of the following procedure:

(*a*) The contact area $\rho \leqslant a_1$ is "frozen"; i.e., no slip is permitted to take place.

(*b*) A distribution of traction is added, such that it will cause the annulus $a_1 \leqslant \rho \leqslant a$ to become free of traction, and, at the same time, obey the injunction stated in (*a*).

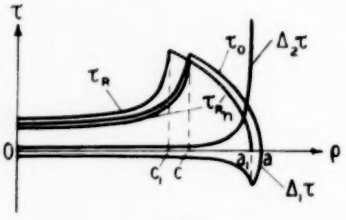

Fig. 9

Such a distribution (see Fig. 9) is given by

$$\left.\begin{aligned} \Delta_1\tau &= -\frac{3fN}{2\pi a^3}\,(a^2-\rho^2)^{1/2}, \quad a_1 \leqslant \rho \leqslant a \\ \Delta_1\tau &= -\frac{3fN}{2\pi a^3}\,[(a^2-\rho^2)^{1/2}-(a_1^2-\rho^2)^{1/2}], \quad \rho \leqslant a_1 \end{aligned}\right\} \quad [27]$$

The resultant traction (which, it should be noted, corresponds to a condition of equilibrium with the force $T - f\Delta N$, but not with T) will be

$$\left.\begin{aligned} \tau_{R_2} &= 0, \quad a_1 \leqslant \rho \leqslant a \\ \tau_{R_2} &= \frac{3f(N-\Delta N)}{2\pi a_1^3}\,(a_1^2-\rho^2)^{1/2}, \quad c \leqslant \rho \leqslant a_1 \\ \tau_{R_2} &= \frac{3f(N-\Delta N)}{2\pi a_1^3}\,[(a_1^2-\rho^2)^{1/2}-(c^2-\rho^2)^{1/2}], \quad \rho \leqslant c \end{aligned}\right\} \quad [28]$$

Since annulus $a_1 \leqslant \rho \leqslant a$ is now free of traction, it is permissible to decrease N by ΔN. The distribution of traction, Equations [28], is the same as if the order of loading had been: (1) $N - \Delta N$, (2) $T_1 = f(N - \Delta N)\,(1 - c^3/a_1^3) = T - f\Delta N$, where the value of T_1 is obtained by applying the integral condition, Equation [11]. The displacement may be thought to follow path AB, Fig. 10.

A portion of the tangential force, represented by the volume under the traction distribution, Equations [27], was removed in the course of the reduction of the normal load. But the spheres must be in equilibrium with T; hence the force $f\Delta N$ is transferred to the remaining contact surface (i.e., $\rho \leqslant a_1$). In consequence of the assumption stated in (*a*) of this section, the additional tangential traction[10] resulting from this transfer is given by (see Fig. 9)

$$\Delta_2\tau = \frac{f\Delta N}{2\pi a_1}\,(a_1^2-\rho^2)^{-1/2}, \quad \rho \leqslant a_1 \qquad [29]$$

[10] See Equation [76], reference (6).

This is the distribution, referred to in Section 3, which increases without limit as ρ approaches a_1.

Now unfreeze the contact surface. Slip will progress in the direction of the applied tangential force in accordance with the fundamental rules. The resultant tangential traction will be distributed as given by Equations [28] with c replaced by c_1, where

$$c_1 = a_1\left(1 - \frac{T}{f(N-\Delta N)}\right)^{1/3}$$

The displacement may be thought to take path BC in Fig. 10.

Now, holding the normal force constant (at $N - \Delta N$), increase

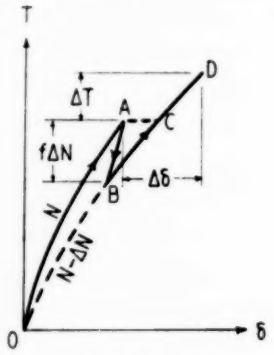

Fig. 10

the tangential force by an amount ΔT. At this point the tangential traction will be given by Equations [28] with c replaced by c_2, where

$$c_2 = a_1\left(1 - \frac{T+\Delta T}{f(N-\Delta N)}\right)^{1/3} < c_1$$

It is interesting that the resultant traction has, qualitatively, the same form as the initial traction, Equations [6].

The displacement will follow path CD on curve O-B-D, Fig. 10. Hence the compliance will be

$$\begin{aligned} c_t &= \lim_{\substack{\Delta N\to 0\\ \Delta T\to 0}} \left\{\frac{1}{\Delta T}\,\frac{2-\nu}{8\mu a}\left[-f\Delta N + \left(1-\frac{T}{fN}\right)^{-1/3}(f\Delta N + \Delta T)\right]\right\} \\ &= \frac{2-\nu}{8\mu a}\left[-f\,\frac{dN}{dT} + \left(1+f\,\frac{dN}{dT}\right)\left(1-\frac{T}{fN}\right)^{-1/3}\right] \end{aligned} \quad [30]$$

Since, inherently, $dN/dT < 0$, its absolute value must be used in this formula.

9 N Increasing, T Decreasing

1 Apply N, increase the tangential force monotonically from zero to T^*, then reduce it to T. The tangential traction is given by Equations [10]; its distribution is shown by τ_0 in Fig. 11.

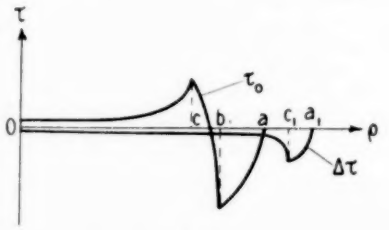

Fig. 11

2 Keeping the tangential load constant, increase the normal load to $N + \Delta N$. The radius a_1 of the new contact area is given by Equation [19]. The tangential traction remains unchanged.

3 Keeping the normal force constant (at $N + \Delta N$), reduce the tangential force by ΔT. The additional tangential traction (see $\Delta\tau$, Fig. 11) will be given by Equations [23] with sign reversed.

Again, if $\Delta T = f\Delta N$, so that $c_1 = a$ (Fig. 11), the resultant traction will be

$$\left.\begin{aligned}
\tau_R &= -\frac{3f(N+\Delta N)}{2\pi a_1^3}(a_1^2-\rho^2)^{1/2}, \quad b \leqslant \rho \leqslant a_1\\
\tau_R &= -\frac{3f(N+\Delta N)}{2\pi a_1^3}[(a_1^2-\rho^2)^{1/2}-2(b^2-\rho^2)^{1/2}], \quad c \leqslant \rho \leqslant b\\
\tau_R &= -\frac{3f(N+\Delta N)}{2\pi a_1^3}[(a_1^2-\rho^2)^{1/2}-2(b^2-\rho^2)^{1/2} + (c^2-\rho^2)^{1/2}], \quad \rho \leqslant c
\end{aligned}\right\} \quad [31]$$

Hence the situation is the same as that obtained by (1) imposing a normal load $N + \Delta N$, (2) applying a tangential load T_1^*, (3) reducing the tangential load to $T_1 = T - f\Delta N$. T_1^* may be found by noting that $T_1^* = f(N + \Delta N)(1 - c^3/a_1^3) = T^* + f\Delta N$.

4 The displacement (see Equation [14]) at the conclusion of step 1 will have traversed the path O-A-B (Fig. 12); following step 3 it will have reached point C, at which stage path O-A-B-C meets path O-A'-C.

If $\Delta T > f\Delta N$, splitting the decrement into $f\Delta N$ and $\Delta T - f\Delta N$ and applying these parts consecutively will yield a result entirely similar to that found in part 3 of this section. The additional displacement will follow path CD along curve $A'D$ (Fig. 12).

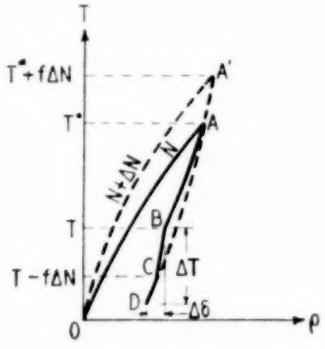

FIG. 12

Remembering that, again, inherently, $dN/dT < 0$, so that its absolute value must be employed, the compliance is

$$\left.\begin{aligned}
c_t &= \lim_{\substack{\Delta N\to 0\\ \Delta T\to 0}}\left\{\frac{1}{\Delta T}\frac{2-\nu}{8\mu a}\left[f\Delta N + \left(1-\frac{T^*-T}{2fN}\right)^{-1/3}(\Delta T - f\Delta N)\right]\right\}\\
&= \frac{2-\nu}{8\mu a}\left[f\frac{dN}{dT} + \left(1-f\frac{dN}{dT}\right)\left(1-\frac{T^*-T}{2fN}\right)^{-1/3}\right], \quad 0 > \frac{dN}{dT} \geqslant -\frac{1}{f}\\
c_t &= \frac{2-\nu}{8\mu a}, \qquad \frac{dN}{dT} \leqslant -\frac{1}{f}
\end{aligned}\right\} \quad [32]$$

10 N Decreasing, T Decreasing

1 Repeat step 1 of Section 9.

2 A decrease of normal load by an amount ΔN must be preceded by the expedients discussed in (a) and (b) of Section 8, i.e., a freezing of the contact area, and freeing of the annulus $a_1 \leqslant \rho \leqslant a$ of tangential traction by adding, with sign reversed, $\Delta\tau$ of Equations [27]. The resultant traction, which is not in equilibrium with the force T, will be (Fig. 13)

$$\left.\begin{aligned}
\tau_{R_n} &= 0, \quad a_1 \leqslant \rho \leqslant a\\
\tau_{R_n} &= -\frac{3f(N-\Delta N)}{2\pi a_1^3}(a_1^2-\rho^2)^{1/2}, \quad b \leqslant \rho \leqslant a_1\\
\tau_{R_n} &= -\frac{3f(N-\Delta N)}{2\pi a_1^3}[(a_1^2-\rho^2)^{1/2}-2(b^2-\rho^2)^{1/2}], \quad c \leqslant \rho \leqslant b\\
\tau_{R_n} &= -\frac{3f(N-\Delta N)}{2\pi a_1^3}[(a_1^2-\rho^2)^{1/2}-2(b^2-\rho^2)^{1/2} + (c^2-\rho^2)^{1/2}], \quad \rho \leqslant c
\end{aligned}\right\} \quad [33]$$

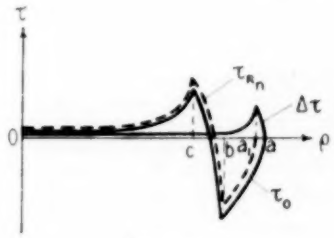

FIG. 13

The decrease in normal load is effected concurrently with the removal of the traction. This distribution may be reached by: (1) applying $N - \Delta N$, (2) applying $T_1^* = T^* - f\Delta N$, (3) reducing from T_1^* to $T + f\Delta N$. The transferred load (see Section 8) gives rise to a distribution of traction given by Equation [29] with sign reversed.

3 Unfreeze: slip will progress in the direction opposite to that of the initial tangential force. The displacement may be thought to take path B-B'-C (Fig. 14). The traction will be given by Equations [33] with b replaced by b_1, where

$$b_1 = a_1\left(1 - \frac{T^*-T}{2f(N-\Delta N)} + \frac{\Delta N}{2(N-\Delta N)}\right)^{1/3}$$

4 Further displacement, due to a decrease of tangential load at constant normal load ($N - \Delta N$), will proceed along curve A'-B'-C to point D. Thus the compliance will be

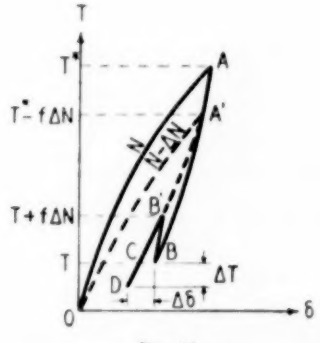

FIG. 14

$$c_t = \lim_{\substack{\Delta N \to 0 \\ \Delta T \to 0}} \left\{ \frac{1}{\Delta T} \frac{2-\nu}{8\mu a} \left[-f\Delta N + \left(1 - \frac{T^* - T}{2fN}\right)^{-1/3} (f\Delta N + \Delta T) \right] \right\}$$

$$= \frac{2-\nu}{8\mu a} \left[-f\frac{dN}{dT} + \left(1 + f\frac{dN}{dT}\right)\left(1 - \frac{T^* - T}{2fN}\right)^{-1/3} \right], \quad \frac{dN}{dT} \geqslant 0 \quad \ldots [34]$$

In the preceding four sections the discussion concerned tangential compliances due to simultaneously varying normal and tangential forces applied at nonzero levels of increasing or decreasing tangential load, in particular, at levels having a given previous history in the direction of the additional tangential force. In each case, the magnitude of the initial tangential force at these levels was reached at constant initial normal load.

In addition, it is of interest to find the values of compliances resulting from oblique loading at levels of tangential load which have no previous loading history in the direction of the tangential component of the system of oblique forces. The cases

(*a*) N increasing, T increasing, at $T^* = 0$
(*b*) N decreasing, T increasing, at $T^* = 0$
(*c*) N increasing, T decreasing, at $T = T^*$

are no more than special instances of loading considered in Sections 7, 8, and 9, respectively. The compliances are obtained directly from the general expressions given in the corresponding sections. On the other hand, there are several cases of interest for which the results cannot be obtained from previously considered cases. These are considered in Sections 11 to 13.

11 N Decreasing, T Decreasing, at $T = T^*$

1 Repeat step 1 of Section 9, with the proviso $T^* - T = \Delta T$ is an infinitesimal.

2 The reduction of the normal load by ΔN again must be preceded by freezing the contact surface and removal of traction, as described in Sections 8 and 10. Here, however, it is necessary to treat separately the cases $\Delta T \geqslant 2f\Delta N$ and $\Delta T < 2f\Delta N$.

(*a*) $\Delta T \geqslant 2f\Delta N$. Reference to Equations [1] and [13] reveals that

$$\left(\frac{b}{a}\right)^3 = 1 - \frac{\Delta T}{2fN} \leqslant 1 - \frac{\Delta N}{N} = \left(\frac{a_1}{a}\right)^3$$

i.e., $a_1 \geqslant b$. Hence the situation is the same as in the general case (Section 10); the compliance, a special case of Equation [34], is given by

$$c_t = \frac{2-\nu}{8\mu a}$$

The connection between this loading and the one discussed in Section 10 may be established by noting that, in Section 10, the load is decreased from T^* with $\Delta N = 0$, i.e., $dT/dN = \infty > 2f$.

(*b*) $\Delta T < 2f\Delta N$. In this case

$$\left(\frac{b}{a}\right)^3 = 1 - \frac{\Delta T}{2fN} > 1 - \frac{\Delta N}{N} = \left(\frac{a_1}{a}\right)^3$$

i.e., $a_1 < b$.

Now freeze the contact area. In order to free annulus $a_1 \leqslant \rho \leqslant a$ of tangential traction, add the following distributions of traction (Fig. 15) neither of which causes slip over circle $\rho \leqslant a_1$

$$\left.\begin{aligned} \Delta_1\tau &= \frac{3fN}{\pi a^3}(a^2 - \rho^2)^{1/2}, \quad b \leqslant \rho \leqslant a \\ \Delta_1\tau &= \frac{3fN}{\pi a^3}[(a^2 - \rho^2)^{1/2} - (b^2 - \rho^2)^{1/2}], \quad \rho \leqslant b \end{aligned}\right\} \quad \ldots [35]$$

$$\left.\begin{aligned} \Delta_2\tau &= -\frac{3fN}{2\pi a^3}(a^2 - \rho^2)^{1/2}, \quad a_1 \leqslant \rho \leqslant a \\ \Delta_2\tau &= -\frac{3fN}{2\pi a^3}[(a^2 - \rho^2)^{1/2} - (a_1^2 - \rho^2)^{1/2}], \quad \rho \leqslant a_1 \end{aligned}\right\} \quad \ldots [36]$$

The resultant traction (not in equilibrium with T), found by adding tractions of Equations [10], [35], and [36], is

$$\left.\begin{aligned} \tau_{R_n} &= 0, \quad a_1 \leqslant \rho \leqslant a \\ \tau_{R_n} &= \frac{3f(N - \Delta N)}{2\pi a_1^3}(a_1^2 - \rho^2)^{1/2}, \quad c \leqslant \rho \leqslant a_1 \\ \tau_{R_n} &= \frac{3f(N - \Delta N)}{2\pi a_1^3}[(a_1^2 - \rho^2)^{1/2} - (c^2 - \rho^2)^{1/2}], \quad \rho \leqslant c \end{aligned}\right\} \quad \ldots [37]$$

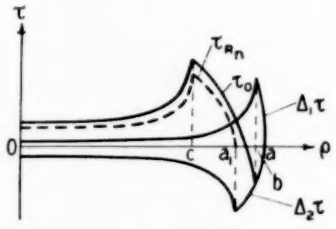

FIG. 15

Again, the normal load may be reduced by ΔN, provided that, concurrently, a traction distribution, similar to Equation [29], is applied over the area $\rho < a_1$. Its magnitude will be such as to provide the tangential force contained in the difference of volumes under the traction surfaces given by Equations [35] and [36]. Hence

$$\Delta\tau = -\frac{\Delta T - f\Delta N}{2\pi a_1}(a_1^2 - \rho^2)^{-1/2}, \quad \rho < a_1 \quad \ldots [38]$$

The traction of Equations [37] is the same as if the order of loading had been: (1) $N - \Delta N$, (2) $T_1^* = T^* - f\Delta N$.

Now unfreeze; slip will progress in the direction indicated by the sign of the traction of Equation [38], i.e., for $\Delta T < f\Delta N$, in the direction of initial tangential force, for $f\Delta N < \Delta T < 2f\Delta N$, in the opposite direction. In the former case, the path of the displacement may be thought to be *O-A-B-A-C-D* (Fig. 16); the expression for the compliance is

$$c_t = \lim_{\substack{\Delta N \to 0 \\ \Delta T \to 0}} \left\{ \frac{1}{\Delta T} \left[\frac{2-\nu}{8\mu a} f\Delta N - \frac{2-\nu}{8\mu a_1}\left(1 - \frac{T_1^*}{f(N - \Delta N)}\right)^{-1/3} (f\Delta N - \Delta T) \right] \right\}$$

$$= \frac{2-\nu}{8\mu a}\left[f\frac{dN}{dT} + \left(1 - f\frac{dN}{dT}\right)\left(1 - \frac{T^*}{fN}\right)^{-1/3} \right], \quad \frac{dN}{dT} > \frac{1}{f} \quad \ldots [39]$$

In the latter case, the displacement may be thought to traverse

path *O-A-B-A-C-D* in Fig. 17, where *CD* is part of an unloading path such as *A'B'* in Fig. 14. The compliance is $c_t = (2-\nu)/8\mu a$; thus this expression is valid for all $0 \leqslant dN/dT \leqslant 1/f$.

The traction of Equation [38] vanishes for $\Delta T = f\Delta N$, indicating that, in this instance, Equations [37] correspond to a condition of equilibrium with the force T; hence no slip accompanies unfreezing.

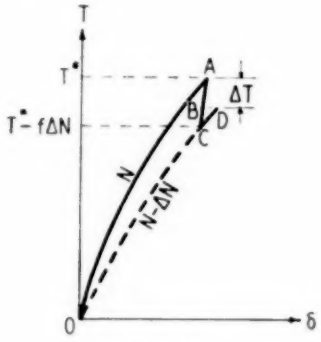

Fig. 16

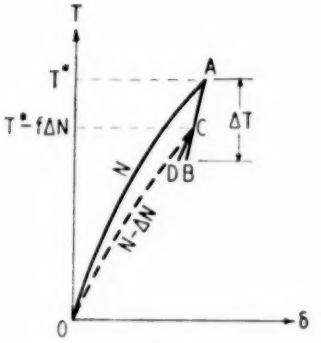

Fig. 17

12 N Increasing, T Increasing, at Point on Unloading Curve

1 Repeat steps 1 and 2 of Section 9.

2 Keeping the normal force constant (at $N + \Delta N$), increase the tangential force by ΔT.

Three cases arise, depending on whether $\Delta T \gtrless f\Delta N$.

(*a*) $\Delta T = f\Delta N$. The additional traction will be such as to cause slip, in the direction of the newly applied force, in an annulus $c_1 \leqslant \rho \leqslant a_1$ and no further slip on circle $\rho \leqslant c_1$. Hence

$$\left.\begin{aligned} \Delta\tau &= \frac{3f(N+\Delta N)}{2\pi a_1^3}(a_1^2-\rho^2)^{1/2}, \quad c_1 \leqslant \rho \leqslant a_1 \\ \Delta\tau &= \frac{3f(N+\Delta N)}{2\pi a_1^3}[(a_1^2-\rho^2)^{1/2}-(c_1^2-\rho^2)^{1/2}], \quad \rho \leqslant c_1 \end{aligned}\right\} \quad [40]$$

where

$$c_1 = a_1\left(1-\frac{\Delta T}{f(N+\Delta N)}\right)^{1/3}$$

Since $\Delta T = f\Delta N$, $c_1 = a$; hence the resultant traction (the sum of Equations [10] and [40]) becomes (see Fig. 18)

$$\left.\begin{aligned} \tau_R &= \frac{3f(N+\Delta N)}{2\pi a_1^3}(a_1^2-\rho^2)^{1/2}, \quad a \leqslant \rho \leqslant a_1 \\ \tau_R &= \frac{3f(N+\Delta N)}{2\pi a_1^3}[(a_1^2-\rho^2)^{1/2}-2(a^2-\rho^2)^{1/2}], \quad b \leqslant \rho \leqslant a \\ \tau_R &= \frac{3f(N+\Delta N)}{2\pi a_1^3}[(a_1^2-\rho^2)^{1/2}-2(a^2-\rho^2)^{1/2} \\ &\qquad +2(b^2-\rho^2)^{1/2}], \quad c \leqslant \rho \leqslant b \\ \tau_R &= \frac{3f(N+\Delta N)}{2\pi a_1^3}[(a_1^2-\rho^2)^{1/2}-2(a^2-\rho^2)^{1/2} \\ &\qquad +2(b^2-\rho^2)^{1/2}-(c^2-\rho^2)^{1/2}], \quad \rho \leqslant c \end{aligned}\right\} \quad [41]$$

Hence the situation is the same as if the order of loading had been: (1) $N + \Delta N$, (2) T_1^*, (3) reduction of tangential load to T_1, (4) its increase by ΔT. It may be noted that

$$A \text{—} \qquad T_1^* = f(N+\Delta N)\left(1-\frac{c^3}{a_1^3}\right) = T^* + f\Delta N$$

$$B \text{—} \qquad T_1^* - T_1 = 2f(N+\Delta N)\left(1-\frac{b^3}{a_1^3}\right) = T^* - T + 2f\Delta N$$

$$\therefore T_1 = T - f\Delta N$$

$$C \text{—} \qquad \Delta T = 2f(N+\Delta N)\left(1-\frac{a^3}{a_1^3}\right) = 2f\Delta N$$

Thus, on the load-displacement curve, Fig. 19, path *O-A-B-C-C'* may be replaced by path *O-A'-B'-C'*. The compliance is given by

$$c_t = \frac{2-\nu}{8\mu a}$$

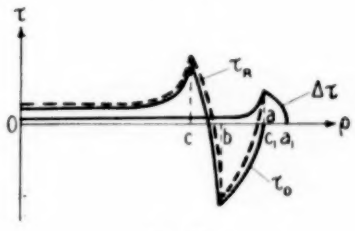

Fig. 18

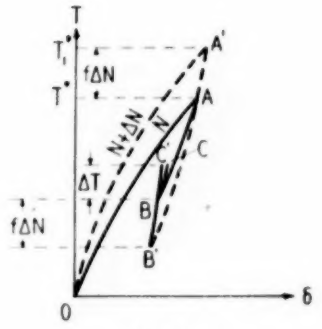

Fig. 19

(*b*) $\Delta T > f\Delta N$ ($c_1 < a$). If the increment ΔT is applied in two steps: $\Delta_1 T = f\Delta N$, $\Delta_2 T = \Delta T - f\Delta N$, in the usual manner, the course of events will be found the same as in (*a*) of this section, with the exception that $\overline{\Delta T} = \Delta T + f\Delta N$. Hence, again

$$c_t = \frac{2-\nu}{8\mu a}$$

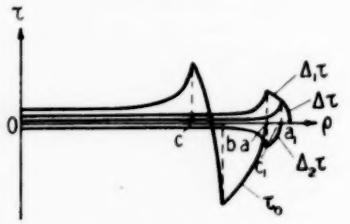

FIG. 20

(*c*) $\Delta T < f\Delta N$ ($c_1 > a$). The additional traction $\Delta\tau$, Equations [40], may be replaced by an equivalent distribution in the form (see Fig. 20)

$$\left.\begin{aligned} \Delta_1\tau &= \frac{3f(N+\Delta N)}{2\pi a_1^3}(a_1^2-\rho^2)^{1/2}, \quad a \leqslant \rho \leqslant a_1 \\ \Delta_1\tau &= \frac{3f(N+\Delta N)}{2\pi a_1^3}[(a_1^2-\rho^2)^{1/2}-(a^2-\rho^2)^{1/2}], \\ & \qquad\qquad \rho \leqslant a \end{aligned}\right\} \quad [42]$$

and

$$\left.\begin{aligned} \Delta_2\tau &= 0, \quad c_1 \leqslant \rho \leqslant a_1 \\ \Delta_2\tau &= \frac{3fN_{c_1}}{2\pi c_1^3}(c_1^2-\rho^2)^{1/2}, \quad a \leqslant \rho \leqslant c_1 \\ \Delta_2\tau &= \frac{3fN_{c_1}}{2\pi c_1^3}[(c_1^2-\rho^2)^{1/2}-(a^2-\rho^2)^{1/2}], \quad \rho \leqslant a \end{aligned}\right\} \quad [43]$$

where $N_{c_1}/c_1^3 = N/a^3$.

It is seen that $\tau_0 + \Delta_1\tau$ is the resultant traction τ_R, Equations [41], obtained in case (*a*). Hence the load-displacement curve will be as shown in Fig. 21. There, path *O-A-B-C-D* may be replaced by path *O-A'-B'-C'-D*. The compliance becomes

$$c_t = \lim_{\substack{\Delta N\to 0 \\ \Delta T\to 0}} \left\{ \frac{1}{\Delta T}\left[\frac{2-\nu}{8\mu a_1} f\Delta N - \frac{2-\nu}{8\mu c_1}(f\Delta N - \Delta T)\right]\right\} = \frac{2-\nu}{8\mu a} \quad [44]$$

Thus, Equation [44] is valid for all values of $dN/dT > 0$.

13 *N* Decreasing, *T* Increasing, at Point on Unloading Curve

1 Repeat step 1 of Section 9.

2 Keeping the normal force constant, increase the tangential load by an amount ΔT. In view of the discussion leading to Equations [10], the increment in traction will be (Fig. 22)

$$\left.\begin{aligned} \Delta_1\tau &= \frac{2fN}{\pi a^3}(a^2-\rho^2)^{1/2}, \quad b_1 \leqslant \rho \leqslant a \\ \Delta_1\tau &= \frac{3fN}{\pi a^3}[(a^2-\rho^2)^{1/2}-(b_1^2-\rho^2)^{1/2}], \quad \rho \leqslant b_1 \end{aligned}\right\} \quad [45]$$

where

$$b_1 = a\left(1-\frac{\Delta T}{2fN}\right)^{1/3}$$

Hence the resultant traction τ_{R_0} is given by Equations [41] in which $N + \Delta N$, a_1 and a are replaced by N, a and b_1, respectively.

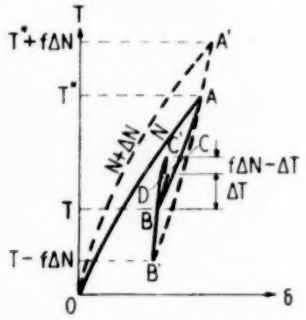

FIG. 21

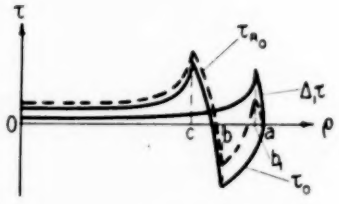

FIG. 22

3 Now, keeping the tangential force constant (at $T + \Delta T$), decrease the normal force by ΔN. The new contact radius is a_1. Several cases arise depending on the relative magnitudes of ΔT and $f\Delta N$. The solution follows the pattern established in Section 8; i.e., (1) freeze the contact area, (2) remove the traction in annulus $a_1 \leqslant \rho \leqslant a$ in such a way that surface $\rho \leqslant a_1$ remains frozen, (3) decrease N by ΔN, (4) unfreeze and permit slip to occur until equilibrium with force $T + \Delta T$ is re-established.

(*a*) $\Delta T \geqslant 2f\Delta N$ ($a_1 \geqslant b_1$). The additional traction necessary to free annulus $a_1 \leqslant \rho \leqslant a$ is $\Delta_2\tau$ (see Fig. 23) given by Equations [36]. Hence the resultant traction (which is not in equilibrium with $T + \Delta T$) becomes

$$\left.\begin{aligned} \tau_{R_a} &= 0, \quad a_1 \leqslant \rho \leqslant a \\ \tau_{R_a} &= \frac{3f(N-\Delta N)}{2\pi a_1^3}(a_1^2-\rho^2)^{1/2}, \quad b_1 \leqslant \rho \leqslant a_1 \\ \tau_{R_a} &= \frac{3f(N-\Delta N)}{2\pi a_1^3}[(a_1^2-\rho^2)^{1/2}-2(b_1^2-\rho^2)^{1/2}], \\ & \qquad\qquad b \leqslant \rho \leqslant b_1 \\ \tau_{R_a} &= \frac{3f(N-\Delta N)}{2\pi a_1^3}[(a_1^2-\rho^2)^{1/2}-2(b_1^2-\rho^2)^{1/2} \\ & \qquad + 2(b^2-\rho^2)^{1/2}], \quad c \leqslant \rho \leqslant b \\ \tau_{R_a} &= \frac{3f(N-\Delta N)}{2\pi a_1^3}[(a_1^2-\rho^2)^{1/2}-2(b_1^2-\rho^2)^{1/2} \\ & \qquad + 2(b^2-\rho^2)^{1/2}-(c^2-\rho^2)^{1/2}], \quad \rho \leqslant c \end{aligned}\right\} \quad [46]$$

This distribution of traction may be attained by applying (1) $N - \Delta N$, (2) T_1^*, then (3) reducing tangential force to T_1, and

(4) again increasing it by $\overline{\Delta T}$, where the values of these load levels are

$$A — \qquad T_1^* = f(N - \Delta N)\left(1 - \frac{c^2}{a_1^2}\right) = T^* - f\Delta N$$

$$B — \qquad T_1^* - T_1 = 2f(N - \Delta N)\left(1 - \frac{b^2}{a_1^2}\right) = T^* - T - 2f\Delta N$$

hence

$$T_1 = T + f\Delta N$$

$$C — \qquad \overline{\Delta T} = 2f(N - \Delta N)\left(1 - \frac{b^2}{a_1^2}\right) = \Delta T - 2f\Delta N$$

$$\left.\begin{aligned}
\tau_{R_n} &= 0, \quad a_1 \leqslant \rho \leqslant a \\
\tau_{R_n} &= -\frac{3f(N-\Delta N)}{2\pi a_1^3}(a_1^2 - \rho^2)^{1/2}, \quad b \leqslant \rho \leqslant a_1 \\
\tau_{R_n} &= -\frac{3f(N-\Delta N)}{2\pi a_1^3}[(a_1^2 - \rho^2)^{1/2} - 2(b^2 - \rho^2)^{1/2}], \quad c \leqslant \rho \leqslant b \\
\tau_{R_n} &= -\frac{3f(N-\Delta N)}{2\pi a_1^3}[(a_1^2 - \rho^2)^{1/2} - 2(b^2 - \rho^2)^{1/2} + (c^2 - \rho^2)^{1/2}], \quad \rho \leqslant c
\end{aligned}\right\} \quad [47]$$

Again, the situation is the same as if the order of loading had been: (1) $N - \Delta N$, (2) $T_1^* = T^* - f\Delta N$, then (3) decrease of tangential load to $T_1 = T + f\Delta N$.

If $f\Delta N \leqslant \Delta T < 2f\Delta N$, path O-A-B-C-B' in load-displacement plane, Fig. 26, may be replaced by path O-A'-B'; unfreezing

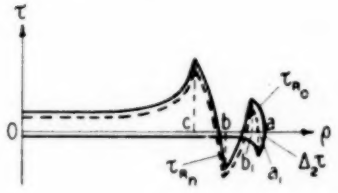

FIG. 23

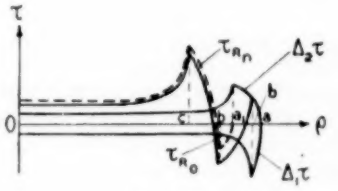

FIG. 25

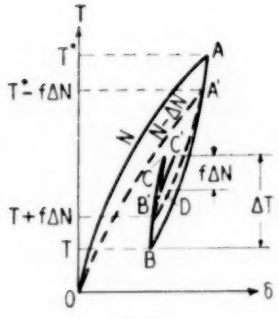

FIG. 24

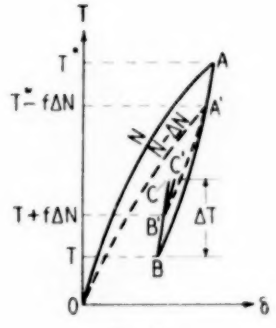

FIG. 26

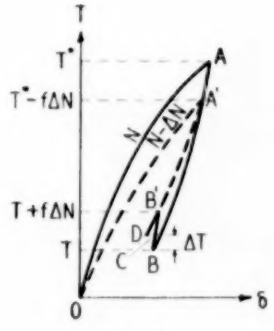

FIG. 27

Thus, in the load-displacement plane, Fig. 24, path O-A-B-C-D may be thought of as replaced by path O-A'-B'-D. Unfreezing will be followed by displacement along DC'.

The resulting compliance is

$$c_t = \lim_{\substack{\Delta N \to 0 \\ \Delta T \to 0}} \left\{ \frac{1}{\Delta T}\left[\frac{2-\nu}{8\mu a}\left(1 - \frac{\Delta T}{2fN}\right)^{-1/3}\Delta T - \frac{2-\nu}{8\mu a}\left(1 - \frac{\Delta T - f\Delta N}{2fN}\right)^{-1/3} f\Delta N + \frac{2-\nu}{8\mu a_1}\left(1 - \frac{f\Delta N}{2f(N-\Delta N)}\right)^{-1/3} f\Delta N\right]\right\} = \frac{2-\nu}{8\mu a}$$

(*b*) $\Delta T < 2f\Delta N$ ($a_1 < b_1$). The addition to the traction in step 1 of $\Delta_1\tau$, Equations [35], and $\Delta_2\tau$, Equations [36], both with signs reversed, and with b_1 replacing b in the expression for $\Delta_1\tau$, will serve to remove the traction in annulus $a_1 \leqslant \rho \leqslant a$. Hence the resultant traction (not in equilibrium with $T + \Delta T$) will be (see Fig. 25)

follows path $B'C'$. The compliance may be seen to be $c_t = (2-\nu)/8\mu a$.

If $\Delta T < f\Delta N$, unfreezing follows path $B'D$, Fig. 27. The compliance is given by

$$c_t = \lim_{\substack{\Delta N \to 0 \\ \Delta T \to 0}} \left\{ \frac{1}{\Delta T}\left[\frac{2-\nu}{8\mu a} f\Delta N - \frac{2-\nu}{8\mu a_1}\left(1 - \frac{T_1^* - T_1}{2f(N-\Delta N)}\right)^{-1/3}(f\Delta N - \Delta T)\right]\right\} = \frac{2-\nu}{8\mu a}\left[f\frac{dN}{dT} + \left(1 - f\frac{dN}{dT}\right)\left(1 - \frac{T^* - T}{2fN}\right)^{-1/3}\right],$$

$$\frac{dN}{dT} \leqslant -\frac{1}{f}$$

and

$$c_t = \frac{2-\nu}{8\mu a}, \quad 0 > \frac{dN}{dT} \geqslant -\frac{1}{f} \qquad [48]$$

Here, once again, the absolute value of dN/dT is to be used in the formula.

In examining the cases of Sections 11 and 13, the reader will discover an apparent paradox to the effect that the expressions for the tangential compliances depend on the order of application of ΔN and ΔT. However, an imposition of a large number of infinitesimal increments, followed by a limiting process, leads to the results obtained regardless of the initial order of application.

14 Tangential Tractions Due to Oblique Loading

In this section a calculation is made of the distribution of tangential traction on the contact area of two spheres, pressed together by an initial force N_0 normal to their common tangent plane, and acted upon by a monotonically increasing oblique force. It is assumed that the resultant force remains planar. A study is made of the traction distribution because, by means of it, it will be possible to calculate the relative displacement of the two spheres.

Let a_0 denote the radius of the initial contact circle. An increase, by an amount $\Delta_i N$, of the normal force increases the contact radius to a value a_i; an application, at constant normal force, of an incremental tangential force $\Delta_i T$ gives rise to a tangential traction $\Delta_i \tau$, expressed by Equations [6] in which the appropriate values of N and T have been inserted. The three cases $\Delta_i T \lessgtr f\Delta_i N$ are considered separately.

(*a*) $\Delta_i T < f\Delta_i N$ ($c_i > a_{i-1}$). After n increments, by amounts $\Delta_i N$, $\Delta_i T$ ($i = 1, 2, \ldots, n$) of the normal and tangential forces, respectively, the resultant traction on circle $\rho < a_0$ will be, from Equations [6] and [1]

$$\tau_n = \frac{3f}{2\pi KR}\sum_{i=1}^{n}\left[(a_i^2-\rho^2)^{1/2}-(c_i^2-\rho^2)^{1/2}\right]$$

$$= \frac{3f}{2\pi KR}\sum_{i=1}^{n} a_i(1-\rho^2/a_i^2)^{1/2}\left[1-\left(1-\frac{1-c_i^2/a_i^2}{1-\rho^2/a_i^2}\right)^{1/2}\right] \quad [49]$$

At the ith stage the value of the normal load is

$$N_i = N_0 + \sum_{\mu=1}^{i}\Delta_\mu N$$

Now, let

$$\sum_{\mu=1}^{i}\Delta_\mu N = \psi_i(T) \quad [50]$$

so that

$$N_i = N_0 + \psi_i(T) \quad [51]$$

Hence

$$a_i = [KR(N_0+\psi_i)]^{1/3} \quad [52]$$

and

$$c_i = a_i\left[1-\frac{\Delta_i T}{f(N_0+\psi_i)}\right]^{1/3} \quad [53]$$

Now, substitution of Equations [52] and [53] in Equation [49], and passage to the limit as $\Delta_i N$ and $\Delta_i T$ approach zero and n becomes infinite, yield

$$\tau = \frac{S^2}{2\pi\rho^2}\int_0^T\left[1-\frac{S^2}{(N_0+\psi)^{2/3}}\right]^{-1/2}(N_0+\psi)^{-2/3}dT \quad [54]$$

where

$$S = \rho(KR)^{-1/3}$$

To proceed further it is necessary to specify $\psi(T)$, i.e., the relation between N and T. The simplest case is

$$\frac{dT}{dN} = \text{const, say, } \beta \quad [55]$$

Using Equations [50] and [55], the integration in Equation [54] can be performed, with the result

$$\tau = \frac{3\beta(N_0+N^*)}{2\pi a_*^3}\left[(a_*^2-\rho^2)^{1/2}-(a_0^2-\rho^2)^{1/2}\right], \quad \rho < a_0 \quad [56]$$

where $N_0 + N^*$ is the final normal load and a_* the corresponding contact radius.

The resultant traction in annulus $a_{r-1} \leqslant \rho \leqslant c_r$ at the rth stage of loading will be

$$\tau_n = \frac{3f}{2\pi KR}\sum_{i=r}^{n}\left[(a_i^2-\rho^2)^{1/2}-(c_i^2-\rho^2)^{1/2}\right]$$

$$= \frac{3f}{2\pi KR}\sum_{i=r}^{n} a_i(1-\rho^2/a_i^2)^{1/2}\left[1-\left(1-\frac{1-c_i^2/a_i^2}{1-\rho^2/a_i^2}\right)^{1/2}\right]$$

which may be rewritten

$$\tau_n = \frac{3f}{2\pi KR}a_r(1-\rho^2/a_r^2)^{1/2}\left[1-\left(1-\frac{1-c_r^2/a_r^2}{1-\rho^2/a_r^2}\right)^{1/2}\right]$$

$$+\frac{3f}{2\pi KR}\sum_{i=r+1}^{n} a_i(1-\rho^2/a_i^2)^{1/2}\left[1-\left(1-\frac{1-c_i^2/a_i^2}{1-\rho^2/a_i^2}\right)^{1/2}\right] \quad [57]$$

Again, employment of Equations [52] and [53] and passage to the limit as vanishing increments of force are applied infinitely many times, followed by imposition of the condition in Equation [55] in conjunction with Equation [50], yield for the value of the resultant traction in Equation [57]

$$\tau = \frac{3\beta(N_0+N^*)}{2\pi a_*^3}(a_*^2-\rho^2)^{1/2}, \quad a_0 \leqslant \rho \leqslant a_* \quad [58]$$

Equations [56] and [58] constitute the expressions for the resultant traction. It may be noted they are exactly like Equations [6], with β playing the role of the coefficient of friction. Since $\tau < f\sigma$, no slip, in the form heretofore understood, has taken place. Instead, there appears to be an overlapping action, proceeding outward from a_0 to a_*, in the direction of the tangential force.

(*b*) $\Delta_i T = f\Delta_i N$ ($c_i = a_{i-1}$), i.e., $\beta = f$. The resultant traction in annulus $a_{r-1} \leqslant \rho \leqslant a_r$ is given by

$$\tau_n = \frac{3f}{2\pi KR}\left\{(a_r^2-\rho^2)^{1/2}+\sum_{i=r+1}^{n}\left[(a_i^2-\rho^2)^{1/2}-(a_{i-1}^2-\rho^2)^{1/2}\right]\right\}$$

$$= \frac{3f}{2\pi KR}(a_n^2-\rho^2)^{1/2}$$

$$= \frac{3fN_n}{2\pi a_n^3}(a_n^2-\rho^2)^{1/2}$$

Thus

$$\tau = \lim_{\substack{\Delta N,\Delta T\to 0\\ n\to\infty}}\{\tau_n\} = \frac{3f(N_0+N^*)}{2\pi a_*^3}(a_*^2-\rho^2)^{1/2}, \quad a_0 \leqslant \rho \leqslant a_* \quad [59]$$

On circle $\rho \leqslant a_0$

$$\tau_n = \frac{3f}{2\pi KR} \sum_{i=1}^{n} [(a_i^2 - \rho^2)^{1/2} - (a_{i-1}^2 - \rho^2)^{1/2}]$$

$$= \frac{3fN_n}{2\pi a_n^3} [(a_n^2 - \rho^2)^{1/2} - (a_0^2 - \rho^2)^{1/2}]$$

so that

$$\tau = \lim_{\substack{\Delta N, \Delta T \to 0 \\ n \to \infty}} \{\tau_n\} = \frac{3f(N_0 + N^*)}{2\pi a_*^3} [(a_*^2 - \rho^2)^{1/2} - (a_0^2 - \rho^2)^{1/2}], \quad \rho \leqslant a_0 \quad \ldots\ldots [60]$$

Equations [59] and [60], which are essentially the same as Equations [6], completely specify the distribution of traction in this case.

(*c*) $\Delta_i T > f\Delta_i N$, i.e., $\beta > f$. The usual division of $\Delta_i T$ into $f\Delta_i N$ and $\Delta_i T - f\Delta_i N$ is made and the two parts applied consecutively. After n applications the expression for the resultant traction will be

$$\tau_n = \frac{3f}{2\pi KR} (a_n^2 - \rho^2)^{1/2}, \quad c_n \leqslant \rho \leqslant a_n$$

$$\tau_n = \frac{3f}{2\pi KR} [(a_n^2 - \rho^2)^{1/2} - (c_n^2 - \rho^2)^{1/2}], \quad \rho \leqslant c_n$$

where

$$c_n = a_n \left(1 - \frac{\sum_{i=1}^{n} \Delta_i T}{fN_n}\right)^{1/2} < a_0$$

Passage to the limit results in

$$\left.\begin{aligned} \tau &= \frac{3f(N_0 + N^*)}{2\pi a_*^3} (a_*^2 - \rho^2)^{1/2}, \quad c_* \leqslant \rho \leqslant a_* \\ \tau &= \frac{3f(N_0 + N^*)}{2\pi a_*^3} [(a_*^2 - \rho^2)^{1/2} - (c_*^2 - \rho^2)^{1/2}], \quad \rho \leqslant c_* \end{aligned}\right\} \ldots [61]$$

where

$$c_* = a_* \left(1 - \frac{T^*}{f(N_0 + N^*)}\right)^{1/2}$$

15 Tangential Tractions Due to Oblique Unloading

Let it now be required to find the tractions when the loading described in the preceding section is followed by a monotonically decreasing oblique force of constant inclination.

(*a*) $\beta \leqslant f$. The traction at the start of unloading is given by Equations [56] and [58]. Keeping the normal load constant, decrease the tangential force by $\Delta_1 T$. Slip will take place in the direction opposite to that of the initial tangential force. By the fundamental rules, the traction over the region on which new slip has occurred will be in the direction of slip and of magnitude $f\sigma$. Let b_1 denote the inner radius of the new slip annulus. Then, in order that no new slip occur in circle $\rho \leqslant b_1$, the additional traction must be the sum, with sign reversed, of the tractions of Equations [56] and [58], in which a_0 is replaced by b_1, and of Equations [6], in which b_1 replaces c. Hence the resultant traction will be

$$\tau_{R_0} = -\frac{3f(N_0 + N^*)}{2\pi a_*^3} (a_*^2 - \rho^2)^{1/2}, \quad b_1 \leqslant \rho \leqslant a_*$$

$$\tau_{R_0} = -\frac{3f(N_0 + N^*)}{2\pi a_*^3} \left[(a_*^2 - \rho^2)^{1/2} - \left(1 + \frac{\beta}{f}\right)(b_1^2 - \rho^2)^{1/2}\right], \quad a_0 \leqslant \rho \leqslant b_1$$

$$\tau_{R_0} = -\frac{3f(N_0 + N^*)}{2\pi a_*^3} \left[(a_*^2 - \rho^2)^{1/2} - \left(1 + \frac{\beta}{f}\right)(b_1^2 - \rho^2)^{1/2} + \frac{\beta}{f}(a_0^2 - \rho^2)^{1/2}\right], \quad \rho \leqslant a_0$$

The equilibrium condition, Equation [11], yields

$$b_1 = a_* \left(1 - \frac{\Delta T}{\left(1 + \frac{\beta}{f}\right) f(N_0 + N^*)}\right)^{1/2}$$

Reduction of the normal load by $\Delta_1 N$ to N_1, resulting in a contact surface of radius a_1 ($a_1 < b_1$, since $\Delta_1 N > \Delta_1 T/f$), must be preceded by a removal of the traction from annulus $a_1 \leqslant \rho \leqslant a$ in such a manner that no slip occur on $\rho \leqslant a_1$ (see, for example, Section 11, 2*b*). This may be accomplished by: (1) subtracting from the foregoing τ_{R_0} the same tractions which, when added to the traction of Equations [56] and [58], yielded τ_{R_0}, (2) adding, with sign reversed, tractions of Equations [56] and [58], in which a_0 is replaced by a_1. This will result in a distribution of traction

$$\tau_{R_1} = \frac{3\beta N_1}{2\pi a_1^3} (a_1^2 - \rho^2)^{1/2}, \quad a_0 \leqslant \rho \leqslant a_1$$

$$\tau_{R_1} = \frac{3\beta N_1}{2\pi a_1^3} [(a_1^2 - \rho^2)^{1/2} - (a_0^2 - \rho^2)^{1/2}], \quad \rho \leqslant a_0$$

where

$$N_1 = N_0 + N^* - \Delta_1 N$$

and

$$\frac{a_0}{a_1} = \left(1 - \frac{T^* - \Delta_1 T}{\beta N_1}\right)^{1/2}$$

which, because it corresponds to a condition of equilibrium (with force $T^* - \Delta_1 T$), remains unaltered by the reduction of normal load and subsequent unfreezing. But this distribution of traction is, qualitatively, the same as at the start of unloading; hence the unloading process may be repeated with similar results.

After the nth reduction the traction will be

$$\tau_{R_n} = \frac{3\beta N_n}{2\pi a_n^3} (a_n^2 - \rho^2)^{1/2}, \quad a_0 \leqslant \rho \leqslant a_n$$

$$\tau_{R_n} = \frac{3\beta N_n}{2\pi a_n^3} [(a_n^2 - \rho^2)^{1/2} - (a_0^2 - \rho^2)^{1/2}], \quad \rho \leqslant a_0$$

where

$$N_n = N_0 + N^* - \sum_{i=1}^{n} \Delta_i N$$

a_n is the contact radius at normal load N_n and

$$\frac{a_0}{a_n} = \left(1 - \frac{T^* - \sum_{i=1}^{n} \Delta_i T}{\beta N_n}\right)^{1/2}$$

Finally

$$\left.\begin{aligned}\tau &= \lim_{\substack{\Delta N,\Delta T\to 0\\ n\to\infty}} \{\tau_{R_n}\}\\ &= \frac{3\beta(N_0+N)}{2\pi a^3}(a^2-\rho^2)^{1/2}, \quad a_0 \leqslant \rho \leqslant a\\ \tau &= \frac{3\beta(N_0+N)}{2\pi a^3}[(a^2-\rho^2)^{1/2}-(a_0^2-\rho^2)^{1/2}],\\ &\qquad \rho \leqslant a_0\end{aligned}\right\} \quad \ldots [62]$$

where

$$\frac{a_0}{a} = \left(1-\frac{T}{\beta(N_0+N)}\right)^{1/2} = \left(\frac{N_0}{N_0+N}\right)^{1/2}$$

and $N_0 + N$, a, $T(>0)$ denote final normal load, contact radius, and tangential load, respectively.

It may be observed that Equations [62] have the same form as their counterpart in loading, Equations [56] and [58].

(*b*) $\beta \geqslant f$. The traction at the start of unloading is given by Equations [61]. Reduction, at constant normal load, of the tangential load by $\Delta_1 T$ changes the traction to that given by Equations [10], in which N, a and $T^* - T$ are replaced by $N_0 + N^*$, a_* and $\Delta_1 T$, respectively.

In the process of reducing the normal force it is necessary to distinguish between the two cases $f \leqslant \beta < 2f$ and $\beta \geqslant 2f$; however, both follow closely the pattern of events discussed in Section 11. Thus the resultant equilibrium traction after one cycle of unloading will be

$$\tau_{R_1} = -\frac{3fN_1}{2\pi a_1^3}(a_1^2-\rho^2)^{1/2}, \quad b_1 \leqslant \rho \leqslant a_1$$

$$\tau_{R_1} = -\frac{3fN_1}{2\pi a_1^3}[(a_1^2-\rho^2)^{1/2}-2(b_1^2-\rho^2)^{1/2}], \quad c \leqslant \rho \leqslant b_1$$

$$\tau_{R_1} = -\frac{3fN_1}{2\pi a_1^3}[(a_1^2-\rho^2)^{1/2}-2(b_1^2-\rho^2)^{1/2} + (c^2-\rho^2)^{1/2}], \quad \rho \leqslant c$$

where the expressions

$$c = a_1\left(1-\frac{T^*}{f(N_0+N^*)}\right)^{1/2}\left(\frac{N_0+N^*}{N_1}\right)^{1/2}$$

and

$$b_1 = a_1\left(1+\frac{\Delta_1 N}{2N_1}-\frac{\Delta_1 T}{2fN_1}\right)^{1/2}$$

are obtained by using Equation [11].

After the nth reduction the traction will be given by the foregoing equations in which the subscript 1 is replaced by n and the symbol $\Delta_n \equiv \sum_{i=1}^{n} \Delta_i$. Hence

$$\left.\begin{aligned}\tau_R &= \lim_{\substack{\Delta N,\Delta T\to 0\\ n\to\infty}} \{\tau_{R_n}\}\\ &= -\frac{3f(N_0+N)}{2\pi a^3}(a^2-\rho^2)^{1/2}, \quad b \leqslant \rho \leqslant a\\ \tau_R &= -\frac{3f(N_0+N)}{2\pi a^3}[(a^2-\rho^2)^{1/2}-2(b^2-\rho^2)^{1/2}],\\ &\qquad c_* \leqslant \rho \leqslant b\\ \tau_R &= -\frac{3f(N_0+N)}{2\pi a^3}[(a^2-\rho^2)^{1/2}-2(b^2-\rho^2)^{1/2}\\ &\qquad + (c_*^2-\rho^2)^{1/2}], \quad \rho \leqslant c_*\end{aligned}\right\} \quad \ldots [63]$$

where $N_0 + N$, a, $T > 0$ are defined in Equations [62]

$$\frac{c_*}{a} = \left(1-\frac{T^*}{f(N_0+N^*)}\right)^{1/2}\left(\frac{N_0+N^*}{N_0+N}\right)^{1/2}$$

and

$$\frac{b}{a} = \left(1-\frac{T^*-T}{2f(N_0+N)}+\frac{N^*-N}{2(N_0+N)}\right)^{1/2}$$

16 Tangential Tractions Due to Oscillating Oblique Force, $dT/dN \geqslant f$

It is now possible to calculate the distribution of traction on the contact surface of a pair of elastic spheres when the spheres are subjected to an initial normal compression, followed by an oscillating oblique force. This is the same problem as that of Section 5 except that the restriction to constant normal force is now removed. As will be seen, the additional variable introduces the complication that a steady state is not reached until after an additional half cycle.

Again, it is necessary to distinguish between cases $dT/dN \geqslant f$ and $dT/dN \leqslant f$. In this section the discussion is limited to the former.

1 Starting with an initial normal load N_0, apply a monotonically increasing oblique load until the contact surface of the two spheres is acted upon by normal and tangential forces $N_0 + N^*$ and T^*, respectively. It should be noted that $N^* = T^*/\beta$. The distribution of tangential traction is given by Equations [61] in which the expression for c_* may now be rewritten

$$\frac{c_*}{a_*} = \left(1-\frac{T^*/fN_0}{1+T^*/\beta N_0}\right)^{1/2} \quad \ldots [64]$$

Since the expression for a_0/a_* may be put in the form

$$\frac{a_0}{a_*} = \left(\frac{N_0}{N_0+N^*}\right)^{1/2} = \left(\frac{1}{1+T^*/\beta N_0}\right)^{1/2} = \left(1-\frac{T^*/\beta N_0}{1+T^*/\beta N_0}\right)^{1/2} \quad \ldots [65]$$

it is evident from a comparison of Equations [64] and [65] that $c_* \leqslant a_0$.

2 Now unload from $\{N_0 + N^*, T^*\}$. The traction at level $\{N_0 + N, T\}$ will be given by Equations [63] in which the expressions for b/a and c_*/a may be written

$$\frac{b}{a} = \left[1-\frac{(T^*-T)/2fN_0}{1+T/\beta N_0}+\frac{(T^*-T)/2\beta N_0}{1+T/\beta N_0}\right]^{1/2} \quad \ldots [66]$$

and

$$\frac{c_*}{a} = \left[1-\frac{(T^*-T)/2fN_0}{1+T/\beta N_0}-\frac{(T^*+T)/2fN_0}{1+T/\beta N_0}+\frac{(T^*-T)/\beta N_0}{1+T/\beta N_0}\right]^{1/2} \quad \ldots [67]$$

It is seen from Equations [66] and [67] that $b = c_*$ for that value of T which satisfies the relation

$$\frac{T}{T^*} = \frac{1/\beta-1/f}{1/\beta+1/f} = \lambda \quad \ldots [68]$$

where $-1 \leqslant \lambda \leqslant 0$.

At $T = \lambda T^*$ the traction of Equations [63] degenerates to

$$\tau = -\frac{3f(N_0+N_\lambda)}{2\pi a_\lambda^3}(a_\lambda^2-\rho^2)^{1/2}, \quad c_* \leqslant \rho \leqslant a_\lambda$$

$$\tau = -\frac{3f(N_0 + N_\lambda)}{2\pi a_\lambda^3}\left[(a_\lambda^2 - \rho^2)^{1/2} - (c_*^2 - \rho^2)^{1/2}\right], \quad \rho \leqslant c_* \qquad \ldots\ldots [69]$$

where

$$N_\lambda = \frac{T_\lambda}{\beta} = \frac{\lambda T^*}{\beta}$$

and

$$\frac{a_\lambda}{a_0} = \left(1 + \frac{\lambda T^*}{\beta N_0}\right)^{1/3} \leqslant 1$$

Further unloading to $\{N_0 - N^*, -T^*\}$ causes the traction to become

$$\left.\begin{aligned} \tau &= -\frac{3f(N_0 - N^*)}{2\pi a_{-*}^3}(a_{-*}^2 - \rho^2)^{1/2}, \quad c_* \leqslant \rho \leqslant a_{-*} \\ \tau &= -\frac{3f(N_0 - N^*)}{2\pi a_{-*}^3}\left[(a_{-*}^2 - \rho^2)^{1/2} - (c_{-*}^2 - \rho^2)^{1/2}\right], \\ &\qquad\qquad \rho \leqslant c_{-*} \end{aligned}\right\} \ldots [70]$$

where a_{-*}, the contact radius corresponding to a normal force $N_0 - N^*$, satisfies the relation

$$\frac{a_{-*}}{a_0} = \left(\frac{N_0 - N^*}{N_0}\right)^{1/3} = \left(1 - \frac{T^*}{\beta N_0}\right)^{1/3} \qquad \ldots\ldots [71]$$

and c_{-*} is given by

$$\frac{c_{-*}}{a_{-*}} = \left(1 - \frac{T^*}{f(N_0 - N^*)}\right)^{1/3} = \left(1 - \frac{T^*/fN_0}{1 - T^*/\beta N_0}\right)^{1/3} \ldots [72]$$

Comparison of Equation [67] at $T = 0$ and Equation [71] reveals that $c_* \gtrless a_{-*}$, according as $\beta \lessgtr 2f$.

3 Reload; the traction at stage $\{N_0 + N, T\}$ will be

$$\left.\begin{aligned} \tau &= \frac{3f(N_0 + N)}{2\pi a^3}(a^2 - \rho^2)^{1/2}, \quad b_r \leqslant \rho \leqslant a \\ \tau &= \frac{3f(N_0 + N)}{2\pi a^3}\left[(a^2 - \rho^2)^{1/2} - 2(b_r^2 - \rho^2)^{1/2}\right], \\ &\qquad\qquad c_{-*} \leqslant \rho \leqslant b_r \\ \tau &= \frac{3f(N_0 + N)}{2\pi a^3}\left[(a^2 - \rho^2)^{1/2} - 2(b_r^2 - \rho^2)^{1/2}\right. \\ &\qquad \left. + (c_{-*}^2 - \rho^2)^{1/2}\right], \quad \rho \leqslant c_{-*} \end{aligned}\right\} \ldots [73]$$

where

$$|N| \leqslant N^*, \qquad |T| \leqslant T^*$$

Using the relation

$$\frac{c_*}{a} = \frac{c_{-*}}{a_{-*}}\,\frac{a_{-*}}{a}$$

and the equilibrium condition, Equation [11], one obtains for the value of b_r/a

$$\frac{b_r}{a} = \left[\frac{1}{2}\left(1 + \frac{N_0 - N^*}{N_0 + N}\right) - \frac{T^* + T}{2f(N_0 + N)}\right]^{1/3} \ldots [74]$$

At $\{N_0 + N^*, T^*\}$

$$a = a_*$$

$$\frac{c_{-*}}{a_*} = \left(1 - \frac{T^*}{f(N_0 - N^*)}\right)^{1/3}\left(\frac{N_0 - N^*}{N_0 + N^*}\right)^{1/3} = \left[1 - \frac{(1 + 2f/\beta)T^*/fN_0}{1 + T^*/\beta N_0}\right]^{1/3} \qquad \ldots\ldots [75]$$

and

$$\frac{b_*}{a_*} = \left(\frac{N_0}{N_0 + N^*} - \frac{T^*}{f(N_0 + N^*)}\right)^{1/3} = \left[1 - \frac{(1 + f/\beta)T^*/fN_0}{1 + T^*/\beta N_0}\right]^{1/3} \qquad \ldots\ldots [76]$$

Hence, comparison of Equations [64], [75], and [76] shows that

$$c_* > b_* > c_{-*}$$

4 Unload once again; the traction at load level $\{N_0 + N, T\}$ will be

$$\left.\begin{aligned} \tau &= -\frac{3f(N_0 + N)}{2\pi a^3}(a^2 - \rho^2)^{1/2}, \quad b_u \leqslant \rho \leqslant a \\ \tau &= -\frac{3f(N_0 + N)}{2\pi a^3}\left[(a^2 - \rho^2)^{1/2} - 2(b_u^2 - \rho^2)^{1/2}\right], \\ &\qquad\qquad b_* \leqslant \rho \leqslant b_u \\ \tau &= -\frac{3f(N_0 + N)}{2\pi a^3}\left[(a^2 - \rho^2)^{1/2} - 2(b_u^2 - \rho^2)^{1/2}\right. \\ &\qquad \left. + 2(b_*^2 - \rho^2)^{1/2}\right], \quad c_{-*} \leqslant \rho \leqslant b_* \\ \tau &= -\frac{3f(N_0 + N)}{2\pi a^3}\left[(a^2 - \rho^2)^{1/2} - 2(b_u^2 - \rho^2)^{1/2}\right. \\ &\qquad \left. + 2(b_*^2 - \rho^2)^{1/2} - (c_{-*}^2 - \rho^2)^{1/2}\right], \quad \rho \leqslant c_{-*} \end{aligned}\right\} \ldots [77]$$

In order for equilibrium with the force T to obtain, the relation

$$\frac{b_u}{a} = \left[\frac{1}{2}\left(1 + \frac{N_0 + N^*}{N_0 + N}\right) - \frac{T^* - T}{2f(N_0 + N)}\right]^{1/3} \ldots [78]$$

must hold (see Equation [11]).

When $T = -T^*$, the contact radius is once again a_{-*}, and $b_u = b_{-*}$. Furthermore

$$\frac{b_{-*}}{a_{-*}} = \left[\frac{N_0}{N_0 - N^*} - \frac{T^*}{f(N_0 - N^*)}\right]^{1/3} = \frac{b_*}{a_{-*}}$$

so that $b_{-*} = b_*$. Hence the distribution of traction, Equations [77], is the same as that obtained on first unloading to $\{N_0 - N^*, -T^*\}$ (see Equations [70]). Henceforth the cycle may be repeated with identical results, i.e., a steady state is reached after one and three-quarter cycles.

17 Load-Displacement Relation for Oscillating Oblique Force, $dT/dN \geqslant f$

The load-displacement relations corresponding to the tractions of the preceding section may be obtained by superposition of equations in the generic form of Equation [7]. By the aid of Equation [1] and the relation $E = 2(1 + \nu)\mu$, the first factor of the right-hand side of Equation [7] may be transformed to

$$\frac{3f(2 - \nu)N}{16\mu a} = \frac{f(2 - \nu)}{2(1 - \nu)}\,\frac{a^2}{R} \qquad \ldots\ldots [79]$$

Hence, during the first loading from $\{N_0, 0\}$ to $\{N_0 + N^*, T^*\}$ the displacement will be given by (see curve OP, Fig. 28)

$$\frac{2(1-\nu)}{f(2-\nu)}\frac{R\delta_l}{a_0^2} = \frac{a^2}{a_0^2}\left(1-\frac{c^2}{a^2}\right)$$

$$= (1+\theta L)^{2/3} - [1-(1-\theta)L]^{2/3}, \quad 0 \leqslant L \leqslant L^* \quad \ldots\ldots [80]$$

where

$$L = \frac{T}{fN_0}, \qquad L^* = \frac{T^*}{fN_0}, \qquad \theta = \frac{f}{\beta}$$

and the subscript on δ_l stands for "loading." The range of θ is $0 \leqslant \theta \leqslant 1$.

From Equation [80], and the fact that

$$a = a_0(1+\theta L)^{1/3} \quad \ldots\ldots [81]$$

the expression for the tangential compliance in this load interval is obtained. Thus

$$c_l = \frac{d\delta_l}{dT} = \frac{2-\nu}{8\mu a}\left[\theta + (1-\theta)\left(1-\frac{L}{1+\theta L}\right)^{-1/3}\right] \quad [82]$$

If, now, Equation [55] and the definition of θ (see Equation [80]) are substituted into Equation [25] for the compliance due to the corresponding incremental process, the resulting relation becomes identical with Equation [82]. This result is to be expected, since the tractions in both cases are identical.

During the unloading process following initial loading, the load-displacement relation takes two different forms, according as $L \gtrless \lambda L^*$. With the aid of the expressions defined in Equations [66] and [67] one obtains (curves *P-R-Y* and *YS*, Fig. 28)

$$\frac{2(1-\nu)}{f(2-\nu)}\frac{R\delta_{u11}}{a_0^2} = \frac{a^2}{a_0^2}\left(2\frac{b^2}{a^2} - \frac{c_*^2}{a^2} - 1\right)$$

$$= 2\left[1+\frac{\theta}{2}(L^*+L) - \frac{1}{2}(L^*-L)\right]^{2/3} - [1-(1-\theta)L^*]^{2/3} - (1+\theta L)^{2/3},$$

$$L^* \geqslant L \geqslant \lambda L^* \quad \ldots [83]$$

where λ is defined in Equation [68] and

$$\frac{2(1-\nu)}{f(2-\nu)}\frac{R\delta_{u12}}{a_0^2} = -(1+\theta L)^{2/3} + [1+(1+\theta)L]^{2/3}, \quad \lambda L^* \geqslant L \geqslant -L^* \quad \ldots\ldots [84]$$

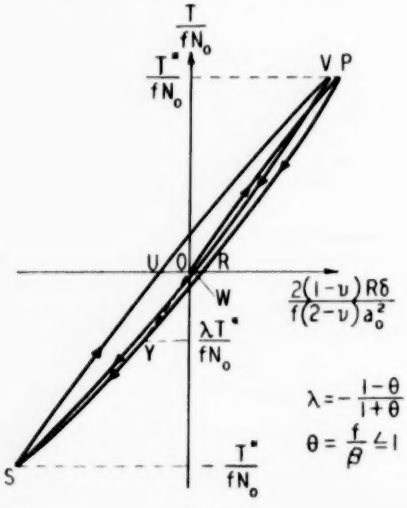

FIG. 28

The subscripts on δ_{u11} and δ_{u12} stand for "first portion of first unloading" and "second portion of first unloading," respectively. At point Y (Fig. 28), curves *P-R-Y* and *YS* have a common tangent.

In the load interval from $\{N_0 + N^*, T^*\}$ to $\{N_0 + N_\lambda, \lambda T^*\}$ the compliance is

$$c_{u11} = \frac{d\delta_{u11}}{dT} = \frac{2-\nu}{8\mu a}\left\{-\theta + (1+\theta)\left[1-(1-\theta)\frac{L^*-L}{2(1+\theta L)}\right]^{-1/3}\right\} \quad \ldots\ldots [85]$$

It will be recalled that the compliance obtained by the corresponding incremental process is given by Equation [34] which, however, does not yield Equation [85] when fdN/dT is replaced by θ. This is because the respective traction distributions, although qualitatively alike, differ quantitatively; that is, in both cases

$$\left.\begin{aligned} \tau &= -\frac{3f\mathfrak{N}}{2\pi a^3}(a^2-\rho^2)^{1/2}, \quad b \leqslant \rho \leqslant a \\ \tau &= -\frac{3f\mathfrak{N}}{2\pi a^3}[(a^2-\rho^2)^{1/2} - 2(b^2-\rho^2)^{1/2}], \quad c_* \leqslant \rho \leqslant b \\ \tau &= -\frac{3f\mathfrak{N}}{2\pi a^3}[(a^2-\rho^2)^{1/2} - 2(b^2-\rho^2)^{1/2} + (c_*^2-\rho^2)^{1/2}], \quad \rho \leqslant c_* \end{aligned}\right\} \quad [86]$$

where $\mathfrak{N}$ denotes the total normal load. However, while in the "incremental" case

$$c_*/a = (1 - T^*/f\mathfrak{N})^{1/3} \text{ and } b/a = [1-(T^*-T)/2f\mathfrak{N}]^{1/3}$$

in the "continuous" case

$$\frac{c_*}{a} = \left(1-\frac{T^*}{f(N_0+N^*)}\right)^{1/3}\left(\frac{N_0+N^*}{N_0+N}\right)^{1/3} = \left(1-\frac{T^*}{f\mathfrak{N}}+\frac{N^*-N}{\mathfrak{N}}\right)^{1/3}$$

and

$$\frac{b}{a} = \left(1-\frac{T^*-T}{2f\mathfrak{N}}+\frac{N^*-N}{\mathfrak{N}}\right)^{1/3}$$

where $|N| \leqslant N^*$.

In the load interval from $\{N_0 + N_\lambda, \lambda T^*\}$ to $\{N_0 - N^*, -T^*\}$ the compliance is

$$c_{u12} = \frac{d\delta_{u12}}{dT} = \frac{2-\nu}{8\mu a}\left[-\theta + (1+\theta)\left(1+\frac{1}{1+\theta L}\right)^{-1/3}\right] \quad \ldots\ldots [87]$$

The constant λ, incidentally, expressed in terms of θ, becomes

$$\lambda = -\frac{1-\theta}{1+\theta} \leqslant 0 \quad \ldots\ldots [88]$$

The displacement during reloading from $\{N_0 - N^*, -T^*\}$ to $\{N_0 + N^*, T^*\}$, obtained by aid of Equations [72] and [74], is (curve *S-U-V*, Fig. 28)

$$\frac{2(1-\nu)}{f(2-\nu)}\frac{R\delta_r}{a_0^2} = \frac{a^2}{a_0^2}\left(1+\frac{c_*^2}{a^2} - 2\frac{b_r^2}{a^2}\right)$$

$$= (1+\theta L)^{2/3} + [1-(1+\theta)L^*]^{2/3} - 2\left[1-\frac{\theta}{2}(L^*-L) - \frac{1}{2}(L^*+L)\right]^{2/3}, \quad -L^* \leqslant L \leqslant L^*$$

$$\ldots\ldots [89]$$

while the displacement during the second unloading process becomes, with reference to Equations [75], [76], and [78] (curve *V-W-S*, Fig. 28)

$$\frac{2(1-\nu)}{f(2-\nu)}\frac{R\delta_{u2}}{a_0^2} = \frac{a^2}{a_0^2}\left(2\frac{b_u^2}{a^2} - 2\frac{b_*^2}{a^2} + \frac{c_{-*}^2}{a^2} - 1\right)$$

$$= 2\left[1 + \frac{\theta}{2}(L^* + L) - \frac{1}{2}(L^* - L)\right]^{2/3} - 2(1 - L^*)^{2/3}$$

$$+ [1 - (1+\theta)L^*]^{2/3} - (1+\theta L)^{2/3}, \quad L^* \geqslant L \geqslant -L^* \qquad \ldots\ldots [90]$$

The subscripts on δ_r and δ_{u2} stand for "reloading" and "second unloading," respectively.

Further repetition of the loading cycle will, of course, yield the displacements of Equations [89] and [90]. These displacements have the same meaning for the case of an oblique oscillating force as displacements of Equations [14] and [16] have for the case of pure tangential oscillating force; the two pairs of equations become identical when $\theta = 0$, so that the loop *S-U'-V-W-S*, Fig. 28, degenerates to *S-U'-P-R-S*, Fig. 5.

It should be noted that the character of the load-displacement curves, Fig. 28, varies with θ. Thus, the curvature (with respect to the abscissa) of OP at O is negative, as in Fig. 30, for values of θ in the interval $^1/_2 < \theta \leqslant 1$ and becomes positive, as shown in Fig. 28, for $\theta < ^1/_2$. The curvature of *S-U'-V* at *S* is positive, as shown in Fig. 28, for values of $\theta < \sqrt{2} - 1$.

For the sake of completeness, the tangential compliances are given for the load intervals corresponding to which the displacements are δ_r and δ_{u2}, respectively. Thus

$$c_r = \frac{d\delta_r}{dT} = \frac{2-\nu}{8\mu a}\left\{\theta + (1-\theta)\left[1 - (1+\theta)\frac{L^* + L}{2(1+\theta L)}\right]^{-1/3}\right\} \qquad \ldots\ldots [91]$$

and

$$c_{u2} = \frac{d\delta_{u2}}{dT} = \frac{2-\nu}{8\mu a}\left\{-\theta + (1+\theta)\left[1 - (1-\theta)\frac{L^* - L}{2(1+\theta L)}\right]^{-1/3}\right\} \qquad \ldots\ldots [92]$$

In all equations of this section there exists a limitation on the value of T^*, namely

$$0 \geqslant \frac{-T^*}{f(N_0 - N^*)} \geqslant -1$$

which may be put in the form

$$0 \leqslant L^* \leqslant \frac{1}{1+\theta} \qquad \ldots\ldots [93]$$

18 Oscillating Oblique Force, $dT/dN \leqslant f$

1 Repeat step 1 of Section 16; the traction is given by Equations [56] and [58]. It will be recalled (see Section 14) that no slip occurs during loading.

2 During unloading from $\{N_0 + N^*, T^*\}$ to $\{N_0, 0\}$ the traction at any level of loading is given by Equations [62], and vanishes at $T = 0$. Again, no slip has taken place.

Further unloading constitutes, in effect, the situation treated in Section 8, except for change in sign of the tangential force and, hence, of the tangential traction. Consequently, the present process yields a distribution of traction expressed by Equations [6] with sign reversed, in which, of course, N stands for the total normal load. At $\{N_0 - N^*, -T^*\}$, $a = a_*$ and $c = c_*$. The expression for the resultant traction is given by Equations [70]; for c_*/a_*, by Equation [72].

It may be noted that, since, in the load interval $0 > T \geqslant -T^*$, the absolute value of the traction in annulus $c_* \leqslant \rho \leqslant a_*$ is $f\sigma$, slip does take place during this portion of the loading cycle.

3 During reloading to $\{N_0 + N^*, T^*\}$, the additional traction to be superposed on the traction of Equations [70] is obtained by the procedure of Section 14, leading, at the terminal load, to Equations [56] and [58] with a_0 replaced by a_*. The distribution of the initial and the additional tractions is illus-

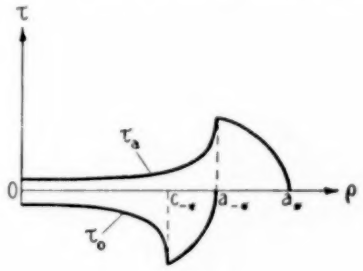

Fig. 29

trated by curves τ_0 and τ_a, respectively, in Fig. 29. Their algebraic sum yields the following resultant traction

$$\left.\begin{aligned}
\tau &= \frac{3\beta(N_0 + N^*)}{2\pi a_*^3}(a_*^2 - \rho^2)^{1/2}, \quad a_{-*} \leqslant \rho \leqslant a_* \\
\tau &= \frac{3\beta(N_0 + N^*)}{2\pi a_*^3}\left[(a_*^2 - \rho^2)^{1/2} - \left(1 + \frac{f}{\beta}\right)(a_{-*}^2 - \rho^2)^{1/2}\right], \quad c_* \leqslant \rho \leqslant a_* \\
\tau &= \frac{3\beta(N_0 + N^*)}{2\pi a_*^3}\left[(a_*^2 - \rho^2)^{1/2} - \left(1 + \frac{f}{\beta}\right)(a_{-*}^2 - \rho^2)^{1/2} + \frac{f}{\beta}(c_{-*}^2 - \rho^2)^{1/2}\right], \quad \rho \leqslant c_*
\end{aligned}\right\} \qquad \ldots [94]$$

Here

$$\frac{a_{-*}}{a_*} = \left(\frac{N_0 - N^*}{N_0 + N^*}\right)^{1/3} = \left(1 - \frac{2T^*/\beta N_0}{1 + T^*/\beta N_0}\right)^{1/3} \qquad \ldots [95]$$

and

$$\frac{c_{-*}}{a_*} = \frac{c_{-*}}{a_{-*}}\frac{a_{-*}}{a_*} = \left(1 - \frac{(2 + \beta/f)T^*/\beta N_0}{1 + T^*/\beta N_0}\right)^{1/3} \qquad \ldots [96]$$

4 In part 1 of Section 15 it was shown that, for the loading under consideration, the distribution of traction during unloading is the same as that during loading. Hence, during unloading from $\{N_0 + N^*, T^*\}$ to $\{N_0 - N^*, -T^*\}$ the additional traction (τ_a in Fig. 29), discussed in part 3 of this section, is gradually removed, until, at $\{N_0 - N^*, -T^*\}$, the remaining traction is, once again, the same as at the end of the first unloading (see part 2 of this section and τ_0 in Fig. 29). A stable cycle is thus established, during which no slip takes place (for further discussion see Section 19).

The load-displacement relations are obtained in a manner

similar to those in Section 17. Thus, during initial loading and unloading

$$\frac{2(1-\nu)}{f(2-\nu)}\frac{R\delta}{a_0^2} = \frac{1}{\theta}\left[(1+\theta L)^{2/3}-1\right], \quad L^* \geqslant L \geqslant 0 \quad [97]$$

$$\frac{2(1-\nu)}{f(2-\nu)}\frac{R\delta}{a_0^2} = -(1+\theta L)^{2/3} + \left[1+(1+\theta)L\right]^{2/3}, \quad 0 \geqslant L \geqslant -L^* \quad [98]$$

The relations of Equation [97] are illustrated by curves OP and PO in Fig. 30; of Equation [98], by curve OS in the same figure.

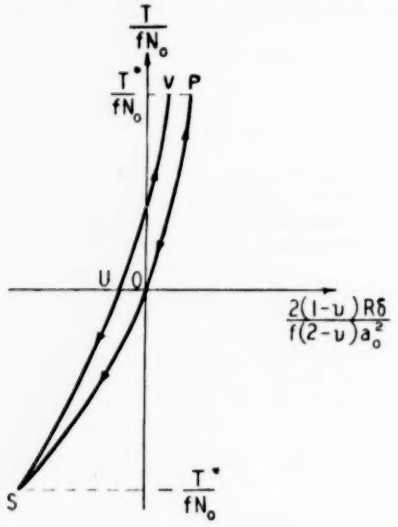

Fig. 30

The tangential compliance corresponding to the cycle in Equation [97] is

$$c_t = \frac{2-\nu}{8\mu a} \quad [99]$$

that corresponding to the load interval of Equation [98]

$$c_t = \frac{2-\nu}{8\mu a}\left[-\theta + (1+\theta)\left(1+\frac{L}{1+\theta L}\right)^{-1/3}\right] \quad [100]$$

During each subsequent loading and unloading the displacement will be given by (curves S-U-V and V-U-S, Fig. 30)

$$\frac{2(1-\nu)}{f(2-\nu)}\frac{R\delta}{a_0^2} = \frac{1}{\theta}(1+\theta L)^{2/3} - \left(1+\frac{1}{\theta}\right)(1-\theta L^*)^{2/3} + \left[1-(1+\theta)L^*\right]^{2/3}, \quad |L| \leqslant L^* \quad [101]$$

The compliance during the stable load cycle $|L| \leqslant L^*$ is the same as in Equation [99].

In Equations [97], [98] and [101] the range of θ is $1 \leqslant \theta \leqslant \infty$.

19 Frictional Energy Loss per Cycle

As in Section 5, the frictional energy loss per cycle is given by the area of the load-displacement loop (S-U-V-W-S, Fig. 28)

$$F = \int_{-T^*}^{T^*}(\delta_{w2}-\delta_r)\,dT = \frac{9(2-\nu)(fN_0)^2}{10\mu a_0}\left\{\frac{1}{4\theta}\left[\frac{1+\theta}{1-\theta}(1-\theta L^*)^{5/3} - \frac{1-\theta}{1+\theta}(1+\theta L^*)^{5/3}\right] - \frac{1}{1-\theta^2}\left(1-\frac{1+5\theta^2}{6}L^*\right)(1-L^*)^{2/3}\right\} \quad [102]$$

in which $0 \leqslant \theta \leqslant 1$, i.e., $\beta \geqslant f$. The expressions for δ_{w2} and δ_r were obtained from Equations [90] and [89], respectively.

For $\theta = 0$, i.e., N = const, Equation [102] reduces to Equation [17].

For small values of L^*, series expansion of Equation [102] yields

$$F = \frac{(2-\nu)T^{*2}}{36\,\mu a_0 f N_0}(1-\theta^2) \quad [103]$$

which expression should be compared with Equation [18].

It should be noted that, in the case for which $1 \leqslant \theta \leqslant \infty$, i.e., $\beta \leqslant f$, the displacement retraces its path in loading and unloading (see Equation [101], and curves S-U-V and V-U-S, Fig. 30), so that no loop is formed; i.e., there is no frictional energy loss involved. This result is to be expected since, by one of the fundamental rules, slip does not occur if $\tau < f\sigma$ (see discussion following Equation [58]). It is interesting that, for $\beta = f$, i.e., $\theta = 1$, the energy, Equation [102], vanishes, indicating that dT/dN must exceed the coefficient of friction if energy is to be dissipated.

Remarks on Combined Bending and Twisting of Thin Tubes in the Plastic Range[1]

By E. T. ONAT[2] and R. T. SHIELD,[3] PROVIDENCE, R. I.

The influence of the loading program on the agreement between the predictions of the Hencky and the Prandtl-Reuss stress-strain relations for a perfectly plastic material is investigated in the case of the combined bending and twisting of thin-walled tubes. The agreement in the values of the bending and twisting moments is found to vary considerably with the particular loading program chosen. The analysis is extended to tubes composed of a work-hardening material. The bending and twisting moments are obtained numerically using the incremental approach for a square tube which is bent and then twisted. Owing to the large amount of labor involved in this solution, an approximate method using the concept of a "composite" beam is developed, and good agreement in the results is found with those obtained from the incremental solution.

Introduction

THE Hencky total-strain relations for a perfectly plastic material are, in general, simpler to apply than incremental stress-strain relations such as the Prandtl-Reuss relations. As is well known[4,5] the Hencky relations are not acceptable physically, and when the strain path is curved, i.e., for straining other than proportional increase of all strain components, different results are predicted by the Hencky and Prandtl-Reuss theories. Since the Prandtl-Reuss relations are to be preferred, it is of value to compare the results given by the two theories for loading programs which give a curved strain path. In the next section the analysis developed in a recent paper by Hill and Siebel[6] is used to compare the bending and twisting moments required in the combined bending and twisting of thin-walled tubes, as predicted by the two theories.

In the last part of the paper a box beam composed of a work-hardening material is considered. The beam is bent and then twisted, and the bending and twisting moments are calculated, using the incremental approach. The labor involved is appreciable and a simpler solution is examined in order to see whether it gives results of sufficient accuracy. The simpler solution is obtained by superposing the results of two beams, one composed of an elastic material and the other composed of a Prandtl-Reuss material, and it is found that the results obtained by the two methods are in close agreement.

Comparison of the Hencky and Prandtl-Reuss Theories

The analysis developed by Hill and Siebel is used and since the results are obtained by a straightforward application of this analysis, the details are omitted.

The cylindrical tube is composed of perfectly plastic material of uniform thickness t. For simplicity the material is taken to be incompressible ($\nu = 1/2$). The cross section of the tube is assumed to have two perpendicular axes of symmetry and the bending moment B, which produces an angle of bend per unit length of amount ψ, is applied about one of these axes. The twisting couple T is applied about the axis of the tube and we denote the angle of twist per unit length by θ.

Two cross sections are considered, a circle of radius a and a square of side $2a$. The axis of bending for the square tube is taken parallel to a side of the square. In each case it can be shown that, under the yield criterion of von Mises, plastic yielding due to twisting alone first occurs in the tube when

$$\frac{Ga\theta}{k} = 1 \qquad [1]$$

and plastic yielding due to bending alone first occurs in the tube when

$$\frac{Ga\psi}{k} = \frac{1}{\sqrt{3}} \qquad [2]$$

where G is the shear modulus of the material of the tube and k is the shear yield stress.

Two different strain paths are considered here. In the first strain path, the tube is twisted until Equation [1] is satisfied; i.e., until $\theta = k/Ga$, and then the angle of twist is held constant while the tube is bent to an amount $\psi = k/Ga$. In the second strain path, the tube is first bent to the amount $\psi = k/Ga$ and then twisted until $\theta = k/Ga$, the angle of bend being held constant during the twisting. The two strain paths, I and II, are shown diagrammatically in Fig. 1.

Fig. 2 shows the variation of the bending and twisting couples with the angle of bend for the circular tube under the deformation of the strain-path I, as predicted by the Prandtl-Reuss stress-strain relations and the Hencky stress-strain relations. It is seen that, for this strain path, the two theories give results which are in close agreement.

In Fig. 3 the corresponding results are given for the circular tube under the deformation of the strain path II. The values of the couples predicted by the two theories differ considerably and at the end of the strain path the difference is approximately 20 per cent. The difference is even more apparent in Fig. 4 which

---

[1] The results presented in this paper were obtained in the course of research sponsored by the Office of Naval Research under Contract N7onr-358 (Task Order 1) with Brown University.

[2] Research Fellow, Graduate Division of Applied Mathematics, Brown University.

[3] Research Associate, Graduate Division of Applied Mathematics, Brown University.

[4] "On the Mechanical Behavior of Metals in the Strain-Hardening Range," by G. H. Handelman, C. C. Lin, and W. Prager, *Quarterly of Applied Mathematics*, vol. 4, 1947, pp. 397–407.

[5] "An Experimental Investigation of Plastic Stress-Strain Relations," by J. L. M. Morrison and W. M. Shepherd, The Institution of Mechanical Engineers, Proceedings of Applied Mechanics, vol. 163, (W.E.P. No. 55), 1949, pp. 1–9.

[6] "On Combined Bending and Twisting of Thin Tubes in the Plastic Range," by R. Hill and M. P. L. Siebel, *Philosophical Magazine*, vol. 42, 1951, pp. 722–733.

Presented at the National Conference of the Applied Mechanics Division, Minneapolis, Minn., June 18–20, 1953, of The American Society of Mechanical Engineers.

Discussion of this paper should be addressed to the Secretary, ASME, 29 West 39th Street, New York, N. Y., and will be accepted until October 10, 1953, for publication at a later date. Discussion received after the closing date will be returned.

Note: Statements and opinions advanced in papers are to be understood as individual expressions of their authors and not those of the Society. Manuscript received by ASME Applied Mechanics Division, June 10, 1952. Paper No. 53—APM-18.

shows the corresponding results for the square tube for strain path II. In this case, when $G\theta/k = 1.8$, the bending moment predicted by the Hencky theory is approximately one half that predicted by the Prandtl-Reuss theory.

Hill and Siebel determined the values of the couples as predicted by the two theories for the deformation of the circular tube under the strain-paths $\theta/\psi = 1$ and $\theta/\psi = 2$, and good agreement was found between the two theories. These two loading programs are represented in Fig. 1 by straight lines through the origin, and, as remarked by Hill and Siebel, it is to be expected that the two theories should not differ greatly for these paths since the curvatures of the two strain paths will be small. Figs. 2, 3, and 4 emphasize the dependence of the agreement in the results given by the two theories upon the particular strain path followed.

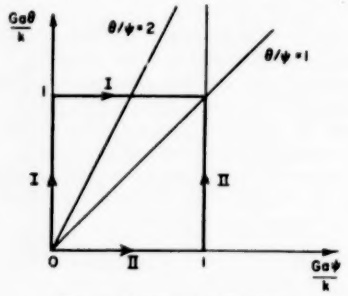

FIG. 1 LOADING PROGRAMS

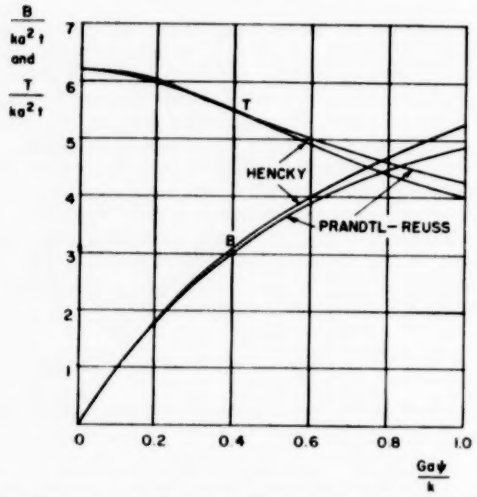

FIG. 2 BENDING AND TWISTING MOMENTS FOR CIRCULAR TUBE UNDER LOADING PROGRAM I, AS PREDICTED BY THE TWO THEORIES

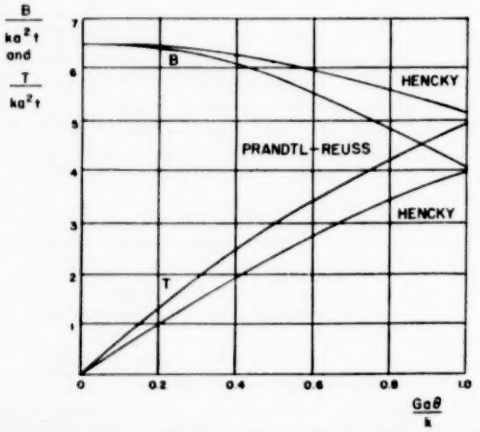

FIG. 3 BENDING AND TWISTING MOMENTS FOR CIRCULAR TUBE UNDER LOADING PROGRAM II, AS PREDICTED BY THE TWO THEORIES

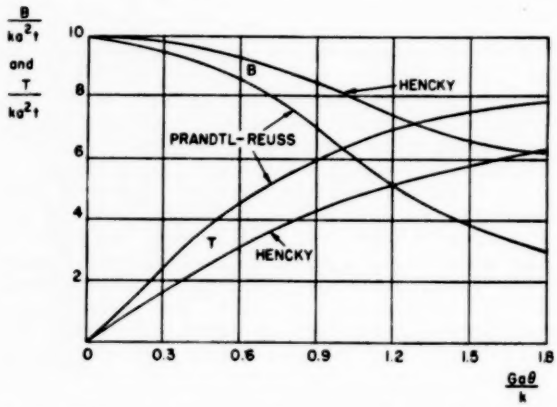

FIG. 4 BENDING AND TWISTING MOMENTS FOR SQUARE TUBE UNDER LOADING PROGRAM II, AS PREDICTED BY THE TWO THEORIES

WORK-HARDENING MATERIAL

In this part of the paper a tube composed of work-hardening material is considered. The stress-strain curve of the material is approximated by two straight lines, as shown in Fig. 5 for pure shear. For simplicity it is also assumed that the material is incompressible. From the viewpoint of the incremental approach, this stress-strain curve can be obtained by taking the plastic potential function to be $f = 4/G \log J_2$, where J_2 is the second invariant of the deviatoric stress tensor, $J_2 = 1/2\ s_{ij}s_{ij}$. The stress-strain relations are then

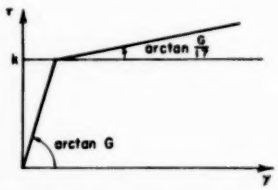

FIG. 5 STRESS-STRAIN DIAGRAM FOR PURE SHEAR OF WORK-HARDENING MATERIAL CONSIDERED

$$de_{ij} = s_{ij}df + ds_{ij}/2G = \frac{4}{G}s_{ij}\frac{s_{pq}ds_{pq}}{J_2} + \frac{ds_{ij}}{2G}$$

in the plastic region and

$$de_{ij} = ds_{ij}/2G$$

in the elastic region. In the problem under consideration, i.e., the combined bending and twisting of a thin tube, there are only two nonzero stress components, σ the longitudinal stress and τ the shearing stress. The stress-strain relations therefore reduce to

$$d\epsilon = \frac{16}{3G}\frac{\sigma}{J_2}\left(\frac{1}{3}\sigma d\sigma + \tau d\tau\right) + \frac{d\sigma}{3G}$$

$$d\gamma = \frac{16}{G}\frac{\tau}{J_2}\left(\frac{1}{3}\sigma d\sigma + \tau d\tau\right) + \frac{d\tau}{G}$$

in the plastic region and

$$d\epsilon = d\sigma/3G, \qquad d\gamma = d\tau/G$$

in the elastic region, where ϵ is the longitudinal strain, γ is the engineering shear strain, and where

$$J_2 = \frac{1}{3}\sigma^2 + \tau^2$$

The method of solution of these equations for a particular cross section of the tube and loading program is similar to that used by Hill and Siebel for a nonhardening material. The beam is taken to be a box beam of side $2a$ which is first bent to the amount $\psi = k/Ga$ about an axis passing through the mid-points of two opposite sides of the square cross section. The beam is then twisted, the angle of bend being kept constant. This cross section and strain path were chosen in order to simplify the numerical work. During the twisting it is found that the stresses are given by the equations

$$\left.\begin{aligned}
\sigma^{1/3}\left(\frac{1}{3}\sigma^2 + \tau^2\right) &= \frac{1}{3}k^{2+1/3}\left[\frac{3}{17}\left(\frac{y}{a} + \frac{16}{\sqrt{3}}\right)\right]^{2+1/3} \\
&\qquad \text{for } 1 \geq \frac{y}{a} \geq \frac{1}{\sqrt{3}} \\
&= k^{2+1/3}\left(\frac{3y}{a}\right)^{1/3} \text{ for } \frac{1}{\sqrt{3}} \geq \frac{y}{a} \geq \frac{c}{a} \\
Gad\theta &= d\tau + 24\,\tau^2 d\tau\left[\frac{1}{(17\sigma^2 + 3\tau^2)_{y=a}}\right. \\
&\qquad \left. + \frac{1}{a}\int_c^a \frac{dy}{(17\,\sigma^2 + 3\tau^2)}\right]
\end{aligned}\right\} \quad \ldots [3]$$

where

$$3\left(\frac{c}{a}\right)^2 = 1 - \left(\frac{\tau}{k}\right)^2, \quad \tau \leq k; \quad c = 0, \quad \tau \geq k$$

with the condition that $\tau = 0$ when $\theta = 0$. The shearing stress τ is constant around the tube while σ is a function of y, y being the distance of a point of the tube from the neutral plane; c is the distance of the plastic region from the neutral plane. The bending and twisting moments are given by

$$\frac{B}{ka^3t} = 4\left(\frac{c}{a}\right)^3 + \frac{4}{k}\left[(\sigma)_{y=a} + \frac{1}{a^2}\int_c^a \sigma y dy\right]$$

$$\frac{T}{ka^3t} = 8\frac{\tau}{k}$$

Equations [3] have to be integrated numerically and in Fig. 6 is shown the calculated variation of the moments B and T with the angle of twist.

The labor involved in computing the moments is considerable so that an alternative method of approach which would give a reasonable approximation to the solution of the problem with less labor is desirable. It is possible to use an equivalent Hencky stress-strain relation but this does not simplify the computations to any great extent, and, in view of the results of Fig. 4, it is probable that the Hencky results would differ considerably from those obtained from the incremental approach.

A good approximation is obtained by superposing the results of two beams, one composed of an incompressible elastic material and the other composed of an incompressible Prandtl-Reuss plastic material, the elastic constants being suitably chosen so that after superposition the stress-strain curve in pure shear is as shown in Fig. 5. The elastic material is taken to have the shear modulus $G/17$ so that for the pure shear of this material

$$\tau_1 = \frac{G}{17}\gamma$$

The perfectly plastic material is taken to have the shear modulus $16\,G/17$ and the yield shear stress $16\,k/17$ so that in pure shear with monotonic loading we have

$$\tau_2' = \frac{16\,G}{17}\gamma, \qquad \gamma \leq \frac{k}{G}$$

$$\tau_2 = \frac{16\,k}{17} = k_2, \qquad \gamma \geq \frac{k}{G}$$

By adding the stress components τ_1, τ_2 the following relations are obtained

$$\tau = \tau_1 + \tau_2 = G\gamma, \qquad \gamma \leq \frac{k}{G}$$

$$\tau = \frac{G\gamma}{17} + \frac{16\,k}{17} = \frac{G}{17}\left(\gamma - \frac{k}{G}\right) + k, \qquad \gamma \geq \frac{k}{G}$$

and these relations give the stress-strain curve in Fig. 5.

For the problem of this section, the bending and twisting of the box beam, it is easily found that when the beam is composed of the elastic material the bending and twisting moments B_1, T_1 during the twisting are given by

$$\frac{B_1}{ka^3t} = \frac{16}{17}, \qquad \frac{T_1}{ka^3t} = \frac{8}{17}\frac{Ga\theta}{k} \quad \ldots\ldots\ldots\ldots [4]$$

When the beam is composed of the Prandtl-Reuss material, the bending moment B_2 and the twisting moment T_2 during the

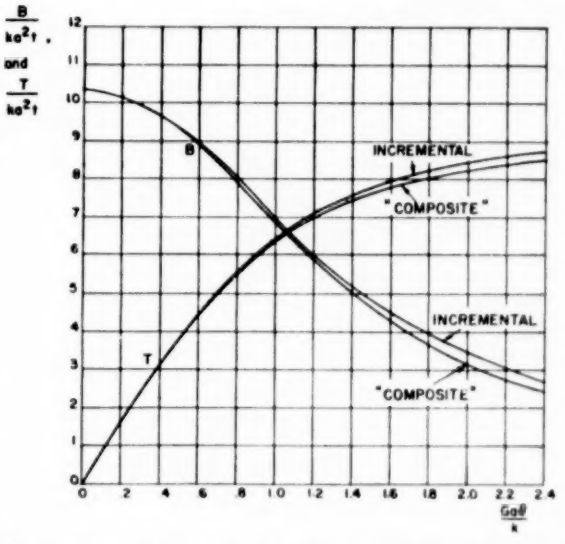

FIG. 6 WORK-HARDENING MATERIAL—INCREMENTAL SOLUTION AND APPROXIMATE COMPOSITE SOLUTION FOR SQUARE TUBE UNDER LOADING PROGRAM II

twisting are deduced readily from the analysis of Hill and Siebel, and the moments are found to be given by

$$\left.\begin{aligned}\frac{B_2}{ka^3t} &= \frac{16}{17}\frac{2}{3\sqrt{3}}\left(1-\frac{\tau_2^2}{k_2^2}\right)^{1/2}\left(26+\frac{\tau_2^2}{k_2^2}\right)\\ \frac{T_2}{ka^3t} &= \frac{16}{17}8\frac{\tau_2}{k_2}\end{aligned}\right\} \quad \ldots [5]$$

where

$$\frac{Ga\theta}{k} = \text{arc tanh}\,\frac{\tau_2}{k_2} + \frac{1}{4\sqrt{3}}\left[\frac{\tau_2}{k_2}\left(1-\frac{\tau_2^2}{k_2^2}\right)^{1/2} - \text{arc sin}\,\frac{\tau_2}{k_2}\right]$$

To obtain the bending and twisting moments for the composite beam the corresponding moments given by Equations [4] and [5] are added

$$\left.\begin{aligned}\frac{B}{ka^3t} &= \frac{16}{17}\left\{1+\frac{2}{3\sqrt{3}}\left(1-\frac{\tau_2^2}{k_2^2}\right)^{1/2}\left[26+\frac{\tau_2^2}{k_2^2}\right]\right\}\\ \frac{T}{ka^3t} &= \frac{8}{17}\left(\frac{Ga\theta}{k}+16\frac{\tau_2}{k_2}\right)\end{aligned}\right.$$

where

$$\frac{Ga\theta}{k} = \text{arc tanh}\,\frac{\tau_2}{k_2} + \frac{1}{4\sqrt{3}}\left[\frac{\tau_2}{k_2}\left(1-\frac{\tau_2^2}{k_2^2}\right)^{1/2} - \text{arc sin}\,\frac{\tau_2}{k_2}\right]$$

The calculated variation of the moments B, T with the angle of twist θ is shown in Fig. 6 in order to compare the curves with these obtained by the incremental approach. It can be seen that the agreement is very close indeed.

Another method of approach would be to approximate to the work-hardening material by using a Prandtl-Reuss material which has a suitably chosen yield stress. As remarked by Lee,[7] the adoption of this ideal material must not be thought of as neglecting work-hardening, but rather as averaging its effect over the field of flow. Computations show that for the problem of this section, the results obtained with such a Prandtl-Reuss material are in fairly good agreement with the exact analysis, although the agreement is not as good as that shown in Fig. 6. However, the choice of the yield stress for this Prandtl-Reuss material depends upon the amount of strain which the material undergoes and usually the maximum strain cannot be estimated a priori. Since the use of a composite beam involves only a little more labor and since it does not depend upon the choice of a suitable yield stress, the method of superposition used in the foregoing seems to be of greater value.

[7] "The Theoretical Analysis of Metal-Forming Problems in Plane Strain," by E. H. Lee, JOURNAL OF APPLIED MECHANICS, Trans. ASME, vol. 74, 1952, pp. 97–103.

An Improved Electrical Analogy for the Analysis of Beams in Bending

By W. T. RUSSELL[1] and R. H. MacNEAL[2]

A practical electrical beam analogy which employs ideal transformers is derived from the equations of a segment of nonuniform beam which is loaded by vertical shears and moments applied at its ends. This analogy is suitable for the solution of static-load problems, vibration problems, and transient-load problems. The superiority of this analogy over an analogy derived by replacing differential operators by difference operators is demonstrated by means of error calculations for uniform cantilever and simply supported beams.

Introduction

In the past decade several electrical analogies have been devised which can be used in the solution of problems concerning the bending of elastic beams. Some of these can only be used in the solution of problems with static loads, while others in addition, can be used in normal mode analyses, and still others can be used in the solution of transient problems. The usefulness of these circuits is not restricted to elementary beam problems because they can serve as building blocks in the construction of analogous circuits for such complicated structures as airplanes, ships' hulls, and gas turbines. In this paper a new analogy is presented and its advantages over others previously published are pointed out.

Survey of Previously Derived Beam Analogies

The first paper, known to the authors, to be published on the subject of beam analogies was presented by G. Kron in 1944 (1).[3] Using tensor analysis he derived circuits for a beam with six degrees of freedom (three translations and three rotations) and discussed the manner of interconnecting beams into frameworks. The only approximation made in deriving these circuits was that the distributed loads were replaced by concentrated loads. Hence his method was intrinsically as accurate as such methods of numerical beam analysis as Myklestad's method (2) or matrix methods employing influence coefficients (3). (The same approximation is made in deriving the circuit described in this paper.) Unfortunately, his circuits could not be used for vibration analysis or the solution of transient problems because they employed unrealizable electrical elements, i.e., "negative inductors." In a later paper (4) Kron makes only the modest claim that his circuits are useful as models from which to organize numerical calculations.

In 1947 S. T. Jennings (5) presented an electrical beam analogy that was derived by replacing the differential equation of a beam by a fourth-order difference equation. The vibration equation for the nth node of a uniform beam is

$$y_{n+2} - 4y_{n+1} + 6y_n - 4y_{n-1} + y_{n-2} - \lambda^4 y_n = 0 \quad \ldots [1]$$

This difference equation can be satisfied by an electrical network which employs inductors, capacitors, and "negative inductors"; hence the circuit is unsuited for the solution of vibration and transient problems. This circuit and Kron's circuit are shown in Fig. 5 of reference (6).

In 1950 McCann and MacNeal (6) published solutions obtained with an electrical analogy that was derived by McCann a few years earlier by replacing the differential equations of a beam by four first-order difference equations. This analogy, which for vibration problems employs inductors, capacitors, and ideal transformers, is shown in Fig. 1. It can be used in the solution of vibration and transient problems because its elements are independent of frequency. This circuit has been used extensively in the solution of practical problems on the California Institute of Technology analog computer.

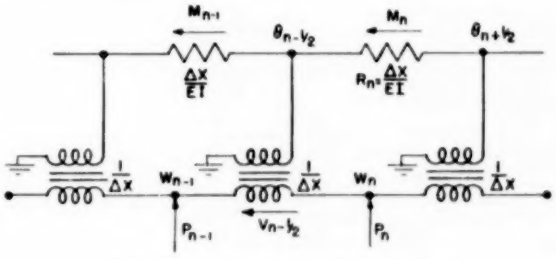

Fig. 1 Finite-Difference Beam Analogy

At about the same time the same circuit was independently derived by H. M. Trent, working at the Naval Research Laboratory (7).

The circuit to be described in this paper was first derived by Russell in his PhD thesis (8) which also appeared in 1950.

In the same year G. Cahen (9) published electrical analogies in which the only approximation made in deriving the circuits was the assumption of concentrated loads. Cahen believed that it was impossible to obtain transformers with properties sufficiently close to those of an ideal transformer. He avoided the use of ideal transformers by making the frequency of oscillation of the electrical circuits proportional to the reciprocal of the frequency of mechanical vibration.

In all of these circuits the differential equation of the beam is replaced by equations governing the displacements at a finite number of points. A different approach has been used by a group working at the University of Michigan (10). In this work an electronic differential analyzer was used to integrate the beam equation. Position on the beam corresponds to time measured on the analyzer. In this approach the inaccuracies associated with difference equations disappear but new difficulties arise. Bound-

---

[1] Lieutenant Colonel, U. S. Army, Fort Sill, Okla.

[2] Assistant Professor of Electrical Engineering, California Institute of Technology, Pasadena, Calif.

[3] Numbers in parentheses refer to the Bibliography at the end of the paper.

Presented at the National Conference of the Applied Mechanics Division, Minneapolis, Minn., June 18–20, 1953, of The American Society of Mechanical Engineers.

Discussion of this paper should be addressed to the Secretary, ASME, 29 West 39th Street, New York, N. Y., and will be accepted until October 10, 1953, for publication at a later date. Discussion received after the closing date will be returned.

Note: Statements and opinions advanced in papers are to be understood as individual expressions of their authors and not those of the Society. Manuscript received by ASME Applied Mechanics Division, October 3, 1952. Paper No. 53—APM-11.

ary conditions can be established on the analyzer at only one instant of time. Since the boundary conditions of a beam are given at two (or more) points, the latter can be satisfied only by obtaining several solutions with different initial conditions, and adjusting the initial conditions after each trial in such a way as to satisfy more nearly the boundary conditions at the far end. In this respect the method is similar to that of Myklestad (2) and Prohl (11). Also, in this method, it is difficult to solve nonuniform beam problems because time-varying electrical components must be used. Transient problems cannot be solved by this method at all because the only independent variable (time) on the analyzer has been used to represent position.

Derivation of Concentrated-Load Analogy

The usual assumptions made in deriving the differential equations of a beam will be made here. In addition, it will be assumed that the distributed loads acting on the beam can be replaced by concentrated loads acting at a finite number of stations. At each station a jump in the shear will occur as a result of the concentrated load. The segment of beam between a pair of stations is unloaded and simple equations can be obtained relating the forces and displacements at the two ends of the segment. An electrical circuit satisfying these equations will be used as an element from which to construct an analogy for the entire beam. The derivation, given in reference (8), employed energy principles and methods of matrix algebra to obtain an electrical circuit. A somewhat different method will be used in this paper.

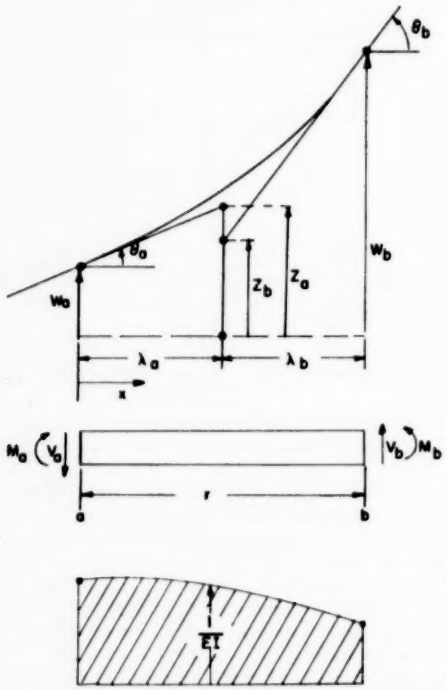

Fig. 2 Segment of Beam Used in Derivation of Concentrated-Load Beam Analogy

A segment of beam of length r is shown in Fig. 2 where all symbols to be used in the derivation are indicated. The segment of beam is assumed to be in a condition of equilibrium under the action of bending moments and shears applied at its ends.

The conditions of equilibrium require that the shear at any point

$$V_x = V_a = V_b \quad [2]$$

and the bending moment at any point

$$M_x = M_b + (r - x)V_b \quad [3]$$

The following equations give the deflection of the beam at any point, λ_a, and the difference in slopes at the two ends. These equations may be derived from standard moment-area principles, from Castigliano's theorem, or by integration of the differential equations

$$w(\lambda_a) = w_a + \lambda_a\theta_a + \int_0^x \frac{M_x}{EI}(\lambda_a - x)dx \quad [4]$$

$$w(\lambda_a) = w_b - \lambda_b\theta_b + \int_x^r \frac{M_x}{EI}(x - \lambda_a)dx \quad [5]$$

$$\theta_b - \theta_a = \int_0^r \frac{M_x}{EI}\,dx \quad [6]$$

Subtract Equation [4] from Equation [5]

$$w_b - w_a = \theta_a\lambda_a + \theta_b\lambda_b - \int_0^r \frac{M_x}{EI}(x - \lambda_a)dx \quad [7]$$

The advantage of expressing the difference in the deflections of the two ends of the segment in terms of the co-ordinate of a third arbitrary point will be revealed presently. The deflections of the extended tangents from points a and b at $x = \lambda_a$ are, from Fig. 2

$$z_a = w_a + \lambda_a\theta_a \quad [8]$$

$$z_b = w_b - \lambda_b\theta_b \quad [9]$$

Hence, by substitution into Equation [7]

$$z_b - z_a = -\int_0^r \frac{M_x}{EI}(x - \lambda_a)dx \quad [10]$$

Insert the value of M_x given by Equation [3] into this equation

$$z_b - z_a = -M_b\int_0^r \frac{x - \lambda_a}{EI}\,dx + V_b\int_0^r \frac{(x - \lambda_a)(x - r)}{EI}\,dx \quad [11]$$

If λ_a is chosen so that $x = \lambda_a$ is at the center of gravity of the $1/EI$ diagram, then the first integral of Equation [11] vanishes and in the second integral $x - r$ may be replaced by $x - \lambda_a$. This choice of λ_a has the effect of uncoupling the equations for deflection and slope

$$z_b - z_a = V_b\int_0^r \frac{(x - \lambda_a)^2}{EI}\,dx \quad [12]$$

Hence $z_b - z_a$ is equal to the shear multiplied by the moment of inertia of $1/EI$ about the center of gravity of the $1/EI$ diagram.

A similar formula for the difference in slopes at the two ends of the segment may be obtained by substituting the value of M_x from Equation [3] into Equation [6]

$$\theta_b - \theta_a = \int_0^r \frac{1}{EI}\{M_b + V_b[\lambda_b + (\lambda_a - x)]\}\,dx \quad [13]$$

since $x = \lambda_a$ is the center of gravity of $1/EI$

$$\theta_b - \theta_a = [M_b]\int_0^r \frac{1}{EI}\,dx \quad [14]$$

where

$$M_0 = M_b + \lambda_b V_b$$

M_0 is the bending moment at the center of gravity of $1/EI$.

The equations that are essential to the development of the electrical circuit are summarized as follows

$$V_a = V_b \quad [15a]$$

$$M_0 = M_b + \lambda_b V_b \quad [15b]$$

$$M_a = M_0 + \lambda_a V_a \quad [15c]$$

$$z_a = w_a + \lambda_a \theta_a \quad [15d]$$

$$z_b = w_b - \lambda_b \theta_b \quad [15e]$$

$$z_b - z_a = V_b R_V \quad [15f]$$

$$\theta_b - \theta_a = M_0 R_M \quad [15g]$$

where

$$R_M = \int_0^r \frac{dx}{EI}$$

$$R_V = \int_0^r \frac{(x - \lambda_a)^2}{EI}\, dx$$

In the electrical analogy, displacement quantities (deflections and slopes) will be represented by voltages to ground, and force quantities (shears and bending moments) will be represented by currents. Fig. 3(a) shows the input and output connections to the circuit. The complete analogous circuit, Fig. 3(b), shows the electrical equivalent of every symbol in Equations [15] and the places where each equation is satisfied. The properties of ideal transformers are used in this circuit. For example, the current flowing in the lower winding of the transformer at the right is equal to V_b. Since the turns ratio of the transformer is λ_b:1, the current flowing in the upper winding is equal to $\lambda_b V_b$. This current adds to M_b to give M_0, thus satisfying Equation [15b]. The same transformer is used to satisfy Equation [15e]. Since the voltage across the upper winding is equal to θ_b, the voltage across the lower winding is equal to $\lambda_b \theta_b$, and this voltage subtracted from w_b gives z_b.

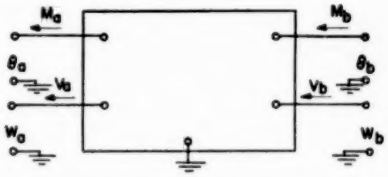

(a) INPUT AND OUTPUT CONNECTIONS

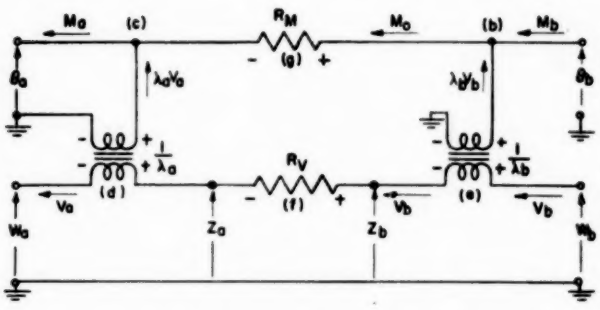

(b) COMPLETE CIRCUIT

FIG. 3 CONCENTRATED-LOAD BEAM ANALOGY

Equations [15c] and [15d] are similarly satisfied by the transformer at the left. Equations [15f] and [15g] applied to the circuit are an expression of Ohm's law for resistors whose resistances are, respectively, R_V and R_M. Equation [15a] is satisfied because no branches occur in the circuit connecting w_a and w_b.

When several such circuits are connected together they form the analogy for a complete beam. Concentrated loads are represented by currents inserted into the deflection circuit at the points of interconnection. Currents representing concentrated moment loads also may be inserted into the slope circuits at these points. Fig. 4(a) shows two such circuits connected together.

The two transformers on either side of the nth node may be replaced by a single transformer with a tapped winding as shown in Fig. 4(b). Thus, except for cells at the extreme ends of a beam, each cell requires two resistors and a single transformer. In this form of the circuit, the bending moments at the ends of each segment no longer can be measured. However, M_0, the bending moment at the center of gravity of $1/EI$ for each segment should provide sufficient information.

For a uniform beam with equal spaces between loading points, $\lambda_a = \lambda_b = {}^1/_2\Delta x$, and each transformer has a center-tapped winding. In this case

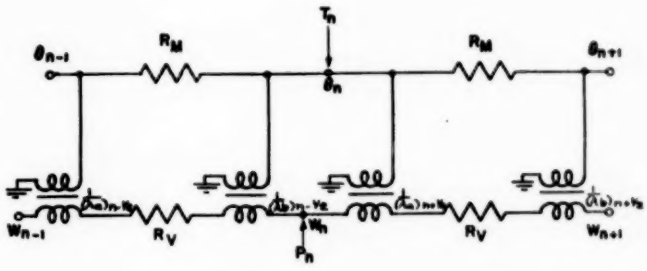

(a) CIRCUIT WITH TWO TRANSFORMERS PER SECTION.

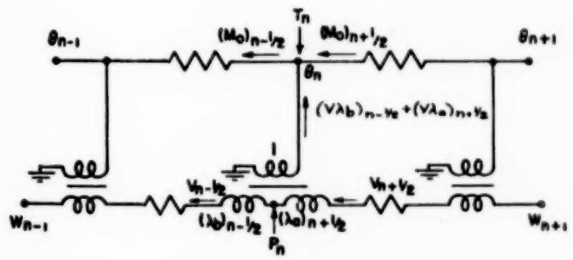

(b) CIRCUIT WITH ONE TAPPED TRANSFORMER PER SECTION.

FIG. 4 SUBSTITUTION OF SINGLE TAPPED TRANSFORMER FOR TWO TRANSFORMERS

$$R_M = \frac{\Delta x}{EI}$$

$$R_V = \frac{\Delta x^3}{12EI}$$

For cells of unit length, $\Delta x = 1$, we see that R_V is equal to $^1/_{12}$ R_M.

In the static-stress analogy just described, flexibility (the inverse of stiffness) is represented by electrical resistance, and strain energy is analogous to electrical power. In vibration problems with distributed mass loads the same form of circuit is used but the resistors are replaced by inductors having the same numerical values; capacitors, having numerical values equal to the mass of each section, are connected between the nodes of the deflection circuit and ground as shown in Fig. 6(*e*). In this case force is analogous to current, velocity is analogous to voltage, and strain energy is analogous to magnetic field energy.

In static-stress problems, it would seem that direct-current generators are required to represent the static loads, and it is well known that transformers function properly only for alternating currents. In actual practice alternating-current generators are used. Since resistors are the only electrical elements besides transformers occurring in the circuit, the behavior of the circuit is independent of the frequency of the current sources and is the same as the theoretical behavior at zero frequency with ideal transformers. Inductors or capacitors could have been used instead of resistors, but resistors are much less expensive. It also should be mentioned that, in preparing a problem for solution on an analog computer, all mechanical quantities must be multiplied by appropriate scale factors upon being converted into electrical quantities (12).

An equivalent form of the beam analogy is shown in Fig. 5 for the case of a uniform segment. This circuit may be derived by setting $\lambda_a = r$ and substituting $M_x = M_a - xV_b$, in Equation [4]. Then

$$w_b = w_a + r\left[\left(\theta_a + M_a \frac{1}{r}\int_0^r \frac{r-x}{EI}\,dx\right)\right] - V_b \int_0^r \frac{x(r-x)}{EI}\,dx \quad [16]$$

In the electrical analogy w_b, w_a, and θ_a are voltages and M_a and V_b are currents, as before.

Define

$$R_1 = \frac{1}{r}\int_0^r \frac{r-x}{EI}\,dx \quad [17a]$$

$$R_2 = \frac{1}{r}\int_0^r \frac{x}{EI}\,dx \quad [17b]$$

$$R_3 = -\frac{1}{r^2}\int_0^r \frac{x(r-x)}{EI}\,dx \quad [17c]$$

Then

$$w_b - w_a = r[(\theta_a + M_a R_1) + V_b r R_2] \quad [18]$$

From Equation [3]

$$M_a = M_b + rV_b \quad [19]$$

If Equation [3] is substituted into Equation [6] and V_b is eliminated by Equation [19], the equation for the difference in the slopes at the two ends of the segment can be expressed as follows

$$\theta_b - \theta_a = M_a R_1 + M_b R_2 \quad [20]$$

Equations [18], [19], and [20] together with Equation [2] are sufficient to design the electrical circuit in Fig. 5(*a*).

Equation [20] is obtained from the circuit diagram by summing the voltage drops across R_1 and R_2. Equation [18] is obtained by adding θ_a to the voltage drops across R_1 and R_3 and multiplying by the transformer-turns ratio. Equation [19] is satisfied by the currents at the junction of R_1 and R_2.

Since R_3 is negative, the circuit in Fig. 5(*a*) is not immediately realizable. However, the T of resistors in Fig. 5(*a*) can be replaced by a realizable circuit containing a transformer as shown in Fig. 5(*b*). Since this circuit requires two transformers per cell and the circuit in Fig. 4(*a*) requires only one, the latter is more practical. However, it is believed that the circuit in Fig. 5(*b*) will be useful in developing a more accurate analogy for thin plates than that given in reference (13), and for thin multicell shells where distributed twisting moments act on the sides of idealized beams. A discussion of this problem is beyond the scope of this paper.

The circuit in Fig. 5(*a*) is interesting because of the similarity in form with the finite-difference beam analogy shown in Fig. 1. If the negative resistances are omitted the circuits are identical. The negative resistance can be regarded as a correction to account for error due to finite-difference approximation. In many cases deflections resulting from shearing strains are included in the analysis of a beam. To account for this effect a resistance equal to $1/(AGr)$ is placed in series with the negative resistance of Fig. 5(*a*).

Hence if

$$\frac{EI}{AG} \geqslant \frac{r^2}{6}$$

this form of the circuit becomes practical. It has the advantage of not requiring a tapped winding on each transformer.

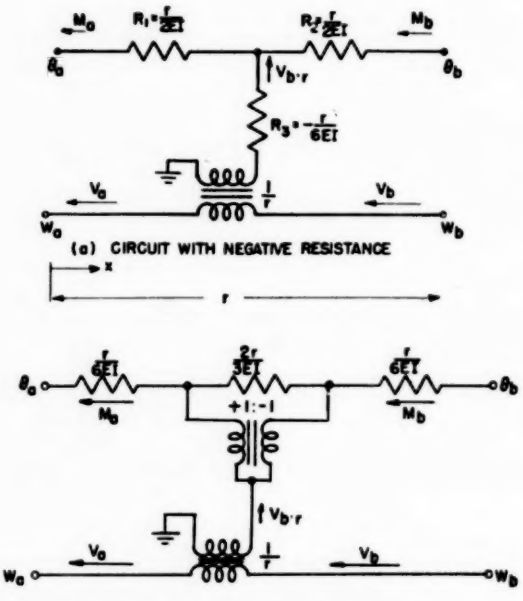

FIG. 5 EQUIVALENT FORM OF CONCENTRATED-LOAD ANALOGY

Comparison of Concentrated-Load Analogy and Finite-Difference Analogy

The scope of the exact solutions of the difference equations governing the various beam analogies is at present restricted to beams with uniform cross section. In this section the results of some calculations for uniformly loaded beams taken from reference (8) will be presented. Experimental solutions obtained on the Cal Tech electric analog computer will not be given because these solutions contain errors due to parasitic effects and the inaccuracy of electrical measurements which in some instances have the same order of magnitude as the errors due to the assumption of concentrated loads.

It should be pointed out that the intrinsic error of the concentrated-load analogy is due only to the substitution of concentrated loads for a distributed load, assuming that the properties of the $1/EI$ curve can be obtained accurately by integration. The intrinsic error of the finite-difference analogy is due to the substitution of difference operators for differential operators in the differential equations. Deflections calculated by the finite-difference analogy will be in error even if the beam is subjected to concentrated loads. For static concentrated loads both analogies give exact results for the shear and the bending moment.

For problems with distributed loads the error depends upon the manner in which the distributed load is replaced by concentrated loads and, unfortunately, there does not appear to be any single method or rule for doing this that can be shown to be clearly superior to all other methods. The general procedure that has been adopted is to divide the beam into segments in such a way that the centers of gravity of the loads on all segments are as near as possible to the concentrated loading points and then to set each concentrated load equal to the load on its respective segment. In vibration problems, distributed masses are concentrated by the same rule.

TABLE 1 ERRORS OF DEFLECTIONS IN PER CENT FOR CONCENTRATED LOAD AND FINITE-DIFFERENCE APPROXIMATIONS TO A UNIFORMLY LOADED CANTILEVER BEAM

n = number of loading points
w_e = exact deflection calculated from differential equations
w_c = deflection calculated from equations of concentrated-load analogy
w_f = deflection calculated from equations of finite-difference analogy

$$\epsilon_c = \frac{w_e - w_c}{w_e} \times 100 \qquad \epsilon_f = \frac{w_e - w_f}{w_e} \times 100$$

	$n = 1$		$n = 2$		$n = 3$	
Position	ϵ_c	ϵ_f	ϵ_c	ϵ_f	ϵ_c	ϵ_f
Δx	5 89	—41 1	1 75	—26 3	0 826	—19 9
$2\Delta x$			2 32	—11 6	1 01	—9 09
$3\Delta x$					1 23	—5 35

	$n = 4$		$n = 5$		$n = 6$	
Position	ϵ_c	ϵ_f	ϵ_c	ϵ_f	ϵ_c	ϵ_f
Δx	0 478	—14 8	0 312	—12 1	0 218	—10 3
$2\Delta x$	0 559	—7 83	0 353	—6 00	0 248	—5 11
$3\Delta x$	0 654	—4 58	0 401	—3 88	0 271	—3 34
$4\Delta x$	0 762	—3 05	0 456	—2 74	0 302	—2 42
$5\Delta x$			0 518	—1 97	0 337	—1 82
$6\Delta x$					0 375	—1 39

TABLE 2 ERRORS IN FREQUENCIES OF FREE VIBRATION FOR CONCENTRATED-LOAD AND FINITE-DIFFERENCE APPROXIMATIONS TO A UNIFORM CANTILEVER BEAM

n = number of loading points
f_e = exact frequency calculated from differential equations
f_c = frequency calculated from equations of concentrated-load analogy
f_f = frequency calculated from equations of finite-difference analogy

$$\delta_c = \frac{f_e - f_c}{f_e} \times 100 \qquad \delta_f = \frac{f_e - f_f}{f_e} \times 100$$

n	mode	δ_c	δ_f
1	1	—10 86	+9 50
2	1	—3 78	+2 89
	2	—1 02	+26 57
3	1	—1 90	+1 38
	2	—6 49	+14 50
	3	—2 15	+35 49
4	1	—1 14	+0 82
	2	—3 99	+9 02
	3	—4 88	+22 91
	4	+3 58	+40 84

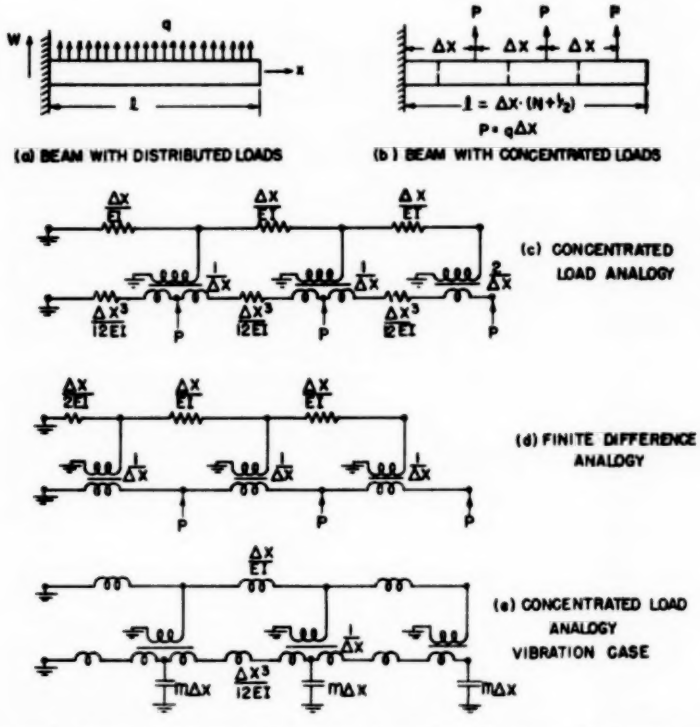

Fig. 6 Circuits for Uniform Cantilever Beam With Uniformly Distributed Load

Circuits for a uniform cantilever beam with a uniform load are shown in Fig. 6. The beam is first divided into $N + {}^1/_2$ sections with equal concentrated loads acting at the center of gravity of each section in the manner shown in Fig. 6(b). This incidentally insures that the bending moment at points midway between the loading points is correct. The load on the half section at the left end is replaced by a load acting at the support. In Fig. 6(c), which shows the concentrated load analogy for a beam with three loading points, the transformer just to the right of the support has been removed because its upper winding is short-circuited.

Results of calculations of the errors in static deflections for both types of analogy are given in Table 1 as a function of distance from the support and the number of loading points. The errors for the concentrated-load analogy are much smaller than for the finite-difference analogy. The large percentage error of the latter in the root region is not serious because the deflections there are small.

Results of calculations of the errors in frequencies of free vibration are given in Table 2 as a function of the number of loading points and the mode index. The concentrated-load analogy gives considerably better results than the finite-difference analogy for higher modes but does not give better results for the lowest mode. This probably may be ascribed to the presence of

TABLE 3 MODE-SHAPE DATA FOR VIBRATING CANTILEVER BEAM WITH FOUR LOADING POINTS

y_1 at $\frac{x}{l} = \frac{2}{9}$ y_2 at $\frac{x}{l} = \frac{6}{9}$

y_3 at $\frac{x}{l} = \frac{4}{9}$ y_4 at $\frac{x}{l} = \frac{8}{9}$

	Mode 1			Mode 2		
	y_2/y_1	y_3/y_1	y_4/y_1	y_2/y_1	y_3/y_1	y_4/y_1
Exact solution (distributed load)	+3.5177	+6.9495	+10.7639	+2.0252	+1.1977	−1.3345
Concentrated-load solution	+3.5457	+6.9919	+10.8074	+1.9794	+1.0764	−1.4383

compensating errors in the finite-difference analogy. Mode-shape data for the vibrating cantilever beam with four loading points are compared with the exact solution in Table 3. The discrepancies for the lowest mode are about 1 per cent.

In the case of the vibration of a uniform simply supported beam with uniform mass loading, the difference equations of the finite-difference analogy and the concentrated-load analogy can be solved easily. An analytical expression for the mode frequencies is obtained for any number of cells n, and for any mode index p.

For the finite-difference beam analogy the ratio of the frequency to the frequency of the continuous beam is

$$\frac{f_f}{f_e} = \frac{\sin^2\left(\frac{p\pi}{2n}\right)}{\left(\frac{p\pi}{2n}\right)^2} \qquad [21]$$

When $(p\pi)/(2n)$ is small, this ratio may be approximated by the first two terms of a power series expansion

$$\frac{f_f}{f_e} = 1 - \frac{1}{3}\left(\frac{p\pi}{2n}\right)^2 + 0\left(\frac{p\pi}{2n}\right)^4 \qquad [22]$$

For the concentrated-load beam analogy the corresponding ratio is

$$\frac{f_c}{f_e} = \frac{\sin^2\left(\frac{p\pi}{2n}\right)}{\left(\frac{p\pi}{2n}\right)^2}\sqrt{\frac{3}{3 - 2\sin^2\left(\frac{p\pi}{2n}\right)}} = 1 - \frac{1}{90}\left(\frac{p\pi}{2n}\right)^4 + 0\left(\frac{p\pi}{2n}\right)^6 \qquad [23]$$

For p/n equal to 1/4, corresponding to the lowest mode of a beam analogy with four cells, the error for the finite-difference analogy computed from Equation [22] is 5.13 per cent whereas the error for the concentrated-load analogy computed from Equation [23] is 0.026 per cent.

In both cases the mode shapes are correct.

Conclusion

Electrical beam analogies are instruments of practical importance only in problems of much greater complexity than those which have been considered in the previous section. In nearly all such problems, the beam, or beams, have variable cross sections. Studies should be made to determine whether or not the magnitude of the errors given in Tables 1, 2, and 3 are typical of those to be expected in complex problems. For the present, the results presented here should provide a rough guide for determining the number of cells required to give satisfactory accuracy in the solution of problems.

Bibliography

1 "Tensorial Analysis and Equivalent Circuits of Elastic Structures," by G. Kron, *Journal of The Franklin Institute*, vol. 238, 1944, p. 400.

2 "A New Method of Calculating Natural Modes of Uncoupled Bending Vibration of Airplane Wings and Other Types of Beams," by N. O. Myklestad, *Journal of the Aeronautical Sciences*, vol. 11, 1944, p. 153.

3 "Solution of Oscillation Problems by Matrices," by W. J. Duncan and A. R. Collar, *Philosophical Magazine*, vol. 17, 1934, pp. 866–909.

4 "Equivalent Circuit for the Numerical Solution of the Critical Speeds of Flexible Shafts," by G. Kron, Journal of Applied Mechanics, Trans. ASME, vol. 68, 1946, pp. A-109–126.

5 "The Solution of the Aircraft Wing Flutter Problems by Means of Electric Circuit Analysis," by S. T. Jennings, PhD thesis, Ohio State University, 1947.

6 "Beam Vibration Analysis With the Electric Analog Computer," by G. D. McCann and R. H. MacNeal, Journal of Applied Mechanics, Trans. ASME, vol. 72, 1950, p. 13.

7 "An Equivalent Circuit for a Vibrating Beam Which Includes Shear Motions," by H. M. Trent, *Journal of the Acoustical Society of America*, vol. 22, 1950, p. 355.

8 "Lumped Parameter Analogies for Continuous Mechanical Systems," by W. T. Russell, PhD thesis, California Institute of Technology, 1950.

9 "Étude des vibrations de flexion et de torsion au moyen d'analogies électromécanique," by G. Cahen, Bulletin de l'Assoc. Tech. Maritime et Aéron, No. 49, 1950.

10 "Application of the Electronic Differential Analyzer to the Oscillation of Beams, Including Shear and Rotary Inertia," by C. E. Howe, R. M. Howe, and L. L. Rauch, Report UMM-67, Aeronautical Research Center, University of Michigan, January, 1951.

11 "A General Method for Calculating Critical Speeds of Flexible Rotors," by M. A. Prohl, Journal of Applied Mechanics, Trans. ASME, vol. 67, 1945, p. A-142.

12 "The Solution of Aeroelastic Problems by Means of Electrical Analogies," by R. H. MacNeal, G. D. McCann, and C. H. Wilts, *Journal of the Aeronautical Sciences*, vol. 18, 1951, p. 777.

13 "The Solution of Elastic Plate Problems by Electrical Analogies," by R. H. MacNeal, Journal of Applied Mechanics, Trans. ASME, vol. 73, 1951, p. 59.

Determination of Stresses in Cemented Lap Joints[1]

By R. W. CORNELL,[2] WINDSOR LOCKS, CONN.

A variation and extension of Goland and Reissner's (1)[3] method of approach is presented for determining the stresses in cemented lap joints by assuming that the two lap-joint plates act like simple beams and the more elastic cement layer is an infinite number of shear and tension springs. Differential equations are set up which describe the transfer of the load in one beam through the springs to the other beam. From the solution of these differential equations a fairly complete analysis of the stresses in the lap joint is obtained. The spring-beam analogy method is applied to a particular type of lap joint, and an analysis of the stresses at the discontinuity, stress distributions, and the effects of variables on these stresses are presented. In order to check the analytical results, they are compared to photoelastic and brittle lacquer experimental results. The spring-beam analogy solution was found to give a fairly accurate presentation of the stresses in the lap joint investigated and should be useful in analyzing other cemented lap-joint structures.

Nomenclature

The following nomenclature is used in the paper:

M = externally applied moment present in beam 2 at discontinuity
F = externally applied force on beam 2 at discontinuity
V = shear load on beam 2 at discontinuity
E = Young's modulus of beams 1 and 2
E_b = Young's modulus of braze or cement
G_b = shear modulus of braze or cement
h_b = braze or cement thickness
h_1, h_2 = thickness of beams 1 and 2
l = free tab length
R = M/E
P = $F/(h_2E)$
Q = V/E
σ_x, σ_y = horizontal and vertical stresses, respectively
τ_{xy} = shear stress
σ_{max} = maximum nominal stress in beam 2 at discontinuity
$K\sigma_{max}$ = maximum stress in beam 2 at discontinuity
σ_t = maximum stress tangential to fillet
I_1, I_2 = moment of inertia of beams 1 and 2
p = major principal stress
θ = angle between major principal stress and plane of beams
δ_1, δ_2 = displacement of a point on braze-beam surface of beams 1 and 2
x, ξ = horizontal distance from y-axis
y_1, y_2 = deflections of beams 1 and 2 as functions of x
η_1, η_2 = deflections of beams 1 and 2 as functions of ξ
$y_2(l)$ = deflection of beam 2 at $x = l$
D = differential operator
$'$ = primes designate order of the derivative with respect to x or ξ as indicated

1 Introduction

In connection with the investigation of the fatigue strength of brazed tab specimens of the type shown in Fig. 1, an analysis was made of the stresses in the base bar and braze layer of such

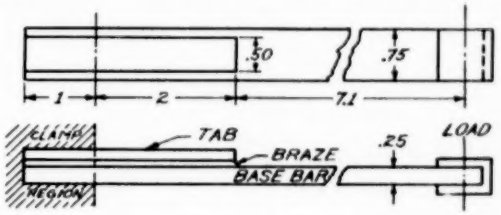

Fig. 1 Brazed Tab Fatigue Specimen

specimens. For this analytical study a method based on spring analogy and beam theory was developed. This variation and extension of Goland and Reissner's (1) method of approach is present here by applying it to the brazed tab fatigue specimen, but it can be expanded easily so as to be applicable to similar problems. Also presented are photoelastic and brittle lacquer experimental work to check the analytical results.[1]

In the brazed tab specimen the thin beam is referred to as the tab, whereas the thicker beam is called the base bar. For fatigue testing, the specimen was subjected to a flatwise cyclic load so that the loading at the tab ending was nearly one of pure bending. In the fatigue experiments the steel base bar was kept a constant thickness of 0.25 in., whereas the braze thickness, braze material, and the tab thickness were varied.

Referring to Fig. 2, showing the tab region with notation, the following stresses were desired: the horizontal normal stress σ_x, the vertical normal stress σ_y, and the shear stress τ_{xy} in the steel and braze at the base bar interface, the maximum base bar stress $K\sigma_{max}$, and the maximum stress tangential to the fillet σ_t. Also wanted were the influence on the tab-region stresses of the braze thickness h_b, the braze moduli of elasticity E_b and G_b, the tab thickness h_1, and the fillet radius r.

Previous methods of analysis which dealt with discontinuous multimaterial structures and lap joints were studied. Most of the solutions were for symmetrical discontinuities, such as Neuber's work (2). Several nonsymmetrical solutions were found, but they dealt with only one material and a sharp discontinuity (3). Three analytical methods were investigated

[1] Based on author's dissertation, "Spring-Beam Analogy Solution of Stresses in Cemented Joints," presented to the Yale School of Engineering for the Degree of Doctor of Engineering, June, 1950.

[2] Analytical Engineer, Hamilton Standard Division of United Aircraft Corporation. Jun. ASME.

[3] Numbers in parentheses refer to the Bibliography at the end of the paper.

Presented at the National Conference of the Applied Mechanics Division, Minneapolis, Minn., June 18–20, 1953, of The American Society of Mechanical Engineers.

Discussion of this paper should be addressed to the Secretary, ASME, 29 West 39th Street, New York, N. Y., and will be accepted until October 10, 1953, for publication at a later date. Discussion received after the closing date will be returned.

Note: Statements and opinions advanced in papers are to be understood as individual expressions of their authors and not those of the Society. Manuscript received by ASME Applied Mechanics Division, March 17, 1952. Paper No. 53—APM-15.

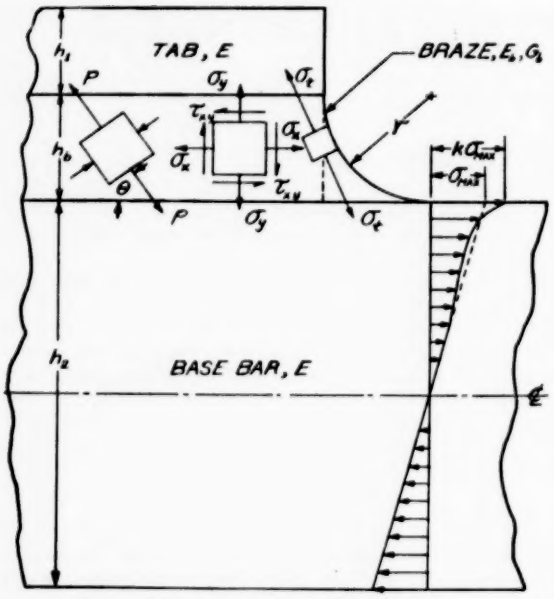

FIG. 2 TAB ENDING REGION WITH NOTATION

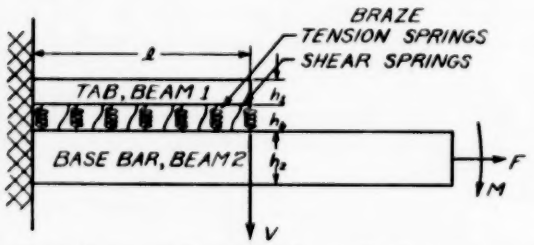

FIG. 3 SCHEMATIC DRAWING OF BRAZED TAB SPECIMEN

which might have been adapted to this problem (1, 4, 5), but it appeared they would require extensive modifications and would be laborious. Therefore the spring-beam method of approach was developed based on the principal assumptions of Goland and Reissner in regard to the cement or braze. For the type of problem considered here, Goland and Reissner's method would call for the setting up of equilibrium equations for the beams and cement and require ten boundary conditions. However, the spring-beam approach makes use of elementary beam theory, requires only four simple-beam boundary conditions, and gives the same results.

The spring-beam solution assumes that the tab and base bar act as if they were simple beams and that the more elastic braze layer is an infinite number of tension and shear springs. These springs are composed of four types: those transmitting normal vertical loads, horizontal shear loads, normal horizontal loads, and vertical-shear loads. Because the braze layer is thin and has little stiffness, the last two types of springs were neglected, Fig. 3. They may be included for problems with thick braze layers, but with more difficulty.[1] The spring constants are based on the properties of the braze material (1, 7).

Under load, the base bar deflects and the fibers along its upper surface are strained. These conditions load the tension and shear springs which pass on their shear and normal loads to the tab. The transmission of the appropriate loads from the base bar to the tab is expressed in a tenth order differential equation. Upon solving the differential equation and applying the boundary conditions of the problem a fairly complete analysis of the brazed tab specimen is obtained.

The following section presents the principal analytical steps in the spring-beam analogy method of approach as applied to the brazed tab specimen. There follows a summary of experimental work, a comparison of analytical and experimental results, and a final section comprising a summary and conclusions.

2 MATHEMATICAL DEVELOPMENT

Only the main steps in the basic derivation of the stresses in the brazed tab specimen under bending, axial, and shear loadings are presented. The brazed tab specimen with these loadings M, F, and V, is shown in Fig. 3. Other mathematical developments which expand on the scope of the solution and which verify some of the assumptions used in the basic derivation can be found in the author's dissertation.[1]

The assumptions used in the spring-analogy and simple-beam method are as follows:

(*a*) The tab and the base bar act separately according to simple-beam theory.

(*b*) The braze layer is an infinite number of shear and tension springs.

(*c*) The deflection of the specimen is small with respect to its dimensions, and its influence on the loading of the specimen is neglected.

(*d*) The free tab length is long enough so as not to influence the local stresses at the discontinuity.

(*e*) The braze layer is thin so that its beam stiffness can be neglected.

(*f*) The tab and base bar are narrow and each a unit wide. If the stresses in a wide joint are desired, EI_1 and EI_2 should be replaced by their respective plate-bending rigidities (6).

Differential Equations and Their General Solutions. There are two ways of obtaining the differential equations for the two beams, from the elementary moment equations of each beam and from the equilibrium equations for elements of each beam. The former method is used here; for the latter see references (footnote 1 and Bibliography 1). The moment equation for beam 1, Fig. 4, is obtained from beam theory as follows: The moment of the shear stress at any point x is

$$-\int_x^l \tau_{xy}\left(\frac{h_1}{2}+\eta_1-y_1\right)d\xi$$

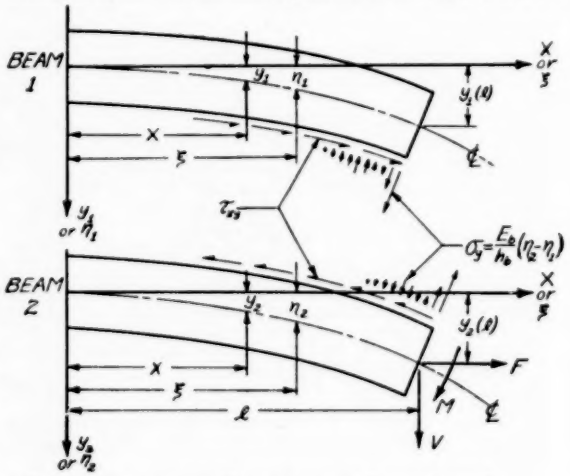

FIG. 4 LOADINGS AND DEFLECTIONS OF BEAMS 1 AND 2

and that of the normal vertical stress at any point x is

$$\int_x^l \frac{E_b}{h_b}(\eta_2 - \eta_1)(\xi - x)d\xi$$

as the normal vertical stress at a point ξ is (7)

$$\frac{E_b}{h_b}(\eta_2 - \eta_1)$$

Therefore

$$EI_1 y_1'' = -\int_x^l \tau_{xy}\left(\frac{h_1}{2} + \eta_1 - y_1\right)d\xi + \frac{E_b}{h_b} \times \int_x^l (\eta_2 - \eta_1)(\xi - x)d\xi \quad [1]$$

The moment equation for beam 2 is obtained in the same way but including the external loads

$$EI_2 y_2'' = -\int_x^l \tau_{xy}\left(\frac{h_2}{2} - \eta_2 + y_2\right)d\xi - \frac{E_b}{h_b}\int_x^l (\eta_2 - \eta_1) \times (\xi - x)d\xi + M + V(l - x) - F[y_2(l) - y_2] \quad [2]$$

Neglecting the second-order effects under assumption *c*, the terms $(\eta_1 - y_1)$, $(\eta_2 - y_2)$, and $[y_2(l) - y_2]$ can be neglected in Equations [1] and [2]. Then, differentiating the moment equations twice with respect to x we have

$$EI_1 y_1'''' = \frac{h_1}{2}\tau_{xy}' + \frac{E_b}{h_b}(y_2 - y_1)$$

$$EI_2 y_2'''' = \frac{h_2}{2}\tau_{xy}' - \frac{E_b}{h_b}(y_2 - y_1)$$

or in operator form

$$\left(D^4 + \frac{E_b}{EI_1 h_b}\right)y_1 - \frac{h_1}{2EI_1}D\tau_{xy} - \frac{E_b}{EI_1 h_b}y_2 = 0 \quad [3]$$

$$\left(D^4 + \frac{E_b}{EI_2 h_b}\right)y_2 - \frac{h_2}{2EI_2}D\tau_{xy} - \frac{E_b}{EI_2 h_b}y_1 = 0 \quad [4]$$

The expression for the shear stress τ_{xy}, at any point x is obtained by considering a small section of the braze layer, Fig. 5, which is deformed due to the displacements δ_1 and δ_2 of the braze surfaces of beams 1 and 2 caused by their bending and axial loads. The shear stress is then

$$\frac{G_b}{h_b}(\delta_2 - \delta_1)$$

Now, the contraction and extension of the outer fibers of beams 1 and 2 due to bending are $-\frac{1}{2}h_1\eta_1''d\xi$ and $\frac{1}{2}h_2\eta_2''d\xi$ in a length $d\xi$, respectively. The extensions of beams 1 and 2 due to axial loads $F_{1\xi}$ and $F_{2\xi}$ are

$$\left(\frac{F_{1\xi}}{Eh_1}\right)d\xi \quad \text{and} \quad \left(\frac{F_{2\xi}}{Eh_2}\right)d\xi$$

in a length $d\xi$. The axial loads change as the shearing stresses transfer the load from one beam to the other, so that

$$F_{1\xi} = \int_{\xi_1}^l \tau_{xy}d\xi_2 \quad \text{and} \quad F_{2\xi} = -\int_{\xi_1}^l \tau_{xy}d\xi_2 + F$$

The total displacement of a point x is the integral from 0 to x of the combined extensions of element $d\xi$, i.e.

$$\delta_1 = \int_0^x \int_{\xi_1}^l \frac{\tau_{xy}}{Eh_1}d\xi_1 d\xi_2 - \int_0^x \frac{1}{2}h_1\eta_1''d\xi_1$$

$$\delta_2 = -\int_0^x \int_{\xi_1}^l \frac{\tau_{xy}}{Eh_2}d\xi_1 d\xi_2 + \int_0^x \frac{1}{2}h_2\eta_2''d\xi_1 + \int_0^x \frac{F}{Eh_2}d\xi_1$$

The shear stress at any point along the braze surfaces is then

$$\tau_{xy} = \frac{G_b}{h_b}\left[\frac{1}{2}\int_0^x (h_1\eta_1'' + h_2\eta_2'')d\xi_1 - \int_0^x \int_{\xi_1}^l \tau_{xy}\left(\frac{1}{Eh_1} + \frac{1}{Eh_2}\right)d\xi_1 d\xi_2 + \int_0^x \frac{F}{Eh_2}d\xi_1\right] \quad [5]$$

Differentiating Equation [5] twice with respect to x we have

$$\tau_{xy}'' = \frac{G_b}{h_b}\left[\frac{1}{2}(h_1 y_1'''' + h_2 y_2'''') + \tau_{xy}\left(\frac{1}{Eh_1} + \frac{1}{Eh_2}\right)\right]$$

or in operator form

$$\left[D^2 - \frac{G_b}{Eh_b}\left(\frac{1}{h_1} + \frac{1}{h_2}\right)\right]\tau_{xy} - \frac{G_b h_2}{2h_b}D^3 y_2 - \frac{G_b h_1}{2h_b}D^3 y_1 = 0 \quad [6]$$

The differential Equations [3], [4], and [6] can be combined to form one tenth order differential equation. Combining Equations [3] and [4] we have

$$\left(\frac{EI_1}{h_1}D^4 + \frac{E_b}{h_1 h_b} + \frac{E_b}{h_2 h_b}\right)y_1 = \left(\frac{EI_2}{h_2}D^4 + \frac{E_b}{h_1 h_b} + \frac{E_b}{h_2 h_b}\right)y_2 \quad [7]$$

and combining Equation [7] with [6] we obtain the final tenth order differential equation

$$D^4\left[D^6 - 4\frac{G_b}{Eh_b}\left(\frac{1}{h_1} + \frac{1}{h_2}\right)D^4 + 12\frac{E_b}{Eh_b} \times \left(\frac{1}{h_1^3} + \frac{1}{h_2^3}\right)D^2 - 12\frac{E_b G_b}{E^2 h_b^2}\left(\frac{h_1 + h_2}{h_1 h_2}\right)^4\right]y_{1 \text{ or } 2} = 0 \quad [8]$$

This differential equation can be put in the form

$$D^4(D^2 - \alpha^2)(D^4 - 2\mathfrak{M}D^2 + \varphi^2)y_{1 \text{ or } 2} = 0$$

with exponential roots $\pm\alpha$, $\pm\beta$, and $\pm\gamma$, where $\beta^2 = 1/2(\mathfrak{M} + \varphi)$ and $\gamma^2 = 1/2(\varphi - \mathfrak{M})$. By inspection of Equations [8] and [6] the deflection and shear equations will be of the form

$$y_1 = a_1 + b_1 x + c_1 x^2 + d_1 x^3 + e_1 \sinh \alpha x + f_1 \cosh \alpha x + \sinh \beta x(g_1 \sin \gamma x + i_1 \cos \gamma x) + \cosh \beta x(j_1 \sin \gamma x + k_1 \cos \gamma x) \quad [9]$$

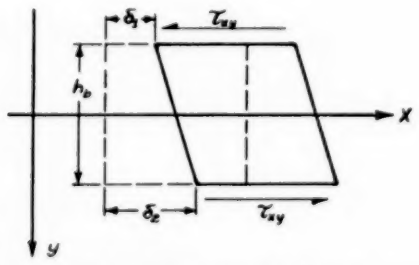

FIG. 5 SHEAR LOADING OF BRAZE

$$y_2 = a_2 + b_2x + c_2x^2 + d_2x^3 + e_2 \sinh \alpha x + f_2 \cosh \alpha x + \sinh \beta x(g_2 \sin \gamma x + i_2 \cos \gamma x) + \cosh \beta x(j_2 \sin \gamma x + k_2 \cos \gamma x) \quad [10]$$

and

$$\tau_{xy} = a_3 + b_3 \sinh \alpha x + c_3 \cosh \alpha x + \sinh \beta x(d_3 \sin \gamma x + e_3 \cos \gamma x) + \cosh \beta x(f_3 \sin \gamma x + g_3 \cos \gamma x) \quad [11]$$

Relationship of Coefficients. The relationships of the coefficients of the deflection and shear Equations [9], [10], and [11] are obtained by substituting them into differential Equations [6] and [7]. Equation [6] is simplified by letting

$$\Delta^2 = \frac{G_b}{Eh_b}\left(\frac{1}{h_1} + \frac{1}{h_2}\right)$$

and $y = h_2y_2 + h_1y_1$, i.e., $y = ax + bx^2 + cx^3 \ldots$ etc., where $a = a_1h_1 + a_2h_2$, etc., so that

$$\tau_{xy}'' - \Delta^2\tau_{xy} = \frac{G_b}{2h_b}\, y''' \quad [12]$$

Substituting in expressions for τ_{xy} and y and equating like terms, the following relationships are obtained

$$a_3 = -\frac{G_b}{2h_b}\frac{6}{\Delta^2}\, d \quad [13]$$

$$b_3 = \frac{\alpha^2}{\alpha^2 - \Delta^2}\frac{G_b}{2h_b}\, f \quad [14]$$

$$c_3 = \frac{\alpha^2}{\alpha^2 - \Delta^2}\frac{G_b}{2h_b}\, e \quad [15]$$

$$d_3 = \frac{G_b}{2h_b}\left[\frac{\mu i + \pi j}{\nu^2 + \lambda^2}\right] \quad [16]$$

$$e_3 = \frac{G_b}{2h_b}\left[\frac{-\mu g + \pi k}{\nu^2 + \lambda^2}\right] \quad [17]$$

$$f_3 = \frac{G_b}{2h_b}\left[\frac{\mu k + \pi g}{\nu^2 + \lambda^2}\right] \quad [18]$$

$$g_3 = \frac{G_b}{2h_b}\left[\frac{-\mu j + \pi i}{\nu^2 + \lambda^2}\right] \quad [19]$$

where

$$\mu = -\gamma(3\beta^2 - \gamma^2)(\beta^2 - \gamma^2 - \Delta^2) + 2\gamma\beta^2(\beta^2 - 3\gamma^2)$$
$$\nu = (\beta^2 - \gamma^2 - \Delta^2)$$
$$\pi = \beta(3\gamma^2 - \beta^2)(\beta^2 - \gamma^2 - \Delta^2) + 2\gamma^2\beta(3\beta^2 - \gamma^2)$$
$$\lambda = 2\gamma\beta$$

In order to obtain the relations between the coefficients of the deflection curves y_1 and y_2, Equation [7] is simplified to

$$[\Gamma h_1^2D^4 + 1]y_1 = [\Gamma h_2^2D^4 + 1]y_2$$

where

$$\Gamma = \frac{E}{12E_b}\left(\frac{h_1h_2h_b}{h_1 + h_2}\right)$$

On substituting in the expressions for y_1 and y_2 and equating like terms, we get

$$a_1 = a_2 \quad [20]$$

$$b_1 = b_2 \quad [21]$$

$$c_1 = c_2 \quad [22]$$

$$d_1 = d_2 \quad [23]$$

$$e_2 = \frac{\Gamma h_1^2\alpha^4 + 1}{\Gamma h_2^2\alpha^4 + 1}\, e_1 \quad [24]$$

$$f_2 = \frac{\Gamma h_1^2\alpha^4 + 1}{\Gamma h_2^2\alpha^4 + 1}\, f_1 \quad [25]$$

$$g_2 = \frac{(\mu\pi + \lambda\nu)g_1 + (\nu - \lambda)k_1}{\mu^2 + \nu^2} \quad [26]$$

$$i_2 = \frac{(\mu\pi + \lambda\nu)i_1 - (\nu - \lambda)j_1}{\mu^2 + \nu^2} \quad [27]$$

$$j_2 = \frac{(\mu\pi + \lambda\nu)j_1 + (\nu - \lambda)i_1}{\mu^2 + \nu^2} \quad [28]$$

$$k_2 = \frac{(\mu\pi + \lambda\nu)k_1 - (\nu - \lambda)g_1}{\mu^2 + \nu^2} \quad [29]$$

where

$$\mu = (\beta^4 - 6\beta^2\gamma^2 + \gamma^4)\Gamma h_2^2 + 1$$
$$\nu = 4\gamma\beta\Gamma h_2^2(\beta^2 - \gamma^2)$$
$$\pi = (\beta^4 - 6\beta^2\gamma^2 + \gamma^4)\Gamma h_1^2 + 1$$
$$\lambda = 4\gamma\beta\Gamma h_1^2(\beta^2 - \gamma^2)$$

Boundary Conditions. Although the three differential Equations [3], [4], and [6] reduce to a tenth order one, they were obtained originally from one zero and two second order equations, so that only four new boundary conditions are needed. The other six are present in the initial Equations [1], [2], and [5]. The four new boundary conditions occur at $x = 0$, where $y_1 = 0$, $y'_1 = 0$, $y_2 = 0$, and $y'_2 = 0$. Applying these boundary conditions to Equations [9] and [10] we have

$$a_1 + f_1 + k_1 = 0 \quad [30]$$

$$a_2 + f_2 + k_2 = 0 \quad [31]$$

$$b_1 + \alpha e_1 + \beta i_1 + \gamma j_1 = 0 \quad [32]$$

$$b_2 + \alpha e_2 + \beta i_2 + \gamma j_2 = 0 \quad [33]$$

The two boundary conditions present in Equation [5] are obtained by introducing the notation $y = h_1y_1 + h_2y_2$ and $\eta = h_1\eta_2 + h_2\eta_2$ and substituting in the expressions for y, η, and τ_{xy}. All of the exponential functions of x cancel, leaving just constant and x terms. Equating the constant terms we have

$$a_2 = \frac{G_b}{2h_b}(-e\alpha - i\beta - j\gamma) - \Delta^2\left[\frac{c_3}{\alpha^2} - \frac{2\gamma B}{(\beta^2 + \gamma^2)^2}\, d_2 + \frac{\beta^2 - \gamma^2}{(\beta^2 + \gamma^2)^2}\, g_2\right] \quad [34]$$

and equating the x terms

$$\Delta^2\left[a_2l + \frac{b_2}{\alpha}\cosh \alpha l + \frac{c_3}{\alpha}\sinh \alpha l + \frac{d_3}{\beta^2 + \gamma^2}(\beta \cosh \beta l \sin \gamma l - \gamma \sinh \beta l \cos \gamma l) + \frac{e_3}{\beta^2 + \gamma^2}(\beta \cosh \beta l \cos \gamma l + \gamma \sinh \beta l \sin \gamma l) + \frac{f_3}{\beta^2 + \gamma^2}(\beta \sinh \beta l \sin \gamma l - \gamma \cosh \beta l \cos \gamma l) + \frac{g_3}{\beta^2 + \gamma^2}(\beta \sinh \beta l \cos \gamma l + \gamma \cosh \beta l \sin \gamma l)\right] = \frac{G_b}{h_b}(c + P) \quad [35]$$

where

$$\Delta^2 = \frac{G_b}{E}\left(\frac{h_1 + h_2}{h_1 h_2 h_b}\right) \quad \text{and} \quad P = \frac{F}{Eh_2}$$

The four boundary conditions present in Equations [1] and [2] are obtained by introducing the notation $y_0 = y_2 - y_1$ and $\eta_0 = \eta_2 - \eta_1$ and substituting in the expressions for τ_{xy}, y_0, and η_0, where $y_0 = (a_2 - a_1) + (b_2 - b_1)x \ldots$ etc. As before, all the exponential terms in x cancel, leaving constant terms and terms in x. By equating the constant terms and x terms from the two moment equations, four boundary equations are obtained. Making use of Equation [13], these four boundary equations are combined and simplified to the following

$$c_1 = c_2 = \frac{6}{(h_1 + h_2)^3}\left[R + lQ - \frac{h_1 h_2}{2}P\right] \ldots\ldots [36]$$

$$d_1 = d_2 = -\frac{2Q}{(h_1 + h_2)^3} \ldots\ldots [37]$$

$$\frac{e_0}{\alpha^2}\sinh \alpha l + \frac{f_0}{\alpha^2}\cosh \alpha l + \frac{g_0}{(\beta^2 + \gamma^2)^2}[(\beta^2 - \gamma^2)\sinh \beta l \sin \gamma l - 2\beta\gamma \cosh \beta l \cos \gamma l]$$
$$+ \frac{i_0}{(\beta^2 + \gamma^2)^2}[(\beta^2 - \gamma^2)\sinh \beta l \cos \gamma l + 2\beta\gamma \cosh \beta l \sinh \gamma l]$$
$$+ \frac{j_0}{(\beta^2 + \gamma^2)^2}[(\beta^2 - \gamma^2)\cosh \beta l \sin \gamma l - 2\beta\gamma \sinh \beta l \cos \gamma l]$$
$$+ \frac{k_0}{(\beta^2 + \gamma^2)^2}[(\beta^2 - \gamma^2)\cosh \beta l \cos \gamma l + 2\beta\gamma \sinh \beta l \sin \gamma l]$$
$$= -\frac{h_1^2 h_b}{(h_1 + h_2)^3}\frac{E}{E_b}\left[(h_1 + 3h_2)R + \frac{1}{2}h_2^2(h_2 - h_1)P\right] \ldots [38]$$

$$\frac{e_0}{\alpha}\sinh \alpha l + \frac{f_0}{\alpha}\cosh \alpha l + \frac{g_0}{\beta^2 + \gamma^2}(\beta \cosh \beta l \sin \gamma l - \gamma \sinh \beta l \cos \gamma l) + \frac{i_0}{\beta^2 + \gamma^2}(\beta \cosh \beta l \cos \gamma l + \gamma \sinh \beta l \sin \gamma l) + \frac{j_0}{\beta^2 + \gamma^2}(\beta \sinh \beta l \sin \gamma l - \gamma \cosh \beta l \cos \gamma l) + \frac{k_0}{\beta^2 + \gamma^2}(\beta \sinh \beta l \cos \gamma l + \gamma \cosh \beta l \sin \gamma l) = \frac{h_1^2 h_b(h_1 + 3h_2)}{(h_1 + h_2)^3}\frac{E}{E_b}Q \ldots\ldots [39]$$

Final Equations for Beam Deflections and Stress Distributions. From the solution of the ten Equations [30] to [39] the coefficients for the deflection curves for the two beams can be obtained, and using these, σ_y and τ_{xy} along the base bar braze surface can be determined. Because the length of the free tab is considered long and the roots α and β are usually large, $\sinh \alpha l \approx \cosh \alpha l \approx {}^1/_2 e^{\alpha l}$, and $\sinh \beta l \approx \cosh \beta l \approx {}^1/_2 e^{\beta l}$. Then the equations for the vertical normal stress and the shear stress in the braze or base bar at the braze surface for $x = l$ are

$$\sigma_y = \frac{E_b}{h_b}(y_2 - y_1) = \frac{E_b}{h_b}\{\tfrac{1}{2}(e_0 + f_0)\sinh \alpha x + [(g_0 + j_0)\sin \gamma x + (i_0 + k_0)\cos \gamma x]\sinh \beta x\} \ldots\ldots [40]$$

$$\tau_{xy} = a_2 + (b_2 + c_2)\sinh \alpha x + [(d_2 + f_2)\sin \gamma x + (e_2 + g_2)\cos \gamma x]\sinh \beta x \ldots\ldots [41]$$

where the coefficients can be obtained from the solution of the following four equations

$$\frac{(b_2 + c_2)}{\alpha^2}\sinh \alpha l + \frac{(d_2 + f_2)}{\beta^2 + \gamma^2}(\beta \sin \gamma l - \gamma \cos \gamma l)\sinh \beta l + \frac{(e_2 + g_2)}{\beta^2 + \gamma^2}(\beta \cos \gamma l + \gamma \sin \gamma l)\sinh \beta l = \frac{G_b}{2h_b}\frac{2E}{G_b}\frac{h_1 h_2 h_b}{(h_1 + h_2)^3}[6lR + (h_1^2 - h_1 h_2 + h_2^2)P] \ldots\ldots [42]$$

$$\frac{(e_0 + f_0)}{\alpha^2}\sinh \alpha l + \frac{(g_0 + j_0)}{(\beta^2 + \gamma^2)^2}[(\beta^2 - \gamma^2)\sin \gamma l - 2\beta\gamma \cos \gamma l]\sinh \beta l + \frac{(i_0 + k_0)}{(\beta^2 + \gamma^2)^2}[(\beta^2 - \gamma^2)\cos \gamma l + 2\beta\gamma \sin \gamma l]\sinh \beta l = -\frac{h_1^2 h_b}{(h_1 + h_2)^3}\frac{E}{E_b}[(h_1 + 3h_2)R + \frac{1}{2}h_2^2(h_2 - h_1)P] \quad [43]$$

$$\frac{(e_0 + f_0)}{\alpha}\sinh \alpha l + \frac{(g_0 + j_0)}{\beta^2 + \gamma^2}(\beta \sin \gamma l - \gamma \cos \gamma l)\sinh \beta l + \frac{(i_0 + k_0)}{\beta^2 + \gamma^2}(\beta \cos \gamma l + \gamma \sin \gamma l)\sinh \beta l = \frac{h_1^2 h_b(h_1 + 3h_2)}{(h_1 + h_2)^3}\frac{E}{E_b}Q \ldots\ldots [44]$$

$$a_2 = \frac{G_b}{h_b}\frac{6Q}{\Delta^2(h_1 + h_2)^2} \ldots\ldots [45]$$

The relationships between $(b_2 + c_2)$, $(d_2 + f_2)$, and $(e_2 + g_2)$ and $(e_0 + f_0)$, $(g_0 + j_0)$, and $(i_0 + k_0)$ are obtained from Equations [14] to [19] and [24] to [29], and α, β, γ, and Δ are obtained from the differential Equations [8] and [12]. Because the stresses are local, and, therefore, depend only on the distance from the tab ending, a convenient length can be assumed for l such that γl is an even multiple of 2π. Then Equations [42], [43],and [44] are simplified by replacing $\cos \gamma l$ with 1 and omitting the $\sin \gamma l$ terms. The principal deflection curves of the beams are

$$y_1 \approx c_1 x^2 + d_1 x^3 \quad \text{and} \quad y_2 \approx c_2 x^2 + d_2 x^3 \ldots\ldots [46]$$

where c_1, c_2, d_1, and d_2 are given by Equations [36] and [37]. The terms not given in Equations [46] are small and make up a slight deviation from the basic curve which produces the local stresses at the discontinuity.

An approximation of the horizontal stress distribution σ_x, at the braze surface of the base bar can be obtained by using nominal values. However, in the vicinity of the tab ending, this approximation will probably be in considerable error because the discontinuity causes a local effect and not an average one. The nominal stress distribution for σ_x is obtained by determining the net moment distribution in the base bar and dividing by its section modulus. The net moment at any distance $(l - x)$ from the tab ending is the externally applied moment minus the moment lost over this distance due to the action of the shear and vertical normal stresses on the braze-base bar surface. The distribution of σ_x in the braze along the braze-base bar surface can be approximated by assuming the horizontal strains in the base bar and braze are equal along this surface. Then

$$\sigma_{x\,(\text{Braze})} = \frac{E_b}{E}\left(\sigma_{x\,(\text{Base bar})} - \frac{1}{3}\sigma_y\right) + \frac{1}{3}\sigma_y \ldots\ldots [47]$$

where a value of $^1/_3$ has been assumed for Poisson's ratio.

The maximum base bar stress $K\sigma_{max}$, which occurs at the foot of

the tab, can be approximated by the major principal tab-ending stress p, in the base bar, whereas the maximum tangential stress σ_t, in the braze can be approximated by the major principal tab-ending stress in the braze. These principal stresses and their angles with respect to the base bar are obtained by making use of the values for σ_x, σ_y, and τ_{xy} at the braze surface and tab ending in the base bar and braze, respectively.

In the analysis, the action of the assumed springs is such that finite shear and vertical normal stresses result at the tab ending. Now, if there were no fillet at the tab ending the shear stress would be zero and the vertical normal stress infinite (3). Therefore the analysis might be said to include the effect of a fillet. It appears logical to assume that the fillet radius would be of the order of the braze thickness, and the experimental results indicate that this assumption is approximately correct.

For convenience, the stresses can be put in dimensionless form by using stress ratios based on the maximum nominal stress in beam 2 at the discontinuity. This maximum nominal stress, σ_{max}, can easily be expressed in terms of the dimensions and properties of the beam and the externally applied loads.

Experimental Work

The experimental program was designed to check the analytical results for the brazed tab specimen. In order to check all the stress distributions and results that the analytical work gives would require the construction and testing of many complex photoelastic specimens. Because of this, the stress distributions were obtained for only one brazed tab specimen design using photoelasticity. Photoelastic results for a specimen of different dimensions were available from work done at the University of Illinois (8). The maximum stress in the base bar at the tab ending, $K\sigma_{max}$ or p, was investigated for all brazed tab specimen designs using brittle-lacquer technique on large-scale models.

Of prime importance in the experimental models is the type and size of the fillet to be used, because no fillet would result in an infinite vertical normal stress at the tab ending (3). Based on the assumption that the fillet radius probably represented by the analytical results is of the order of the braze thickness, all experimental specimens were made this way except when it was physically impossible to machine the fillets in specimens with very thin braze.

Brittle-Lacquer Program. The brittle-lacquer program was used to determine the effects of the tab thickness, braze thickness, and braze elasticity on the maximum principal stress in the base bar. Flat-sided specimens 2 and 4 times the size of the brazed tab specimen were used. The former were used for test specimens representing brazed tab specimens with thick braze layers, whereas the large-scale ones were used to represent specimens with thin braze layers. Four double and 10 quadruple-size steel specimens were made with various braze thicknesses to cover equivalent braze thicknesses in the fatigue specimens of 0.001 to 0.05 in. To obtain the effect of braze elasticity, seven quadruple-size specimens were made with soft solder, four having steel and three having brass base bars and tabs. All the specimens were made with thick tabs which subsequently were ground down twice, so that the effect of equivalent tab thicknesses of 0.08 in., 0.04 in. and 0.02 in. could be obtained from each specimen. It was realized that for the thicker braze thicknesses and thinner tab thicknesses the theory would not give very accurate results, but it was desired to learn how much in error the theory was for such cases.

The brittle-lacquer experiments were performed in an air-conditioned room using standard Stresscoat procedure. The specimens were loaded by placing weights at the end of the extra long base bars and, while under load, the tab regions on each side of the specimens were inspected for the first signs of a crack. Two tests were conducted on each specimen unless the results did not agree within 15 per cent in which case more tests were run. The Stresscoat results were put in stress-ratio form by dividing the maximum measured or principal base bar stress at the tab ending by the nominal one. The maximum base bar stress was obtained by using the average of the load at which the first Stresscoat crack was noticed in the base bar at the tab ending and the preceding load.

Photoelastic Program. The photoelastic work was based on that done at the University of Illinois (8) on the same brazed tab problem. Kriston and CR-39 were used to simulate the steel and braze, respectively, as their moduli of elasticity are nearly 2 to 1 and they both have good photoelastic properties. A polymerizing resin glue[4] was used to join the tab, braze, and base bar sections together. This glue cures at room temperature, thereby decreasing the possibility of thermal and residual stresses. A 5-times size specimen was made which was equivalent to a brazed tab specimen having a base bar 0.25 in., a tab 0.04 in., and a braze layer 0.01 in. The model was approximately $^1/_4$ in. thick and 10 in. long. A great deal of trouble was encountered in obtaining joints free of air bubbles, and five specimens were made (three reported previously[1]) before a specimen was obtained which was nearly free of air bubbles.

The specimen was loaded in pure bending, and fringe patterns were obtained with the fillet under tension and compression. The results were averaged so as to nullify any residual stresses. The directions of the principal stresses were obtained by Stresscoat. The stresses in the specimen were determined by a modification of the shear difference method (8, 9). Because only stress ratios were wanted, the fringe orders were divided by the maximum nominal base bar fringe order.

Analytical and Experimental Results

Analytical results were obtained for the brazed tab specimen under pure bending for various tab and braze thicknesses, and the results were put in the form of stress ratios based on the maximum nominal stress in the base bar at the tab ending, σ_{max}. All of the results were calculated using a base bar 0.25 in. thick and a Young's modulus of elasticity of 30×10^6 and 15×10^6 psi for the steel and braze, respectively. Based on the measured shear moduli of the brazed constituents,[1] the shear modulus for the braze was estimated to be about 5×10^6 psi. Because the braze moduli of elasticity and braze thickness always appear as ratios E_b/h_b and G_b/h_b in the analytical solution, only one of them had to be varied to obtain the effects of both. For simplicity, the elastic properties of the braze were kept constant and the braze thickness varied.

Stress distributions of σ_y/σ_{max}, τ_{xy}/σ_{max}, and σ_x/σ_{max} in the steel along the base bar-braze surface for pure bending were obtained for specimens with a tab 0.04 in. thick and braze thicknesses of 0.10 in., 0.01 in., and 0.001 in., Figs. 6, 7, and 8. Apparent from the distribution curves is the very local effect of the tab ending. They also indicate that the thicker and/or more elastic the braze layer the deeper the depth of influence becomes. Both τ_{xy}/σ_{max} and σ_y/σ_{max} are shown to increase very rapidly near the tab ending, more sharply the thinner the braze layer. The effect of braze thickness and tab thickness on the maximum σ_y/σ_{max}, τ_{xy}/σ_{max}, p/σ_{max} stress ratios which occur at the tab ending for pure bending are given in Figs. 9 and 11. These graphs show that the thicker the tab the higher the maximum stresses become and that the tab thickness has more influence on the maximum stresses of specimens with thin braze layers than thick. The angle that p makes with the base bar was found to be nearly 0 deg for h_b greater than 0.01 in. and nearly 90 deg for h_b less than 0.001 in. These maximum stresses

[4] Resin glue L-1373 made by the Specialty Resin Corporation.

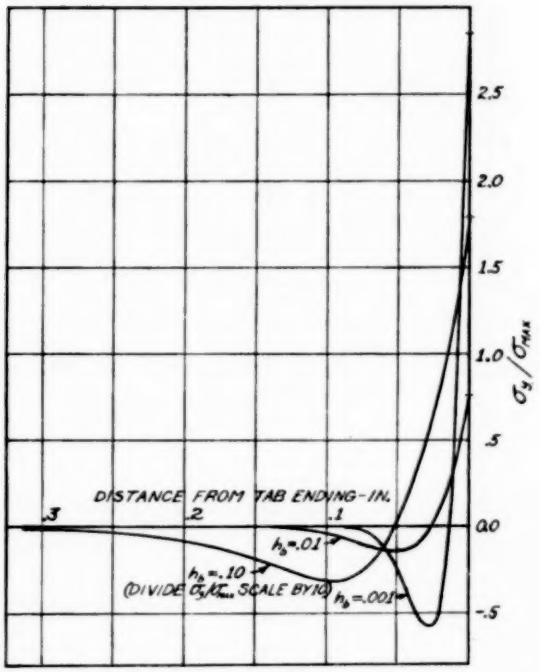

FIG. 6 σ_y/σ_{max} IN BRAZE AND BASE BAR AT BRAZE SURFACE FOR PURE BENDING; h_1 = 0.04 IN. AND h_2 = 0.25 IN.

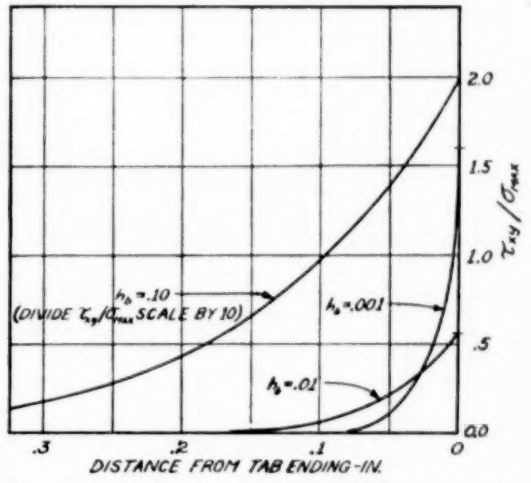

FIG. 7 τ_{xy}/σ_{max} IN BRAZE AND BASE BAR AT BRAZE SURFACE FOR PURE BENDING; h_1 = 0.04 IN. AND h_2 = 0.25 IN.

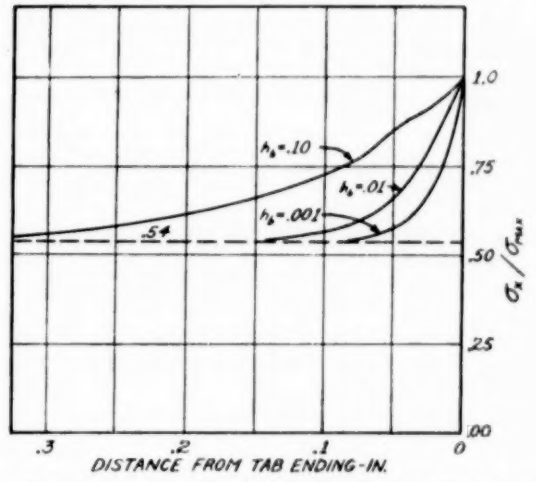

FIG. 8 σ_x/σ_{max} IN BASE BAR AT BRAZE SURFACE FOR PURE BENDING; h_1 = 0.04 IN. AND h_2 = 0.25 IN.

were also investigated for specimens with a bond thickness of 0.01 in. and tab thicknesses up to 1.00 in., and were found to approach a maximum magnitude.

Because the solution presented in this paper neglects the vertical shear in the braze, the vertical normal stress is constant across the braze layer. The effect of vertical shear in the braze was investigated for two cases. It was found that the maximum stresses at the base bar-braze surface were decreased slightly, more the thicker the braze. In general, it was found that the base bar and braze stresses were not influenced greatly by vertical shear for specimens with braze layers that are thin compared to their tab thickness.

The Stresscoat and photoelastic results are believed to be accurate enough to be used to determine the adaptability and accuracy of the analytical results. The main difficulties in both testing techniques were in constructing such small specimens and in detecting the patterns on them. Because of the controlled conditions, it is believed that the accuracy of the Stresscoat results is good, within 15 per cent.

The Stresscoat results are presented in Figs. 10 and 11, and a sample Stresscoat pattern is shown in Fig. 13. On the first figure are plotted the effects of braze thickness on the maximum base bar stress for three different tab thicknesses. The braze thicknesses of the soft-solder specimens were changed on the basis of the theoretical solution to put them on a par with the silver-soldered steel ones. This was done by multiplying h_b by $(E_{\text{brass or steel}} E_{\text{braze}})/(E_{\text{steel}} E_{\text{soft solder}})$. Fig. 11 compares all three experimental curves of Fig. 10 with the corresponding analytical ones.

For the brazed tab specimens with tab thickness of 0.08 in., Fig. 10(*a*), the effect of braze thickness on p/σ_{max} in the base bar at the tab ending and braze surface is found to be nearly the same as determined analytically, but the magnitudes are slightly greater. The greater the braze thickness, the greater is the difference between the analytical and experimental values. Undoubtedly, this is due to the fact that the analytical stresses in question are at the tab ending, whereas the experimental are at the end of the fillet. Because the values for the soft-soldered specimens fall in line with the brazed-specimen values when their braze thicknesses are adjusted according to theory, the moduli of elasticity of the braze material must influence the stresses in the same way as the reciprocal of the braze thickness. Figs. 10(*b*) and (*c*) show the same results as Fig. 10(*a*), but for tab thicknesses of 0.04 in. and 0.02 in., respectively. It is apparent that the difference between the analytical and experimental results is greater the thinner the tab, which is probably due to the fact that the braze layer is proportionately greater compared to the tab thickness and was neglected in the analytical solution.

Inspection of Fig. 11 shows that not only the effect of the braze thickness on the value of p/σ_{max} is similar to that determined analytically but that the effect of the tab thickness is similar also. Because the braze thickness was neglected in the analytical solu-

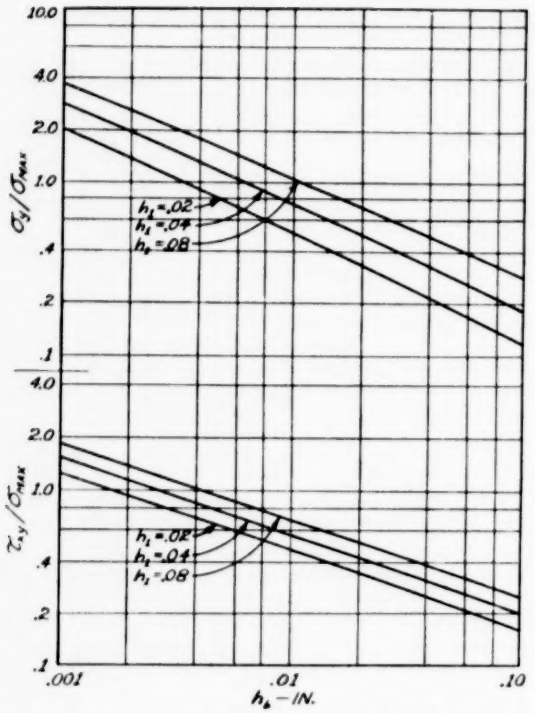

FIG. 9 σ_y/σ_{max} AND τ_{xy}/σ_{max} IN BRAZE AND BASE BAR AT TAB ENDING AND BRAZE SURFACE FOR PURE BENDING; h_2 = 0.25 IN.

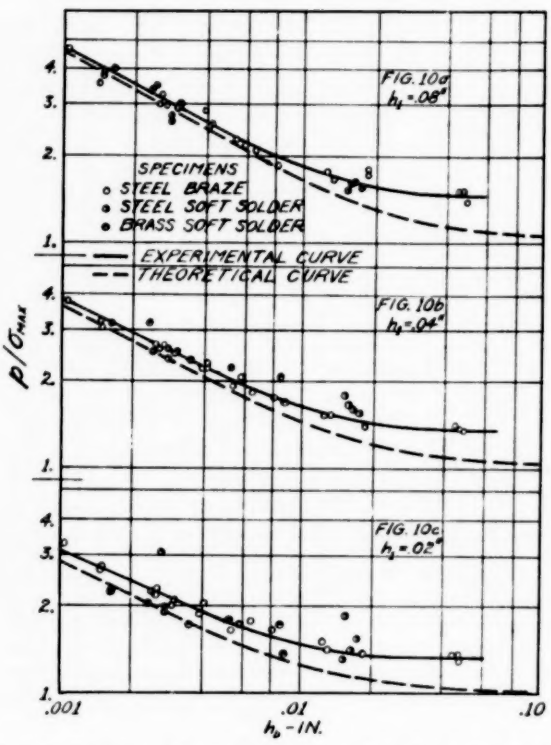

FIG. 10 STRESSCOAT RESULTS FOR p/σ_{max} IN BASE BAR AT TAB ENDING AND BRAZE SURFACE FOR PURE BENDING; h_2 = 0.25 IN.

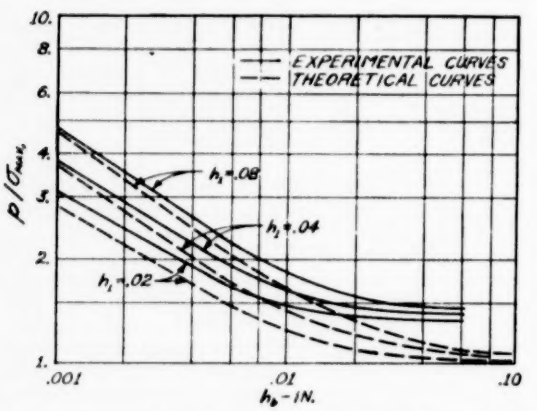

FIG. 11 ANALYTICAL AND STRESSCOAT RESULTS FOR p/σ_{max} IN BASE BAR AT TAB ENDING AND BRAZE SURFACE FOR PURE BENDING; h_2 = 0.25 IN.

tion, the effect of increasing the tab thickness on the major principal stress in the base bar at tab ending is slightly less than that shown by the analytical. The effect of tabs up to 1 in. was determined experimentally for one braze thickness, and p/σ_{max} was found to approach a maximum as predicted by theory. As before, the magnitudes were found to be slightly greater than those given by the analytical solution.

The fringe pattern of the photoelastic model for the fillet under compression and the Stresscoat pattern are shown in Figs. 12 and 13. This model represents a brazed tab specimen where h_2 = 0.25 in., h_1 = 0.04 in., and h_b = 0.01 in. The fringe patterns for the fillet under tension and compression were nearly the same. The values at station 0, Fig. 16, were checked by using the applied moment and the optical coefficient for Kriston and found to be in error by 1 per cent. The fringe values became constant again at about the 24th station, where the fringe values were found to be in error by less than 4 per cent. The angles of the principal stresses were found to be difficult to measure accurately.

The photoelastic results are presented in Figs. 14, 15, and 16, along with the corresponding analytical results so that they can be compared. Fig. 14 indicates that the analytical and experimental distribution curves for σ_y/σ_{max} along the base bar-braze surface are similar. In the tab region the experimental results are of lower magnitude than the analytical. However, the area under the experimental curve is not zero as it should be but slightly negative, probably indicating that the experimental stresses at the tab ending are a little low. The results of the photoelastic work on a model equivalent to a brazed tab specimen where h_2 = 0.25 in., h_1 = 0.03 in. ,and h_b = 0.03 in. (8) are similar to those shown here.

The distribution of τ_{xy}/σ_{max} along the base bar-braze surface is shown in Fig. 15, and is not subject to integration errors, whereas σ_y/σ_{max} is. It is almost the same as the analytical as to both shape and magnitude. The area under the experimental curve was found to be about 10 per cent too great with the braze layer included. However, if the theoretical curve is used away from the tab ending instead of the experimental, the area would be correct. It appears, therefore, that the experimental values away from the tab ending are slightly high, probably due to error in measuring the small angles of the principal stresses. The

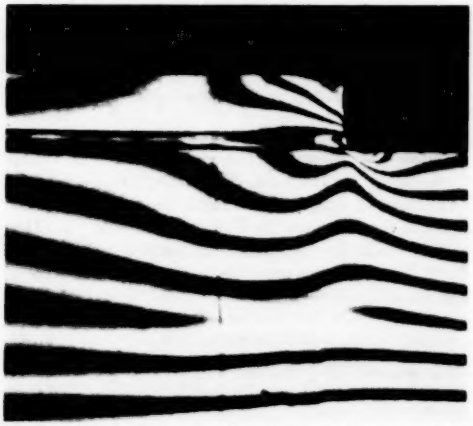

FIG. 12 PHOTOELASTIC FRINGE PATTERN FOR FILLET IN COMPRESSION; $h_1 = 0.04$ IN., $h_2 = 0.25$ IN., AND $h_b = 0.01$ IN.

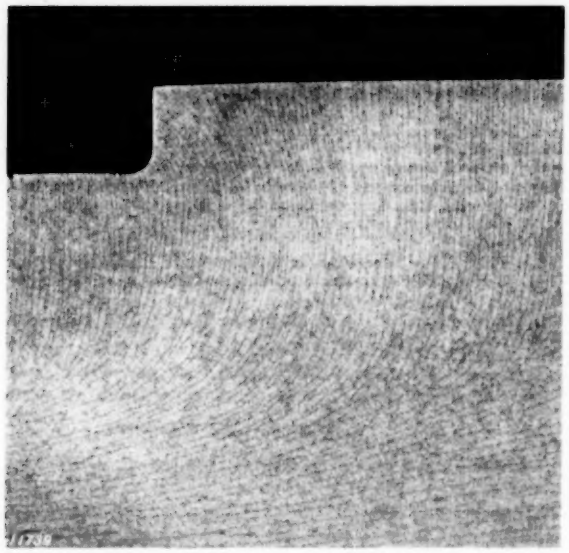

FIG. 13 STRESSCOAT PATTERN ON PHOTOELASTIC SPECIMEN; $h_1 = 0.04$ IN., $h_2 = 0.25$ IN., AND $h_b = 0.01$ IN.

experimental value for the angle of the principal stress in the base bar at the tab ending, station 7, was found to be 37 deg, whereas the analytical value was 39 deg. For the specimen in reference (8), this angle was found to be 17 deg compared to an analytical value of 21 deg. Thus the principal stress angle in the base bar at the tab ending is given quite accurately by the theory.

The distribution of σ_x/σ_{max} is given in Fig. 16 and is subject to integration errors. Because σ_x/σ_{max} is obtained from the σ_y/σ_{max} values, its magnitude is probably low in the region between stations 6.2 and 9. However, on comparing the analytical curve with the experimental, it is obvious that there is considerable error in assuming the stresses in the base bar are their nominal values, especially in the fillet region.

On comparing the Stresscoat and photoelastic results, it is found that the maximum base bar stress ratios agree fairly well. For a brazed tab specimen with $h_2 = 0.25$ in., $h_1 = 0.04$ in., and $h_b = 0.01$ in., the Stresscoat value for p/σ_{max} in the base bar at the tab ending is 1.65, whereas the photoelastic value is 1.55.

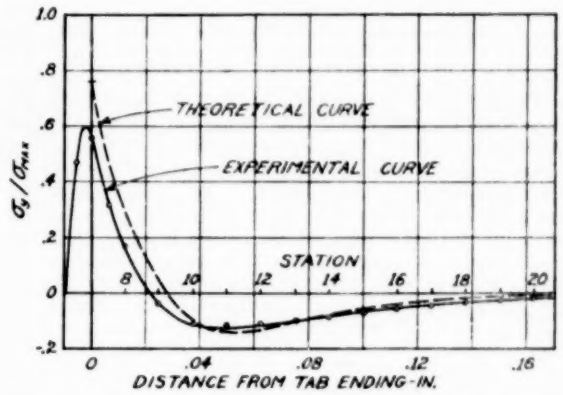

FIG. 14 PHOTOELASTIC RESULTS FOR σ_y/σ_{max} IN BASE BAR AT BRAZE SURFACE FOR PURE BENDING; $h_1 = 0.04$ IN., $h_2 = 0.25$ IN., AND $h_b = 0.01$ IN.

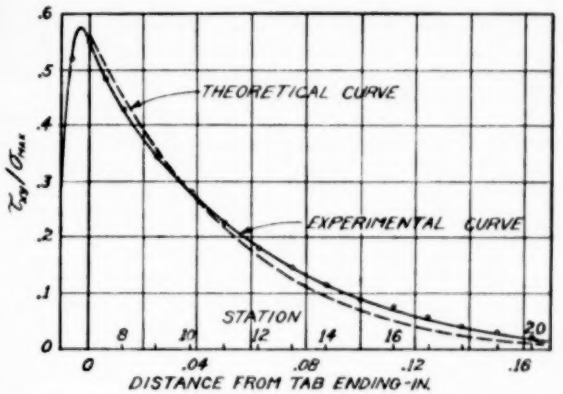

FIG. 15 PHOTOELASTIC RESULTS FOR τ_{xy}/σ_{max} IN BASE BAR AT BRAZE SURFACE FOR PURE BENDING; $h_1 = 0.04$ IN., $h_2 = 0.25$ IN., AND $h_b = 0.01$ IN.

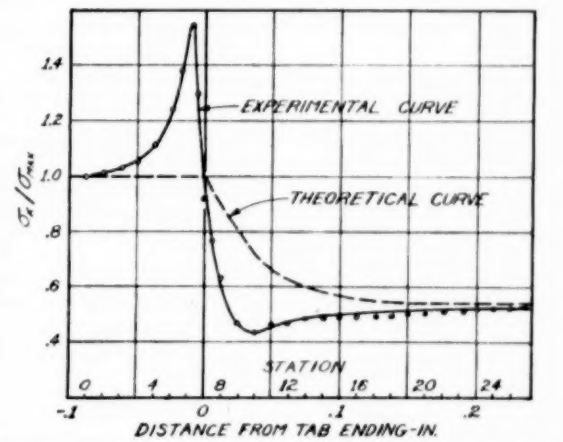

FIG. 16 PHOTOELASTIC RESULTS FOR σ_x/σ_{max} IN BASE BAR AT BRAZE SURFACE FOR PURE BENDING; $h_1 = 0.04$ IN., $h_2 = 0.25$ IN., AND $h_b = 0.01$ IN.

For a specimen with $h_2 = 0.25$ in., $h_1 = 0.03$ in., and $h_b = 0.03$ in., the values are 1.38 and 1.50 (8), respectively.

Summary and Conclusions

The application of the spring-beam method of approach to the brazed tab specimen showed that a fairly complete investigation of the stresses can be made for bending, axial, and shear loadings. Although this solution could not give the effect of the fillet radius and the magnitude of the tangential stresses along the fillet, the peak tab-ending stress in the base bar was found to be approximated by the major principal stress in the base bar at the tab ending. In regard to fillet radius, the analytical results are such as if a fillet was present, and the experimental work indicates that the assumption that the fillet radius is of the order of the cement or braze-layer thickness is approximately correct for the problem considered.

In general, the experimental results were found to check the analytical results quite well, the main discrepancies being in the vicinity of the fillet. For braze thicknesses of the order of or greater than that of the tab, the analytical results were found to be considerably lower than the experimental values because the braze stiffness as a beam was neglected. The beam stiffness of the braze layer can be included in the analysis but with much difficulty.[1] Only the magnitudes of σ_x/σ_{max} were found to be in great error near the tab ending. This error was caused by assuming nominal stresses for σ_x, which neglects the local effect of the tab ending.

The analytical and experimental results show that for pure bending the tab-ending effect is local, more so the thinner or less elastic the braze layer. Also, the local tab-ending stresses are higher the thinner or less elastic the braze layer and the thicker the tab. However, the local tab-ending stresses were found to approach a maximum as the tab thickness increased. Similar analytical results have been obtained for axial loading.[1]

In conclusion, the spring-beam method of attack permits a relatively elementary and yet complete and fairly accurate analysis of the stresses in the brazed tab specimen. It is believed that this type approach will be helpful in analyzing other similar bimetallic, discontinuous structures.

Acknowledgments

The analytical investigation was a part of a research program being conducted at Hamilton Standard Division of United Aircraft Corporation for the U. S. Air Forces, Propeller Laboratory of the Air Materiel Command, Wright-Patterson Air Force Base. The author wishes to thank the U. S. Air Forces and the Hamilton Standard Division for permission to publish this material, and Prof. E. O. Waters for his valuable assistance in the experimental program.

BIBLIOGRAPHY

1 "The Stresses in Cemented Joints," by M. Goland and E. Reissner, Journal of Applied Mechanics, Trans. ASME, vol. 66, 1944, pp. A-17–27.

2 "Theory of Notch Stresses, Principles for Exact Stress Calculations," by H. Neuber, Translated for The David Taylor Model Basin by F. A. Raven, Edward Brothers, Inc., Ann Arbor, Mich., 1946.

3 "Stress Distribution in Reentrant Corner," by J. H. A. Brahtz, Trans. ASME, vol. 55, 1933, Paper APM—55-6, pp. A-31–37.

4 "Solution of Problems of Elasticity by the Framework Method," by A. Hrennikoff, Journal of Applied Mechanics, Trans. ASME, vol. 63, 1941, pp. A-169–175.

5 "Analysis of Resin Bonded Tab Tests," by S. J. Loring, Technical Investigation Memorandum No. 6, to Hamilton Standard Division, May 8, 1946.

6 "Note on Beams and Plates," by George Gerard, *Journal of the Aeronautical Sciences*, vol. 19, March, 1952, pp. 207–208.

7 "Bending of an Infinite Beam on an Elastic Foundation," by M. A. Biot, Journal of Applied Mechanics, Trans. ASME, vol. 59, 1937, pp. A-1–7.

8 "Photoelastic Investigation of Stresses in a Brazed Joint," by C. E. Taylor, HSP-760 Hamilton Standard Division, February 9, 1950.

9 "Photoelasticity," by M. M. Frocht, John Wiley & Sons, Inc., New York, N. Y., vol. 1, 1941.

Effect of Range of Stress on Fatigue of 76S-T61 Aluminum Alloy Under Combined Stresses Which Produce Yielding

By W. N. FINDLEY,[1] URBANA, ILL.

Fatigue test data under bending, torsion, and combined bending and torsion are presented for mean stresses from zero to values which cause substantial yielding. The mean nominal stresses in the bending and the torsion tests were corrected for the effect of the nonlinear distribution of stress resulting from yielding. Static tests in tension, compression, bending, and torsion also are described. The applicability of several theories of failure are compared with these test data. The role of anisotropy of the material, mechanism of crack formation, mean stress, and maximum stress are discussed.

IN another paper (1)[2] the results of fatigue tests of 76S-T61 aluminum alloy under combined bending and torsion have been presented and compared with various theories of failure. In the present paper these data have been extended to include the additional variable of "range-of-stress" and its effect under different combinations of bending and torsion. The term range-of-stress is used here in the broadest sense, as employed by Smith (2), for example, to describe in a general way a relationship between the maximum and minimum stress in a cycle of stress.

A complete description of a sinusoidal cycle of stress requires two algebraic quantities, such as maximum and minimum stress, alternating stress amplitude and mean stress, range ratio and maximum stress, alternating stress amplitude and maximum stress, alternating stress amplitude and minimum stress, and so on.

Previous Work

The effect of range of stress has been investigated and discussed widely. The problem was reviewed by Peterson (3) in 1937 and existing data interpreted by Smith (2) in 1942. Some of the subsequent investigations (4 to 13) were reviewed, and Smith's interpretation for tensile mean stresses was brought up to date by Schwartz (14) in 1948.

Various empirical relations have been proposed to describe the observed effect of mean stresses in fatigue. Among these are the modified-Goodman law (15), the Gerber parabola (16), the Soderberg linear relation (17), Smith's equation for brittle metals (2), and Seliger's parameter (18).

The most widely used of these expressions for tension or bending are of the form

$$\frac{\sigma_a}{\sigma_r} + \frac{\sigma_m}{\sigma_z} = 1 \quad \ldots\ldots [1]$$

Where σ_a is the fatigue strength expressed as the alternating stress for a given mean stress, σ_m is the mean stress, σ_r is the fatigue strength for completely reversed stresses, and σ_z is either the ultimate strength or the yield strength. Equation [1] has been modified by some by introducing a constant before either the first or second term.

For torsion fatigue, Smith (2) observed that the fatigue strength was nearly independent of the mean stress.

At the time these tests were started in August, 1942, fatigue tests of aluminum alloys under combined bending and torsion were unknown to the author (although it is now known that tests by Nisihara and Kawamoto (19), had just been published in Japan) and no tests had been reported for combined stress-fatigue tests with different values of mean stress superimposed on the alternating stresses. Recently H. J. Gough (20) published results of such tests on steels, but so far as is known the test data contained herein are the first to be reported for an aluminum alloy under combined bending and torsion with superimposed mean stresses.

Fatigue Tests

The material, apparatus, specimen, and testing technique employed have been described in a previous paper (1). In Figs. 1 to 3 are shown the S-N diagrams for fatigue tests in bending, combined bending and torsion, and torsion, respectively. In each, several values of mean stress have been employed. It should be noted that the proportion of bending to torsion is the same for all tests shown in Fig. 2. S-N diagrams for other combinations of bending and torsion with zero mean stress are reported in another paper (1). Fatigue data in bending of notched specimens were reported by Dolan (5) for the same alloy under different mean stresses.

The curves for all diagrams have log-log co-ordinates and were drawn on separate sheets by inspection before being combined as shown. The ordinate in Fig. 2 represents only the bending component of the applied stress. The torsion component is equal to one half the bending stress for all stresses given in this figure.

It was observed that as the mean stress increased the S-N diagrams for bending and for combined bending and torsion showed a greater tendency toward an endurance limit like that of ferrous metals and some plastics. This trend was not apparent for torsion. It also appeared that there was greater scatter in the results of the torsion tests than the other states of stress.

In Fig. 1 are also plotted data reported earlier by Dolan (5) from bending tests of the same material using a specimen with a larger radius. The agreement is satisfactory.

Fatigue tests in torsion are shown in Fig. 3 for two different-type machines: the H. F. Moore torsion machine, and the combined bending and torsion machine. Initially it was planned to use the Moore machine for all torsion tests. However, the plan was changed because of the scatter of data and because it was

[1] Research Associate Professor of Theoretical and Applied Mechanics, University of Illinois.

[2] Numbers in parentheses refer to the Bibliography at the end of the paper.

Presented at the National Conference of the Applied Mechanics Division, Minneapolis, Minn., June 18–20, 1953, of The American Society of Mechanical Engineers.

Discussion of this paper should be addressed to the Secretary, ASME, 29 West 39th Street, New York, N. Y., and will be accepted until October 10, 1953, for publication at a later date. Discussion received after the closing date will be returned.

Note: Statements and opinions advanced in papers are to be understood as individual expressions of their authors and not those of the Society. Manuscript received by ASME Applied Mechanics Division, March 28, 1952. Paper No. 53—APM-12.

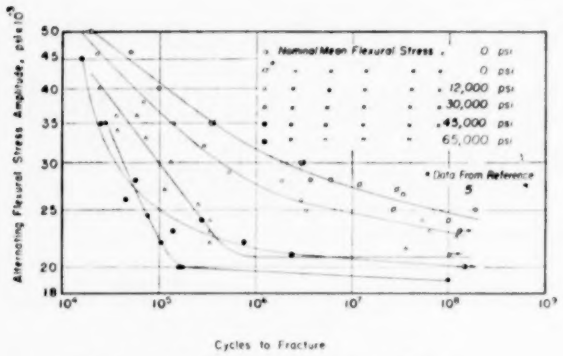

FIG. 1 S-N DIAGRAMS FOR BENDING FATIGUE

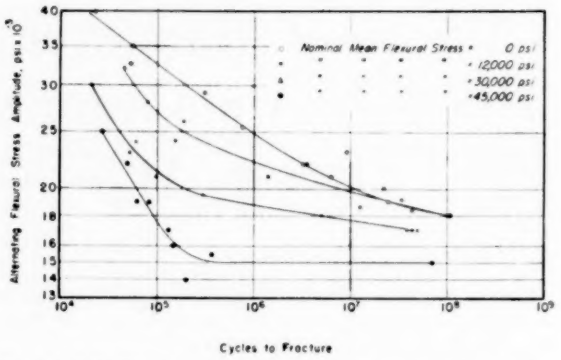

FIG. 2 S-N DIAGRAMS FOR COMBINED BENDING AND TORSION FATIGUE

(Alternating stress amplitudes and mean torsional stresses are equal to 1/2 times corresponding flexural stresses.)

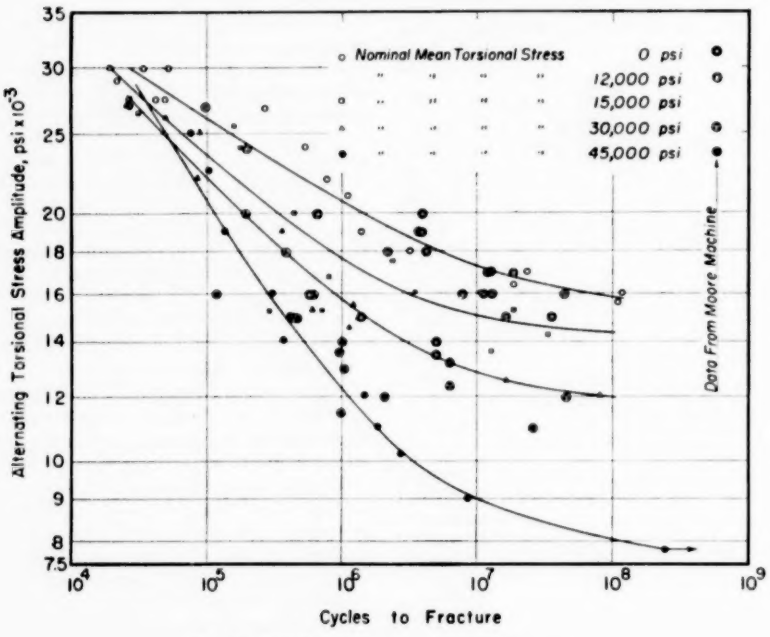

FIG. 3 S-N DIAGRAMS FOR TORSION FATIGUE

observed that unpredictable static bending stresses could not be avoided in clamping the specimen in the Moore machine. However, the results show that the amount of scatter from the two machines was comparable and the results agree fairly well. The results obtained from the Moore machine were not considered in drawing the curves in Fig. 3 nor in the analysis which follows.

During many of the tests reported in Figs. 1 to 3 the specimens were subjected to loads which caused yielding to occur in the test section of the specimen. Because of this yielding the stress distribution in the specimen changed so that the actual stresses produced were unknown. Hence the stresses plotted in Figs. 1 to 3 are the nominal values obtained by the ordinary formulas and not necessarily the actual stresses.

In order to determine more accurately the actual stresses in the specimens when yielding occurred, plasticity theory was employed as described in another section of this paper. The application of the theory required the determination of stress-strain relations for the material both on loading and unloading. Results of these static tests are described in the next section.

STATIC TESTS

Representative stress-strain curves for tension, compression, and torsion, together with a representative curve of strain versus time obtained during the compression tests, are shown in Fig. 4. The tension tests are taken from the report by Dolan (5). Several static properties measured from such curves are given in Table 1.

Because of the shortage of material for these tests, supplementary static tests were made on specimens cut lengthwise from the root section of a propeller blade forged of the same alloy. The data obtained are listed also in Table 1.

The values of stress in the torsion test from an original bar of the alloy have been corrected as described later for the nonlinear

TABLE 1 STATIC TESTS

	Elastic modulus, psi	Apparent proportional limit, psi	—Yield strength— 0.05 per cent offset, psi	0.2 per cent offset, psi	Ultimate strength, psi	True fracture stress, psi	Strain rate, in/in, min
Tension tests:							
Data as reported by Dolan (5), avg of 6 tests	9.69×10^6		64200	67200	72500		
Revised from Dolan's Fig. 8, avg of 3 tests:							
Normal stress and strain	9.66×10^6	51000	64000	67400	73100	95000	
Shearing stress and strain		25500	31500	33500	36500	47500	
Specimens from propeller blade, avg of 2 tests:							
Normal stress and strain	10.2×10^6	47000	65000	69900	75200		
Shearing stress and strain		23500	31900	34500	37600		
Compression tests:							
Specimens from original bars, avg of 2 tests:							
Normal stress and strain	10.5×10^6	60000	67800	72300	77100[a]		0.00065
Shearing stress and strain		30000	33500	35700	38500[a]		
Specimens from propeller blade, one test:							
Normal stress and strain	10.9×10^6	61000	71400	75400	83300[a]		0.0005
Shearing stress and strain		30500	35200	37300	41600[a]		
Data from average curve of tension and compression:							
Average of 4 tests:							
Normal stress and strain	10.1×10^6	54000	65500	69800			
Shearing stress and strain		27000	32300	34600			
Torsion tests, data based on shear stress and strain:							
Data as reported by Dolan (5), avg of 3 tests:							
Specimens 0.56 in. diam, nominal stress	4.06×10^6		59500		63600		
Specimen from original bars, 1 test, 0.261 in. diam:							
Nominal values of stress	3.85×10^6	31000	38800	44200	60800		0.0021
Stresses corrected for yielding		27000	32600	36000		45600	
Specimens from propeller blade, avg of 2 tests:							
Nominal stresses, specimen 0.261 in. diam	3.73×10^6	31000	35500	40100	59000		0.0024

[a] Load was still increasing; did not fracture.

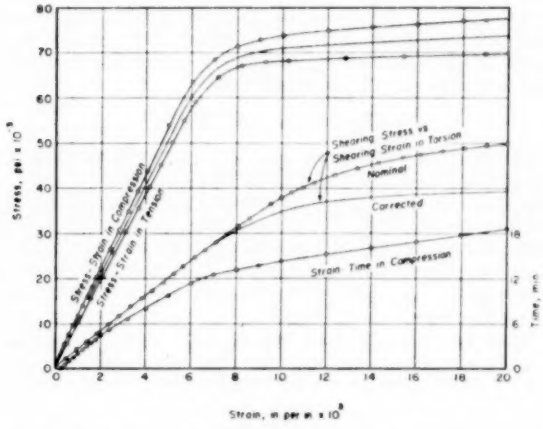

FIG. 4 STRESS-STRAIN CURVES FOR TENSION, COMPRESSION, AND TORSION

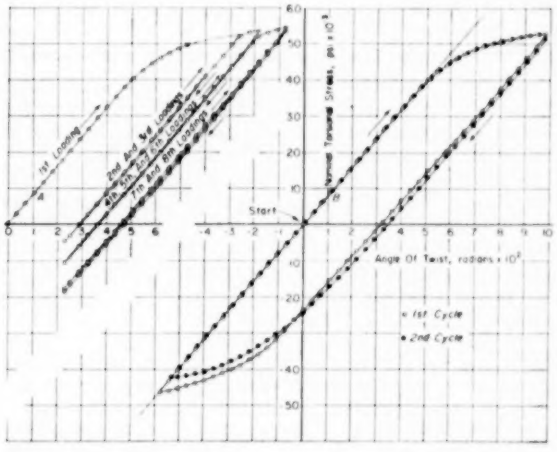

FIG. 5 LOAD-DEFLECTION TESTS OF FATIGUE SPECIMENS IN TORSION

stress distribution resulting from yielding. The corrected stress-strain diagram is also given in Fig. 4. Corrected values of yield strength and proportional limit are given in Table 1, together with a corrected value of the fracture stress in torsion. The latter was calculated on the assumption that the stress on the cross section of the test bar was constant along any diameter at the ultimate torque. This calculation yields the result that the corrected ultimate strength is equal to $^3/_4$ the nominal value regardless of the diameter.

For purposes of comparison the yield strengths in tension and compression tests have been calculated in terms of shearing stresses at the given values of offset corresponding to shearing strain; that is, for the same value of shearing strain (or offset) in both tension and torsion the normal strain in the tension test would equal the shearing strain in the torsion test divided by $1 + \mu$, where μ is Poisson's ratio. A value of Poisson's ratio of 0.3 was used. It was observed from Table 1 that the shearing stress from the tension tests was nearly equal that from the torsion tests at the proportional limit, yield strength, and fracture stress. Thus the static test data are in good agreement with the principal shear-stress theory.

Static tests beyond the proportional limit are illustrated in Fig. 5 for torsion of two specimens A and B of the same shape as the fatigue specimens. For the first loading of the virgin specimen A, deflections were applied in increments until the maximum deflection encountered in the fatigue tests was reached. Then the specimen was unloaded until a substantial negative load was reached, which was less than the corresponding minimum load in a fatigue test. Above the proportional limit a decided curvature in the diagram was observed. However, on unloading a nearly linear relation was obtained at the same slope as the initial tangent. Subsequent loading and unloading between these two deflections produced curves which followed the first unloading line rather closely but showed a small hysteresis loop.

On the fifth and sixth loadings the maximum deflection was increased somewhat. The curve showing the increase in deflection followed approximately the trend of the original plastic-flow curve. The maximum strain was increased again for the

seventh and eighth loadings with similar results. A slight Bauschinger effect was observed in the last four unloadings.

The presence of a Bauschinger effect is shown much more clearly in the test of specimen B, Fig. 5. The two complete cycles of loading and unloading illustrated were obtained by loading the specimen to the maximum deflection, unloading, applying reverse loading until the reverse-loading curve intersected the negative extension of the initial tangent line, and then removing the reverse load. The second loading duplicated the first loading almost exactly. However, the remainder of the second cycle did not repeat exactly, possibly because the maximum deflection was somewhat greater.

Since the maximum variation in shearing stress (twice the alternating stress) in the torsion-fatigue tests was 60,000 psi, it is evident from Fig. 5 that the minimum stress was never low enough for the Bauschinger effect to be significant even at the highest mean stress, where the Bauschinger effect would be most pronounced.

Since the unloading curves and subsequent reloading curves were linear as long as the unloading proceeded no farther than was required in the fatigue tests (as shown by Fig. 5, specimen A), changes in load within this linear region produce changes in stress which are elastic and can be calculated by ordinary formulas. Thus the nominal values of the alternating stresses calculated on the assumption of elastic behavior and reported in Figs. 1 to 3 are the correct values and were not influenced by yielding.

Correction of Mean Stresses for Effect of Yielding

Inasmuch as the object of this investigation was to determine the effect of the mean stress it seemed necessary to extend the range of mean stresses to as large values as possible and then to correct the nominal mean stresses for yielding.

In instances in which the maximum stress of the cycle was above the proportional limit the actual maximum stress was less than the nominal maximum stress calculated from the deflection of the specimen. Thus the mean stress also was lower by an equal amount since the mean stress was equal to the maximum stress minus the alternating stress and the latter was not influenced by yielding.

The tests at zero mean stress and at some of the small values of mean stress did not require correction. Also, no correction was attempted for yielding under combined bending and torsion. Plasticity theory and experiment have not yet been developed to a point where the problem of yielding under combined bending and torsion of a material having a curved stress-strain diagram is readily solved.

Corrections were made where needed for all tests in bending and torsion. The correction of the maximum stress (and from that the mean stresses) required a knowledge of the maximum load applied to the specimen. Since in these fatigue tests only the maximum and minimum deflection and the elastic stiffness were determined, it was necessary to prepare calibration curves of load versus deflection for the shape of specimen and test conditions employed in the fatigue tests. From these curves the maximum load in a given fatigue test was determined. Instead of correcting the mean stress of each individual specimen, the fatigue strength was measured from all S-N diagrams at 3×10^4, 10^5, 10^6, 10^7, and 10^8 cycles and the corrections and all subsequent calculations and diagrams were based on these values.

Corrections for Bending

The correction employed was a semigraphical procedure based on an extension of the Herbert equation by Morkovin and Sidebottom (21). The steps involved were as follows:

The stress-strain curve in tension was found to be nearly the same as that in compression for the range of strain employed in the fatigue tests. Hence the analysis was based on relationships applicable only when the stress-strain relation was the same in tension and compression.

From two static tension and two static compression tests an average stress-strain curve was constructed and the stress and strain at the apparent proportional limit were obtained.

From this curve a dimensionless stress-strain curve was constructed by dividing the stresses and strains by their corresponding value at the proportional limit. Since the plastic stress-strain diagram for this aluminum alloy was a curve above the proportional limit a point-by-point graphical procedure described by Sidebottom (22) was employed to construct a dimensionless moment-strain diagram.

The corrected maximum stress for any specimen could then be obtained by determining the dimensionless bending moment for the specimen and locating the corresponding value of the dimensionless strain from the moment-strain curve. The dimensionless stress corresponding to the maximum stress was then found from the dimensionless stress-strain curve at the same value of dimensionless strain. From the dimensionless stress the maximum stress and mean stress were calculated.

It should be noted that this correction is probably not exact because of several simplifications from actual material behavior among which are the following: The yielding probably was not homogeneous or continuous and the specimen shape confined yielding to a small region which may have further complicated the geometry of plastic straining; and the rate of straining in the static tests was much slower than the rate of straining during the first load application in the fatigue tests.

Correction for Torsion

The graphical technique employed was that outlined by Nadai (23) for determining the shearing stress at the surface of a specimen of circular cross section having a nonlinear stress-strain relation and subjected to a torque. This technique required a curve of torque versus angle of twist for a cylindrical specimen of circular cross section. The graphical procedure was applied to this curve to determine the corrected shearing stress at the extreme fiber caused by the torque.

From the results of these calculations a corrected shearing-stress versus shearing-strain curve was constructed as shown in Fig. 4, and a curve of nominal shearing stress versus corrected shearing stress was constructed. By means of the latter curve the corrected maximum stress was determined and from this the mean stress was calculated. It should be observed that the same limitations apply to this correction procedure as apply to the bending procedure.

Theories of Fatigue Failure Under Combined Stress

On the basis of the results and the analysis reported in another paper (1) for the tests at several combinations of bending and twisting for zero mean stress, several of the more promising theories were selected for a complete study at all values of mean stress. The theories selected were principal shear stress corrected for anisotropy (24), complete Guest's law, magnitude of state of stress vector, and total energy of deformation. As reported by Gough (20) and discussed by the author (24) the ellipse-arc "theory" is related to the complete Guest law and in a way which makes the ellipse arc too general. Hence in the complete analysis the ellipse arc was not considered. Similarly, the ellipse-quadrant "theory" was not considered since, as described in a discussion (24), the ellipse quadrant is indentical to a squared form of the equation for the greatest principal shear stress when corrected for anisotropy.

The principal shear-stress theory corrected for anisotropy really represents six different theories as explained later. The correc-

tion for anisotropy proposed earlier (24) is based on the idea that rolled bars may have internal "shape" characteristics caused by slag or other inclusions, and so on, which may produce an effect similar to the anisotropic stress concentration of a straight groove on the surface of a flat plate of isotropic material. The groove would raise the local stress above the nominal stress for stresses normal or at an angle to the direction of the groove but not for stresses parallel to it.

Thus in specimens cut lengthwise from bar stock and tested so that the plane of bending and axis of twisting are always parallel to the lengthwise direction of the stock, one may expect that anisotropy of the material will raise (or lower) the nominal stress computed from the twisting moment more than (or less than) the stress computed from the bending moment; the resulting bending or twisting stresses caused by anisotropy will be linear functions of the nominal bending or twisting stresses, respectively; and the resulting bending and twisting stresses will be the same functions of the nominal stresses regardless of the combination of bending and twisting employed.

Under these conditions all the rational theories of inelastic action can be re-examined by multiplying the nominal twisting stress τ by a correction constant for each material of such magnitude that the resulting equation agrees with the test data for pure bending and pure twisting. A correction constant could just as well be applied to the bending stress instead of the twisting stress or to both; the result would be the same.

For example, the theory of a limiting principal shearing stress τ_1 may be written for combined bending and torsion as follows

$$\tfrac{1}{2}\sqrt{\sigma^2 + 4\tau^2} = \text{a const, such as } \tau \quad [2]$$

where σ and τ are the applied bending and torsion (shear) stress, respectively. This equation requires that the ratio of the fatigue strength in bending b to that in torsion t must equal 2. Therefore, in accordance with the foregoing suggestions one can correct for anisotropy by multiplying every value of τ introduced in Equation [2] by $b_1/2t_1$ where b_1 and t_1 are the measured values of the fatigue strength in bending and in torsion, respectively. The number of cycles for which b_1 and t_1 are determined is the same as the number which is expected to produce failure under the given values of σ and τ. If the adjusted value

$$\tau_1 = \frac{b_1\tau}{2t_1}$$

is substituted in Equation [2] the following results

$$\tfrac{1}{2}\sqrt{\sigma^2 + \left(\frac{b_1}{t_1}\right)^2 \tau^2} = \tau_1 \quad [3]$$

In a similar way this correction may be applied to the other rational theories of failure. The resulting equations are given in reference (1). It is significant to note that the equations for six of these theories, when rationalized, are identical and the same as the empirical ellipse-quadrant equation proposed by Gough. The six theories are: (*a*) Principal shear stress, (*b*) principal shear strain, (*c*) energy of distortion, (*d*) octahedral shear stress, (*e*) total energy of deformation, and (*f*) magnitude of state-of-stress vector.

By the theory of a limiting magnitude of the state-of-stress vector it is suggested that fatigue failure may be expected when a limiting value of the vector sum of the three principal stress vectors is reached. The vector representing this sum is called the state-of-stress vector since it uniquely describes the given combination of principal stresses. No physical significance is attached to this theory.

Effect of Mean Stress

The following quantities were computed from the alternating stresses corresponding to the fatigue strength and from the mean stresses (corrected for yielding whenever possible) at each value of fatigue strength considered:

Principal shear stress corrected for anisotropy

$$\tau_1 = \tfrac{1}{2}\sqrt{\sigma^2 + \left(\frac{b_1}{t_1}\right)^2 \tau^2} \quad [3]$$

Complete Guest's law

$$t = \tfrac{1}{2}\left[\sqrt{\sigma^2 + 4\tau^2} + \left(\frac{2t_1}{b_1} - 1\right)\sigma\right] \quad [4]$$

Magnitude of state-of-stress vector

$$S = \sqrt{\sigma^2 + 2\tau^2} \quad [5]$$

Total energy of deformation

$$W = \frac{1}{2E}\left[\sigma^2 + 2(1 + \mu)\,\tau^2\right] \quad [6]$$

where the symbols are the same as described before. Values of 9.69×10^6 psi for the elastic modulus and 0.3 for Poisson's ratio were employed in these calculations as described previously (1). Poisson's ratio during yielding probably has a higher value as shown by Stang, Greenspan, and Newman (25). However, on unloading and reloading after yielding it seems probable that Poisson's ratio would be similar to that of virgin material.

The value of each of the four theories (i.e., the right-hand side of Equations [3] to [6]) based on the alternating stresses was plotted as a function of the corresponding value of the same theories based on the mean stresses. The resulting curves were similar to Figs. 6 to 8, for the first three theories but not for the fourth (strain energy). One of the diagrams for the total strain-energy theory is shown in Fig. 9. The magnitude of the correction for yielding and its effect on the amplitude-of-stress versus mean stress diagram is also illustrated in Figs. 6 and 8 in which both corrected and uncorrected values are plotted. In addition to the data obtained under dynamic conditions, the value of each theory computed from the yield strength at 0.05 per cent offset was represented by a diagonal line in the diagrams for bending fatigue and torsion fatigue.

The values of b_1 and t_1 used in correcting for anisotropy and in calculating Guest's law were the same for all mean values at a given number of cycles and equal to the bending and twisting fatigue strengths, respectively, at zero mean stress and the given number of cycles. There is no reason to think that the values of b_1 and t_1 are any more accurate than the fatigue strength at any other combination of bending and twisting. Thus a certain latitude commensurate with the scatter of the data might be allowed in the value of b_1/t_1 used in correcting for anisotropy if indicated by the trend of data for combined bending and torsion.

The following observations were made from these alternating versus mean diagrams:

1 For all four theories, at any of the number-of-cycles-to-failure considered, the value of the theory based on the alternating stress decreased with increase in the value of the theory based on the mean stress.

2 In bending and in combined bending and torsion the effect which an increase in the value of the theory, based on the mean stress, had on the value of the theory, based on the alternating stress, was less at large numbers of cycles to failure than small numbers of cycles to failure. This suggests that the material may

have an endurance limit which for some states of stress and for high mean stresses may be reached at about 10^6 cycles, but for lower mean stresses may not be reached until perhaps 10^{12} cycles (see also Figs. 1 and 2).

3 There is poor agreement between the test data and common empirical formulas such as the modified Goodman or Soderberg linear equations or the Gerber parabola, although the latter is the best representation. This is true whether the ordinary stresses or the quantities corresponding to the theories are plotted. The slopes of the curves for the first three theories were not steep enough, the curves for torsion did not converge with increasing mean stress, and the lower four curves for bending curved in the wrong sense for the Gerber parabola. These empirical formulas are not shown in the figures in order to avoid confusing them.

4 In all except the energy theory there was only a slight decrease in fatigue strength with increasing mean stress for maximum stresses below the proportional limit. As the maximum stresses began to cause yielding the fatigue strength decreased more rapidly in the torsion tests and in the bending tests at high alternating stresses than in tests at other combinations of stresses. This may be the effect on the fatigue strength of changes in microstructure resulting first from a nominally elastic static stress and next from the plastic deformation at yielding.

5 Examination of these curves revealed poor correlation between (*a*) the values of maximum stress beyond which the fatigue strength decreased markedly and (*b*) the yield strength from static tests. A marked decrease in fatigue strength was apparent in the torsion tests. For bending, however, the fatigue strengths at 3×10^4 cycles suggested only that a marked decrease in fatigue strength may be impending at higher values of maximum stress. Little could be said about the combined bending and torsion tests, since corrections for yielding were not made. The indications were that no marked decrease occurred within the range of the tests under combined bending and torsion.

An excellent correlation was observed between the yield strengths at 0.05 per cent offset from static tests and static yielding predicted by the principal shear theory. The yield strengths based on shearing stress and shearing strain were nearly identical for tension, compression, and torsion tests when the stresses in the torsion tests were corrected for the stress distribution resulting from yielding, Table 1. This suggests that the original material may have been nearly isotropic in so far as general yielding is concerned and that the material may have been anisotropic only at the level of the localized action which initiated fatigue failure.

If this was the case then the correction for anisotropy should have been applied only to the alternating components of the stress. Curves which were prepared in this way are shown in Figs. 6 to 8. It was observed that the correlation between (*a*) the values of maximum stress beyond which the fatigue strength decreased markedly and (*b*) the static yield strength was satisfactory in Figs. 6 and 8; that is, the apparent effect of yielding on the fatigue strength resulting from a high mean stress was in much better agreement with static yielding when the correction for anisotropy was applied only to the alternating component.

The same reasoning when applied to the Guest theory had a similar result although the agreement was not as favorable.

Strain Energy and Mean Stress

A difficulty arises in trying to apply any energy theory to the problem of fatigue failure when the mean stress is not zero. The variation of strain energy with time when calculated from stresses must be based on the variation of the total stress—not components such as alternating and mean stress. Residual stresses also must be added to the applied stresses before calculating the energy. If this is not done, large errors in energy will result since stresses are squared in computing the strain energy. Thus diagrams such as Fig. 9 in which the alternating and mean energies are computed directly from the alternating and mean stresses, respectively, do not present the correct relation between the components of energy. For example, the mean value, W_{mean}, of a cycle of total-energy-of-deformation computed for pure bending is

$$W_{mean} = \frac{1}{4E}\left[(\sigma_m + \sigma_a)^2 - (\sigma_m - \sigma_a)^2\right] = \frac{\sigma_m \sigma_a}{E} \quad \ldots [7]$$

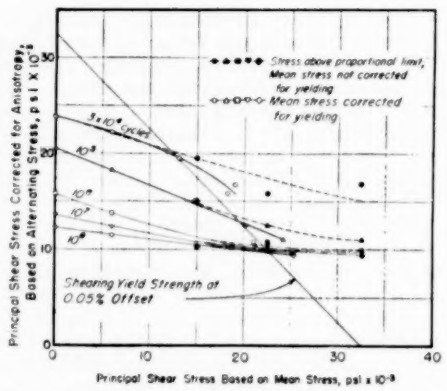
Stress above proportional limit, Mean stress not corrected for yielding
Mean stress corrected for yielding
3x10⁴ Cycles
10⁵
10⁶
10⁷
10⁸
Shearing Yield Strength at 0.05% Offset
Principal Shear Stress Corrected for Anisotropy, Based on Alternating Stress, psi x 10⁻³
Principal Shear Stress Based on Mean Stress, psi x 10⁻³

Fig. 6 Alternating Versus Mean Stress for Bending Fatigue

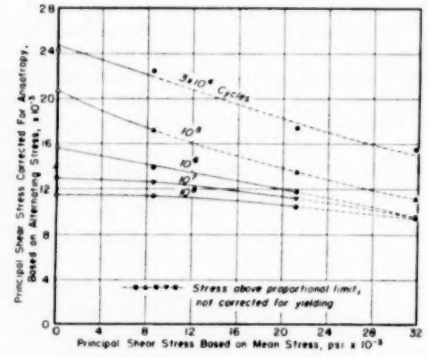
3x10⁴ Cycles
10⁵
10⁶
10⁷
10⁸
Stress above proportional limit, not corrected for yielding
Principal Shear Stress Corrected For Anisotropy, Based on Alternating Stress, x10⁻³
Principal Shear Stress Based on Mean Stress, psi x 10⁻³

Fig. 7 Alternating Versus Mean Stress for Combined Bending and Torsion
(Torsional stresses equal ½ flexural stresses.)

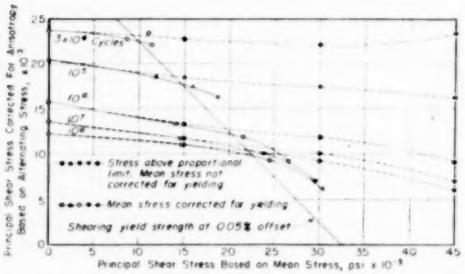
3x10⁴ Cycles
10⁵
10⁶
10⁷
10⁸
Stress above proportional limit, Mean stress not corrected for yielding
Mean stress corrected for yielding
Shearing yield strength at 0.05% offset
Principal Shear Stress Corrected For Anisotropy, Based on Alternating Stress, x10⁻³
Principal Shear Stress Based on Mean Stress, psi x 10⁻³

Fig. 8 Alternating Versus Mean Stress for Torsion

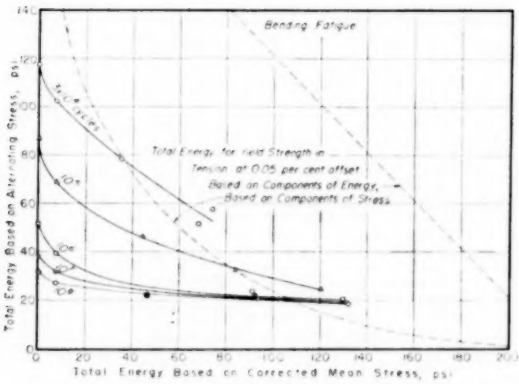
Bending Fatigue
Total Energy, for Yield Strength in Tension at 0.05 per cent offset
Based on Components of Energy
Based on Components of Stress
Total Energy Based on Alternating Stress, psi
Total Energy Based on Corrected Mean Stress, psi

FIG. 9 TOTAL ENERGY BASED ON ALTERNATING STRESS VERSUS TOTAL ENERGY BASED ON MEAN STRESS

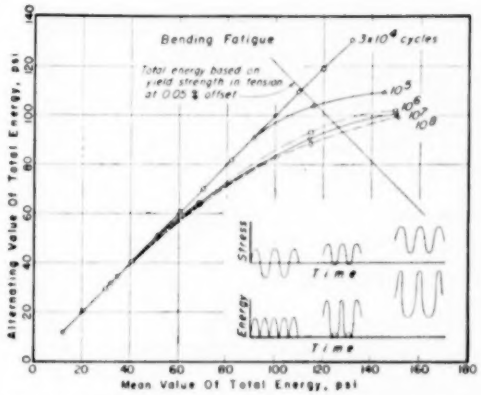

FIG. 10 ALTERNATING VERSUS MEAN TOTAL ENERGY BASED ON ACTUAL FLUCTUATION IN ENERGY CYCLE

not

$$W_{mean} = \frac{\sigma_m^2}{2E} \quad [8]$$

An attempt to make a more accurate presentation of the energy relation discloses the following difficulties:

1 When the minimum stress of the cycle is of the same sign as the maximum stress the only difficulty is that the energy cycle is not sinusoidal as the stress cycle was. The maximum energy is calculated from the maximum stress and the minimum energy from the minimum stress. The alternating and mean energies are calculated as one half the difference and one half the sum of these maxima and minima (see Equation [7]).

2 Since energy is a scalar and always positive, a completely reversed sinusoidal cycle of stress will produce not a completely reversed cycle of strain energy but a cycle of energy varying from zero (at zero stress) to a maximum (at both maximum or minimum stress) which is not sinusoidal and has a frequency twice the frequency of the stress cycle (see inset in Fig. 10). Thus the total number of energy cycles sustained before fracture is twice the total number of stress cycles sustained. These facts have not been discussed (in so far as is known) in previous studies of energy theories of failure applied to fatigue.

3 When the stress during the cycle is partly of one sign but mostly of the opposite sign, the energy cycle consists of two alternate pulses of the same sign but different magnitude. The frequency of the largest pulse is the same as that of the stress cycle (see inset in Fig. 10).

When the foregoing factors are taken into account, a new diagram representing the actual alternating energy versus actual mean energy may be constructed as shown in Fig. 10. This is accomplished by computing the alternating and mean energies as described in item 1 of the preceding paragraph, by accounting for the change in frequency noted in item 2, and by neglecting the smallest pulse described in item 3. A zero value of mean energy is not possible. Fig. 10 shows that the alternating energy for fatigue failure increases equally with increase in mean energy until the minimum energy of the cycle becomes greater than zero. This behavior does not seem reasonable as a theory of fatigue failure under combined stress. The stress and corresponding energy cycles are also illustrated in Fig. 10 for typical values of mean stress. While the relations shown in Fig. 10 are for total energy, similar relations would obtain for distortion energy.

Another possible way of handling the strain-energy relationship that avoids the difficulties just enumerated is to give energy an arbitrary sign the same as the sign of the corresponding stress. If this is done the alternating energy decreases, then increases markedly with increase in mean stress.

The least unreasonable of these methods of handling energy is that shown in Fig. 9. However, the most reasonable explanation for this interpretation seems to require that fatigue failure is associated with the dynamic (fluctuating) strain energy independent of the mean strain energy; and that the mean energy, whether from externally applied mean stress, macro- or micro-residual stresses, merely acts in a manner similar to a change in the internal structure of the alloy. Such a change in structure may or may not affect the fatigue strength of the alloy greatly. Of course it may be that the change in structure is caused by some other factor than mean energy such as mean shearing stress while the alternating energy controls the initiation of fatigue fracture.

The foregoing explanation of the relation between strain energy (either total or distortional) and fatigue failure at different values of mean stress would seem rather plausible if it were not for the other difficulties with an energy theory which are discussed in another paper (26).

STATE-OF-STRESS AT DIFFERENT MEAN STRESSES

From ordinates at four values of mean stress (or mean energy, and so on) in diagrams such as Figs. 6 to 9 and the data at other states of stress for zero mean stress, diagrams showing the effect of state of stress were constructed such as shown in Fig. 11 for the theory of a limiting value of principal shear stress (with a correction for anisotropy applied to the alternating stress).

For each value of the theory based on the mean stress the value of the theory based on the alternating stress was plotted as a function of the state of stress for each of the theories, as illustrated in Fig. 11, for the principal shear-stress theory with a correction for anisotropy applied to the alternating stress. The measure used for the state of stress was the least direction cosine n, of the state-of-stress vector S.

$$n = \sigma_3/S \quad [9]$$

where the state-of-stress vector is the vector sum of the three principal stresses and σ_3 is the smallest principal stress. For the range of states-of-stress employed in this investigation only one direction cosine was necessary to identify the state-of-stress since all the state-of-stress vectors lay in one plane. The direction cosine n was chosen because it spaced the test values of state-of-stress more evenly than the first direction cosine.

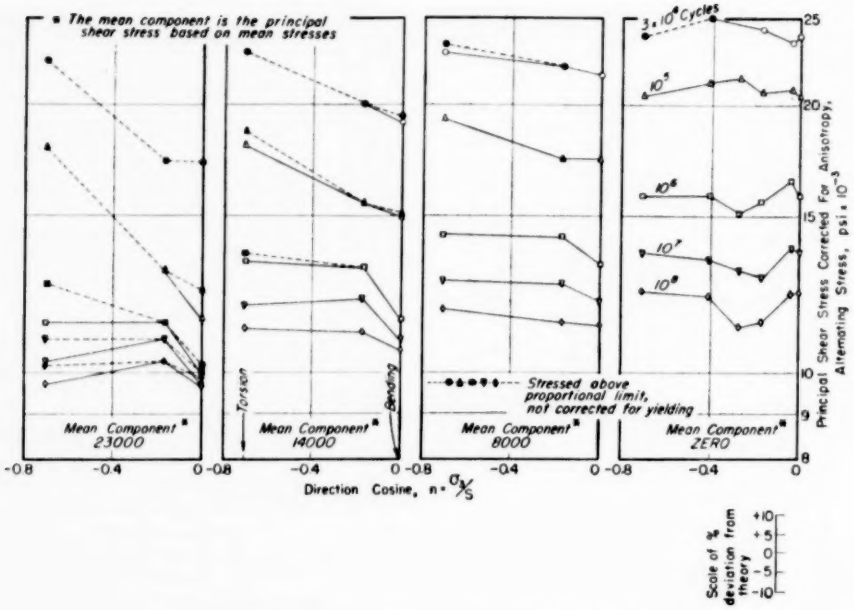

FIG. 11 PRINCIPAL SHEAR STRESS VERSUS STATE OF STRESS
(Alternating stress corrected for anisotropy.)

On the type of diagram shown in Fig. 11 exact agreement with the theory would be represented by straight horizontal lines. A logarithmic ordinate was used in all of these diagrams because the per cent change in a quantity is represented by the same linear distance on a logarithmic scale regardless of the magnitude of the quantity. Thus logarithmic diagrams permit direct comparison (between the various curves) of the relative deviation of the test values from the theory. A scale is inset in Fig. 11 by which the per cent deviation from the theory may be measured. An examination of these diagrams indicated the following order of merit (as indicated by the present data) for the theories considered:

1 Principal shear stress corrected for anisotropy.
2 Complete Guest's law.
3 Magnitude of state-of-stress vector.
4 Total strain energy.

The first of the theories represented the test data the closest. There was, however, not much choice between the first two theories.

It should be recalled that the alternating values in Fig. 11 are the same, except for a constant factor, for six theories when corrected for anisotropy—not just the shear-stress theory. The shape of the diagrams for mean stresses above zero are, however, dependent on the particular theory chosen since the mean component does not contain a correction for anisotropy.

The effect of the correction for yielding is indicated in Fig. 11 by showing the ordinates of both the corrected and uncorrected curves of alternating versus mean stress.

ALTERNATING STRESS VERSUS MAXIMUM STRESS

If, as seems to be the case, general yielding affects the fatigue strength then perhaps it should be questioned whether the fatigue strength should be expressed in terms of the mean stress. Perhaps the maximum stress would be a more logical parameter. The alternating principal shear stress as corrected for anisotropy has been plotted as a function of the maximum value (occurring in a cycle of stress) of the principal shearing stress (corrected for yielding). This is shown in Fig. 12 for bending and in Fig. 13 for torsion. The limit of proportionality, yield strength, ultimate strength, and fracture stress are also shown in Figs. 12 and 13.

It is evident that the region of the alternating stress versus maximum stress diagrams above the diagonal line is unavailable for testing—especially in torsion. In bending or at least for axial loading this region would be available if the material had a much higher yield strength in compression than in tension. Since this is not the case for ductile metals we can only speculate on the shape of curves in this region. Points on the vertical axis would represent the fatigue strength of virgin material unaffected by stresses which might cause yielding or other alterations of the material.

The reason for the difference in shape and slope of these curves for bending and for torsion may be found in the mode of fracturing in fatigue as discussed in another paper (27) in the light of the observed fractures of this alloy. In the torsion tests it was observed that the fatigue cracks propagated mostly by repeated slip under cyclic shearing stress (or shearing strain) and the major effect of an increase in the maximum stress was to produce a change in the structure of the material, especially when the maximum stress produced yielding.

In bending, however, there was the additional factor of tension stresses on the slip planes which tended to change the mechanism of crack propagation and perhaps to accelerate it. It was shown (27) that the initiation of fatigue cracks always resulted from alternating shear stress but that for bending, the mechanism of crack propagation changed quickly from a shear crack to a tensile fracture which was dependent on the maximum principal stress. Since the magnitude of the maximum (tension) principal stress increased with the maximum stress of the cycle whereas the alternating shear stress was independent of the maximum stress, the rate of crack propagation may have been greater at

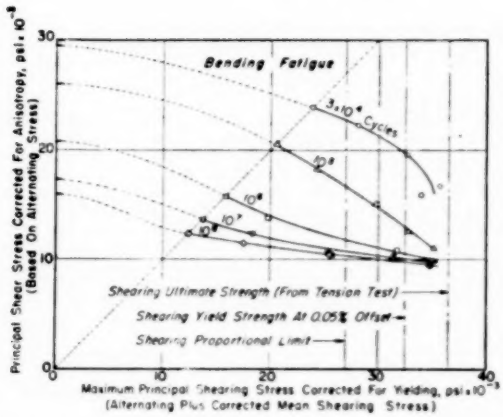
Bending Fatigue
3×10⁴ Cycles
10⁵
10⁶
10⁷
10⁸
Shearing Ultimate Strength (From Tension Test)
Shearing Yield Strength At 0.05% Offset
Shearing Proportional Limit
Principal Shear Stress Corrected For Anisotropy, psi × 10⁻³ (Based On Alternating Stress)
Maximum Principal Shearing Stress Corrected For Yielding, psi × 10⁻³ (Alternating Plus Corrected Mean Shearing Stress)

FIG. 12 ALTERNATING SHEAR STRESS VERSUS MAXIMUM SHEAR STRESS

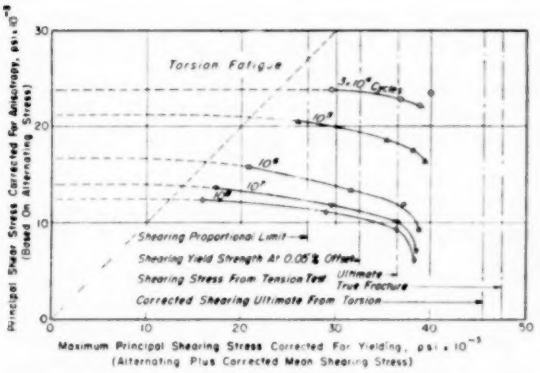
Torsion Fatigue
3×10⁴ Cycles
10⁵
10⁶
10⁷
Shearing Proportional Limit
Shearing Yield Strength At 0.05% Offset
Shearing Stress From Tension Test Ultimate
True Fracture
Corrected Shearing Ultimate From Torsion
Principal Shear Stress Corrected For Anisotropy, psi × 10⁻³ (Based On Alternating Stress)
Maximum Principal Shearing Stress Corrected For Yielding, psi × 10⁻³ (Alternating Plus Corrected Mean Shearing Stress)

FIG. 13 ALTERNATING SHEAR STRESS VERSUS MAXIMUM SHEAR STRESS

higher maximum stresses for bending tests. Thus it seems entirely possible that both anisotropy and the factors controlling crack propagation may influence the results of fatigue tests.

The curves in the unavailable region may be as shown by the dash lines in Figs. 12 and 13. These considerations might account at least in part for the divergence observed between the test data and the uncorrected principal shear-stress theory. The values of the alternating stress at zero mean stress (uncorrected) obtained from the torsion tests are shown plotted on the curve for bending tests Fig. 12, as short dash lines on the vertical axis. This corresponds to an assumption that the principal shear theory governs fatigue under these conditions and that the maximum stress has no effect on the fatigue strength within the unavailable region of the torsion diagram, Fig. 13. It was observed that the values from the torsion tests were consistent with a possible shape of the dashed curves for the bending tests as shown in Fig. 12.

While the maximum stress seems to be the most logical parameter from a theoretical standpoint, it is probable that from a design standpoint the mean stress is the more useful in describing the range of stress because of the unavailable region in the alternating stress versus maximum stress diagram.

CONCLUSIONS

1 An increase in the mean stress of the stress cycle caused a decrease in the fatigue strength for all states of combined stress studied.

2 In bending and in combined bending and torsion the effect of the mean stress on the fatigue strength decreased as the number of cycles to fracture decreased.

3 As the maximum stress began to cause yielding the fatigue strength decreased more rapidly in the torsion tests and in the bending tests at high alternating stresses than in tests at other combinations of stress.

4 There was poor agreement between the test data and common empirical formulas for the effect of range of stress.

5 A correction for possible anisotropy of the material appeared to be applicable to the alternating stresses but not to the mean stresses.

6 There are several observations concerning the effect of range of stress which make energy theories of fatigue failure of doubtful validity.

7 When the data of all states of combined stress, all values of mean stress, and all cycles to failure were considered the theories of fatigue failure were found to have the following order of merit (where the first theory represented the test data the closest):

(*a*) Principal shear stress corrected for anisotropy.
(*b*) Guest's law (complete).
(*c*) Magnitude of state-of-stress vector.
(*d*) Total strain energy.

8 The analysis presented suggests that the effect of the mean stress on the fatigue strength results from two phenomena distinct from the fatigue process: (*a*) The maximum stress may produce elastic or plastic structural changes in the material which affect its fatigue strength, (*b*) one mode of crack propagation (by repeated slip) is apparently dependent on the alternating principal shear stress and the magnitude and sign of the normal stress on the plane of the principal shear stress. The other mode of crack propagation (propagation by tension separation) is a function of the maximum (alternating plus mean) principal stress. Cracks which propagate by tension separation propagate more rapidly under high mean (i.e., maximum) stresses.

ACKNOWLEDGMENT

The project was conducted in the Department of Theoretical and Applied Mechanics of the University of Illinois. The author is grateful to the following agencies for financial support of portions of the project: The University of Illinois Engineering Experiment Station, Hamilton Standard Division of United Aircraft Corporation, and The National Advisory Committee for Aeronautics.

The following, to whom the author is greatly indebted, performed various phases of the project: Testing—S. Yurenka, W. J. Worley, O. M. Sidebottom, W. I. Mitchell; analysis—F. Mergen, M. Peterson, B. A. Century, A. H. Rosenberg, D. D. Strohbeck; drafting—C. K. Liu, J. H. Dabbert, and H. W. Peithman.

It is also a pleasure to acknowledge the helpful suggestions of the author's colleagues.

BIBLIOGRAPHY

1 "Fatigue of 76S-T61 Aluminum Alloy Under Combined Bending and Torsion," by W. N. Findley, Proceedings of the ASTM, vol. 52, 1952, pp. 818–836.
"Combined-Stress Fatigue Strength of 76S-T61 Aluminum Alloy With Superimposed Mean Stresses and Corrections for Yielding," by W. N. Findley, NACA Tech. Note 2924, May, 1953.

2 "The Effect of Range of Stress on the Fatigue Strength of Metals," by J. O. Smith, University of Illinois Engineering Experiment Station, Bulletin No. 334, Urbana, Ill., February, 1942.

3 Discussion of "Nomenclature on Range in Stress in Fatigue,"

by R. E. Peterson, Proceedings of the ASTM, vol. 37, part 1, 1937, p. 162.

4 "Fatigue Strength of Simple Metallic Structural Members," by F. Bollenrath and H. Cornelius, *Zeitschrift Verein deutscher Ingenieure*, vol. 84, 1940, p. 407.

5 "Effects of Range of Stress and of Special Notches on Fatigue Properties of Aluminum Alloys Suitable for Airplane Propellers," by T. J. Dolan, NACA TN, No. 852, 1942.

6 "Mechanical Tests of Macerated Phenolic Molding Material," by W. N. Findley, NACA Wartime Report W-99, June, 1943.

7 "Certain Mechanical Strength Properties of Aluminum Alloys, 25S-T and X76S-T," by T. J. Dolan, National Advisory Committee for Aeronautics, Technical Note No. 914, October, 1943.

8 "Axial Fatigue Tests at Zero Mean Stress of 24ST Aluminum Alloy Sheet With and Without a Circular Hole," by W. C. Brueggeman, M. Mayer, Jr., and W. H. Smith, NACA TN 955, 1944.

9 "The Application of Data on Strength Under Repeated Stresses to the Design of Aircraft," by L. R. Jackson and H. J. Grover, NACA, ARR, No. 5H27, 1945.

10 "Fatigue Tests of a Laminated Mitscherlich-Paper Plastic," by W. N. Findley, Proceedings of the ASTM, vol. 45, 1945, pp. 878–903.

11 "Fatigue Strengths and Related Characteristics of Aircraft Joints–II Fatigue Characteristics of Sheet and Riveted Joints of 0.040 Inch 24ST, 75ST, and R303-T 275 Aluminum Alloys," by H. W. Russell, L. R. Jackson, H. J. Grover, and W. W. Beaver, NACA TN 1485, February, 1948.

12 "Fatigue Strengths of Aircraft Materials—Axial-Load Fatigue Tests on Unnotched Sheet Specimens of 24S-T3 and 75S-T6 Aluminum Alloys and of SAE 4130 Steel," by H. J. Grover, S. M. Bishop, and L. R. Jackson, NACA TN 2324, 1951.

13 "Effect of Steady Stress on Fatigue Behavior of Aluminum," by J. A. Sauer and D. C. Lemon, Trans. ASM, vol. 42, 1950, pp. 559–576.

14 "Correlation of Data on the Effect of Range of Stress on the Fatigue Strength of Metals for Tensile Mean Stresses," by R. T. Schwartz, Master's thesis, Ohio State University, 1948.

15 "The Fatigue of Metals," by H. F. Moore and J. B. Kommers, McGraw-Hill Book Company, Inc., New York, N. Y., 1927.

16 "Relation Between the Superior and the Inferior Stresses of a Cycle of Limiting Stress," by W. Gerber, *Zeit. Bayerischen Archie Ingenieur-Vereines*, 1874 (see also reference 15).

17 "Factors of Safety and Working Stresses," by C. R. Soderberg, Trans. ASME, vol. 52, 1930, p. 13; "Working Stresses," Trans. ASME, vol. 55, 1933, p. 131; and "Working Stresses," Trans. ASME, vol. 57, 1935, p. A-106.

18 "A Suggested New Parameter for Fatigue Strength Analysis," by Victor Seliger, ASTM Bulletin, January, 1945, p. 29.

19 "Fatigue Testing of Duralumin Under Combined Bending and Torsion," by T. Nisihara and M. Kawamoto, Trans. Institute of Metals, Japan, vol. 5, 1941, pp. 110–115. Abstract, *Journal of the Institute of Metals*, Metallurgical Abstracts, vol. 8, 1941, pp. 238-239.

20 "Engineering Steels Under Combined Cyclic and Static Stresses," by H. J. Gough, *The Engineer*, London, I, October 28, 1949, pp. 497–500; II, November 4, 1949, pp. 510–514; III, November 11, 1949, pp. 540–543; IV, November 18, 1949, pp. 570–573; see also Proceedings of the Institution of Mechanical Engineers, vol. 160, no. 4, pp. 417–440, and Trans. ASME, vol. 72, 1950, pp. 113–125.

21 "The Effect of Non-Uniform Distribution of Stress on the Yield Strength of Steel," by D. Morkovin and O. Sidebottom, University of Illinois Engineering Experiment Station, Bulletin No. 372, December, 1947.

22 "Determination of Residual Stresses in an Inelastically Strained Beam," by O. M. Sidebottom, unpublished work, University of Illinois, 1948.

23 "Theory of Flow and Fracture of Solids," by A. Nadai, Engineering Societies Monographs, McGraw-Hill Book Company, Inc., New York, N. Y., vol. 1, second edition, 1950, p. 349.

24 Discussion by W. N. Findley, of "Engineering Steels Under Combined Cyclic and Static Stresses," by H. J. Gough, JOURNAL OF APPLIED MECHANICS, Trans. ASME, vol. 73, 1951, p. 211.

25 "Poisson's Ratio of Some Structural Alloys for Large Strains," by A. H. Stang, Martin Greenspan, and S. B. Newman, *Journal of Research National Bureau of Standards*, vol. 37, October, 1946, p. 211.

26 "Critical Review of Combined Loading in Fatigue," by W. N Findley (in preparation).

27 "Fatigue Fractures Under Combined Stress and a Qualitative Theory of Fatigue Fracturing" (in preparation), by W. N. Findley

Calculation of Elastic Displacements From Photoelastic Curves

By H. PORITSKY[1] and R. P. JERRARD,[2] SCHENECTADY, N. Y.

A method of utilizing photoelastic fringe patterns for purposes of calculating elastic displacements of stressed members is developed. This method utilizes only the lines of constant principal stress difference and does not require knowledge of the directions of the principal stresses. The method developed should prove useful in many cases where measurements of elastic displacements cannot be carried out conveniently but photoelastic fringe patterns are readily available. As an example, the two-dimensional case of a beam in bending with a change in thickness is treated. The correction that must be applied to simple beam theory is determined.

1 Introduction

THERE are many occasions where the exact analysis of the performance and behavior of a machine member or a structure requires accurate knowledge of elastic displacements.

As an example, consider the action of a mating gear and a pinion under load. The geometrical theory by means of which the shapes of the mating teeth are designed is based upon the assumptions that the teeth are infinitely rigid and do not yield under load. Thus involute tooth shapes will produce perfect mating between a pinion and a gear; that is, will transform a uniform rotation about the axis of the one into a uniform rotation about the axis of the other, provided the teeth are rigid. Actually, under load the teeth will bend, and also compress at the contact area. These displacements will disturb the relative angular motions of the pinion and the gear by an amount which will vary as contact proceeds along the teeth. Further changes in the relative angular motions are caused by the number of teeth in the arc of action. The resulting nonuniform rotation ratio is one of the factors leading to higher dynamical stresses in gears and may limit their load-carrying ability.

One further example where knowledge of the elastic displacements would be useful will be mentioned, namely, in bending of a plate (or beam) with a sudden change of thickness. The bending of such plates is generally computed by ignoring the actual stress distribution at the site of the thickness change, and merely assuming a uniform curvature to each side of it. More exact information regarding the bending is useful in the calculation, say, by Rayleigh's method, of frequencies of bending vibration of disks with sudden changes of thickness. The stress pattern, it will be recalled, is the same for both plane stress and plane strain. For this reason the example to be given is applicable to a plate or a thin beam in bending. A slight difference occurs in the calculation of the displacements.

The direct measurement of the very small displacements and the deformation of contacting gear teeth, while it can be carried out by properly refined techniques, is a difficult procedure. A method of computing these displacements purely from photoelastic patterns which are available and are often relatively easy to obtain in other cases, could be useful. The following is concerned with such a method.

Denoting the sum of the principal stresses by

$$p + q \qquad [1]$$

the method utilizes the $(p + q)$-curves, or isopachics, and the curves orthogonal to them. The basic expressions for the displacements in terms of these functions are given in Section 2. There are several experimental ways of obtaining the function $(p + q)$ by means of interference fringes or by direct measurements.[3] In addition, the required functions can be obtained by various classical methods from the "boundary values" of $(p - q)$ which are available from photoelastic stress patterns. The authors have started with $(p - q)$-patterns (which are widely available), and have used a free-hand drawing method known as "flux plotting." While this procedure is rapid and convenient the authors wish to emphasize that the calculation of the displacements in no way depends upon the method of obtaining the $(p + q)$-curves and their orthogonal curves.

2 Analytic Expression of Stresses and Displacements

Airy's stress function can be expressed in terms of two analytic functions $f(z)$, $g(z)$ of the complex variable

$$z = x + iy \qquad [2]$$

as follows[4]

$$F = \mathrm{Re}[f(z) + \bar{z}g(z)] \qquad [3]$$

where $\bar{z}$ is the conjugate of z

$$\bar{z} = x - iy \qquad [4]$$

and Re denotes "the real part of." Calculation of the stresses from Airy's function[5] leads to

$$\left.\begin{aligned} X_x &= -\mathrm{Re}[f'' + \bar{z}g'' - 2g'] \\ X_y &= -\mathrm{Im}[f'' + \bar{z}g''] \\ Y_y &= \mathrm{Re}\,[f'' + \bar{z}g'' + 2g'] \end{aligned}\right\} \qquad [5]$$

The sum of the two principal stresses $p + q$ is thus equal to

$$p + q = X_x + Y_y = 4\mathrm{Re}(g') \qquad [6]$$

From Equations [5] one may derive expressions for the traction

---

[1] Consulting Engineer, General Engineering Laboratory, General Electric Company. Mem. ASME.

[2] Engineer, General Engineering Laboratory, General Electric Company.

Presented at the National Conference of the Applied Mechanics Division, Minneapolis, Minn., June 18–20, 1953, of The American Society of Mechanical Engineers.

Discussion of this paper should be addressed to the Secretary, ASME, 29 West 39th Street, New York, N. Y., and will be accepted until October 10, 1953, for publication at a later date. Discussion received after the closing date will be returned.

Note: Statements and opinions advanced in papers are to be understood as individual expressions of their authors and not those of the Society. Manuscript received by ASME Applied Mechanics Division, June 10, 1952, Paper No. 53—APM-16.

[3] See for instance, "Photoelasticity," by M. M. Frocht, John Wiley & Sons, Inc., New York, N. Y., first edition, 1948, pp. 193–230.

[4] For example, refer to "Application of Analytic Functions to Two-Dimensional Biharmonic Analysis," by H. Poritsky, Trans. of the American Mathematical Society, vol. 59, 1946, pp. 248–279.

[5] "A Treatise on the Mathematical Theory of Elasticity," by A. E. H. Love, Cambridge University Press, Cambridge, England, fourth edition, 1927.

components X, Y across any curve segment[6] P_1P_2

$$X - iY = i(f' + \bar{g} + \bar{z}g')]_{P_1}^{P_2} \quad [7]$$

where $]_{P_1}^{P_2}$ denotes the difference between the values at P_2, P_1.

A portion of the boundary across which no tractions are applied will be referred to as a "free boundary." From Equation [7] follows that along a free boundary the following relation holds

$$f' + g + \bar{z}g' = \text{const} \quad [8]$$

We denote the real and imaginary parts of g' by φ, ψ

$$\left.\begin{aligned} g' &= \varphi + i\psi \\ \varphi &= \text{Re}(g') = (p + q)/4 \\ \psi &= \text{Im}(g') \end{aligned}\right\} \quad [9]$$

The functions φ, ψ are conjugate harmonic functions and satisfy the Cauchy-Riemann equations. As shown by Love's equations[7] for plane strain, φ and ψ are, respectively, proportional to the dilatation Δ and the local rotation or angular displacement ω

$$\left.\begin{aligned} \varphi &= \frac{p+q}{4} = \frac{\lambda + G}{2}\Delta = \frac{E}{4(1+\sigma)(1-2\sigma)}\Delta \\ \psi &= \frac{G(\lambda + G)}{\lambda + 2G}\omega = \frac{E}{4(1-\sigma^2)}\omega \end{aligned}\right\} \quad [10]$$

where

E = Young's modulus
σ = Poisson's ratio
G = shear modulus $= E/2(1 + \sigma)$
λ = Lamé's constant $= E\sigma/(1 + \sigma)(1 - 2\sigma)$

For plane strain, as shown elsewhere,[4] the displacement vector (u, v) is given by

$$(u + iv)2G = \gamma g - \bar{f}' - z\bar{g}' \quad [11]$$

where[8]

$$\gamma = 3 - 4\sigma \quad [12]$$

Addition of Equations [8] and [12] leads to the following equation for the displacement along a free boundary

$$(u + iv)2G]_{P_1}^{P_2} = (\gamma + 1)g]_{P_1}^{P_2} \quad [13]$$

Equations [9], [10], and [13] do not involve the function $f(z)$ at all, and will be used in the following to determine the displacements. The more general Equation [11] requiring the knowledge of f, too, will be discussed in Section 6.

3 Determination of Displacements From Photoelastic Fringe Patterns

From the foregoing relations it follows that one may utilize photoelastic patterns to obtain displacements along a free boundary as follows: Along a free boundary q vanishes, and the following relations obtain

$$\left.\begin{aligned} q &= 0 \\ p + q &= p = p - q \end{aligned}\right\} \quad [14]$$

Thus the $p - q$ fringe lines of the photoelastic pattern cross the free boundary at the same points at which the value $(p + q)$ increases by a constant amount equal to the fringe difference between adjacent fringes. As indicated in the foregoing the sum $(p + q)/4 = \varphi$ is a harmonic function.

In order to obtain the functions g', g which are related by means of Equations [9], [10], [13] to the rotation ω and the displacements, one must first determine ψ, the conjugate harmonic of φ.

As mentioned in Section 1, there are several methods available for the determination of the harmonic function φ. Once φ is determined and the curves

$$\varphi = \text{const} \quad [15]$$

drawn, one proceeds to calculate the function ψ, particularly along the boundary. This may be done by utilizing the Cauchy-Riemann equations, and integrating these numerically; or again, by utilizing the property of the curves

$$\psi = \text{const} \quad [16]$$

which states that the curves [15], [16] intersect each other at right angles, and when drawn for equal increments $\Delta\varphi = \Delta\psi$ of the right-hand values, divide the plane into small squares. The direct free-hand construction of the curves [15], [16] based on these rules, is known as "flux plotting."

The small-square rule applies, in general, though at the exceptional points at which the gradients $\nabla\varphi$, $\nabla\psi$ vanish, this construction breaks down and the small squares are replaced by configuration of Fig. 1, involving arcs of rectangular hyperbolas.

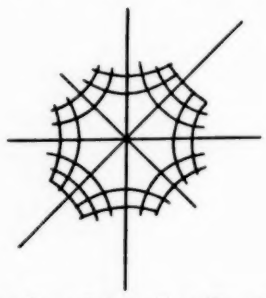

Fig. 1 Aspect of Small Square Plot Near Point of Vanishing Field Strength

After the determination of φ and ψ has been carried out to the desired accuracy (by whatever method), both the real and the imaginary part of the function g' are known, and the function g is found by means of the integration

$$g(z) = \int g'(z)dz \quad [17]$$

especially along the boundary. Equation [13] is then used to calculate the displacement along the free boundary. The angular displacement can be determined directly from Equations [10] without carrying out the Integration [17].

4 Example. Bending of a Plate With Change of Thickness. Flux Plot

As an example of the foregoing we shall consider the second example mentioned in Section 1, namely, an elastic plate with a change of thickness carried out through a quarter-circle fillet, and assume that this plate is stressed by means of a bending moment as shown in Figs. 2 and 3. As stated in Section 1, customarily the bending of such a plate is calculated by assuming that over the thinner section the curvature is constant as for a plate of constant thickness $2h$, subject to a linear stress distribution of moment M clear down to the section BB, and that similar uniform bending takes place over the thicker section as for a plate of uniform thickness $2H$, subject to a similar linear stress distribution of moment M while at the transition BB the moment M is transmitted from one portion to the other as if there were an

[6] Reference 4, p. 254.
[7] Reference 5, equations [2], [4], pp. 204 and 205, respectively.
[8] In reference 5, ν is used instead of γ for this constant.

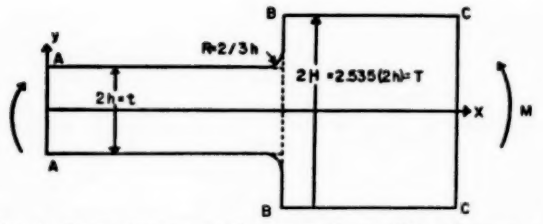

FIG. 2 CROSS SECTION OF PLATE, OR BEAM, WITH CHANGE OF THICKNESS

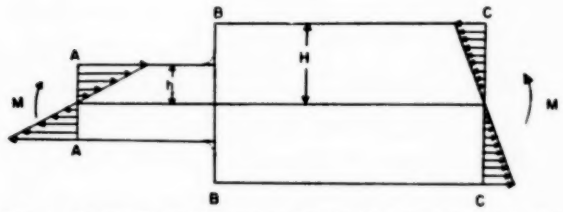

FIG. 3 SIMPLE BEAM THEORY OF STRESS DISTRIBUTION OF PLATE WITH CHANGE OF SECTION IN BENDING

infinitely thin and rigid strip BB (see Fig. 3), connecting the two portions. Actually, of course, no such magic strip BB exists and the stress transition takes place in quite a different way, and as a result the net angular displacement of the plate between two ends such as AA and CC which are far enough away from the change of section area for the stress to have become uniform, is larger than the value obtained above.

Fig. 4[9] shows the pattern of photoelastic $p - q$ curves for a thin beam in bending of the dimensions shown in Fig. 2. This corresponds more nearly to a case of plane stress rather than plane strain, but, as known, for simply connected regions the stress patterns are the same for both cases if the applied tractions are similar.

In the photograph in Fig. 4 neither the fringes nor the boundary values of $p - q$ can be considered to correspond to the manner of stress application at $x = +\infty$ shown in Fig. 3. For the actual specimen the distance BC was too short, and there was a further enlargement of thickness. This, however, does not matter, because in terms of the stress difference corresponding to one fringe space, there are 7.5 fringe spaces in the left half of the figure, and only 1.123 fringe spaces on the right. Thus only a single $(p - q)$- and $(p + q)$-curve will emerge over the free boundary BC; any reasonable manner of increase of $(p + q)$ from zero at B to 1.123 to the right, reaching $1/e$ of this value, say, within a distance H from B, will do.

From the equations of the preceding section it follows that to determine the displacements on the boundary one must determine the values of ψ, the conjugate harmonic of $\varphi = (p + q)/4$, then carry out the Integration [17] and apply Equation [13]. To determine the angular displacement ω a knowledge of ψ is sufficient (see Equation [10]). Flux-plotting methods will be used to find ψ.

The photoelastic data in Fig. 4 are used only to copy the points at which the fringe lines cross the boundary. A flux plot is then drawn for φ and ψ, the real and imaginary parts of the function g', in such a way that the curves of constant φ cross the boundaries of the region under consideration at the same points as the successive photoelastic fringe lines. At the corner point B all stress components vanish, and therefore the real part of g' also

[9] From "Theory of Elasticity," by S. Timoshenko, McGraw-Hill Book Company, Inc., New York, N. Y., first edition, 1934, p. 133.

FIG. 4 PHOTOELASTIC PATTERN FOR PLATE, OR BEAM, WITH CHANGE OF SECTION IN BENDING

vanishes. From the oddness of the Airy function in y it will be seen that the real part of g' also vanishes along $y = 0$ so that the x-axis constitutes one of the φ-curves of the flux plot, namely, $\varphi = 0$. The pattern of Fig 4 may be restricted to $y > 0$.

Along the left-hand half of the beam the stress distribution eventually becomes linear in y as indicated in Fig. 3 and is given by

$$X_x = -\frac{12My}{t^3}, \quad X_y = 0, \quad Y_y = 0 \qquad [18]$$

where M is the applied moment per unit z. On the right-hand side the stress approaches similarly the values

$$X_x = -\frac{12My}{T^3}, \quad X_y = 0, \quad Y_y = 0 \qquad [19]$$

The ratio of the maximum stress to the left and to the right is given by

$$\frac{H^3}{h^3} \qquad [20]$$

and corresponding to the 7.5 fringe spaces on the left over half the plate thickness, there are 1.123 spaces to the right.

The flux plot under consideration giving the curves [15], [16], is shown in Fig. 5. One of the difficulties encountered in the construction of this plot turned out to be the existence of a point of the type shown in Fig. 1 at which the gradient of φ (and hence also of ψ) vanishes; that is, a point at which

$$g''(z) = 0 \qquad [21]$$

and where "small squares" are replaced by a configuration previously shown in Fig. 1.

The presence of such a point was first suspected after attempts to carry through a flux plot without it proved unsuccessful. Its existence can be inferred by noting that if the curves $-\varphi = \text{const}$ be considered as "level" or "contour lines" of a country map, the level $\varphi = 0$ occurs along the lower boundary of Fig. 5 as well as at the corner point B, while the height of the upper boundary starts with 7.5 at A, rises to a high value at the

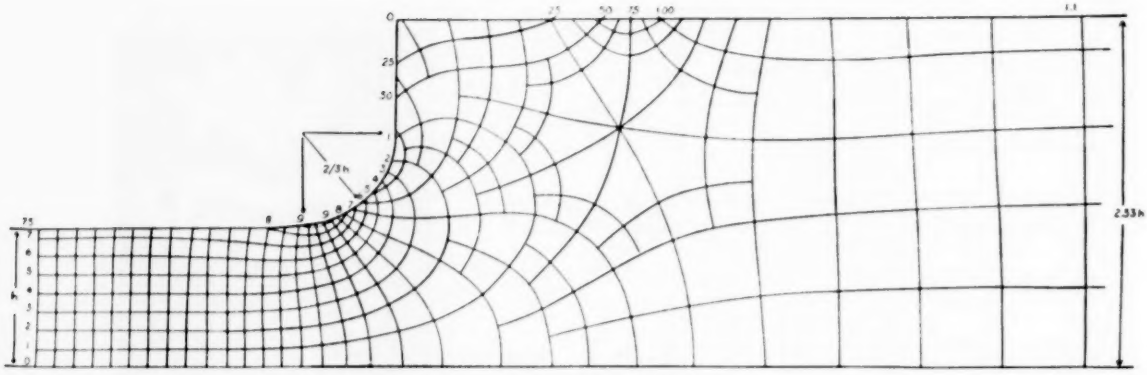

FIG. 5 SMALL SQUARE PLOT OF $(p + q)$-LINES

stress-concentration point in the fillet, descends to zero at point B, and rises to the value 1.123 to the right. In crossing over from the lower boundary $y = 0$ to B there is a rising hill both to the right and to the left, and there must be a "mountain pass" in the region; this is the point in question. Considerable amount of trial and error in regard to its position was required before the plot was judged to be sufficiently accurate.

From Equations [9] and [18] follows for $x = -\infty$

$$\varphi = \frac{p+q}{4} = \frac{-3My}{t^3} = \frac{-3My}{8h^3} \quad \ldots\ldots\ldots [22]$$

The fringe spaces in Fig. 4 thus correspond to a change of φ of amount

$$\Delta\varphi = \frac{3M}{8h^3 \times 7.5} = \frac{M}{20h^3} \quad \ldots\ldots\ldots [23]$$

and this is also the increase of ψ in the plot in Fig. 5

$$\Delta\psi = \Delta\varphi = \frac{M}{20h^3} \quad \ldots\ldots\ldots [24]$$

In Fig. 6 are plotted versus x, the values of $\psi/\Delta\psi$ obtained from the plot in Fig. 5 (curve A-B-C). The slopes in Fig. 6 for $x = \pm\infty$ agree with the curvatures of uniform thickness plates to within 1.6 per cent accuracy (see Appendix, Comparison With Simple Beam Theory). Also shown in Fig. 6, as the line A-D-E, is the angular displacement corresponding to the ordinary approximate treatment of bending in the manner indicated in Fig. 3, for the plate in Fig. 2. One can calculate the added angular displacement $\delta\omega$ which is shown by the vertical portion FG in Fig. 6. This angular displacement can be expressed in turn as the equivalent of an added plate length $\Delta x = KF$, of the smaller thickness $2h$, which for the present example is given by

$$(\Delta x)_h = 0.200\, h \quad \ldots\ldots\ldots [25]$$

or again, as an added length, $\Delta x = GE$, of the greater thickness $2H$

$$(\Delta x)_H = 1.33\, H \quad \ldots\ldots\ldots [26]$$

It is to be understood that if other methods of determining φ and ψ are to be used, the final result will be a figure similar to Fig. 6, but obtained differently.

5 ALTERNATIVE PROCEDURE

Since the foregoing graphical procedure depends to a considerable extent on the flux plot in Fig. 5, it is desirable to check the result in other ways. To this end we shall vary the procedure by

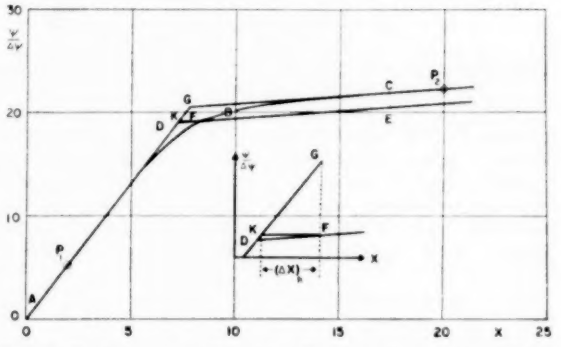

FIG. 6 COMPARISON OF ROTATION CALCULATED BY SIMPLE BEAM THEORY AND BY PRESENT METHOD

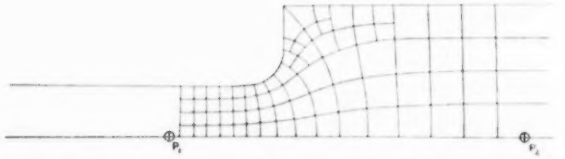

FIG. 7 FREE-HAND FLUX PLOT USED TO MAP PLATE CROSS SECTION ON UNIFORM STRIP

making a conformal map of the region in Fig. 2 upon a strip of uniform thickness h' shown in Fig. 8, and proceed to determine ψ in the latter plane.

This mapping is effected by means of the flux plot shown in Fig. 7. This plot, too, has been constructed freehand by means of the small square rule. However, it is a plot which is considerably easier to draw than the one in Fig. 5; in particular, it possesses no singular points of the type shown in Fig. 1, and both its upper and lower boundaries coincide with flux (or potential) lines. The plot also can be adapted more easily to experimental methods, such as the electrolytic tank or conducting paper. Fig. 7 may be considered to constitute a change of co-ordinates from the x, y-co-ordinates in Figs. 2 and 7 to the (ξ,η)-co-ordinates in the ζ-plane in Fig. 8, $\zeta = \xi + i\eta$; its objective is to simplify the upper boundary in Fig. 2 by "straightening it out."

As known, an analytic function, such as $g'(z)$, is transformed into an analytic function of ζ by means of conformal mapping of the z-plane onto the ζ-plane. The boundary values of $\varphi = \mathrm{Re}(g')$ along the upper boundary in Fig. 4 are carried over into boundary

values along $\eta = h'$ of the strip in Fig. 8. Because the region in Fig. 8 has a relatively simple boundary, the values of φ and its conjugate harmonic ψ through this region can be computed in terms of the boundary values of φ analytically, by means of certain definite integrals. Thus if φ vanishes along $\eta = 0$, the values of ψ there are expressed in terms of the φ-values along $\eta = h'$ as follows

$$\psi(0, \xi) = C\xi + D - \frac{1}{\pi}\int_{\xi' = -\infty}^{\xi' = +\infty} \ln\left[e^{\pi\xi/h'} + e^{\pi\xi'/h'}\right] d[\varphi(\xi')] \quad \ldots\ldots [27]$$

where

$$C = -\lim_{\xi \to -\infty} \varphi(\xi, h')/h'$$

and D is a constant. The derivation of Equation [27] is indicated in the Appendix.

From the boundary values of φ along the upper boundary in Fig. 4 and Fig. 7, the boundary values of $\varphi(\xi)$ were found for Fig. 8.

Fig. 9 shows a plot of φ versus ξ along the upper boundary of

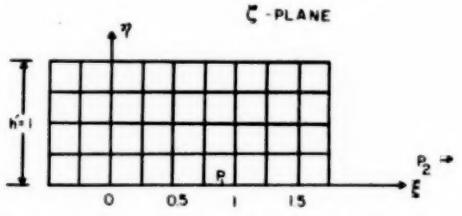

FIG. 8 UNIFORM STRIP IMAGE OF PLATE CROSS SECTION OF FIG. 7

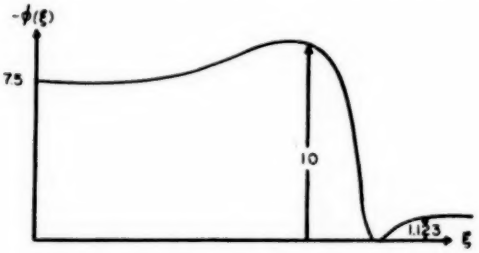

FIG. 9 BOUNDARY VALUES OF HARMONIC FUNCTION IN THE TRANSFORMED PLANE OF FIG. 8

Fig. 8; along the lower boundary φ vanishes.

Equation [27] was applied for $h' = 1$ for the two points marked P_1, P_2, $\xi_{p(1)} - \xi_{p(2)} = 4$, in Figs. 6 and 7, and the difference of the ψ-values determined by numerical integration. There resulted

$$\Delta\psi = 18.82 \quad \ldots\ldots [28]$$

In Fig. 6 the corresponding points are also indicated by P_1, P_2 and yield

$$\Delta\psi = 17.74 \quad \ldots\ldots [29]$$

The value, Equation [28], is regarded as the more accurate one.

6 Boundary With Tractions

Suppose the boundary is not free but has known tractions applied over it. Let the boundary be parallel locally to the y-axis; then the applied tractions are X_x, X_y. Consider the Mohr circle for the local boundary point, in an (α, β)-plane. The points

$$\alpha = X_x, \quad \beta = X_y \quad \ldots\ldots [30]$$

$$\alpha = Y_y, \quad \beta = X_y \quad \ldots\ldots [31]$$

lie on this circle, whose diameter end points are at

$$\alpha = p, \qquad \beta = 0 \quad \ldots\ldots [32]$$

$$\alpha = q, \qquad \beta = 0 \quad \ldots\ldots [33]$$

The diameter of the Mohr circle is

$$p - q \quad \ldots\ldots [34]$$

and its center lies at

$$\alpha = (p + q)/2, \quad \beta = 0 \quad \ldots\ldots [35]$$

Thus the Mohr circle may be constructed from the known traction [31] and the known value of $(p - q)$ by plotting the point P: (X_x, X_y) in the plane of the Mohr circle diagram shown in

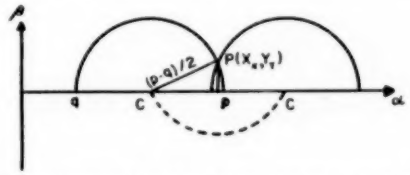

FIG. 10 MOHR CIRCLES YIELDING VALUES OF $(p + q)$ ON BOUNDARY WITH TRACTIONS

Fig. 10, and locating the center C of the Mohr circle by swinging an arc of a circle of radius $(p - q)/2$ with center at P. The x-co-ordinate of C is then equal to $(p + q)/2$.

As shown in Fig. 10, the construction leads to two possible positions for C, yielding

$$\frac{(p + q)}{2} = X_x \pm \left[\left(\frac{p - q}{2}\right)^2 - (X_y)^2\right]^{1/2} \quad \ldots\ldots [36]$$

The sign ambiguity must be settled so that the $(p + q)$-values over the nonfree boundary join on continuously to the corresponding values over the free boundary.

For a general boundary point, Equation [36] holds with X_x, X_y replaced by the normal tensile, and shear components of traction.

From here on the determination of displacements proceeds as follows:

From the known values of $p - q$, one determines g' again over the boundary, and g by integration. Equation [7] is now utilized to calculate f'. The displacement components (u, v) are then determined from Equation [11].

Acknowledgment

The authors gratefully acknowledge the assistance of Miss Bergitte Jensen with the flux plots and numerical calculations.

Appendix. Comparison With Simple Beam Theory

It will be shown that the slopes of the curve in Fig. 6 agree with the slopes computed for simple beam theory when far enough away from the change of thickness. The stress distribution, Equation [18], in a uniform plate $-h < y < h$, by itself, would cause the lines parallel to the x-axis to be bent to a curvature

$$k_x = \frac{M}{EI} \quad \ldots\ldots [37]$$

about the z-axis, and lines parallel to the z-axis to an "anticlastic" curvature about the x-axis

$$k_x = -\sigma M/EI \quad [38]$$

In plane strain the latter curvature is prevented by means of the moment

$$M_x = -\sigma M \quad [39]$$

and Equation [37] is replaced by

$$k_x = \frac{M}{EI} + \frac{M_x\sigma}{EI} = \frac{M(1-\sigma^2)}{EI} \quad [40]$$

The curvature, Equation [40], corresponds to the angular deflection

$$\omega = \int k_x dx = \frac{M(1-\sigma^2)}{EI}\, x + \text{const} \quad [41]$$

This indeed checks for $x = -\infty$ with Equations [10] and [18] which yield

$$\varphi = \frac{p+q}{4} = \frac{X_x + Y_y}{4} = -\frac{3My}{t^3} \quad [42]$$

whence there follows from the Cauchy-Riemann equations

$$\psi = \frac{3Mx}{t^3} + \text{const} = \frac{Mx}{AI} + \text{const} \quad [43]$$

while Equation [10] yields

$$\left.\begin{aligned} \omega &= \frac{12M(1-\sigma^2)}{Et^3}\, x + \text{const} \\ &= \frac{M(1-\sigma^2)}{EI}\, x + \text{const} \end{aligned}\right\} \quad [44]$$

Recalling Equation [24] one replaces Equation [43] by

$$\begin{pmatrix} \psi \\ \Delta\psi \end{pmatrix} = (7.5)\begin{pmatrix} x \\ h \end{pmatrix} + \text{const} \quad [45]$$

Similarly, for $x \to +\infty$ one obtains

$$\begin{pmatrix} \psi \\ \Delta\psi \end{pmatrix} = 1.123\begin{pmatrix} x \\ H \end{pmatrix} + \text{const} \quad [46]$$

Proof of Equation [27]

To prove Equation [27] we further map the strip in Fig. 8 on the half plane $\eta_1 > 0$ in Fig. 11 by means of the tranformation

$$\zeta_1 = \exp(\pi\zeta/h'), \quad \zeta = (h'/\pi)\log\zeta_1, \quad \zeta_1 = \xi_1 + i\eta_1 \quad [47]$$

The upper boundary $\eta = h'$ in Fig. 8 is transformed into the negative ξ_1-axis, and the lower boundary $\eta = 0$ into the positive ξ_1-axis.

For the half plane $\eta_1 > 0$ consider the function

$$\frac{i}{\pi}\ln(\zeta_1 - \xi_1') \quad [48]$$

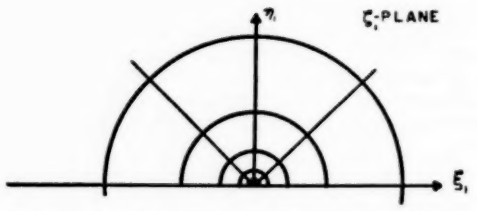

Fig. 11 Map of Strip of Fig. 8 on a Half Plane

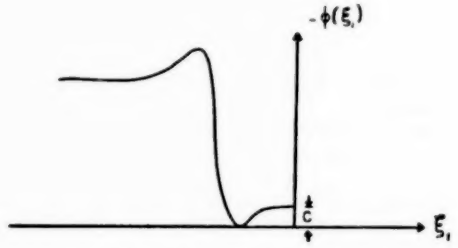

Fig. 12 Boundary Values of Harmonic Function in Transformed Plane of Fig. 11

where ξ_1' is real. Along $\eta_1 = 0$ this reduces to

$$\left.\begin{aligned} &-1 + \frac{i}{\pi}\ln|\xi_1 - \xi_1'| \quad \text{for} \quad \xi_1 < \xi_1' \\ &0 + \frac{i}{\pi}\ln|\xi_1 - \xi_1'| \quad \text{for} \quad \xi_1 > \xi_1' \end{aligned}\right\} \quad [49]$$

Thus $\ln|\xi_1 - \xi_1'|$ constitutes the boundary values of the conjugate harmonic to the function φ which is constant to each side of ξ_1' but discontinuous at ξ_1' by the amount $\Delta\varphi = 1$.

By Duhamel's superposition it follows that the conjugate harmonic boundary values of ψ for the half plane $\eta_1 > 0$ in Fig. 11 is given by

$$\psi(\xi_1) = \frac{1}{\pi}\int_{\xi_1'=-\infty}^{\xi_1'=+\infty} \ln|\xi_1 - \xi_1'|\, d[\varphi(\xi_1')] \quad [50]$$

The boundary values in Fig. 9 are plotted in Fig. 12 versus ξ_1. Since $\varphi(\xi_1) = 0$ for $\xi_1 > 0$, the range of integration may be confined to $\xi_1 > \epsilon$ where ϵ is any positive constant. There results for $\xi_1 > 0$

$$\psi(\xi_1) = \frac{C}{\pi}\ln\xi_1 + \frac{1}{\pi}\int_{\xi_1'=-\infty}^{\xi_1'=0} \ln(\xi_1 - \xi_1')d[\varphi(\xi_1')] \quad [51]$$

where, as indicated, the integration is confined to $\xi_1 > 0$; the term involving $\ln\xi_1$ arises from the discontinuity in φ at $\xi_1 = 0$.

Transforming the variable of integration in Equation [51] to ξ', there results Equation [27].

The Vibration of Rotating, Tapered-Twisted Beams

By G. W. JARRETT[1] and P. C. WARNER,[2] LESTER, PA.

This paper presents an extension of Myklestad's adaptation[3] of the Holzer method of calculating natural frequencies and mode shapes of systems to the case of a tapered-twisted beam with certain elastic constraints. The details of the solution are so arranged that the bulk of the numerical calculations can be carried out by a technician with only a high-school mathematical background. This extension makes possible the evaluation of the effect of rotation of a beam on a radial line, of certain elastic constraints such as the lashing wires and shrouding used on turbine blades, and of coupling between the torsional and flexural vibrations. In this paper, however, the effects of coupling between the torsional and flexural vibrations will not be considered.[4] The basic differential equation will be solved by the tabular method due to Holzer.

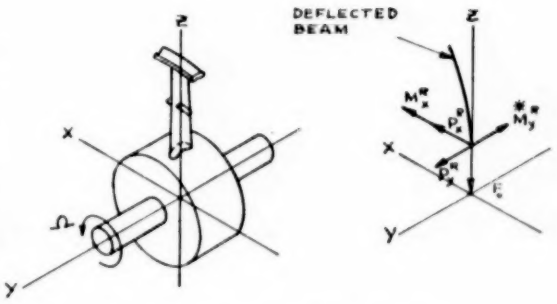

Fig. 1 Illustration of Nomenclature

Nomenclature

The following nomenclature is used in the paper:

X, Y, Z = set of fixed orthogonal, right-handed axis. X and Y-axes are directed in direction of rotation, and in axial direction, respectively. Z-axis is directed along line of centers of gravity of cross sections of beam. Origin is on axis of rotation

U, V = components of displacement of center of gravity from its initial position. U is in X-Z-plane, and V in Y-Z-plane

P_x, P_y = shearing forces acting over a section, directed in positive sense of axis indicated by subscripts

M_x, M_y^* = bending moments about X and Y-axis, respectively (* indicates that this convention violates the right-hand rule)

E, G = moduli of elasticity in tension and shear, respectively

A = area of cross section of beam

ρ = mass density of beam material

I_x, I_y, I_{xy} = moments and product of inertia about X and Y-axis

γ = angle between axis of minimum moment of inertia and X-axis at any section

Ω = angular velocity of rotation of blade

R = radius at which base of beam is located

ω = natural frequency of vibration

L = length of beam

t = time, sec

F_0 = total centrifugal force of beam

N = denotes Nth station

ϵ = infinitesimal distance

m^N = mass concentrated at Nth station

$1/K^i$ = lashing-wire spring constant; i.e., angle at end of lashing wire due to moments at its ends of which sum is unity

Mathematics

If we assume that the beam under consideration is long and thin, and that the loci of centers of twist and gravity are initially straight and coincident, the following equations may be written for small vibrations

$$\left.\begin{aligned}\frac{\partial^2}{\partial Z^2}\left(EI_y\frac{\partial^2 U}{\partial Z^2}+EI_{xy}\frac{\partial^2 V}{\partial Z^2}\right)-\frac{\partial}{\partial Z}\left[\left(F_0-\int_R^Z A\rho\Omega^2 Z\,dZ\right)\frac{dU}{dZ}\right]-A\rho\Omega^2 U&=-A\rho\frac{\partial^2 U}{\partial t^2}\\ \frac{\partial^2}{\partial Z^2}\left(EI_x\frac{\partial^2 V}{\partial Z^2}+EI_{xy}\frac{\partial^2 U}{\partial Z^2}\right)-\frac{\partial}{\partial Z}\left[\left(F_0-\int_R^Z A\rho\Omega^2 Z\,dZ\right)\frac{\partial V}{\partial Z}\right]&=-A\rho\frac{\partial^2 V}{\partial t^2}\end{aligned}\right\}\quad\ldots\ [1]$$

[1] Deceased; formerly member of faculty of Towne Scientific School, University of Pennsylvania and Turbine Engineering Department, Westinghouse Electric Corporation.

[2] Design Engineer, Turbine Engineering Department, Westinghouse Electric Corporation. Jun. ASME.

[3] "New Method of Calculating Natural Modes of Uncoupled Bending Vibrations," by N. O. Myklestad, *Journal of Aeronautical Sciences*, vol. 11, April, 1944, pp. 153–162.

"A General Method of Calculating Critical Speeds of Flexible Rotors," by M. A. Prohl, Journal of Applied Mechanics, Trans. ASME, vol. 67, 1945, p. A-142.

"Calculation of the Multiple-Span Critical Speeds of Flexible Shafts by Means of Punched-Card Machines," by A. W. Rankin, Journal of Applied Mechanics, Trans. ASME, vol. 68, 1946, p. A-117–A-126.

[4] See thesis by G. W. Jarrett, "Vibration of Airplane Propellers," library, University of Pennsylvania, Philadelphia, Pa.

Presented at the National Conference of the Applied Mechanics Division, Minneapolis, Minn., June 18–20, 1953, of The American Society of Mechanical Engineers.

Discussion of this paper should be addressed to the Secretary, ASME, 29 West 39th Street, New York, N. Y., and will be accepted until October 10, 1953, for publication at a later date. Discussion received after the closing date will be returned.

Note: Statements and opinions advanced in papers are to be understood as individual expressions of their authors and not those of the Society. Manuscript received by ASME Applied Mechanics Division, November 5, 1952. Paper No. 53—APM-17.

Assuming simple harmonic motion

$$\left.\begin{aligned}\frac{d^2}{dZ^2}\left(EI_y\frac{d^2U}{dZ^2}+EI_{xy}\frac{d^2V}{dZ^2}\right)&=A\rho\omega^2U+A\rho\Omega^2U+\frac{d}{dZ}\left[\left(F_0-\int_R^Z A\rho\Omega^2Z\,dZ\right)\frac{dU}{dZ}\right]\\ \frac{d^2}{dZ^2}\left[EI_x\frac{d^2V}{dZ^2}+EI_{xy}\frac{d^2U}{dZ^2}\right]&=A\rho\omega^2V+\frac{d}{dZ}\left[\left(F_0-\int_R^Z A\rho\Omega^2Z\,dZ\right)\frac{dV}{dZ}\right]\end{aligned}\right\}\quad\ldots[2]$$

Integrating Equations [2] the integration starting at the base of the beam

$$\left.\begin{aligned}\frac{d}{dZ}\left[EI_y\frac{d^2U}{dZ^2}+EI_{xy}\frac{d^2V}{dZ^2}\right]&=P_x{}^R+\int_R^Z A\rho\omega^2U\,dZ+\int_R^Z A\rho\Omega^2U\,dZ\\&\quad+\left(F_0-\int_R^Z A\rho\Omega^2Z\,dZ\right)\frac{dU}{dZ}+\sum_i\left(\frac{dU^i}{dZ}\frac{K^i}{Z^i}-\frac{U^iK^i}{(Z^i)^2}\right)=P_x\\ \frac{d}{dZ}\left[EI_x\frac{d^2V}{dZ^2}+EI_{xy}\frac{d^2U}{dZ^2}\right]&=P_y{}^R+\int_R^Z A\rho\omega^2V\,dZ+\left(F_0-\int_R^Z A\rho\Omega^2Z\,dZ\right)\frac{dV}{dZ}=P_y\end{aligned}\right\}\quad\ldots[3]$$

where the summation is due to the fact that the lashing wires produce a shear as well as a moment.

Integrating Equations [3]

$$\left.\begin{aligned}EI_y\frac{d^2U}{dZ^2}+EI_{xy}\frac{d^2V}{dZ^2}&=M_y{}^{*R}+P_x{}^R(Z-R)+\int_R^Z dZ\int_R^Z A\rho\omega^2U\,dZ+\int_R^Z dZ\int_R^Z A\rho\Omega^2U\,dZ\\&\quad+F_0U-\int_R^Z\frac{dU}{dZ}\,dZ\int_R^Z A\rho\Omega^2Z\,dZ+\int_R^Z\left[\sum_i\left(\frac{dU^i}{dZ}\frac{K^i}{Z^i}-\frac{U^iK^i}{(Z^i)^2}\right)\right]dZ+\sum_i\left(\frac{dU^i}{dZ^i}K^i-\frac{U^iK^i}{(Z^i)}\right)=M_y{}^*\\ EI_x\frac{d^2V}{dZ^2}+EI_{xy}\frac{d^2U}{dZ^2}&=M_x{}^R+P_y{}^R(Z-R)+\int_R^Z dZ\int_R^Z A\rho\omega^2V\,dZ+F_0V\\&\quad-\int_R^Z\frac{dV}{dZ}\,dZ\int_R^Z A\rho\Omega^2Z\,dZ=M_x\end{aligned}\right\}\quad\ldots[4]$$

Rewriting Equations [4]

$$\left.\begin{aligned}EI_y\frac{d^2U}{dZ^2}+EI_{xy}\frac{d^2V}{dZ^2}&=M_y{}^*\\ EI_x\frac{d^2V}{dZ^2}+EI_{xy}\frac{d^2U}{dZ^2}&=M_x\end{aligned}\right\}\quad\ldots[5]$$

Solving for

$$\frac{d^2U}{dZ^2}\quad\text{and}\quad\frac{d^2V}{dZ^2}$$

and noting that $I_xI_y-I_{xy}{}^2=I_{x0}I_{y0}$, where I_{x0} and I_{y0} are the principal moments of inertia of the cross section

$$\left.\begin{aligned}\frac{d^2U}{dZ^2}&=\frac{I_xM_y{}^*}{EI_{x0}I_{y0}}-\frac{I_{xy}M_x}{EI_{x0}I_{y0}}\\ \frac{d^2V}{dZ^2}&=\frac{I_yM_x}{EI_{x0}I_{y0}}-\frac{I_{xy}M_y{}^*}{EI_{x0}I_{y0}}\end{aligned}\right\}\quad\ldots[6]$$

Equations [6] are basic. They replace the single equation used in single-plane beam theory ($EIU''=M$). The effect of coupling between the two planes is indicated by the second term on the right-hand side of Equations [6].

The solution is to be numerical, the beam being broken into sections with discrete mass concentrations at the ends of the sections, so by integrating Equations [6] and subtracting the derivatives at two consecutive mass concentrations we have

$$\left.\begin{aligned}\frac{dU^{N+1}}{dZ}&=\frac{dU^N}{dZ}+\int_{Z^N}^{Z^{N+1}}\frac{I_xM_y{}^*}{EI_{x0}I_{y0}}\,dZ-\int_{Z^N}^{Z^{N+1}}\frac{I_{xy}M_x}{EI_{x0}I_{y0}}\,dZ\\ \frac{dV^{N+1}}{dZ}&=\frac{dV^N}{dZ}+\int_{Z^N}^{Z^{N+1}}\frac{I_yM_x}{EI_{x0}I_{y0}}\,dZ-\int_{Z^N}^{Z^{N+1}}\frac{I_{xy}M_y{}^*}{EI_{x0}I_{y0}}\,dZ\end{aligned}\right\}\quad\ldots[7]$$

Integrating Equations [6] twice and subtracting deflections at two consecutive mass concentrations

$$\left.\begin{aligned}U^{N+1}&=U^N+(Z^{N+1}-Z^N)\frac{dU^N}{dZ}+\int_{Z^N}^{Z^{N+1}}dZ\int_{Z^N}^{Z}\left(\frac{I_xM_y{}^*}{EI_{x0}I_{y0}}-\frac{I_{xy}M_x}{EI_{x0}I_{y0}}\right)dZ\\ V^{N+1}&=V^N+(Z^{N+1}-Z^N)\frac{dV^N}{dZ}+\int_{Z^N}^{Z^{N+1}}dZ\int_{Z^N}^{Z}\left(\frac{I_yM_x}{EI_{x0}I_{y0}}-\frac{I_{xy}M_y{}^*}{EI_{x0}I_{y0}}\right)dZ\end{aligned}\right\}\quad\ldots[8]$$

Since the mass of the beam is concentrated at the end of the sections of the beam

$$\left.\begin{aligned}M_y{}^*&=M_y{}^{*N}+P_x{}^N(Z-Z^N)\\ M_x&=M_x{}^N+P_y{}^N(Z-Z^N)\end{aligned}\right\}\quad Z^N\le Z\le Z^{N+1}\quad\ldots[9]$$

Substituting Equations [9] into Equations [7] and [8]

$$\left.\begin{aligned}
\frac{dU^{N+1}}{dZ} &= \frac{dU^N}{dZ} + M_y{}^{*N}\int_{Z^N}^{Z^{N+1}}\frac{I_x dZ}{EI_{x0}I_{y0}} + P_x{}^N\int_{Z^N}^{Z^{N+1}}\frac{I_x(Z-Z^N)dZ}{EI_{x0}I_{y0}} - M_x{}^N\int_{Z^N}^{Z^{N+1}}\frac{I_{xy}dZ}{EI_{x0}I_{y0}} \\
&\quad - P_y{}^N\int_{Z^N}^{Z^{N+1}}\frac{I_{xy}(Z-Z^N)dZ}{EI_{x0}I_{y0}} \\
\frac{dV^{N+1}}{dZ} &= \frac{dV^N}{dZ} + M_x{}^N\int_{Z^N}^{Z^{N+1}}\frac{I_y dZ}{EI_{x0}I_{y0}} + P_y{}^N\int_{Z^N}^{Z^{N+1}}\frac{I_y(Z-Z^N)dZ}{EI_{x0}I_{y0}} - M_y{}^{*N}\int_{Z^N}^{Z^{N+1}}\frac{I_{xy}dZ}{EI_{x0}I_{y0}} \\
&\quad - P_x{}^N\int_{Z^N}^{Z^{N+1}}\frac{I_{xy}(Z-Z^N)dZ}{EI_{x0}I_{y0}}
\end{aligned}\right\} \quad [10]$$

$$\left.\begin{aligned}
U^{N+1} &= U^N + (Z^{N+1}-Z^N)\frac{dU^N}{dZ} + M_y{}^{*N}\int_{Z^N}^{Z^{N+1}}dZ\int_{Z^N}^{Z}\frac{I_x dZ}{EI_{x0}I_{y0}} + P_x{}^N\int_{Z^N}^{Z^{N+1}}dZ\int_{Z^N}^{Z}\frac{I_x(Z-Z^N)dZ}{EI_{x0}I_{y0}} \\
&\quad - M_x{}^N\int_{Z^N}^{Z^{N+1}}dZ\int_{Z^N}^{Z}\frac{I_{xy}dZ}{EI_{x0}I_{y0}} - P_y{}^N\int_{Z^N}^{Z^{N+1}}dZ\int_{Z^N}^{Z}\frac{I_{xy}(Z-Z^N)dZ}{EI_{x0}I_{y0}} \\
V^{N+1} &= V^N + (Z^{N+1}-Z^N)\frac{dV^N}{dZ} + M_x{}^N\int_{Z^N}^{Z^{N+1}}dZ\int_{Z^N}^{Z}\frac{I_y dZ}{EI_{x0}I_{y0}} + P_y{}^N\int_{Z^N}^{Z^{N+1}}dZ\int_{Z^N}^{Z}\frac{I_y(Z-Z^N)dZ}{EI_{x0}I_{y0}} \\
&\quad - M_y{}^{*N}\int_{Z^N}^{Z^{N+1}}dZ\int_{Z^N}^{Z}\frac{I_{xy}dZ}{EI_{x0}I_{y0}} - P_x{}^N\int_{Z^N}^{Z^{N+1}}dZ\int_{Z^N}^{Z}\frac{I_{xy}(Z-Z^N)dZ}{EI_{x0}I_{y0}}
\end{aligned}\right\} \quad [11]$$

For simplicity let

$$A_i{}^N = \int_{Z^N}^{Z^{N+1}}\frac{I_i dZ}{EI_{x0}I_{y0}};\quad B_i{}^N = \int_{Z^N}^{Z^{N+1}}\frac{I_i(Z-Z^N)dZ}{EI_{x0}I_{y0}};\quad C_i{}^N = \int_{Z^N}^{Z^{N+1}}\frac{I_i(Z-Z^N)^2dZ}{EI_{x0}I_{y0}}$$

and remembering that

$$\int^b dx\int^x f(x)dx = (b-a)\int_a^b f(x)dx - \int_a^b f(x)(x-a)dx$$

$$\left.\begin{aligned}
\frac{dU^{N+1}}{dZ} &= \frac{dU^N}{dZ} + M_y{}^{*N}A_x{}^N + P_x{}^N B_x{}^N - M_x{}^N A_{xy}{}^N - P_y{}^N B_{xy}{}^N \\
\frac{dV^{N+1}}{dZ} &= \frac{dV^N}{dZ} + M_x{}^N A_y{}^N + P_y{}^N B_y{}^N - M_y{}^N A_{xy}{}^N - P_x{}^N B_{xy}{}^N \\
U^{N+1} &= U^N + (Z^{N+1}-Z^N)\frac{dU^N}{dZ} + M_y{}^{*N}[(Z^{N+1}-Z^N)A_x{}^N - B_x{}^N] + P_x{}^N[(Z^{N+1}-Z^N)B_x{}^N - C_x{}^N] \\
&\quad - M_x{}^N[(Z^{N+1}-Z^N)A_{xy}{}^N - B_{xy}{}^N] - P_y{}^N[(Z^{N+1}-Z^N)B_{xy}{}^N - C_{xy}{}^N] \\
V^{N+1} &= V^N + (Z^{N+1}-Z^N)\frac{dV^N}{dZ} + M_x{}^N[(Z^{N+1}-Z^N)A_y{}^N - B_y{}^N] + P_y{}^N[(Z^{N+1}-Z^N)B_y{}^N - C_y{}^N] \\
&\quad - M_y{}^{*N}[(Z^{N+1}-Z^N)A_{xy}{}^N - B_{xy}{}^N] - P_x{}^N[(Z^{N+1}-Z^N)B_{xy}{}^N - C_{xy}{}^N]
\end{aligned}\right\} \quad [12]$$

The procedure now is to substitute in Equations [12] the values of P_x, P_y, M_x, $M_y{}^*$ given by Equations [3] and [4]. First, however, the equations must be altered since the beam has been broken into sections with mass concentrations rather than distributed mass. Denoting by ϵ an infinitesimal distance

$$\left.\begin{aligned}
P_x{}^{N+\epsilon} &= P_x{}^R + \sum_{i=0}^{N} m^i\omega^2 U^i + \sum_{i=0}^{N} m^i\Omega^2 U^i + \left(F_0 - \sum_{i=0}^{N} m^i\Omega^2 Z^i\right)\frac{dU^N}{dZ} + \sum_{i=0}^{N}\left[\frac{dU^i}{dZ}\frac{K^i}{Z^i} - \frac{U^iK^i}{(Z^i)^2}\right] \\
P_y{}^{N+\epsilon} &= P_y{}^R + \sum_{i=0}^{N} m^i\omega^2 V^i + \left[F_0 - \sum_{i=0}^{N} m^i\Omega^2 Z^i\right]\frac{dV^N}{dZ} \\
M_y{}^{*N+\epsilon} &= M_y{}^{*R} + P_x{}^R(Z^N - R) + \sum_{j=0}^{N-1}\sum_{i=0}^{j} m^i\omega^2 U^i(Z^{j+1} - Z^j) + \sum_{j=0}^{N-1}\sum_{i=0}^{j} m^i\Omega^2 U^i(Z^{j+1} - Z^j) + U^N F_0 \\
&\quad - \sum_{j=0}^{N-1}\sum_{i=0}^{j} m^i\Omega^2 Z^i(U^{j+1} - U^j) + \sum_{j=0}^{N-1}\sum_{i=0}^{j}\frac{dU^i}{dZ}\frac{k^i}{Z^i}(Z^{j+1} - Z^j) - \sum_{j=0}^{N-1}\sum_{i=0}^{j}\frac{U^iK^i}{(Z^i)^2}(Z^{j+1} - Z^j) + \sum_{i=0}^{N}\left(\frac{dU^i}{dZ}K^i - \frac{U^iK^i}{Z^i}\right) \\
M_x{}^{N+\epsilon} &= M_x{}^R + P_y{}^R(Z^N - R) + \sum_{j=0}^{N-1}\sum_{i=0}^{j} m^i\omega^2 V^i(Z^{j+1} - Z^j) + V^N F_0 - \sum_{j=0}^{N-1}\sum_{i=0}^{j} m^i\Omega^2 Z^i(V^{j+1} - V^j)
\end{aligned}\right\} \quad [13]$$

By substituting Equations [13] into Equations [12], and defining some new symbols as

$$l^i = Z^{i+1} - Z^i, \quad c = \frac{\omega^2 L^4 m^1/l}{EI_{y0}{}^R}, \quad s = \frac{l}{L}, \quad A_j{}^i = A_j{}^i \frac{EI_{y0}{}^R}{L}, \quad B_j{}^i = B_j{}^i \frac{EI_{y0}{}^R}{L^2}, \quad C_j{}^i = C_j{}^i \frac{EI_{y0}{}^R}{L^3}$$

we obtain the following equations

$$\left.\begin{aligned}
U^N &= \frac{M_y{}^{*R}}{m^1 l\omega^2} F_a{}^N + \frac{P_x{}^R}{m^1\omega^2} F_b{}^N + \frac{M_x{}^R}{m^1 l\omega^2} F_c{}^N + \frac{P_y{}^R}{m^1\omega^2} F_d{}^N \\
V^N &= \frac{M_y{}^{*R}}{m^1 l\omega^2} F_f{}^N + \frac{P_x{}^R}{m^1\omega^2} F_g{}^N + \frac{M_x{}^R}{m^1 l\omega^2} F_h{}^N + \frac{P_y{}^R}{m^1\omega^2} F_i{}^N \\
L\frac{dU^N}{dZ} &= \frac{M_y{}^{*R}}{m^1 l\omega^2} F_a{}'^N + \frac{P_x{}^R}{m^1\omega^2} F_b{}'^N + \frac{M_x{}^R}{m^1 l\omega^2} F_c{}'^N + \frac{P_y{}^R}{m^1\omega^2} F_d{}'^N \\
L\frac{dV^N}{dZ} &= \frac{M_y{}^{*R}}{m^1 l\omega^2} F_f{}'^N + \frac{P_x{}^R}{m^1\omega^2} F_g{}'^N + \frac{M_x{}^R}{m^1 l\omega^2} F_h{}'^N + \frac{P_y{}^R}{m^1\omega^2} F_i{}'^N
\end{aligned}\right\} \quad [14]$$

Where four F are given by

$$\left.\begin{aligned}
F^{N+1}{}_{a,b,c,d} &= F^N{}_{a,b,c,d} + \frac{l^N}{L} F'^{N+1}{}_{a,b,c,d} - csC_x{}^N \left[0,1,0,0 + \sum_{i=0}^{N} \frac{m^i}{m^1}\left(1+\frac{\Omega^2}{\omega^2}\right) F^i{}_{a,b,c,d} + F'^N{}_{a,b,c,d}\left(\frac{F_0}{\omega^2 m^1 L}\right.\right. \\
&\quad \left.\left. - \sum_{i=0}^{N} \frac{m^i}{m^1}\frac{\Omega^2}{\omega^2}\frac{Z^i}{L}\right) + \sum_{i=0}^{N} \frac{K^i}{\omega^2 m^1 Z^i L} F'^i{}_{a,b,c,d} - \sum_{i=0}^{N} \frac{K^i}{\omega^2 m^1 (Z^i)^2} F^i{}_{a,b,c,d} \right] \\
&\quad - cs^2 B_x{}^N \left\{ 1,0,0,0 + \sum_{j=0}^{N-1} \frac{l^j}{l}\left[0,1,0,0 + \sum_{i=0}^{j} \frac{m^i}{m^1}\left(1+\frac{\Omega^2}{\omega^2}\right) F^i{}_{a,b,c,d}\right] + \sum_{j=0}^{N-1} (F^{j+1}{}_{a,b,c,d} - F^j{}_{a,b,c,d}) \right. \\
&\quad \left. \times \left[\frac{F_0}{\omega^2 m^1 l} - \sum_{i=0}^{j} \frac{m^i}{m^1}\frac{\Omega^2}{\omega^2}\frac{Z^i}{l}\right] + \sum_{j=0}^{N-1} \frac{l^j}{l} \sum_{i=0}^{j} \frac{F'^i{}_{a,b,c,d} K^i}{Z^i \omega^2 m^1 L} - \sum_{j=0}^{N-1} \frac{l^j}{l} \sum_{i=0}^{j} \frac{F^i{}_{a,b,c,d} K^i}{(Z^i)^2 \omega^2 m^1} + \sum_{i=0}^{N} \frac{F'^i{}_{a,b,c,d} K^i}{\omega^2 m^1 l L} \right. \\
&\quad \left. - \sum_{i=0}^{N} \frac{F^i{}_{a,b,c,d} K^i}{Z^i \omega^2 m^1 l} \right\} + csC_{xy}{}^N \left\{ 0,0,0,1 + \sum_{i=0}^{N} \frac{m^i}{m^1} F^i{}_{f,g,h,i} + F'^N{}_{f,g,h,i}\left(\frac{F_0}{\omega^2 m^1 L} - \sum_{i=0}^{N} \frac{m^i}{m^1}\frac{\Omega^2}{\omega^2}\frac{Z^i}{L}\right)\right\} \\
&\quad + cs^2 B_{xy}{}^N \left\{ 0,0,1,0 + \sum_{j=0}^{N-1} \frac{l^j}{l}\left[0,0,0,1 + \sum_{i=0}^{j} \frac{m^i}{m^1} F^i{}_{f,g,h,i}\right] + \sum_{j=0}^{N-1} (F^{j+1}{}_{f,g,h,i} - F^j{}_{f,g,h,i})\left[\frac{F_0}{\omega^2 m^1 l} - \sum_{i=0}^{j} \frac{m^i}{m^1}\frac{\Omega^2}{\omega^2}\frac{Z^i}{l}\right]\right\}
\end{aligned}\right\} \quad [15]$$

The other twelve F may be found by performing the substitution. This is not necessary fortunately, since by defining four new symbols from Equation [15], we may represent the F as follows

$$\left.\begin{aligned}
F^{N+1}{}_{a,b,c,d} &= F^N{}_{a,b,c,d} + \frac{l^N}{L} F'^{N+1}{}_{a,b,c,d} - csC_x{}^N (6)^{N+\epsilon}{}_{a,b,c,d} - cs^2 B_x{}^N (10)^{N+\epsilon}{}_{a,b,c,d} + csC_{xy}{}^N (15)^{N+\epsilon}{}_{f,g,h,i} \\
&\quad + cs^2 B_{xy}{}^N (18)^{N+\epsilon}{}_{f,g,h,i} \\
F^{N+1}{}_{f,g,h,i} &= F^N{}_{f,g,h,i} + \frac{l^N}{L} F'^{N+1}{}_{f,g,h,i} + csC_{xy}{}^N (6)^{N+\epsilon}{}_{a,b,c,d} + cs^2 B_{xy}{}^N (10)^{N+\epsilon}{}_{a,b,c,d} - csC_y{}^N (15)^{N+\epsilon}{}_{f,g,h,i} \\
&\quad - cs^2 B_y{}^N (18)^{N+\epsilon}{}_{f,g,h,i} \\
F'^{N+1}{}_{a,b,c,d} &= F'^N{}_{a,b,c,d} + csB_x{}^N (6)^{N+\epsilon}{}_{a,b,c,d} + cs^2 A_x{}^N (10)^{N+\epsilon}{}_{a,b,c,d} - csB_{xy}{}^N (15)^{N+\epsilon}{}_{f,g,h,i} - cs^2 A_{xy}{}^N (18)^{N+\epsilon}{}_{f,g,h,i} \\
F'^{N+1}{}_{f,g,h,i} &= F'^N{}_{f,g,h,i} + csB_{xy}{}^N (6)^{N+\epsilon}{}_{a,b,c,d} - cs^2 A_{xy}{}^N (10)^{N+\epsilon}{}_{a,b,c,d} + csB_y{}^N (15)^{N+\epsilon}{}_{f,g,h,i} + cs^2 A_y{}^N (18)^{N+\epsilon}{}_{f,g,h,i}
\end{aligned}\right\} \quad [16]$$

Equations [13], [14], and [16] are the basis for calculating the natural frequency of the beam. A frequency is assumed, and the values of the F are calculated. If the assumed frequency is a natural frequency, the boundary conditions at the free end of the beam will be satisfied; that is, $P_x{}^{M+\epsilon}$, $P_y{}^{M+\epsilon}$, $M_x{}^{M+\epsilon}$, $M_y{}^{*M+\epsilon}$, will all be equal to zero if M is the last mass. To check this we return to Equations [13], but write them in terms of $(6)^{M+\epsilon}$; $(10)^{M+\epsilon}$, and so on, that is

$$\left.\begin{aligned}
M_x{}^{M+\epsilon} &= M_y{}^{*R}(18)_f{}^{M+\epsilon} + P_x{}^R l(18)_g{}^{M+\epsilon} + M_x{}^R(18)_h{}^{M+\epsilon} + P_y{}^R l(18)_i{}^{M+\epsilon} \\
lP_y{}^{M+\epsilon} &= M_y{}^{*R}(15)_f{}^{M+\epsilon} + P_x{}^R l(15)_g{}^{M+\epsilon} + M_x{}^R(15)_h{}^{M+\epsilon} + P_y{}^R l(15)_i{}^{M+\epsilon} \\
M_y{}^{*M+\epsilon} &= M_y{}^{*R}(10)_a{}^{M+\epsilon} + P_x{}^R l(10)_b{}^{M+\epsilon} + M_x{}^R(10)_c{}^{M+\epsilon} + P_y{}^R l(10)_d{}^{M+\epsilon} \\
lP_x{}^{M+\epsilon} &= M_y{}^{*R}(6)_a{}^{M+\epsilon} + P_x{}^R l(6)_b{}^{M+\epsilon} + M_x{}^R(6)_c{}^{M+\epsilon} + P_y{}^R l(6)_d{}^{M+\epsilon}
\end{aligned}\right\} \quad [17]$$

In order that $M_x^{M+\epsilon}$, $M_y^{M+\epsilon}$, $lP_y^{M+\epsilon}$, and $lP_x^{M+\epsilon}$ all equal zero the following determinant must equal zero.

$$\Delta = \begin{vmatrix} (18)_f^{M+\epsilon} & (18)_g^{M+\epsilon} & (18)_h^{M+\epsilon} & (18)_k^{M+\epsilon} \\ (15)_f^{M+\epsilon} & (15)_g^{M+\epsilon} & (15)_h^{M+\epsilon} & (15)_k^{M+\epsilon} \\ (10)_a^{M+\epsilon} & (10)_b^{M+\epsilon} & (10)_c^{M+\epsilon} & (10)_d^{M+\epsilon} \\ (6)_a^{M+\epsilon} & (6)_b^{M+\epsilon} & (6)_c^{M+\epsilon} & (6)_d^{M+\epsilon} \end{vmatrix} = 0$$

By plotting Δ versus ω, the values of ω at which $\Delta = 0$ may be obtained.

Once the natural frequency has been found, the deflection curve may be obtained from Equations [14], and the moment and shear distribution from Equations [17]. To do this it is only necessary to set one of the shears or moments at the base of the beam equal to some arbitrary number, say 1, and calculate the other shears and moments at the base of the beam from Equations [17]. If in these Equations [17], we replace $M+\epsilon$ by $N+\epsilon$, and allow N to vary from 1 to M, we can calculate the shear and moment distribution. The same values of the shears and moments at the base of the beam which were calculated in the foregoing may be substituted in to Equations [14], and the deflection curve calculated by letting N vary from 1 to M.

Numerical Example

Since many of the formulas developed in the preceding text are rather formidable in appearance, a numerical example will be worked in the hope that the procedure will be clarified.

The blade chosen for this illustration is a long, low-pressure turbine blade having two lashing wires and a shroud, Fig. 2. The blade is mounted on a disk and rotates at a speed of 1800 rpm. After the curves of area distribution, moments of inertia, and angle between minimum moment-of-inertia axis and the axis of rotation have been obtained, the procedure is as follows:

1 Locate point of fixity Z^R. This point need not be the same in both planes, but for the purpose of this example this will be assumed to be true. The chosen point of fixity is shown in Fig. 2.

2 Divide blade above Z^R into a number of sections commensurate with the mode to be calculated. In this case where the third mode will be calculated, five sections should be adequate. Calculate the volume of each section and place it at the center of gravity of the section. The volume of lashing wire and shroud are assumed to be concentrated at those points, making for our example a total of eight concentrated masses, Fig. 2.

TABLE 1 CALCULATION OF A-FACTORS

N	I_{x0}	I_{y0}	γ	$\cos^2\gamma$	$\sin^2\gamma$	I_{x0}/I_{y0}	$\frac{I}{I_{x0}} = \cos^2\gamma + \frac{I_{y0}}{I_{x0}}\sin^2\gamma$	$\frac{I_{y0}{}^R}{I_{y0}} I$
2	1.670	0.1430	11.0	0.964	0.0364	0.0857	0.967	$3.02 \times 1 = 3.02$
..	1.265	0.1023	15.7	0.926	0.0736	0.0809	0.932	$4.06 \times 4 = 16.24$
3	0.950	0.0670	20.7	0.875	0.1255	0.0705	0.884	$5.89 \times 1 = 5.89$
								Σ 25.15

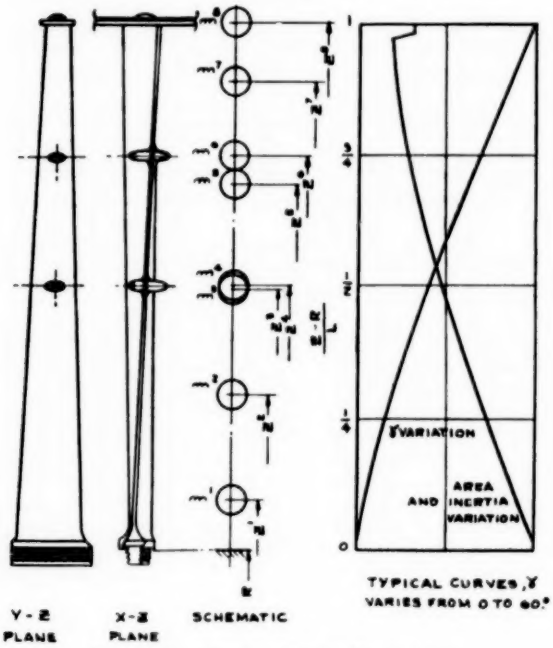

Fig. 2 Beam Used in Sample Calculation

3 Calculate $A^N_{x,y,xy}$, $B^N_{x,y,xy}$, and $C^N_{x,y,xy}$ for the sections between mass concentrations by means of the formulas given previously. For example

$$A_x{}^N = A_x{}^N \frac{EI_{y0}{}^R}{L} = \int_{Z^N}^{Z^{N+1}} \frac{I_y{}^R}{I_{y0}} \left(\cos^2\gamma + \frac{I_{y0}}{I_{x0}}\sin^2\gamma\right)\frac{dZ}{L}$$

Take the blade section between the second and third mass concentrations. Table 1 illustrates the method of calculation.

By Simpson's rule

$$A_x{}^2 = \frac{l^2(25.15)}{L \quad 6} = 0.1994\left(\frac{25.15}{6}\right) = 0.836$$

By a similar procedure the A, B, and C for all the sections may be calculated. These values for the beam under consideration are given in Table 2.

4 Calculate miscellaneous constants (K^i, C, S) as follows:

Here we can consider the lashing-wire factor for an infinite row of blades and

$$\frac{1}{K^i} = \frac{(\tau_i{}^*)^3}{12\tau_i{}^3 EI_{wi}} + \frac{k\tau_i{}^*}{\tau_i{}^3 A_{wi} G}$$

where τ = pitch of blades at wire
τ^* = flexible length of wire
I_{wi} = moment of inertia of wire
A_{wi} = area of wire
k = numerical factor (4/3 for elliptical or circular wire; 3/2 for rectangular wire)

TABLE 2 VALUES OF A, B, C FOR BEAM

	N 0	1	2	3	4	5	6	7
A_x	0.1236	0.466	0.836	0.03582	1.551	0.748	3.104	3.625
A_y	0.01072	0.0480	0.1401	0.007618	0.555	0.4546	3.38	7.24
A_{xy}	−0.003044	−0.05235	−0.2255	−0.012527	−0.789	−0.5355	−3.074	−4.97
B_x	0.006946	0.05055	0.0930	0.0001080	0.1674	0.0222	0.246	0.1900
B_y	0.006262	0.00549	0.01688	0.0000230	0.0675	0.01410	0.2987	0.396
B_{xy}	−0.002132	−0.00672	−0.02743	−0.00003785	−0.0926	−0.01632	−0.259	−0.2665
C_x	0.0004854	0.00703	0.01318	4.33×10^{-7}	0.0229	0.000860	0.0247	0.01281
C_y	0.0000426	0.000791	0.002505	0.924×10^{-7}	0.00977	0.000560	0.03213	0.02665
C_{xy}	−0.00001591	−0.00102	−0.00409	-1.52×10^{-7}	−0.01319	−0.000641	−0.0270	−0.01799

The blade under consideration has three wires, one of which is calculated as follows: For the bottom wire

$$\frac{1}{K^4} = \frac{(2.01)^3}{12(2.427)^2(29)10^6(0.00555)} + \frac{(4/3)(2.01)}{(2.427)^2\left(\frac{0.794}{2.01}\right)(11.5)10^6}$$

$$\frac{1}{K^4} = 0.713 \times 10^{-6} + 0.100 \times 10^{-6} = 0.813 \times 10^{-6}$$

Also

$$\frac{1}{K^6} = 2.791 \times 10^{-6} \quad \text{and} \quad \frac{1}{K^8} = 0.6174 \times 10^{-6}$$

$$s = \frac{l}{L} = 0.2$$

The lower modes of vibration of grouped turbine blades are modes in which the blades move in unison approximately tangentially (first mode), approximately axially (second mode), and again approximately tangentially (third mode).

Let us calculate the third mode, which would correspond to the second mode of vibration in the tangential direction. For this, we assume $\omega = 235(2\pi) = 470\pi$ radians per sec (rad/sec), then

$$c = \frac{\omega^2 L^4 m^1}{EI_{y0}{}^R l} = 592.15; \quad \frac{\Omega}{\omega} = \frac{30}{235} = 0.1278$$

5 If now the total centrifugal force of the blade is calculated, we have all the information necessary for checking the assumed frequency of 235 cycles per sec (cps). We now turn to Form 1 and fill in columns (1), (2), (3), (7), (11), and (12), the data for which we now have at hand. We also calculate the values of the terms $csB_x{}^N$, $cs^2A_x{}^N$, and so on, for each mass location and place them in the left-hand column under the appropriate heading. The typewritten numbers on Form 1 have now all been filled in and these numbers apply to the calculations for all the F for a particular frequency. We note from Equations [15] that the F are calculated four at a time, so four sheets similar to Form 1 will be required to process the trial frequency of 235 cps. From Equations [14] all the F equal zero at $Z = Z^R$. The initial values of $(6)_{a,b,c,d}$, $(10)_{a,b,c,d}$, and so on, are given in Equations [15]. These initial values are the only difference between the calculation of the F. As an illustration, Form 1 has been used to calculate F_a, F_a', F_f, and F_f'. The column headings for Form 1 are such that the F may be calculated by merely following the headings and referring to Equations [16]. After the F have been calculated, we substitute the last calculated values of $(6)_{a,b,c,d}$, $(10)_{a,b,c,d}$, and so on, into the determinant Δ and calculate its value. Carrying this out for the beam under consideration gives a value of $\Delta = 318$. A previous calculation assuming $\omega = 230(2\pi) = 460\pi$ rad/sec gave $\Delta = 1151$, so by extrapolation $\omega = 474\pi$ rad/sec or 237 cps.

Since the last lashing wire enters the calculations at the very end, it is relatively easy to carry its mass and spring constant along as unknowns and determine the various values of mass and spring constant required to make 235 cps the natural frequency. The mass of the lashing wire also enters the calculations through its effect on F_0, but since other considerations limit the size of the lashing wires to a fairly limited range, any reasonable size will suffice for this part of the calculation. Varying m^8 and K^8 to make $\Delta = 0$ gives a curve of the form shown in Fig. 3.

We now undertake the calculation of the shear and moment distribution. To do this we turn to Equations [17]. Since 235 cps is not the natural frequency of the system, the boundary conditions will not be satisfied; hence the left-hand side of Equations [17] may not be set equal to zero. We may, however, set three of these quantities equal to zero, let $M_y{}^{*R}$ equal, say, 1, and solve for $M_x{}^R$, $lP_x{}^R$, and $lP_y{}^R$. These values may

	(1)	(2)	(3)	(4)	(5)	(6)	(7)	(8)	(9)	(10)
n										
0	0	0	.06650	0	0	0	.4775	0	0382	1
1	1	.01630	.04839	.1169	1416	.2585	.9950	.1163	.4144	1.0382
2	.6456	.01051	.01462	1.1992	.3519	1.8680	.9980	1.3108	1.2335	1.5688
3	.4650	.007588	.02317	4.2315	1.5798	7.1274	.0299	.1659	.0485	4.1132
						.019479				.14779 F⁴
						-.0128 F				-.0874 F⁴
						1.2788				8.7014
4	.0405	.000660	.02217	.3858	1.5932	8.6095	.9660	6.9671	7.6324	14.0290
5	.3320	.005409	.01293	28.3842	10.1063	43.7128	.2830	9.5106	4.0027	28.6285
						.006589				-.04383 F⁴
						-.003764 F				-.02439 F⁴
						6.8935				6.83816
6	.0329	.000536	.01198	4.6857	17.8488	23.0243	.7100	32.0746	49.7659	102.8334
						.017499				.1788 F⁴
						-.008757				-.0885 F⁴
						248.936				8389.1262
8	.1630	.002654	0	737.0062	0	1842.1396				3011.8094

	(11)	(12)	(13)	(14)	(15)	(16)	(17)	(18)
n								
0		.3325	0	0	0	.4775	0	.0006105	0
1		.2419	.001836	.003489	.005325	.9950	.001827	.027950	.0006105
2		.1731	.075766	.054366	.131968	.9980	.077292	.222977	.030387
3		.1158	.653555	.378608	1.110765	.0299	.021862	.011785	.330636
4		.1108	.061046	.392320	1.184523	.9660	.785268	3.216874	.364313
5		.0665	10.135088	5.052451	15.979742	.2830	3.092423	2.242174	4.346455
6		.0329	2.145380	10.922859	23.995530	.7100	9.281556	42.258177	9.681052
7		.0268	164.15681	64.082568	241.31175	.5670	100.48885	114.13931	61.220825
8		0	818.82765	0	997.05685				275.84908

Form 1 Table of Calculations

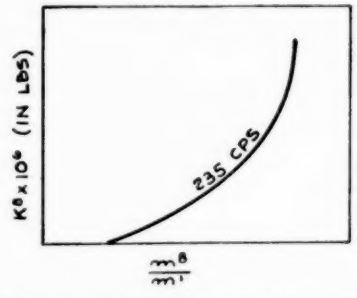

Fig. 3 Variation in Shroud Mass and Spring Constant for Constant Frequency

$(11)^{**}$

$CSB_x^{**}(6)^{**}$		$CS^2A_x^{**}(10)^{**}$		$-CS^3B_x^{**}(15)^{**}$		$-CS^4A_x^{**}(18)^{**}$		P_x^{**}	$\frac{1}{L}^{**}$	$(11)^{**}P_x^{**}$	$-CSC_x^{**}(6)^{**}$		$-CS^2B_x^{**}(10)^{**}$		$CSC_x^{**}(15)^{**}$		$CS^2B_x^{**}(18)^{**}$		P_x^{**}
.8226	0	2.927	2.927	.02529	0	.07210	0	0	.0955	.2795	-.05748	0	-.1645	-.1645	-.001884	0	-.005050	0	0
5.487	1.548	11.04	11.462	.7958	.004	1.249	.001	2.927	.199	3.1725	-.8325	-.2152	-1.198	-1.2438	-.1208	-.0006	-.1991	-.00010	.1150
11.02	20.585	19.80	31.064	3.249	.429	5.341	.162	15.942	.1992	13.5819	-1.541	-2.9159	-2.203	-3.4563	-.4844	-.0639	-.6497	-.01974	1.8278
.0128	0912	.848	3.488	.00449	.005	.296	.098	68.182	.0598	42975	-.9264	-.0004	-.00256	-.0105	-.1804	-.0000	-.000896	-.00030	8.9539
19.82	174.525	36.74	515.425	10.77	12.994	18.69	6.806	71.864	.1932	51.0084	-2.712	-23.8805	-3.965	-55.6250	-1.562	-1.8502	-2.193	-.7989	9.3724
2.63	114.965	17.77	507.297	1.933	30.889	12.68	55.113	781.617	.0566	44.3273	-.102	-4.4587	-.526	-15.0586	-.076	-1.2145	-.387	-1.6821	78.2262
29.13	1835.8875	73.53	7561.340	10.67	735.943	72.81	704.577	1489.881	.142	1150.5635	-2.926	-184.4091	-5.827	-599.2102	-3.198	-76.73770	-6.135	-58.39325	140.1386
22.50	7232.382	85.87	15857.948	11.46	7615.789	117.7	7205.681	12327.939	.1134	5697.1887	-1.517	-487.6233	-4.500	-831.0326	-2.130	-513.9946	-6.312	-386.42585	970.95664
								50239.759											4449.0686

FORM # 1 ω = 470.11 rad./sec. (Rotating)

$(11)^{**}$

$-CSB_y^{**}(6)^{**}$		$-CS^2A_y^{**}(10)^{**}$		$CSB_y^{**}(15)^{**}$		$CS^2A_y^{**}(18)^{**}$		P_y^{**}	$\frac{1}{L}^{**}$	$(11)^{**}P_y^{**}$	$CSC_y^{**}(6)$		$CS^2B_y^{**}(10)^{**}$		$-CSC_y^{**}(15)^{**}$		$-CS^2B_y^{**}(18)^{**}$		P_y^{**}
.02529	0	.07210	.07210	.07616	0	.2539	0	0	.0955	.006886	-.001884	0	-.005050	-.005050	-.005052	0	-.01483	0	0
.7958	.20571	1.2410	1.28841	.6931	.00346	1.137	.00069	.07210	.199	.312304	-.1208	-.031227	-.1591	-.165178	-.09368	-.000499	-.1300	-.000079	.001836
3.249	6.04913	5.341	8.37949	1.499	.26380	3.318	.10082	1.57037	.1992	3.263615	-.6844	-.904859	-.6497	-1.019314	-.2967	-.038155	-.3958	-.01249	.117357
.00449	.03200	.246	1.21751	.00272	.00302	.181	.05985	16.38361	.0598	1.05022	-.1804	-.000128	-.000896	-.003685	-.1068	-.000012	-.000945	-.000180	1.405485
10.97	86.54634	18.49	262.20201	7.946	9.46908	11.15	4.79072	17.69599	.1932	75.49.1001	-1.562	-13.754191	-2.193	-30.765991	-1.158	-1.371678	-1.598	-.582172	1.507312
1.933	84.49684	17.68	363.00938	1.670	26.68617	10.77	46.81132	390.75414	.0566	51.605494	-.076	-3.322173	-.387	-11.079230	-.067	-1.070643	-.334	-1.451716	30.527334
10.67	1932.9553	72.81	7487.2595	35.37	848.72190	80.05	774.96821	911.75785	.142	1687.7098	-3.198	-201.55171	-6.135	-630.88291	-3.805	-91.302892	-7.075	-68.493443	65.209106
31.56	10144.621	117.7	21736.118	46.90	11317.521	171.5	10499.371	11955.703	.1134	7445.088	-2.130	-684.66380	-6.312	-1165.6617	-3.156	-761.57988	-9.380	-574.25134	770.68785
								65653.334											5029.6175

FORM 1 TABLE OF CALCULATIONS *(continued)*

then be substituted into the fourth of Equations [17] to obtain $lP_x^{M+\epsilon}$. Of course the selection of the equations to be set equal to zero and the shear or moment to be set equal to 1 is arbitrary.

We have then for the beam under consideration

$$0 = 275.84908M_y^{*R} + 291.17688P_x^R l + 49.009526M_z^R + 87.246161P_y^R l$$

$$0 = 997.05683M_y^{*R} + 1051.5778P_x^R l + 167.44360M_z^R + 292.54252P_y^R l$$

$$0 = 9011.8034M_y^{*R} + 9498.1883P_x^R l + 1489.1951M_z^R + 2592.4785P_y^R l$$

If M_y^{*R} is set equal to 1, the solution becomes

$$M_y^{*R} = 1.0000; \quad lP_x^R = -1.0423;$$

$$lP_y^R = -0.8217; \quad M_z^R = 2.0266$$

Term $lP_x^{M+\epsilon}$ then equals 0.0233 or $2^1/_4$ per cent of the value of lP_x^R. These values of M_y^{*R}, M_z^R, and so on may now be used in conjunction with Equations [17] to calculate the shear and moment distribution by replacing $M+\epsilon$ by $N+\epsilon$ and allowing N to vary from 1 through 8. This has been done for both 235 and 230 cps. The results were then extrapolated to give the values at the natural frequency of 237 cps. Fig. 4 is the result for the moments. The values of the shears times the length l are given in Table 3.

The calculation of the deflection curve is quite similar; the previously calculated values of M_y^{*R}, M_z^R, and so on, are used in conjunction with Equations [14] to calculate

$$(m^1/\omega^2)U, (m^1/\omega^2)V, (m^1/\omega^2)\frac{LdU}{dZ}, (m^1/\omega^2)\frac{LdV}{dZ}$$

at the various mass locations. Since it is the shape of the deflection curve which is of interest, the factor $m^1/\omega^2 U$ has been called U, with similar simplifications in the case of

$$V, L\frac{dU}{dZ} \text{ and } L\frac{dV}{dZ}$$

TABLE 3 VALUE OF SHEARS TIMES LENGTH

N	0	1	2	3	..	4	5	..	6	7	.	8
lP_x	—1.0455	—0.8399	—0.2059	—0.3957	—0.0098	—0.4431	—0.6278	—0.0376	0.5988	0.3294	—0.0235	—0.0016[a]
lP_y	—0.8285	—0.7851	—0.5720	—0.2688	...	—0.2436	—0.0365	.	—0.0193	—0.0422	...	0.0000

[a] Should equal zero.

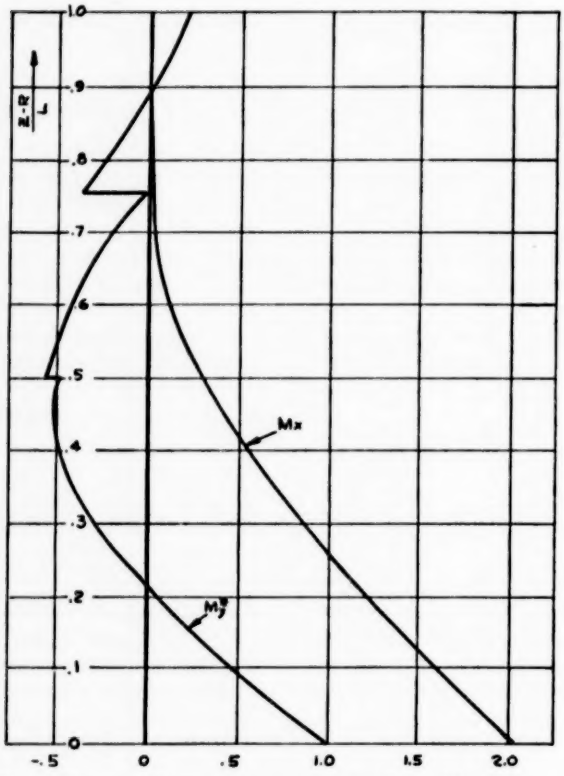

FIG. 4 BENDING-MOMENT DISTRIBUTION FOR THIRD-MODE VIBRATION

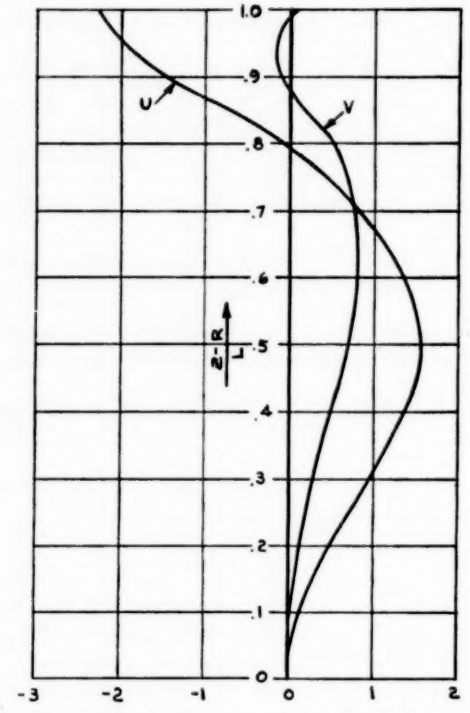

FIG. 5 DEFLECTION CURVES FOR THIRD-MODE VIBRATION

The deflection curves have been calculated for both 235 and 230 cps and extrapolated to obtain the curve for 237 cps. This curve is shown in Fig. 5. The values of the slopes have been used in the construction of the curves, and hence will not be tabulated.

It is important to note that the deflections, slopes, moments, and shears are obtained from small differences of large numbers; hence it is better to calculate the curves for the trial frequencies and interpolate or extrapolate rather than interpolating or extrapolating the (18), (10), and so on, and F-values and calculating the required quantities.

RESULTS AND DISCUSSION

In the consideration of any calculation method, it is, of course, of primary importance to have an experimental check of calculated values. Such a comparison is given in Table 4.

TABLE 4 COMPARISON OF THEORETICAL AND TEST RESULTS

Mode	Calculated value, cps	Average experimental value, cps	Error, per cent
1st (stationary)	63.6	65.4	−2.76
1st (rotating)	79.5	75.1	5.54
2nd (rotating)	115	106.3	7.57
3rd (rotating)	237	225.7	4.77

These percentage differences are quite large, and indicate an appreciable discrepancy between the actual behavior of the physical system and the assumptions involved in the calculation. A careful analysis of the situation reveals the following to be the source of the difficulty:

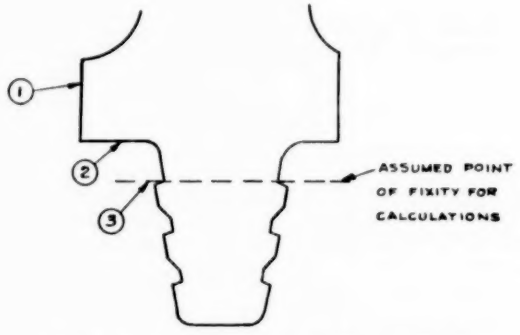

FIG. 6 POINT OF ATTACHMENT OF BEAM IN FIG. 2

Consider a schematic drawing of the root of the blade, Fig. 6. When the blade is not rotating there is a force fit between the groove and the blade root at surfaces 2 and 3, as well as contact between adjacent blades at surface 1. This serves to make the point of fixity higher than surface 3; hence the actual stationary frequency will be higher than the calculated value. Table 4 confirms this. When the blade is rotating, the centrifugal forces lift the blade and there is no contact at surfaces 1 and 2. This makes surface 3 the first contact between root and groove. The dimensions of the root and groove are small compared to the dimensions of the blade, so during rotation the point of fixity will be below surface 3, and the actual frequencies will be lower than the calculated values. This is again borne out by Table 4. The second mode of vibration is predominantly in the Y-Z-plane and this mode will be lowered still further by disk flexibility. Subsequent calculations by this method on other blades proved

to be more accurate, indicating that the method is sufficiently accurate for practical calculations.

Acknowledgments

The basis of this paper was worked out by Mr. Jarrett in his thesis "Vibration of Airplane Propellers," available in the library of the University of Pennsylvania. The method was adapted to turbine-blade calculations by Mr. Jarrett, and this paper in its preliminary form was prepared by him before his death.

Mr. Warner, the coauthor, put the paper in final form for publication and supplied the numerical example and test results which were obtained at the Steam Division of Westinghouse Electric Corporation.

Two-Dimensional Flow Through a Diffuser With an Exit Length

By K. R. GALLE[1] and R. C. BINDER[2]

A diffuser with an "exit length" is one with a channel of uniform cross section following the diffuser. Tests were made of different diffusers with and without exit lengths. The data were for steady, incompressible, two-dimensional flow. The performance of each diffuser was improved by the presence of an exit length. As compared to flow without an exit length, flow with an exit length is characterized by a reduced boundary-layer growth, by a small decrease in the pressure rise across the diverging section, and by a decrease in the static-pressure gradient at the diffuser inlet.

Nomenclature

The following nomenclature is used in the paper:

D = width of exit channel
L = length of wall in diverging channel
p = static pressure at any point along the diffuser
p_0 = static pressure at end of exit length
u = value of v in boundary layer
U = value of v outside boundary layer
v = velocity at any point in section
N = average velocity at inlet to diffuser
X = distance along wall from inlet to diffuser
y = distance from and normal to diffuser boundary
δ = disturbance thickness of boundary layer, value of y when $u = U$
ν = kinematic viscosity of fluid
ρ = density of fluid

Introduction

Various problems in fluid mechanics are associated with the flow in a diffuser. One problem is that of flow in a diffuser with a "discharge length" or an exit length. The terms discharge length or exit length indicate a channel of uniform cross section following the diffuser.

Some previous tests, such as those by Peters,[3] indicated that the pressure rise was incomplete in the diffuser section and that the point of maximum pressure was downstream from the diffuser in the exit length. These previous tests did not give all the desired information. The possibility of increasing the efficiency of a diffuser by means of a discharge length is very attractive. It would be helpful to know the nature of the action. Accordingly, an experimental investigation was made to obtain further basic data.

Description of Apparatus

Fig. 1 is a diagrammatic sketch of the apparatus. Air from a fan was passed through an inlet or plenum chamber, then through a diffuser with diverging walls, and then through a discharge length with parallel walls. The boundary layer was removed from the top and bottom flow-channel walls to maintain two-dimensional flow in the mid-plane.

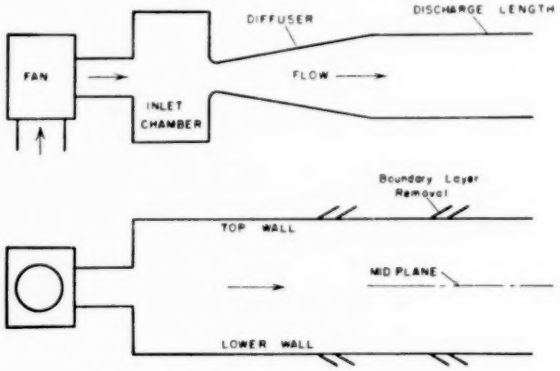

Fig. 1 Diagrammatic Sketch of Apparatus

The static pressure distribution along the walls of the diffuser and the discharge length was measured by wall taps at the mid-plane and a multiple manometer. Boundary-layer traverses, normal to the wall, at different stations at the mid-plane, were made with a cylindrical total-head tube mounted with a micrometer head. With this arrangement, a cylinder was held with its axis normal to the flow. An opening in the cylinder pointing directly upstream gave the total pressure. One tube was 0.049 in. diam., and another was $^1/_{16}$ in. diam.

Table 1 gives the main dimensions of three different channels used in the tests.

TABLE 1 DIMENSIONS OF CHANNELS

Channel	A	B	C
Throat width, in.	2.20	2.18	2.20
Exit width, in.	5.75	6.63	5.75
Total angle, deg, between walls of diverging section	8.14	10.20	8.14

In channel C, wires were stretched at the throat to produce the effect of an initial boundary layer.

The surfaces in contact with the flowing fluid were smooth, shellacked wood.

Test Results

The flow velocities were low enough so that the flow could be regarded as incompressible. Thus the following data apply to

[1] Research Engineer, Boeing Airplane Company, Seattle, Washington.

[2] Professor of Mechanical Engineering, Purdue University, West Lafayette, Indiana. Mem. ASME.

[3] "Energieumsetzung in Querschnittserweiteninger bei verschiedenen Zulaufbedingungen," by H. Peters, *Ingenieur Archiv*, vol. 2, 1931, pp. 92–107.

Presented at the National Conference of the Applied Mechanics Division, Minneapolis, Minn., June 18–20, 1953, of The American Society of Mechanical Engineers.

Discussion of the paper should be addressed to the Secretary, ASME, 29 West 39th Street, New York, N. Y., and will be accepted until October 10, 1953, for publication at a later date. Discussion received after the closing date will be returned.

Note: Statements and opinions advanced in papers are to be understood as individual expressions of their authors and not those of the Society. Manuscript received by ASME Applied Mechanics Division, October 10, 1952. Paper No. 53—APM-20.

the steady, incompressible two-dimensional flow in the midplane.

In Fig. 2 the pressure at each position in terms of a dimensionless ratio is plotted as a function of distance. The value X/L of one refers to the end of the diverging section. The circles in Fig. 2 refer to the flow in the combination of diverging section with exit length, whereas the crosses refer to the flow in the diverging section with no exit length. The boundary layer was induced at the diffuser inlet by a wire. Fig. 3 shows a similar type of plot for a different diffuser.

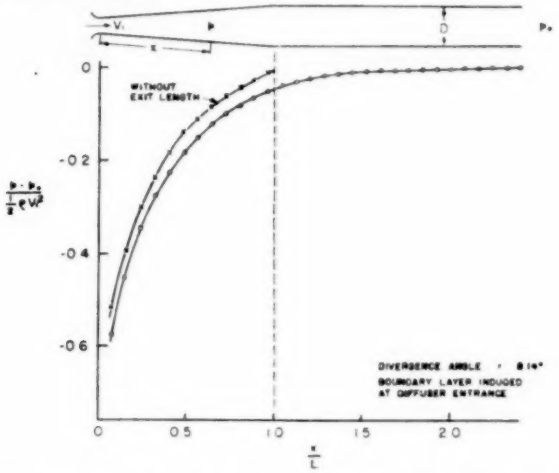

Fig. 2 Pressure Rise in Diffuser and Discharge Length With Boundary Layer Induced at Diffuser Entrance

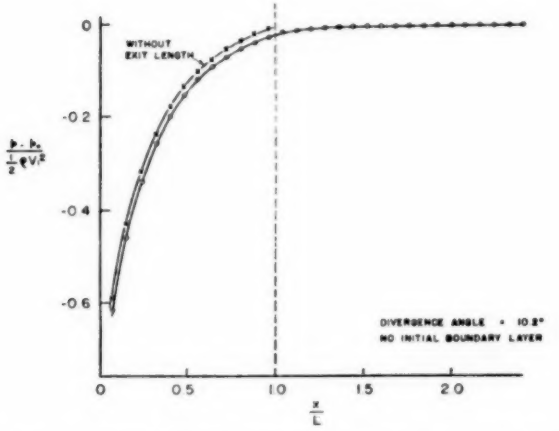

Fig. 3 Pressure Rise in Diffuser and Discharge Length With No Initial Boundary Layer

In each channel tested there was a pressure rise in the discharge length. The pressure rise in the case of the diffuser with an initial boundary layer was greater than the corresponding pressure rise in the channel with no initial boundary layer.

Fig. 4 shows typical velocity profiles in the diverging section. Fig. 5 shows typical velocity profiles in the discharge length.

Tests of all channels revealed a tendency of the velocity profile to flatten out in the discharge length, so that the velocity of the main flow continued to decrease beyond the end of the diverging section. As long as a core of potential flow exists in the region of

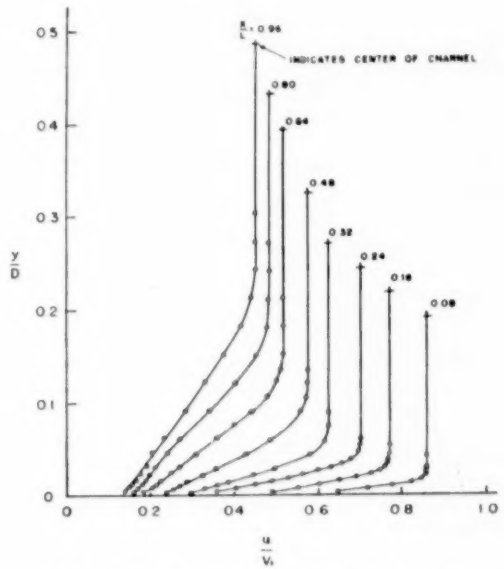

Fig. 4 Velocity Profiles in Diverging Section

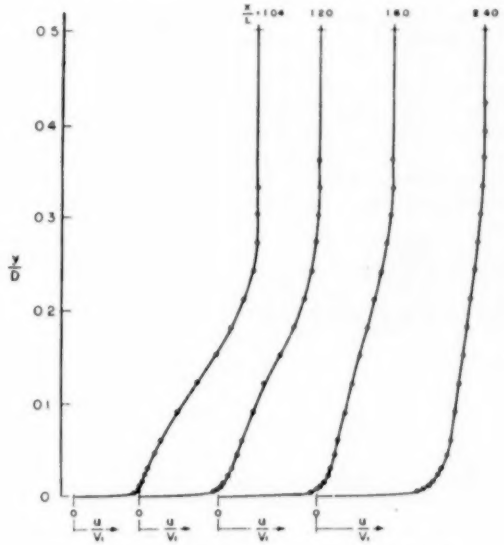

Fig. 5 Velocity Profiles in Discharge Length

decreasing velocity, retarding the main flow should result in a rising pressure.

The "displacement thickness" is defined by the relation

$$T = \frac{1}{U}\int_0^{\delta} (U - u)dy$$

where U is the uniform velocity in the frictionless or potential core outside the boundary layer. The disturbance thickness δ is the value of y at $u = U$. Studies of all test results showed that the displacement thickness decreased in the discharge length, and that the discharge length reduced the growth of the boundary layer in the diverging portion.

Adaptation of Data

Various adaptations or organizations of data are possible. One method will be used, primarily because it is convenient for calculation of diffuser efficiency. Binder[4] called attention to a method of calculating boundary-layer growth in extending some work by Buri.[5]

Let the functions ψ and Γ represent the following dimensionless quantities.

$$\psi = \frac{d}{dx}\left[T\left(\frac{UT}{\nu}\right)^{1/4}\right] \quad [1]$$

$$\Gamma = \frac{T}{\rho U^2}\frac{dp}{dx}\left(\frac{UT}{\nu}\right)^{1/4} \quad [2]$$

A simple relation between the two foregoing relations is assumed as

$$\psi = a + b\Gamma \quad [3]$$

where a and b are dimensionless constants. Experimental data checked this relation for flow without separation. Fig. 6 shows a plot of ψ as a function of Γ for all the tests. Fig. 6 applies only to the diverging portion. In the diverging portion, Equation [3] was satisfied by $a = 0.013$ and $b = 5.94$. The constants a and b for flow with a discharge length were essentially unchanged from those found in tests without a discharge length. Integration of Equation [3] gives a relation which can be used for calculating boundary-layer growth.

The function Γ may be used as a criterion for separation. For values of Γ less than 0.08, the possibility of separation is remote, although the possibility of separation is strong if Γ exceeds 0.12, averaged from values obtained on opposite sides of the channel. In tests on diffuser channels, values of Γ as high as 0.19 were obtained on one side before separation occurred, owing to unsymmetrical development of the boundary layer. When exit lengths were added to these channels, the maximum value of Γ was 0.13, due to a reduction in boundary-layer growth and greater symmetry of flow.

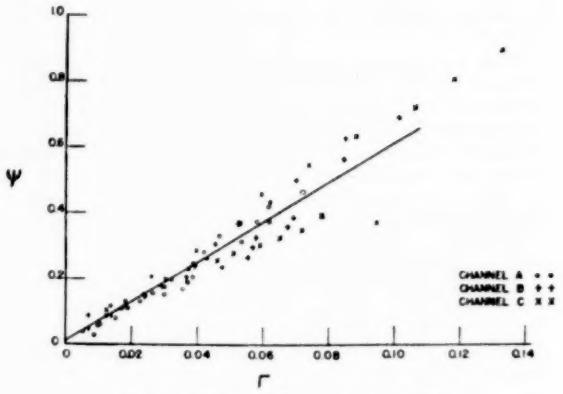

Fig. 6 Relation Between ψ and Γ

Conclusion

To summarize, the performance of each diffuser tested was improved by the presence of a discharge length. As compared to flow without a discharge length, flow with a discharge length is characterized by a reduced boundary-layer growth, by a small decrease in the pressure rise across the diverging channel alone, and by a decrease in the static-pressure gradient at the diffuser entrance. If the state of flow at the entrance and the over-all pressure rise are the same, the tendency for separation to occur is reduced substantially by the presence of a discharge length which retards the growth of the boundary layer.

Acknowledgment

The authors are grateful to A. A. Potter, Dean of Engineering, and Prof. H. L. Solberg, both of Purdue University. These gentlemen made available the facilities for the tests. This paper includes material adapted from a master's thesis.[6]

[4] "Calculation of Diffuser Efficiency for Two-Dimensional Flow," by R. C. Binder, Journal of Applied Mechanics, Trans. ASME, vol. 69, 1947, p. A-213.

[5] "Eine Berechnungsgrundlage für die turbulente Grenzschicht bei beschleurigter und vezogerter Grundstromung," by A. Buri, dissertation, Zurich, Switzerland, 1931.

[6] "Investigation of Two-Dimensional Diffuser Flow," by K. R. Galle, MS thesis, Purdue University, West Lafayette, Ind., August, 1949.

Axisymmetric Flow of an Ideal Incompressible Fluid About a Solid Torus[1]

By E. STERNBERG[2] AND M. A. SADOWSKY,[3] CHICAGO, ILL.

This paper contains an exact solution in series form to the problem presented by the irrotational, axisymmetric flow of an ideal, incompressible fluid past a solid torus of circular cross section. At infinity the fluid is assumed to be in a state of uniform motion parallel to the axis of the torus. The solution is based on the use of toroidal co-ordinates, and is given in terms of Legendre functions of fractional order as well as complete and incomplete elliptic integrals of the first and second kind. The individual component solutions employed here are interpreted physically through their relation to the basic ring singularities represented by the source ring and the vortex ring. The problem is first approached via Stokes's stream function exclusively and is subsequently re-solved independently in terms of the velocity potential alone. The convergence of the pertinent series developments is found to be unusually favorable, and a complete streamline pattern, corresponding to an illustrative numerical example, is included.

Introduction

POTENTIAL problems involving toroidal boundaries have received repeated attention in the literature. Apparently the first investigation of this kind is due to Carl Neumann (1)[4] who dealt with the distribution of temperature in a solid torus and with the analogous problem in electrostatics. The corresponding axisymmetric problem in ideal fluid flow was first investigated by Hicks (2) and was reconsidered later by Dyson (3), who also examined certain unsymmetric flow cases associated with the torus. The rigorous treatment of allied problems in the theory of elasticity is more recent; Freiberger (4) disposed of the problem of pure torsion of a torus of circular cross section, whereas the case of pure bending was treated by the current authors (5). It is this last investigation which motivated the present study, and the analytical prerequisites needed here were established to a considerable extent in connection with the work described in (5).

Although the hydrodynamic investigations cited previously yielded formal solutions characterizing the irrotational axisymmetric flow of an inviscid, incompressible fluid past a torus of circular center line and circular cross section, the problem appears to be in need of further attention. Hicks (2) based his analysis on toroidal co-ordinates and toroidal harmonics but did not deal with the determination of the stream function, which is of primary physical interest. Dyson (3), on the other hand, arrived at a representation of the potential and stream functions in terms of series of definite integrals; the significance of this representation for numerical evaluations of the results appears to be rather limited. In view of the currently available numerical tabulations of the Legendre functions of fractional order (6), a re-examination of the problem would seem to serve a useful purpose.

In 1948 Weinstein (7) discussed axially symmetric potential flows and, in particular, considered an extension of the method of sources and sinks to cases in which the singularities are no longer confined to the axis of symmetry. This paper stimulated further interest in related problems. Thus Streeter (8), with the aid of ring and disk singularities, obtained streamline patterns corresponding to flows around various blunt-nosed half bodies and annular-shaped bodies; this approach is based on a semi-numerical procedure. At the same time elliptic integral representations were established (9) for the potential and stream functions appropriate to rotationally symmetric distributions of sources and vorticity over circular rings and disks. Concurrently, Van Tuyl (10) deduced a similar analytical representation of the flow generated by a uniform source disk, and applied it to the study of a new family of half bodies. Still more recently, Streeter (11) arrived at the flow around a torus of nearly circular cross section by superposition of a ring doublet upon a uniform stream. This solution will be identified later as a first approximation to the rigorous solution for the torus of exactly circular cross section; moreover, the results to be developed here are free from the indirect trial-and-error features inherent in Streeter's approach. Reference also should be made to a paper by Schiffman and Spencer (12) in which toroidal co-ordinates are used to study the flow about a lens-shaped object.

In what follows we examine certain pertinent sequences of singular solutions of the governing equations referred to toroidal co-ordinates. The physical significance of these component solutions, in terms of which the solution to the torus problem ultimately will be expanded, is investigated with particular attention to the presence or absence of a circulation in the corresponding potential and stream functions. It is shown how the foregoing component solutions may be generated through successive limit processes applied to the basic axisymmetric ring singularities of the source ring and the vortex ring. This part of the paper may be of interest beyond the present application. The torus problem is then formulated and solved on the basis of the stream-function approach. A second, independent solution, resting on the potential-function approach, is indicated merely since it provides further insight into the problem under consideration. In order to render the present exposition sensibly self-contained, some of the material given in (5) also has been included here briefly.

The Governing Equations. Toroidal Co-Ordinates

For the sake of convenience we summarize at this place the basic equations governing the steady irrotational flow of an ideal incompressible fluid in the presence of axial symmetry. With reference to the cylindrical co-ordinates (ρ, γ, z), where the z-

---

[1] The results presented in this paper were obtained in the course of an investigation conducted under contract N7onr-32906 with the Office of Naval Research, Department of the Navy, Washington, D. C.

[2] Professor of Mechanics, Illinois Institute of Technology. Jun. ASME.

[3] Associate Professor of Mathematics, Illinois Institute of Technology. Mem. ASME.

[4] Numbers in parentheses refer to the Bibliography at the end of the paper.

Presented at the National Conference of the Applied Mechanics Division, Minneapolis, Minn., June 18–20, 1953, of The American Society of Mechanical Engineers.

Discussion of this paper should be addressed to the Secretary, ASME, 29 West 39th Street, New York, N. Y., and will be accepted until October 10, 1953, for publication at a later date. Discussion received after the closing date will be returned.

Note: Statements and opinions advanced in papers are to be understood as individual expressions of their authors and not those of the Society. Manuscript received by ASME Applied Mechanics Division, August 7, 1952. Paper No. 53—APM-7.

axis is assumed coincident with the axis of symmetry, the velocity potential $\phi(\rho, z)$ satisfies Laplace's equation in the form

$$\frac{\partial}{\partial \rho}(\rho \phi_\rho) + \frac{\partial}{\partial z}(\rho \phi_z) = 0 \quad \ldots\ldots [1]^5$$

and the velocity components are given by

$$v_\rho = \phi_\rho, \quad v_z = \phi_z \quad \ldots\ldots [2]$$

Stokes's stream function $\psi(\rho, z)$ is introduced through the relations

$$\psi_z = -\rho \phi_\rho, \quad \psi_\rho = \rho \phi_z \quad \ldots\ldots [3]$$

and, alternatively, admits the representation

$$\psi(\rho, z) = \int_{(\rho_0, z_0)}^{(\rho, z)} (\rho \phi_z \, d\rho - \rho \phi_\rho \, dz) \quad \ldots\ldots [4]$$

in which (ρ_0, z_0) are the co-ordinates of an arbitrary fixed point in the meridional half plane $\rho \geq 0$. In view of Equation [1], which may be regarded as an integrability condition for Equations [3], the line Integral [4] is independent of the path, and $\psi(\rho, z)$ is single valued, in any simply connected domain throughout which $\phi(\rho, z)$ is regular. As was emphasized by Weinstein (7), the single valuedness of ψ no longer can be inferred if the domain of regularity of ϕ is multiply connected. Similarly, and under analogous circumstances, a single-valued stream function may give rise to a multiple-valued velocity potential. A potential function and a stream function which are related according to Equations [3] henceforth will be called conjugate with respect to each other.

It follows from Equations [1], [3] that ψ conforms to the "stream equation"

$$\frac{\partial}{\partial \rho}\left(\frac{1}{\rho}\psi_\rho\right) + \frac{\partial}{\partial z}\left(\frac{1}{\rho}\psi_z\right) = 0 \quad \ldots\ldots [5]$$

and Equations [2], [3] further imply

$$v_\rho = -\frac{1}{\rho}\psi_z, \quad v_z = \frac{1}{\rho}\psi_\rho \quad \ldots\ldots [6]$$

A specific velocity field determines its associated potential as well as the conjugate stream function only within an arbitrary additive constant. Finally, we recall that the curves $\psi(\rho, z) = \text{const}$ are the streamlines and that $2\pi(\psi_2 - \psi_1)$ constitutes the total flow between the stream surfaces generated by $\psi = \psi_1$ and $\psi = \psi_2$.

In what follows we shall have occasion to refer to toroidal co-ordinates (α, β, γ) which are defined through the transformation

$$x = \frac{\bar{q}}{q - p}\cos\gamma, \quad y = \frac{\bar{q}}{q - p}\sin\gamma, \quad z = \frac{\bar{p}}{q - p} \quad \ldots\ldots [7]$$

where (x, y, z) are the Cartesian co-ordinates and

$$p = \cos\alpha, \quad \bar{p} = \sin\alpha, \quad q = \cosh\beta, \quad \bar{q} = \sinh\beta \quad \ldots\ldots [8]$$

The ranges of the curvilinear co-ordinates are given by

$$0 \leq \alpha \leq 2\pi, \quad 0 \leq \beta < \infty, \quad 0 \leq \gamma \leq 2\pi \quad \ldots\ldots [9]$$

so that

$$-1 \leq p, \bar{p} \leq 1, \qquad 1 \leq q < \infty, \qquad 0 \leq \bar{q} < \infty \quad \ldots\ldots [10]$$

Furthermore, with the auxiliary notation

$$\mu = (q - p)^{1/2} \quad \ldots\ldots [11]$$

we have

$$\rho = (x^2 + y^2)^{1/2} = \frac{\bar{q}}{\mu^2} \quad \ldots\ldots [12]$$

Equations [7], [8], [11] imply

$$\left(\rho - \frac{q}{\bar{q}}\right)^2 + z^2 = \frac{1}{\bar{q}^2}, \quad \rho^2 + \left(z - \frac{p}{\bar{p}}\right)^2 = \frac{1}{\bar{p}^2} \quad \ldots\ldots [13]$$

The co-ordinate surfaces $\alpha = \text{const}$ are thus spherical bowls of radius $|\bar{p}|^{-1}$ centered on the z-axis at $z = p/\bar{p}$. The surfaces $\beta = \text{const}$ are tori, the meridional cross sections of which are the circles of radius $\bar{q}^{-1}$ centered on the ρ-axis at $\rho = q/\bar{q}$. As $\beta \to \infty$ the tori degenerate into the circle[6] $\rho = 1, z = 0$. Fig. 1 shows the traces of the foregoing two mutually orthogonal families of co-ordinate surfaces upon a meridional half plane $\gamma = \text{const}$.

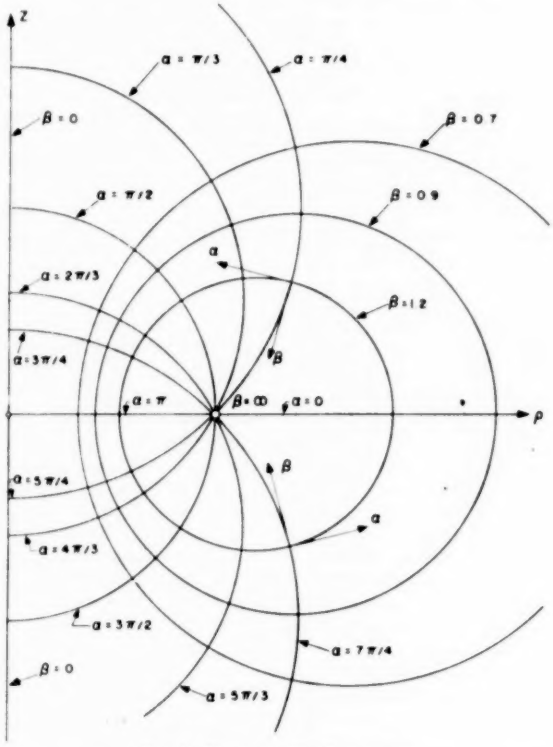

FIG. 1 TOROIDAL CO-ORDINATES
(Traces of surfaces $\alpha = \text{const}$ and $\beta = \text{const}$, on a half plane $\gamma = \text{const}$.)

The differential of arc length is defined by

$$ds^2 = \left(\frac{d\alpha}{h_1}\right)^2 + \left(\frac{d\beta}{h_2}\right)^2 + \left(\frac{d\gamma}{h_3}\right)^2 \quad \ldots\ldots [14]$$

and the metric coefficients here appear as

$$h_1 = h_2 = \mu^2, \quad h_3 = \frac{\mu^2}{\bar{q}} \quad \ldots\ldots [15]$$

A routine computation now yields for Laplace's Equation [1] in toroidal co-ordinates

$$\mu^2\bar{q}(\phi_{\alpha\alpha} + \phi_{\beta\beta}) - p\bar{q}\phi_\alpha + (1 - pq)\phi_\beta = 0 \quad \ldots\ldots [16]$$

Subscripts attached to functions which originally bear no subscript denote differentiation with respect to the argument indicated.

[6] This normalization of the co-ordinate transformation [7] is, of course, unessential.

whereas the stream Equation [5] becomes

$$\mu^2\bar{q}(\psi_{\alpha\alpha} + \psi_{\beta\beta}) + p\bar{q}\psi_\alpha - (1 - pq)\psi_\beta = 0 \quad [17]$$

The toroidal transform of Equations [3] is

$$\phi_\alpha = -\frac{\mu^2}{\bar{q}}\psi_\beta, \quad \phi_\beta = \frac{\mu^2}{\bar{q}}\psi_\alpha \quad [18]$$

and the toroidal components of the velocity vector assume the form

$$\left.\begin{aligned} v_\alpha &= \mu^2\phi_\alpha = -\frac{\mu^4}{\bar{q}}\psi_\beta \\ v_\beta &= \mu^2\phi_\beta = \frac{\mu^4}{\bar{q}}\psi_\alpha \end{aligned}\right\} \quad [19]$$

Toroidal Potential and Stream Functions[7]

In this section we consider certain aggregates of solutions to Laplace's Equation [16] and to the stream Equation [17], in toroidal co-ordinates. Neither of these two equations is separable in the strict sense. There do exist, however, pseudo-product solutions of the form

$$\phi(\alpha, \beta) = \mu A(\alpha)B(\beta) \quad [20]$$

to Laplace's equation, whereas the stream equation admits the pseudo-product solutions

$$\psi(\alpha, \beta) = \frac{\bar{q}^2}{\mu}C(\alpha)D(\beta) \quad [21]$$

Substitution of Equations [20], [21] into Equations [16], [17], subsequent separation of variables, and adherence to the restriction that the solutions sought have a period 2π in α, ultimately yield

$$\left.\begin{aligned} \phi(\alpha, \beta) &= \mu\,(\cos n\alpha \text{ or } \sin n\alpha)[P_{n-1/2}(q) \text{ or } Q_{n-1/2}(q)] \\ \psi(\alpha, \beta) &= \frac{\bar{q}^2}{\mu}\,(\cos n\alpha \text{ or } \sin n\alpha) \\ &\qquad [P'_{n-1/2}(q) \quad \text{or} \quad Q'_{n-1/2}(q)] \\ &\qquad (n = 0, 1, 2, \ldots) \end{aligned}\right\} \quad [22][8]$$

where $P_{n-1/2}$ and $Q_{n-1/2}$ are the Legendre functions of the first and second kind, respectively.

For future reference, we cite Legendre's equation

$$\bar{q}^2 P''_{n-1/2} + 2qP'_{n-1/2} - \left(n^2 - \frac{1}{4}\right)P_{n-1/2} = 0 \quad [23]$$

and recall the recursion formulas

$$\left.\begin{aligned} P_{-n-1/2} &= P_{n-1/2} \\ 4nqP_{n-1/2} &= (2n + 1)P_{n+1/2} + (2n - 1)P_{n-3/2} \\ 2\bar{q}^2P'_{n-1/2} &= (2n - 1)(qP_{n-1/2} - P_{n-3/2}) \end{aligned}\right\} \quad [24]$$

Equations [24] are valid for all integral values of n, and remain valid if $P_{n-1/2}$ is replaced with $Q_{n-1/2}$. We also note the bilinear identity

$$P'_{n-1/2}Q'_{n-1/2} - P'_{n-1/2}Q'_{n-1/2} = -\frac{2n - 1}{2\bar{q}^2} \quad [25][9]$$

Furthermore, we shall need to refer to Laplace's integral

$$P_{-1/2}(q) = \frac{1}{\pi}\int_0^\pi \frac{d\alpha}{\sqrt{q + \bar{q}\cos\alpha}} \quad [26][10]$$

and to the integral representation

$$Q_{n-1/2}(q) = \frac{1}{\sqrt{2}}\int_0^\pi \frac{\cos n\alpha}{\mu}\,d\alpha \quad [27][11]$$

which gives rise to the Fourier expansion

$$\frac{1}{\mu} = \frac{\sqrt{2}}{\pi}Q_{-1/2} + \frac{2\sqrt{2}}{\pi}\sum_{n=1}^{\infty} Q_{n-1/2}\cos n\alpha \quad [28][12]$$

where μ is defined in Equation [11].

Equations [26], [27] supply the link to the representation of the Legendre functions of fractional index in terms of elliptic integrals. Thus let

$$k = \sqrt{\frac{2}{q + 1}} = \frac{1}{\cosh\beta/2}, \quad k' = \sqrt{1 - k^2} = \frac{\bar{q}}{q + 1} \quad [29]$$

Setting $\theta = \alpha/2$ in Equation [26], we arrive at

$$P_{-1/2} = \frac{2k}{\pi}\int_0^{\pi/2} \frac{d\theta}{\sqrt{1 - k^2\sin^2\theta}} = \frac{2k}{\pi}K' \quad [30]$$

and setting $\theta = (\pi - \alpha)/2$ in Equation [27], we reach

$$Q_{-1/2} = kK \quad [31]$$

where K and K' are the complete elliptic integrals of the first kind referred to the modulus k and the complementary modulus k', respectively. Alternatively, we may define moduli

$$k_1 = \sqrt{\frac{2\bar{q}}{q + \bar{q}}}, \quad k_1' = \sqrt{1 - k_1^2} = \frac{1}{q + \bar{q}} = e^{-\beta} = \frac{r_2}{r_1} \quad [32]$$

in which

$$\left.\begin{aligned} r_1 &= [(\rho + 1)^2 + z^2]^{1/2} = \frac{\sqrt{2}\,e^{\beta/2}}{\mu} \\ r_2 &= [(\rho - 1)^2 + z^2]^{1/2} = \frac{\sqrt{2}\,e^{-\beta/2}}{\mu} \end{aligned}\right\} \quad [33]$$

The new moduli are related to k and k', introduced in Equations [29], through the Landen transformation[13]

$$k_1 = \frac{2\sqrt{k'}}{1 + k'}, \quad k_1' = \frac{1 - k'}{1 + k'} \quad [34]$$

so that

$$\left.\begin{aligned} K_1 &= (1 + k')K' = \frac{k}{\sqrt{k_1'}}K' \\ E_1 &= (k' - 1)K' + \frac{2}{1 + k'}E' \end{aligned}\right\} \quad [35][14]$$

Here K_1 and E_1 are the complete elliptic integrals of the first and second kind based on k_1. The moduli k_1, k_1' are identical with those previously employed by Hicks (2), Fouquet (15), and the current authors (9, 5).

[7] See (13), chapter x, for a discussion of toroidal harmonics. Toroidal stream functions are also dealt with in (5).

[8] The primes denote differentiation with respect to the argument q.

[9] See (13), art. 45.

[10] See (13), p. 381.

[11] See (14), p. 443.

[12] The argument of $P_{n-1/2}$ and $Q_{n-1/2}$ is henceforth assumed to be q, unless otherwise specified.

[13] See (14), p. 507.

[14] The second Equation [35] is obtained by differentiating the first with respect to k'.

Symmetric and Antisymmetric Flow Fields

Among the potential and stream functions listed in Equations [22], those involving the Legendre functions of the second kind become infinite as $q \to 1$, and therefore violate the regularity requirements on the z-axis inherent in the torus problem to be considered subsequently. Thus we shall limit the present discussion to the potential and stream functions involving $P_{n-1/2}$ and its derivative, which remain analytic for every finite q and vanish at Cartesian infinity; they become singular on the "limit circle," as $q \to \infty$.

We may distinguish between two basic flow cases according as the velocity field is symmetric or antisymmetric with respect to the plane $z = 0$, that is, according as the velocity potential is an even or odd function of z and α. Symmetric flows are generated by the potentials and stream functions

$$\left.\begin{aligned} \Phi_n &= \mu P_{n-1/2} \cos n\alpha \\ \Psi_n &= \frac{\bar{q}^2}{\mu} P'_{n-1/2} \sin n\alpha \\ (n &= 0, 1, 2, \ldots) \end{aligned}\right\} \quad \ldots\ldots [36]$$

It is important to observe that Φ_n and Ψ_n do not constitute a conjugate pair in the sense of Equations [18]. We now seek to establish the stream function $\bar{\Psi}_n$ and the velocity potential $\bar{\Phi}_n$ which are conjugate to Φ_n and Ψ_n, respectively. To this end we confirm with the aid of Equations [18] that

$$\left.\begin{aligned} \bar{\Psi}_{n+1} - \bar{\Psi}_n &= \frac{2}{2n+1} (\Psi_{n+1} - \Psi_n) \\ \bar{\Phi}_{n+1} - \bar{\Phi}_n &= \frac{2n+1}{2} (\Phi_{n+1} - \Phi_n) \\ (n &= 0, 1, 2, \ldots) \end{aligned}\right\} \quad \ldots\ldots [37]$$

Since $\Psi_0 = 0$, we may take $\bar{\Phi}_0$ to be zero, and the foregoing recursion relations yield

$$\left.\begin{aligned} \bar{\Psi}_n &= \bar{\Psi}_0 + 2 \sum_{i=1}^{n} \frac{1}{2i-1} (\Psi_i - \Psi_{i-1}) \\ \bar{\Phi}_n &= \frac{1}{2} \sum_{i=1}^{n} (2i-1)(\Phi_i - \Phi_{i-1}) \\ (n &= 1, 2, 3, \ldots) \end{aligned}\right\} \quad \ldots\ldots [38]$$

In order to complete the determination of $\bar{\Psi}_n$ for $n = 0, 1, 2, \ldots$, we need to find $\bar{\Psi}_0$. For this purpose we introduce the parameter t through

$$\mathrm{am}(t,k) = \theta = \frac{\pi - \alpha}{2} \quad \ldots\ldots [39]$$

or, equivalently, through

$$t = F(\theta,k) = \int_0^{\theta} \frac{d\vartheta}{(1 - k^2 \sin^2 \vartheta)^{1/2}} \quad \ldots\ldots [40]$$

$\mathrm{am}(t,k)$ being the amplitude function and $F(\theta,k)$ the incomplete elliptic integral of the first kind, both referred to the modulus k given in Equations [29]. Thus

$$\mathrm{sn}\, t = \sin\theta = \cos\frac{\alpha}{2}, \quad \mathrm{cn}\, t = \cos\theta = \sin\frac{\alpha}{2}, \quad \mathrm{dn}\, t = \frac{k\mu}{\sqrt{2}}. \quad [41]$$

where sn, cn, dn denote the Jacobian elliptic functions[15] for the modulus k.

[15] See (14), chapter xxii, for a discussion of Jacobian elliptic functions and integrals.

According to Equations [30], [36], and [41], we may write

$$\Phi_0 = \mu P_{-1/2} = \frac{2\sqrt{2}}{\pi} K' \mathrm{dn}\, t \quad \ldots\ldots [42]$$

Equations [18], applied to the conjugate pair $(\Phi_0, \bar{\Psi}_0)$, by virtue of Equation [42], now lead to

$$\left.\begin{aligned} \frac{\partial \bar{\Psi}_0}{\partial \alpha} &= \frac{\sqrt{2}}{\pi} \left[\frac{E'}{\mathrm{dn}\, t} - k^2 K' \frac{\mathrm{cn}^2 t}{\mathrm{dn}^3 t} \right] \\ \frac{\partial \bar{\Psi}_0}{\partial \beta} &= -\frac{\sqrt{2}\, k^2 k'}{\pi} K' \frac{\mathrm{sn}\, t\, \mathrm{cn}\, t}{\mathrm{dn}^3 t} \end{aligned}\right\} \quad \ldots\ldots [43]$$

where E' is the complete elliptic integral of the second kind based on the modulus k'. Equations [43] are explicitly integrable by recourse to identities listed in reference (14).[16] There results

$$\bar{\Psi}_0 = \frac{2\sqrt{2}}{\pi} \left[(K' - E')t + k^2 K' \frac{\mathrm{sn}\, t\, \mathrm{cn}\, t}{\mathrm{dn}\, t} - K' E(t) \right]. \quad [44][17]$$

in which $\mathrm{E}(t)$ designates the incomplete elliptic integral of the second kind for the modulus k. We note from Equations [38] that $\bar{\Psi}_n$ and $\bar{\Phi}_n$, which are conjugate to the pseudo-product solutions Φ_n and Ψ_n of the potential and stream equations, no longer possess the pseudo-product structure. Indeed, a single potential function Φ_i gives rise to a conjugate stream function ψ_i, whose representation requires an infinite series of stream functions in pseudo-product form; the closed representation given by Equations [38], [44] was made possible only through the introduction of elliptic functions and integrals.

Since

$$\left.\begin{aligned} \mathrm{am}(t + 2K) &= \mathrm{am}\, t + \pi \\ \mathrm{E}(t + 2K) &= E(t) + 2E \end{aligned}\right\} \quad \ldots\ldots [45]$$

and recalling Legendre's identity

$$EK' + E'K - KK' = \frac{\pi}{2} \quad \ldots\ldots [46]$$

as well as the periodicity properties of the Jacobian elliptic functions, we conclude from Equations [44], [38] that

$$\bar{\Psi}_n(\alpha + 2\pi, \beta) - \bar{\Psi}_n(\alpha,\beta) = 2\sqrt{2}, (n = 0, 1, 2, \ldots). \quad [47]$$

The single-valued potentials Φ_n thus correspond to associated conjugate stream functions $\bar{\Psi}_n$ which are many valued for $-\infty < \alpha < \infty$, or else discontinuous along the cut $\alpha = 0$ in the meridional half plane corresponding to $0 \leq \alpha \leq 2\pi, 0 \leq \beta < \infty$. This result is consistent with our previous observations regarding the singular character of Φ_n as $q \to \infty$. On the other hand, the conjugate sequences $(\bar{\Phi}_n, \Psi_n)$ $(n = 1, 2, 3, \ldots)$ are both single-valued.

The treatment of the antisymmetric flow fields generated by

$$\left.\begin{aligned} \phi_n &= \mu P_{n-1/2} \sin n\alpha \\ \psi_n &= \frac{\bar{q}^2}{\mu} P'_{n-1/2} \cos n\alpha \end{aligned}\right\} \quad \ldots\ldots [48]$$

is strictly analogous to the preceding discussion of symmetric fields, and we may confine ourselves to stating the pertinent results. If $(\phi_n, \bar{\psi}_n)$ and $(\bar{\phi}_n, \psi_n)$ are conjugate pairs of potential and stream functions, then

$$\left.\begin{aligned} \bar{\psi}_{n+1} - \bar{\psi}_n &= \frac{-2}{2n+1} (\psi_{n+1} - \psi_n) \\ \bar{\phi}_{n+1} - \bar{\phi}_n &= -\frac{2n+1}{2} (\phi_{n+1} - \phi_n) \\ (n &= 0, 1, 2, \ldots) \end{aligned}\right\} \quad \ldots\ldots [49]$$

[16] Reference (14), p. 516.

[17] It should be noted that the Jacobian elliptic functions appearing here may be eliminated by means of Equations [41].

and consequently

$$\left.\begin{aligned} \bar{\Psi}_n &= -2\sum_{i=1}^{n}\frac{1}{2i-1}(\Psi_i - \Psi_{i-1}) \\ \bar{\phi}_n &= \bar{\phi}_0 - \frac{1}{2}\sum_{i=1}^{n}(2i-1)(\phi_i - \phi_{i-1}) \\ &(n = 1, 2, 3, \ldots) \end{aligned}\right\} \quad \ldots\ldots [50]$$

Here we may take $\bar{\Psi}_0 = 0$ since ϕ_0 vanishes, whereas $\bar{\phi}_0$ turns out to be given by

$$\bar{\phi}_0 = \frac{\sqrt{2}}{\pi}[(K' - E')t - K'E(t)] \quad \ldots\ldots [51]$$

The functions ϕ_n, Ψ_n, and $\bar{\Psi}_n$ are periodic with period 2π in α. On the other hand, we find that

$$\bar{\phi}_n(\alpha + 2\pi, \beta) - \phi_n(\alpha, \beta) = \sqrt{2}, \quad (n = 0, 1, 2, \ldots) \quad [52]$$

which indicates a circulation in the velocity potentials $\bar{\phi}_n$ conjugate to the single-valued stream functions Ψ_n.

We now turn to a physical interpretation of the potential and stream functions discussed in this section. With regard to symmetric flows, we note on the basis of equation [3.9] of reference (9) that the potential of a uniform source ring of total strength m and unit radius (coincident with the limit circle of the toroidal co-ordinate system) in our present notation appears as

$$\phi = \frac{2m}{\pi}\frac{K_1}{r_1} \quad \ldots\ldots [53]$$

with r_1 and K_1 defined as in Equations [33], [35]. A trivial computation, involving Equations [53], [35], [33], [32], and [30], identifies

$$\phi = \frac{m}{\sqrt{2}}\Phi_0, \quad \Psi = \frac{m}{\sqrt{2}}\bar{\Psi}_0 \quad \ldots\ldots [54]$$

as the potential and stream functions appropriate to the source ring under consideration. Moreover, we confirm[18] with the aid of Equation [47] that the stream function possesses a cyclic period of $2m$, as is consistent with hydrodynamic theory.

In a similar manner, guided by equation [7.5] of reference (9), we recognize

$$\phi = \frac{\Gamma}{\sqrt{2}}\bar{\phi}_0, \quad \Psi = \frac{\Gamma}{\sqrt{2}}\Psi_0 \quad \ldots\ldots [55]$$

as the potential and stream functions belonging to the antisymmetric flow generated by a uniform vortex ring of unit radius and total circulation Γ. The circulation constant Γ of the velocity potential is readily verified by means of Equation [52].

Equations [54], [55] establish the significance of the initial members in the sequences of symmetric and antisymmetric flows discussed previously. The remaining members in these two aggregates of singular flows, which are characterized by singularities of progressively higher order on the limit circle, may be generated through successive z-differentiations applied to the basic singular solutions which represent the source ring and the vortex ring. Indeed, a somewhat tedious computation, depending on the repeated use of the Legendre Relations [24], yields the result

$$\left.\begin{aligned} \frac{\partial \Phi_n}{\partial z} &= -\frac{(2n-1)}{4}\phi_{n-1} + n\phi_n - \frac{2n+1}{4}\phi_{n+1} \\ \frac{\partial \Psi_n}{\partial z} &= -\frac{2n+1}{4}\Psi_{n-1} + n\Psi_n - \frac{(2n-1)}{4}\Psi_{n+1} \\ &(n = 0, 1, 2, \ldots) \end{aligned}\right\} \quad \ldots [56][19]$$

Moreover, these recursion formulas remain valid if Φ and ϕ, as well as Ψ and ψ, are interchanged while the signs of the right-hand members are reversed. As an illustrative example we determine the solution corresponding to a ring doublet, whose potential is the first derivative with respect to z of the potential for a source ring. By Equations [54], [56], [50], the ring doublet is thus represented by

$$\left.\begin{aligned} \phi &= -\frac{m}{2\sqrt{2}}\phi_1 \\ \psi &= -\frac{m}{2\sqrt{2}}\bar{\Psi}_1 = \frac{m}{\sqrt{2}}(\Psi_1 - \Psi_0) \end{aligned}\right\} \quad \ldots\ldots [57]$$

and these formulas are readily transformed into the expressions derived by Streeter (11).

Solution of Torus Problem

Stream-Function Approach. We are now in a position to consider the main problem of this investigation. Let the boundary of the torus coincide with the parametric surface $\beta = \beta_0$, Fig. 1. Then, according to Equations [13]

$$\Delta = \frac{b}{a} = q_0 = \cosh \beta_0 \quad \ldots\ldots [58][20]$$

where a and b are the radii of the cross section and of the center line, respectively, and Δ will be called the "shape-ratio" of the torus.

The problem consists in determining a stream function $\psi(\alpha,\beta)$ which satisfies Equation [17] throughout the domain $0 \leq \alpha \leq 2\pi$, $0 \leq \beta \leq \beta_0$, and conforms to the boundary and regularity conditions

$$\psi(\alpha, \beta_0) = c, \quad \psi(\alpha, \beta) \to \psi_\infty = \frac{\rho^2}{2} \text{ as } (\alpha, \beta) \to (0,0) \quad [59]$$

where c is the initially unknown value of ψ on the surface of the torus, and ψ_∞ designates the stream function associated with the uniform velocity field $v_\rho = 0$, $v_z = 1$ at infinity.

Guided by the antisymmetric nature of the uniform velocity field at infinity, we assume the desired solution in the form

$$\psi(\alpha, \beta) = \frac{\rho^2}{2} + \sum_{n=0}^{\infty} a_n \Psi_n \quad \ldots\ldots [60]$$

with Ψ_n defined by the second of Equations [48], and note that $\psi(\alpha, \beta)$ automatically conforms to the condition at infinity since $\Psi_n(0, 0) = 0$. The coefficients of superposition a_n $(n = 0, 1, 2, \ldots)$ are to be determined consistent with the boundary conditions for $\beta = \beta_0$. By virtue of Equations [60], [59], [48], [12], this leads to

$$\sum_{n=0}^{\infty} a_n P'_{n-1/2}(q_0)\cos n\alpha = \frac{c\mu_0}{\rho_0^2} - \frac{1}{2\mu_0^3} \quad \ldots\ldots [61]$$

[18] See (9), equation [5.7].

[19] Observe that $\phi_{-1} = -\phi_1$ and $\Psi_{-1} = -\Psi_1$, according to Equations [24], [36], [48].

[20] The subscript, zero, attached to any function of β, henceforth will indicate its evaluation for $\beta = \beta_0$.

In order to expand the right-hand member of Equation [61] in a Fourier series, we recall the Expansion [28]. With the aid of this expansion, and making use of the Identities [24] applied to the Legendre functions of the second kind, we thus arrive at

$$\sum_{n=0}^{\infty} a_n P'_{n-1/2}(q_0)\cos n\alpha = \frac{2\sqrt{2}}{\pi}\sum_{n=0}^{\infty}\left(\frac{2c}{4n^2-1}+1\right)\frac{Q'_{n-1/2}(q_0)}{1+\delta_{n0}}\cos n\alpha \quad [62]$$

in which δ_{n0} designates the Kronecker delta. Equation [62] implies

$$a_n = \left(\frac{2c}{4n^2-1}+1\right)A_n \quad [63]$$

provided

$$A_n = \frac{2\sqrt{2}\,Q'_{n-1/2}(q_0)}{\pi(1+\delta_{n0})P'_{n-1/2}(q_0)} \quad [64]$$

and, in accordance with Equation [60], the appropriate velocity potential appears as

$$\phi(\alpha,\beta) = z + \sum_{n=0}^{\infty} a_n\bar{\phi}_n \quad [65]$$

the functions $\bar{\phi}_n$ being defined in Equations [50] and [51].

It is apparent from the preceding developments that the boundary Conditions [59] do not suffice to determine the yet unknown value c of ψ on the surface of the torus. This observation is in agreement with the well-known fact that the boundary conditions fail to characterize uniquely the solution to a steady-flow problem if the flow domain is multiply connected.[21] It follows from Equation [52] that the velocity potential represented by Equation [65] is multiple-valued unless c is chosen appropriately. In view of Equation [52], a circulation-free potential is assured if and only if

$$\sum_{n=0}^{\infty} a_n = 0 \quad [66]$$

or, by Equation [63]

$$c = -\frac{1}{2}\left(\sum_{n=0}^{\infty} A_n\right)\left(\sum_{n=0}^{\infty}\frac{A_n}{4n^2-1}\right)^{-1} \quad [67]$$

The complete solution to our problem is now given by Equations [60], [65], where $\bar{\psi}_n$ and $\bar{\phi}_n$ are defined in Equations [48], [50], [51], and the coefficients a_n follow from Equations [63], [64], [67]. The toroidal velocity components are readily obtained from Equations [60], [48], [12], with the aid of Equations [18]

$$\left.\begin{aligned} v_\alpha &= \frac{pq-1}{\mu^2} + \frac{\mu}{4}\sum_{n=0}^{\infty} a_n[2\bar{q}^2 P'_{n-1/2} \\ &\qquad -(4n^2-1)\mu^2 P_{n-1/2}]\cos n\alpha \\ v_\beta &= \frac{-\bar{p}\bar{q}}{\mu^2} - \frac{\bar{q}\mu}{2}\sum_{n=0}^{\infty} a_n P'_{n-1/2}[2n\mu^2\sin n\alpha + \bar{p}\cos n\alpha] \end{aligned}\right\} \quad [68]$$

Finally, we note for future reference, that the Series [60] admits the rearrangement

$$\psi = \frac{\rho^2}{2} + \sum_{n=0}^{\infty}\left(\sum_{m=0}^{n} a_m\right)(\bar{\psi}_n - \bar{\psi}_{n+1}) \quad [69]$$

Potential-Function Approach. In this section we sketch a second, independent approach to the problem, in terms of the velocity potential. Although this method of attack is more cumbersome than the one adopted previously, nevertheless it should prove to be instructive. The alternative formulation of the problem as a problem of Neumann, requires the determination of a function $\phi(\alpha,\beta)$ which is harmonic in the domain $0 \le \alpha \le 2\pi$, $0 \le \beta \le \beta_0$, and obeys the boundary and regularity conditions

$$\left.\frac{\partial\phi}{\partial\beta}\right|_{(\alpha,\beta_0)} = 0, \quad \phi(\alpha,\beta) \to \phi_\infty = z \text{ as } (\alpha,\beta) \to (0,0) \quad [70]$$

where ϕ_∞ is the potential of the uniform velocity field at infinity. We thus put

$$\phi(\alpha,\beta) = z + \sum_{n=1}^{\infty} b_n\phi_n \quad [71]$$

with reference to the definition, Equations [48], of the potential functions ϕ_n. Applying the first of Conditions [70], we reach with the aid of Equation [28]

$$\left.\begin{aligned} &(b_{n+1}-b_n)P'_{n+1/2}(q_0) - (b_n - b_{n-1})P'_{n-1/2}(q_0) \\ &\quad = \frac{4\sqrt{2}}{\pi}[Q'_{n-1/2}(q_0) - Q'_{n+1/2}(q_0)], \quad b_0 = 0, \\ &\qquad\qquad (n = 0, 1, 2, \ldots) \end{aligned}\right\} \quad [72]$$

Equation [72] is a finite-difference equation of the second order for the unknown coefficients of superposition $b_n (n = 1, 2, 3, \ldots)$ which possesses an integrating factor $P'_{n-1/2}(q_0)$.

Now let

$$c_n = (b_n - b_{n-1})P'_{n-1/2}P'_{n-1/2} \quad [73][22]$$

and Equation [72] may be written as

$$c_{n+1} - c_n = \frac{4\sqrt{2}}{\pi}[Q'_{n-1/2} - Q'_{n+1/2}]P'_{n-1/2} \quad [74]$$

This difference equation of the first order is integrable; by use of the bilinear Identity [25], we obtain

$$\left.\begin{aligned} \frac{c_n}{P'_{n-1/2}P'_{n-1/2}} &= b_n - b_{n-1} \\ &= \frac{\sqrt{2}}{\pi}\left[\left(2n-3+\frac{4\bar{q}^2\lambda}{2n-1}\right)\frac{Q'_{n-1/2}}{P'_{n-1/2}} \right. \\ &\qquad \left. -\left(2n+1+\frac{4\bar{q}^2\lambda}{2n-1}\right)\frac{Q'_{n-1/2}}{P'_{n-1/2}}\right] \end{aligned}\right\} \quad [75]$$

in which λ is an arbitrary constant of integration. A second integration, based on Equation [75], yields

$$b_n = -\sum_{m=0}^{n}\left(1+\frac{4\bar{q}^2\lambda}{4m^2-1}\right)A_m - \frac{1}{2}\left(2n-1+\frac{4\bar{q}^2\lambda}{2n+1}\right)A_n, (n = 1, 2, 3, \ldots) \quad [76]$$

[21] This statement, of course, in no way contradicts the uniqueness theorems of hydrodynamics, which require also the specification of the initial conditions; see, for example (16), p. 422.

[22] The argument of the Legendre functions appearing in this and the following equations is understood to be q_0.

the notation being that of Equation [64]. In order that the Series [71] be convergent, it is necessary that

$$\lim_{n\to\infty} b_n = 0 \quad [77]$$

This formal convergence condition, which here takes the place of the single-valuedness Condition [66],[23] serves to determine the parameter λ. Indeed, since

$$\lim_{n\to\infty} nA_n = 0 \quad [78]$$

we conclude from Equations [77], [76], that

$$\lambda = \frac{c}{2\bar{q}^2} \quad [79]$$

with c defined by Equation [67], and thus

$$b_n = -\sum_{m=0}^{n} a_m - \frac{2n-1}{2} a_n, \quad (n = 1, 2, 3, \ldots) \quad [80]$$

the coefficients a_n retaining their previous definition given by Equations [63], [64], [67]. This completes the independent determination of the velocity potential introduced in Equation [71].

With a view toward demonstrating the equivalence of the solutions derived in this and the preceding sections, we note from Equation [80] that

$$\sum_{m=0}^{n} b_m = \frac{a_0}{2} - \frac{2n+1}{2} \sum_{m=0}^{n} a_m, \quad (n = 0, 1, 2, \ldots), \; b_0 = 0 \quad [81]$$

Consequently, Equation [69] may be written as

$$\psi = \frac{\rho^2}{2} + \sum_{n=0}^{\infty} \left(\frac{a_0}{2n+1} - \frac{2}{2n+1} \sum_{m=0}^{n} b_m \right) (\psi_n - \psi_{n+1}) \quad [82]$$

[23] Recall that the functions ϕ_n entering Equation [71] and the conjugate stream functions ψ_n are all single valued.

It now follows from Equations [82], [49] that the conjugate velocity potential appears as

$$\phi = z + \sum_{n=0}^{\infty} \left(\sum_{m=0}^{n} b_m - \frac{a_0}{2} \right) (\phi_n - \phi_{n+1}) \quad [83]$$

which, after a permissible rearrangement, assumes the form

$$\phi = z - \frac{a_0}{2} \phi_0 + \sum_{n=0}^{\infty} b_n \phi_n \quad [84]$$

Since $\phi_0 = 0$, Equation [84] is identical with Equation [71]. It is interesting to observe that the Representation [71] for $\phi(\alpha, \beta)$, in contrast to that given by Equation [65], does not involve any elliptic functions or integrals.

Discussion—Numerical Example

A comparison of Equations [69] or [83] with the second of Equations [57], or of Equation [71] with the first of Equations [57], reveals that the leading term in the series contributions to $\psi(\alpha, \beta)$ and $\phi(\alpha, \beta)$ are precisely the stream and potential functions belonging to the ring doublet. This observation identifies Streeter's solution (11), for the torus of nearly circular cross section, as a first approximation to the exact solution presented here. The fact that already a one-term approximation corresponds to a torus whose cross section is very close to a circle, is accounted for by the extremely rapid convergence of the series under consideration.

Although the convergence of the Representation [69] for the stream function is even more favorable than that given in Equation [60], it was still found to be more expedient to use the latter representation in the numerical example which follows. The reason for this lies in the loss of numerical accuracy caused by the difference formations inherent in Equation [69].

The stream pattern shown in Fig. 2 applies to a shape-ratio $\Delta = b/a = 3$. It was obtained by choosing various fixed values of z, and by subsequently selecting α and β judiciously and consistent with the last of Equations [7]. For these values of α and

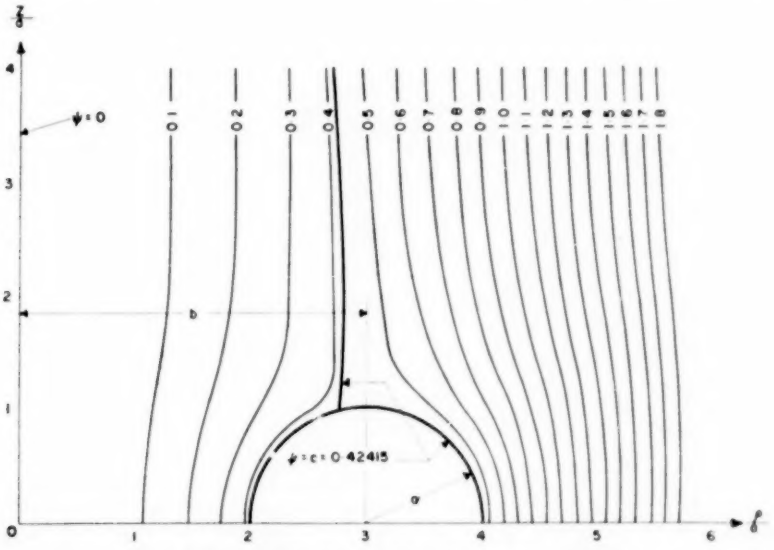

Fig. 2 Streamlines for $\Delta = b/a = 3$, $\tau_z = 1$ at Infinity

β the corresponding values of ψ were computed from Equation [60] with the aid of the numerical tables (6). A maximum of five terms in the series for ψ was needed in order to reach an accuracy of four significant figures. Once a sufficient number of z-profiles of the stream surface had been established, the streamlines $\psi =$ const, were determined graphically. In order to locate the stagnation point—the point of intersection of the separation streamline with the meridional section of the torus—Equation [68] was solved for $v_\alpha(\alpha, \beta) = 0$. A suitable method of successive approximations revealed that $v_\alpha(\alpha, \beta_0)$ vanishes to four significant figures for $\cos \alpha = 0.121$.

Acknowledgment

The authors wish to express their great appreciation to Mr. R. A. Eubanks, Assistant Research Engineer at Illinois Institute of Technology, who conducted all of the numerical and graphical work connected with this investigation. Acknowledgment is also due to Mr. W. F. Darsow, Project Computer, for his assistance in the numerical computations.

BIBLIOGRAPHY

1 "Theorie der Elektricitäts- und Wärmevertheilung in einem Ringe," by Carl Neumann, Verlag der Buchhandlung des Waisenhauses, Halle, 1864.

2 "On Toroidal Functions," by W. M. Hicks, *Philosophical Transactions*, Royal Society of London, vol. 172, 1881, p. 609.

3 "On the Potential of an Anchor Ring," by F. W. Dyson, *Philosophical Transactions*, Royal Society of London, series A, vol. 184, 1893, p. 43.

4 "The Uniform Torsion of Incomplete Tore," by W. Freiberger, *Australian Journal of Scientific Research*, series A, vol. 2, 1949, p. 354.

5 "Pure Bending of an Incomplete Torus," by M. A. Sadowsky and E. Sternberg, JOURNAL OF APPLIED MECHANICS, Trans. ASME, vol. 75, 1953, pp. 215–226.

6 "Tables of the Associated Legendre Functions," Mathematical Tables Project, Columbia University Press, New York, N. Y., 1945.

7 "On Axially Symmetric Flows," by Alexander Weinstein, *Quarterly of Applied Mathematics*, vol. 5, 1948, p. 429.

8 "Axially Symmetric Flow Through Annular Bodies," by V. L. Streeter, First Phase Report to the Office of Naval Research, Department of the Navy, Washington, D. C., under Contract N7onr-32905, February 1, 1949.

9 "Elliptic Integral Representation of Axially Symmetric Flows," by M. A. Sadowsky and E. Sternberg, *Quarterly of Applied Mathematics*, vol. 8, 1950, p. 113.

10 "On the Axially Symmetric Flow Around a New Family of Halfbodies," by A. Van Tuyl, *Quarterly of Applied Mathematics*, vol. 7, 1950, p. 399.

11 "The Ring Doublet in Ideal Fluid Flow," by V. L. Streeter, Proceedings of the Midwestern Conference on Fluid Dynamics, University of Illinois, May, 1950.

12 "The Flow of an Ideal Incompressible Fluid About a Lens," by Max Schiffman and D. C. Spencer, *Quarterly of Applied Mathematics*, vol. 5, 1947, p. 270.

13 "The Theory of Spherical and Ellipsoidal Harmonics," by E. W. Hobson, University Press, Cambridge, England, 1931.

14 "A Course of Modern Analysis," by E. T. Whittaker and G. N. Watson, fourth edition, University Press, Cambridge, England, 1931.

15 "Dipolare Koordinaten und Kugelfunktionen," by Walter Fouquet, *Zeitschrift für angewandte Mathematik und Mechanik*, vol. 17, 1937, p. 51.

16 "Grundlagen der Hydromechanik," by Leon Lichtenstein, Julius Springer, Berlin, Germany, 1929.

Analysis of Viscous Laminar Incompressible Flow Through Axial-Flow Turbomachines With Infinitesimal Blade Spacing[1]

By T. P. TORDA,[2] H. H. HILTON,[3] AND F. C. HALL,[4] URBANA, ILL.

The Lorenz theory has been extended to the viscous, laminar, incompressible flow through axial-flow turbomachines with infinitesimal blade spacing. Expressions are derived for the velocity components, pressure, power input and output for arbitrary blade surfaces. A numerical example is presented and the flow variables and blade surfaces are plotted.

Introduction

THE several methods which have been developed to analyze flow through axial turbomachines may be divided into two main categories. In the direct method the flow variables are derived from given geometric configurations, while in the indirect method the geometric configuration of the blades is determined from a desired distribution of the flow parameters.

Sources and sinks, vortex distribution, or conformal mapping may be employed in the direct method of analysis to determine the flow field around the individual blades of turbomachines. However, the interference of the blades when arranged in cascades is difficult to determine by the use of this method and the results are valid only if the cascade blades are far apart.

The indirect method of analysis treats the passages between the cascade blades as channels and is, therefore, the more suitable of the two for the analysis of viscous effects in turbomachines. H. Lorenz (1)[5] was the first to develop the indirect method of analysis. He simplified the mathematical formulation of the problem of flow through blade systems by means of a continuous axially symmetric force field. The Lorenz theory, representing an infinitesimally spaced blade system, can be used as a first approximation for calculating the pressure distribution, velocity distribution, blade shape, and the torque of modern turbomachines with their closely spaced blades.

H. J. Reissner (2, 3, 4, 5) has extended Lorenz's method to the compressible two and three-dimensional cases of nonviscous flows through turbomachines. In reference (5) the two-dimensional, viscous, laminar steady compressible flow through a system of equidistant narrowly spaced stationary blades is treated.

In the present paper the effect of viscosity is taken into account for the case of steady incompressible flow through rotating-blade systems. Only the case of infinitesimal blade spacing is treated here. This analysis forms the basis of the finitely spaced blade problem and its extension to the latter case will be presented in a subsequent paper.

Although this analysis is carried out for an axial-flow compressor, it is equally applicable to all types of turbomachines.

Analysis

An axially symmetric incompressible viscous flow through a rotating infinitesimally spaced blade system is considered with the reference co-ordinate system rotating at a constant angular velocity. The Navier-Stokes equations defining such a flow are in cylindrical co-ordinates

$$\rho(u\,\partial u/\partial r + w\,\partial u/\partial z - v^2/r - 2v\omega - \omega^2 r) = -\partial p/\partial r + f_r \quad [1]$$

$$\rho(u\,\partial v/\partial r + w\,\partial v/\partial z + uv/r + 2\omega u) = f_\phi \quad [2]$$

$$\rho(u\,\partial w/\partial r + w\,\partial w/\partial z) = -\partial p/\partial z + f_z \quad [3]$$

where

r, z, ϕ = cylindrical co-ordinates
u, v, w = respective velocity components relative to rotating blade system
p = pressure
ρ = density
ω = constant angular velocity
f = force field per unit of volume
r, z, ϕ = subscripts denoting directions

In the viscous case, the force field f_j is inclined to the streamlines in order to account for the effects of shear and dilatation stresses. This force field is composed of two components, such that

$$f_j = g_j + h_j \quad [4]$$

where

g_j = force components per unit of volume in jth direction perpendicular to streamlines
h_j = force components per unit of volume in jth direction due to shear

The total relative velocity vector is given by

$$V^2 = u^2 + v^2 + w^2 \quad [5]$$

For laminar viscous flow the shear stress τ equals

$$\tau = \mu\{[\partial V/\partial n]_{n=d/2} + [\partial V/\partial(-n)]_{n=-d/2}\} \quad [6]$$

where

n = direction normal to streamlines
d = blade spacing
μ = viscosity (taken as constant)

---

[1] This analysis was carried out under the sponsorship of the Propulsion Research Branch, Flight Research Laboratory, USAF, Contract No. AF 33(616)-52.

[2] Professor, Department of Aeronautical Engineering, University of Illinois.

[3] Assistant Professor, Department of Aeronautical Engineering, University of Illinois. Jun. ASME.

[4] Research Assistant, Department of Aeronautical Engineering, University of Illinois.

[5] Numbers in parentheses refer to the Bibliography at the end of the paper.

Presented at the National Conference of the Applied Mechanics Division, Minneapolis, Minn., June 18–20, 1953, of THE AMERICAN SOCIETY OF MECHANICAL ENGINEERS.

Discussion of this paper should be addressed to the Secretary, ASME, 29 West 39th Street, New York, N. Y., and will be accepted until October 10, 1953, for publication at a later date. Discussion received after the closing date will be returned.

NOTE: Statements and opinions advanced in papers are to be understood as individual expressions of their authors and not those of the Society. Manuscript received by ASME Applied Mechanics Division, January 16, 1953. Paper No. 53—APM-28.

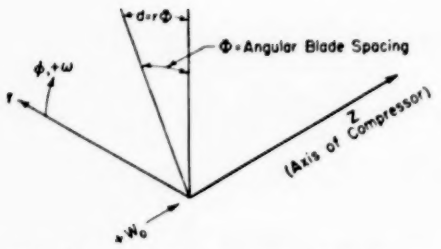

FIG. 1 NOTATION FOR INFINITESIMAL BLADE SPACING

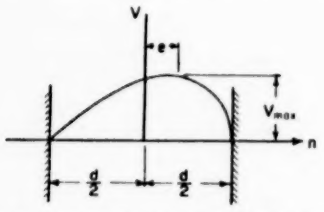

FIG. 2 RESULTANT VELOCITY DISTRIBUTION
(Infinitesimal blade spacing.)

The blade spacing, Fig. 1, is

$$d = r\Phi \quad [7]$$

and Φ is the pitch angle.

Since the flow is laminar, one may assume that the velocity distribution in each channel between the blades is a nonsymmetric parabola, Fig. 2, of the nondimensional form[6]

$$\eta = (1 - \xi^2)/(1 - 2a\xi + a^2) \quad |a| < 1 \quad [8]$$

where

$$\left.\begin{array}{ll} \eta = V/V_{max} & \xi = \eta/b \\ a = e/b & b = d/2 \end{array}\right\} \quad [9]$$

and e is the eccentricity.

The resultant shear force per unit volume may now be calculated from Equations [6] and [8]

$$h = \tau/d = -12\mu V_{avg}(1 + a^2)/kb^2(1 - a^2)^2 \quad [10]$$

where

$$V_{max} = 3V_{avg}/2k \quad [11]$$

For $0 < |a| < 1$

$$k = (3/8)\{[(1 - a^2)^2/2a^3] \ln |(1 - a)/(1 + a)| + (1 + a^2)/a^2\} \quad [12]$$

and for

$$a = 0,\ k = 1$$
$$a = 1,\ k = 3/4$$

The three components of the resultant shear force h are

$$h_r = hu/V, \quad h_\phi = hv/V, \quad h_z = hw/V \quad [13]$$

Multiplication of Equation [5] by the quantity h/V results in

$$uh_r + vh_\phi + wh_z = hV \quad [14]$$

For infinitesimally spaced blades, the assumption

$$V = V_{avg} \quad [15]$$

is valid. Equations [10] and [14] yield

$$uh_r + vh_\phi + wh_z = hV_{avg} = -12\mu V^2(1 + a^2)/kb(1 - a^2)^3 \quad [16]$$

Since the g-forces, Equation [4], are perpendicular to the streamlines, one finds that

$$ug_r + vg_\phi + wg_z = 0 \quad [17]$$

The continuity equation in an axially symmetric incompressible flow in cylindrical co-ordinates is

$$\rho[\partial(ru)/\partial r + \partial(rw)/\partial z] = 0 \quad [18]$$

In an axial-flow compressor, the velocity component in the axial direction is usually constant, or

$$w = w_0 \quad [19]$$

The continuity Equation [18] now reduces to

$$\partial(ru)/\partial r = 0 \quad [20]$$

with the solution

$$u = Z_1(z)/r \quad [21]$$

where $Z_1(z)$ is an arbitrary function of z to be determined by the boundary conditions of the problem.

Multiplying the Navier-Stokes Equations [1], [2], and [3], respectively, by u, v, and w, adding the results and using Equations [16] and [17], one finds that

$$D\lambda/Dt = -12\mu V^2(1 + a^2)/\rho kb^2(1 - a^2)^2 \quad [22]$$

where

$$D/Dt = u\partial/\partial r + w\partial/\partial z \quad [23]$$

$$\lambda = V^2/2 - \omega^2 r^2/2 + P \quad [24]$$

$$P = \int (1/\rho)dp \quad [25]$$

If the quantity a, Equation [9], is taken as constant, then essentially all the points of maximum velocity V_{max} in the channel lie along a radius at any particular z. Substitution for b^2 from Equation [9] and use of Equations [7] and [9] reduces Equation [22] to

$$u\partial\lambda/\partial r + w\partial\lambda/\partial z = AV^2/r^2 \quad [26]$$

with

$$A = -48\mu(1 + a^2)/\rho k\Phi(1 - a^2)^2 \quad [27]$$

Equation [26] is a Lagrange partial differential equation (7), and the solution is obtained from its subsidiary equation

$$dr/u = dz/w = r^2 d\lambda/AV^2 \quad [28]$$

The subsidiary equation yields three total differential equations

$$w\,dr = u\,dz \quad [29]$$

$$r^2 w d\lambda = AV^2 dz \quad [30]$$

$$r^2 u d\lambda = AV^2 dr \quad [31]$$

By substituting Equation [29] into [31], one can see that the latter is equivalent to Equation [30].

A solution of Equation [26] is obtainable from Equation [30]. Substituting for w from Equation [19], one obtains

$$\lambda = (A/w_0)\int (V^2/r^2)\,dz + C_1 \quad [32]$$

where C_1 is an arbitrary constant.

Let

$$V^2/r^2 = \partial\theta/\partial z, \quad \theta = \theta(r,z) \quad [33]$$

[6] The concept of parabolic velocity distribution in the channel was first introduced in reference (6).

then Equation [32] becomes

$$\lambda = A\theta/w_0 + C_1 \quad [34]$$

Eliminating λ and V^2/r^2 with help of Equations [33] and [34], the differential Equation [26] simplifies to

$$u\,\partial\theta/\partial r = 0 \quad [35]$$

Since $u \neq 0$, the solution is

$$\theta = Z_2(z) \quad [36]$$

where $Z_2(z)$ is an arbitrary function of z.

With the use of Equations [36], [33], [34], [24], [21], and [5], the solution of the problem is completed. Thus

$$V^2 = r^2 Z_2'(z) \quad [37]$$

$$P = [-r^2 Z_2'(z)/2 + AZ_2(z)/w_0 + \omega^2 r^2/2 + C_1] \quad [38]$$

$$v^2 = r^2 Z_2'(z) - [Z_1(z)/r]^2 - w_0^2 \quad [39]$$

where the primes denote differentiation with respect to z.

The velocity and pressure fields in the compressor are described completely by the foregoing equations. The traces of the streamlines may be determined from

$$dr/u = rd\phi/v = dz/w \quad [40]$$

The integration of pairs of differential equations will then yield the streamline traces in any plane.

For any given stage of the compressor, the angular velocity ω, the magnitude and direction of the entrance velocity, the entrance pressure, and hub and shroud radii at the entrance are prescribed.[7]

These known quantities are used to determine the arbitrary functions $Z_1(z)$ and $Z_2(z)$ and the constant C_1. It should be remembered that since these latter functions are arbitrary it is permissible to assume their type. Such assumptions in no way detract from the uniqueness of the solution, since for any given combination of Z_1, Z_2, and C_1 one and only one blade profile is found. Different velocity and pressure fields naturally will require different blade shapes.

Numerical Example

The aim of the numerical work was to determine under which conditions a maximum pressure rise could be achieved through one rotating stage of infinitesimally spaced blades (stream surfaces). At the same time large twist and large curvatures of these surfaces were to be avoided. Several numerical examples were worked; however, only one is presented in this paper showing trend and limitations of the design.

There are two arbitrary functions of z, $Z_1(z)$, and $Z_2(z)$, and one arbitrary constant C_1 in the analysis. C_1 may be determined from Equation [38] with the intake conditions. Thus

$$C_1 = p_i/\rho + V_i^2/2 - \omega^2 r^2/2 - AZ_2(0)/w_0 \quad [41]$$

where subscript i denotes values at the intake of the rotating stage.

The choice of the arbitrary functions, $Z_1(z)$ and $Z_2(z)$, determines the blade shape.

Equation [21] shows that the variation of the radial component u of the resultant velocity V depends on the arbitrary function Z_1. Through the equation of the streamlines. Equation [40], Z_1 also determines the r-z variation of shroud and hub. The requirement of small curvature of the stream surfaces restricts the choice of functions used for Z_1.

[7] Appropriate entrance conditions have to be prescribed if the analysis is to be applied to turbines.

The pressure rise through the rotating stage along each streamline is due to dynamic recovery and centrifugal action.

The pressure rise due to dynamic recovery is a maximum if the resultant velocity at the exit V_e is zero. (Subscript e denotes exit conditions.) Since, however, the axial component of the relative velocity w_0 is taken as constant and since the influence of the radial-velocity component is small, the tangential velocity component at the exit v_e was taken as zero. Thus from Equations [5], [19], [21], and [37]

$$w_0^2 + [Z_1(l)/r_e]^2 = r_e^2 Z_2'(l) \quad [42]$$

where l is the value of z at exit. With the condition of v_e, the stream surface at the exit is tangential to the r-z plane.

The pressure rise resulting from centrifugal action is directly dependent on the ratio of the exit and intake radii, i.e., r_e/r_i, and on the angular velocity ω. Use of Equation [41] in Equation [38] yields

$$p/\rho = [p_i/\rho + (V_i^2 - \omega^2 r_i^2)/2] + (\omega^2 - Z_2'^2)r^2/2 + AZ_2/w_0 \quad [43]$$

The angular velocity is prescribed for any particular design problem. Then the pressure rise due to centrifugal action is a function of the exit radius r_e. If this radius is chosen, e.g., the exit hub radius might be prescribed as an allowable maximum, then the maximum pressure is defined. The shape of each streamline in the r-z plane is, thus, completely determined by prescribed values of the respective r_i and by a compromise between the value of a maximum pressure rise and a reasonable hub exit radius, and by the requirement of gentle variation from intake to exit. The choice of Z_1 yielding a straight conical shroud and slightly conical hub shape is thought to be appropriate, and this is the reason for the choice of the function

$$Z_1(z) = w_0(\partial r_s/\partial z)_s[r_{si} + (\partial r_s/\partial z)_s z] \quad [44]$$

where subscript s denotes shroud. For the case of straight conical shroud it should be noted that $\partial r_s/\partial z = \text{const} = M_s$.

Once the r-z variation of the streamlines is given, the twist of the stream surface is defined by Z_2, since $V^2/r^2 = Z_2'(z)$. In order to reduce the length of the stream surfaces, and, thus, reduce the magnitude of the viscous dissipation, the twist angle should be small. This requirement and also the necessity of avoiding sharp curvatures of the stream surfaces allow the choice of Z_2. From the various functions examined, a hyperbolic form was selected

$$Z_2'(z) = Z_1^2/r^4 + w_0^2/r^2 + \omega^2\{[1 - (z/l)]/[1 + (z/l)/\beta]\}^2 \quad [45]$$

in which the parameter β permits the choice of the total twist angle.

It should be noted that the numerical work for the infinitesimal blade spacing is exploratory at best, and the final design of axial-flow turbomachines will be the result of the analysis involving a finite number of blades.

From the condition on the selected shroud shape, i.e.

$$\partial r_s/\partial z = \text{const} = M_s \quad [46]$$

the shroud radius may be obtained as

$$r_s = r_{si} + M_s z \quad [47]$$

Hence $Z_1(z)$ takes the form

$$Z_1 = w_0 M_s(r_{si} + M_s z) \quad [48]$$

From Equation [21]

$$u = w_0 M_s(r_{si} + M_s z)/r \quad [49]$$

Equation [40] yields for the r-z variation of the streamlines

$$r^2 = r_i^2 + 2M_s r_{si} z + M_s^2 z^2 \quad [50]$$

From Equation [45] the tangential component of the velocity is

$$v = r\omega[1 - (z/l)]/[1 + (z/l)/\beta] \quad [51]$$

and Equation [40] yields for the ϕ-z variation of the streamlines

$$\phi = (\omega\beta/w_0)\{l(\beta + 1)\ln[(z/l\beta) + 1] - z\} \quad [52]$$

At the exit

$$\phi(l) = (\omega\beta l/w_0)\{(\beta + 1)\ln[(1/\beta) + 1] - 1\} \quad [53]$$

This represents the total twist of the "blade" (streamline surface). The arbitrary constant β which appears in Equation [53] allows the selection of the total twist.

The expression for the pressure distribution is obtained by substituting Equation [41] into Equation [38]. This gives

$$P = P_i + (V_i^2 - \omega^2 r_i^2)/2 + (\omega^2 r^2 - V^2)/2 + (A/w_0)\int_0^z (V^2/r^2)dz \quad [54]$$

For the case of no prerotation of the flow entering the rotating stage, $v_i = \omega r_i$. If the total energy is taken as constant for all entering streamlines, then

$$P_i = P_{Ti} - (w_0^2 + u_i^2)/2 \quad [55]$$

where P_{Ti} denotes the ratio of the total pressure to the density at entrance. Use of Equation [55] in Equation [54] yields

$$P = P_{Ti} + (\omega^2 r^2 - V^2)/2 + (A/w_0)\int_0^z (V^2/r^2)dz \quad [56]$$

The pressure-density ratio distribution at the entrance is

$$P_i = P_{Ti} - w_0^2/2 - (w_0^2 M_s^2 r_{si}^2)(1/r_i^2)/2 \quad [57]$$

The power input to rotor, i.e., the power required, is given by

$$(\text{Power}_{in}) = T\omega \quad [58]$$

where (Power_{in}) is the power input, T is the torque. The torque is equal to the net change in angular momentum per unit time through the rotor. For the case of no prerotation, the torque becomes

$$T = (\omega/2)(r_{se}^2 + r_{He}^2)\rho w_0 \pi(r_{se}^2 - r_{He}^2) \quad [59]$$

where r_{se} and r_{He} are the radii of the shroud and hub at exit, respectively.

Since the mass rate of flow (MRF) is given by

$$(\text{MRF}) = \rho w_0 \pi(r_{se}^2 - r_{He}^2) = \rho w_0 \pi(r_{si}^2 - r_{Hi}^2) \quad [60]$$

Equation [59] may be written as

$$T = (\omega/2)(r_{se}^2 + r_{He}^2)(\text{MRF}) \quad [61]$$

Hence from Equation [58] the power input becomes

$$(\text{Power}_{in}) = (\omega^2/2)(r_{se}^2 + r_{He}^2)(\text{MRF}) \quad [62]$$

The useful power output to the flow is defined as the net change in pressure energy per unit time through the rotor.

The power output is given by

$$(\text{Power}_{out}) = (\bar{P}_{Te} - \bar{P}_{Ti})\rho w_0 \pi(r_{se}^2 - r_{He}^2) \quad [63]$$

where (Power_{out}) is the power output, and $\bar{P}_{Te}$ and $\bar{P}_{Ti}$ are the ratios of total pressure to density (at exit and inlet, respectively) averaged over their respective cross-sectional areas.

Use of Equation [60] yields

$$(\text{Power}_{out}) = (\bar{P}_{Te} - \bar{P}_{Ti})(\text{MRF}) \quad [64]$$

P_{Te} is given by

$$P_{Te} = \int_{r_{He}}^{r_{se}} 2P_{Te} r_e dr/(r_{se}^2 - r_{He}^2) \quad [65]$$

Similarly

$$P_{Ti} = \int_{r_{Hi}}^{r_{si}} 2P_{Ti} r_i dr/(r_{si}^2 - r_{Hi}^2) \quad [66]$$

It should be noted that P_{Ti} was assumed constant and therefore

$$P_{Ti} = P_{Ti} \quad [66a]$$

Also

$$\left.\begin{aligned} P_i &= \int_{r_{Hi}}^{r_{si}} 2P_i r_i dr/(r_{si}^2 - r_{Hi}^2) \\ \text{and} \\ P_e &= \int_{r_{He}}^{r_{se}} 2P_e r_e dr/(r_{se}^2 - r_{He}^2) \end{aligned}\right\} \quad [67]$$

The average pressure ratio $\bar{n}$ is given by the ratio of the average static pressure at exit to the average static pressure at entrance as

$$\bar{n} = \bar{p}_e/\bar{p}_i = \bar{P}_e/\bar{P}_i \quad [68]$$

Substitution from Equation [67] into Equation [68] yields

$$\bar{n} = \int_{r_{He}}^{r_{se}} P_e r_e dr \Big/ \int_{r_{Hi}}^{r_{si}} P_i r_i dr \quad [69]$$

Table 1 contains the numerical values used in the illustrative example. Table 2 is a summary of significant over-all properties of the compressor with infinitesimally spaced blades. This includes torque, revolutions per minute, power input and output, mass rate of flow, average total and static pressures at inlet and exit, and the average pressure ratio.

The r-z variation of streamlines is shown in Fig. 3 and their ϕ-z variation in Fig. 4. The radius variation with z is presented in Fig. 5 in nondimensional form. Figs. 6 and 7 show

TABLE 1 DESIGN PARAMETERS FOR NUMERICAL EXAMPLE

Length of stage (l)	0.250 ft
Intake radii:	
Hub (r_{Hi})	0.250 ft
Medium (r_{mi})	0.293 ft
Shroud (r_{si})	0.333 ft
Slope of shroud (constant) (M_s)	0.5
Number of blades	16
Parameter in Equation [45] (β)	0.043
Pitch angle (Φ)	$\pi/8$ radians
Axial-velocity component (w_0)	100 fps
Intake radial-velocity component at shroud (u_{si})	50 fps
Angular velocity (ω)	15,000 rpm
Eccentricity of velocity parabola (a)	0
Intake pressure-density ratios:	
Hub (P_{Hi})	882,770 ft^2/sec^2
Medium (P_{mi})	883,377 ft^2/sec^2
Shroud (P_{si})	883,742 ft^2/sec^2
Density (ρ)	0.002378 slugs/ft^3

TABLE 2 SUMMARY OF OVER-ALL STAGE PROPERTIES

Average pressure-density ratios (ft^2/sec^2):

	Static	Total
Intake	$\bar{P}_i$ = 883,330	$\bar{P}_{Ti}$ = 889,992
Exit	$\bar{P}_e$ = 1,112,680	$\bar{P}_{Te}$ = 1,348,200

Average pressure ratio: $\bar{n}$ = 1.2596

Power (hp):

Input (Power_{in}) = 30.2646 Output (Power_{out}) = 30.2550

Torque (ft-lb): T = 10.597

Mass rate of flow (slugs/sec): (MRF) = 0.03632

the variation along z of the velocity components and of the resultant velocity. The pressure-ratio distribution is presented in Fig. 8. Fig. 9 is a schematic drawing of the resulting streamline surface ("blade").

BIBLIOGRAPHY

1 "Neue Theorie und Berechnung der Kreiselräder," by H. Lorenz, Oldenbourg, München, Germany, 1906.

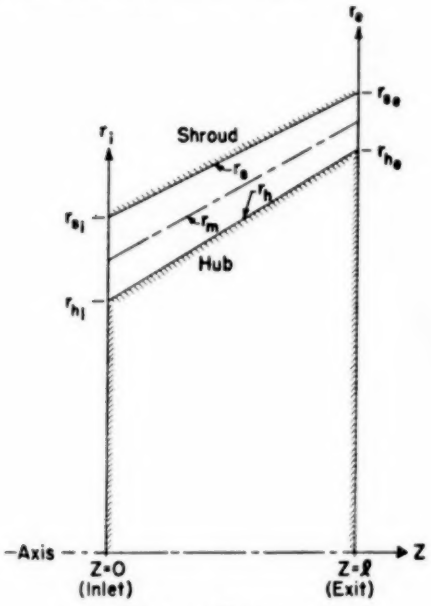

Fig. 3 r, z Projection
(Section with axial plane.)

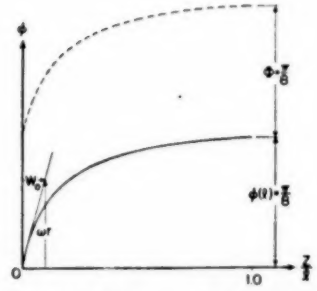

Fig. 4 ϕ, z Projection of Streamlines

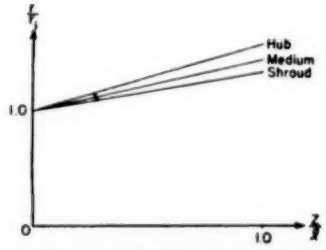

Fig. 5 Radius Ratio Versus z/l

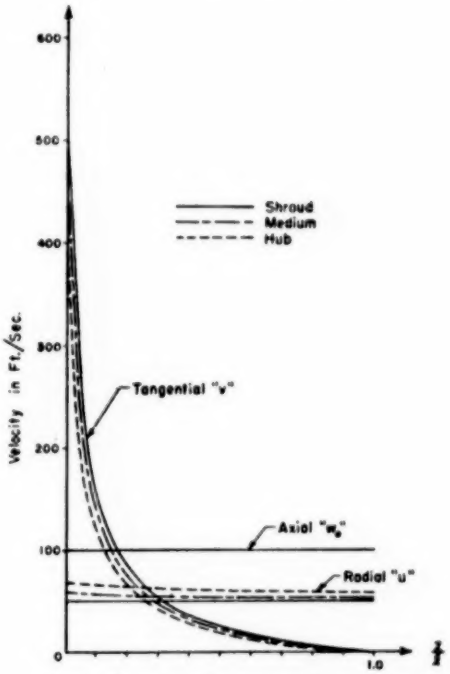

Fig. 6 Velocity Components Versus z/l

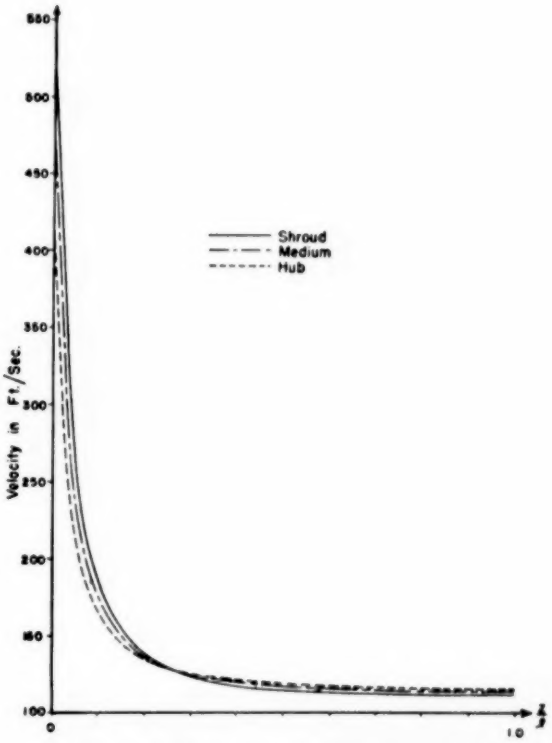

Fig. 7 Total Relative Velocity Versus z/l

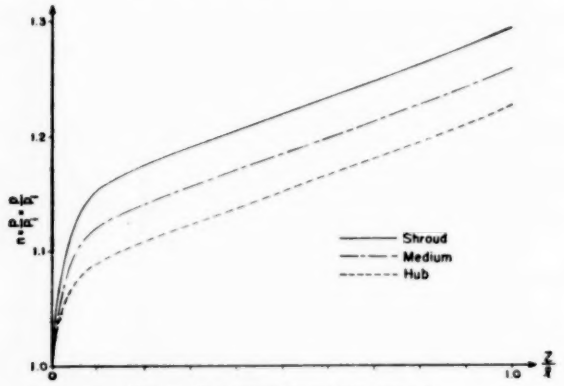

FIG. 8 PRESSURE RATIO VERSUS z/l

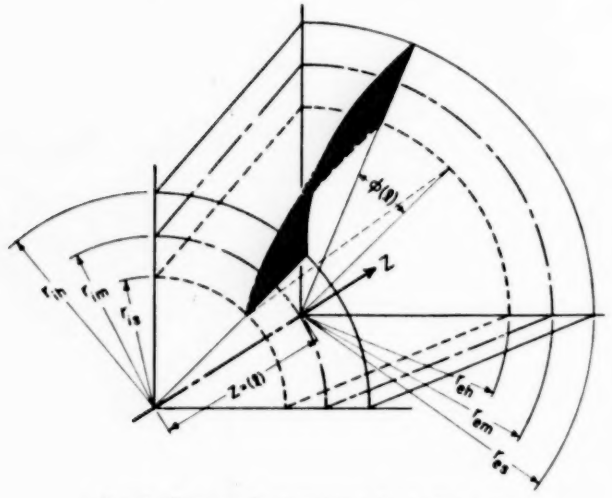

FIG. 9 HUB AND INFINITESIMAL BLADE SURFACE
(Three-dimensional view.)

2 "On a Design Theory of Blade Systems in Steady Compressible Flow," by H. J. Reissner, Polytechnic Institute of Brooklyn, Brooklyn, N. Y. Unpublished lecture notes, 1948.

3 "Blade Systems of Circular Arrangement in Steady Compressible Flow," by H. J. Reissner. Studies and Essays Presented to R. Courant on His Sixtieth Birthday, Interscience Publishers, Inc., New York, N. Y., 1948, pp. 307–327.

4 "Analysis of an Axial Compressor Stage With Infinitesimal and Finite Blade Spacing," by H. J. Reissner and L. Meyerhoff, NACA TN 2493, October, 1951.

5 "Two-Dimensional Steady Nonviscous and Viscous Compressible Flow Through a System of Equidistant Blades," by H. J. Reissner, L. Meyerhoff, and M. Bloom, NACA TN 2718, June, 1952.

6 "Analysis of a Steady, Compressible, Viscous Axially Symmetric Flow Through the Rotating State of Turbomachines," by T. P. Torda, Polytechnic Institute of Brooklyn, Brooklyn, N. Y. Unpublished paper, January, 1949.

7 "Partial Differential Equations," by F. H. Miller, John Wiley & Sons, Inc., New York, N. Y., 1941, pp. 85–94.

Temperature Distribution in the Wake of a Heated Sphere

By D. H. BAER,[1] W. G. SCHLINGER,[2] V. J. BERRY,[3] AND B. H. SAGE[4]

The temperature distribution in the wake of a heated sphere 0.5 in. diam was determined at a gross stream velocity of 30 fps. Measurements were carried out in a channel 0.70 in. in height and 12 in. in width. The surface temperature of the sphere and the energy dissipation from it were determined as a function of gross stream velocities between 10 and 90 fps. The temperature distribution in the wake was correlated on the basis of methods developed for cylinders and satisfactory agreement was obtained.

Nomenclature

The following nomenclature is used in the paper:

A = surface area of sphere, ft^2
C_p = heat capacity at constant pressure, Btu/lb deg F
D = diameter of sphere, ft
D_w = diameter of wire, ft
d = differential operator
e = base of natural logarithm
h = coefficient of heat transfer, Btu/sec ft^2 deg F
k = thermal conductivity, Btu/sec ft deg F
l = vertical distance from center of sphere, ft
l_0 = vertical distance from center of sphere to upper or lower wall of channel, ft
ln = natural logarithm
Pr = turbulent or total Prandtl number
Q = thermal flux, Btu/sec
R = resistance, ohms
Re = Reynolds number
r_0 = radius of sphere, ft
T = average surface temperature of sphere, deg F
t = point temperature, deg F
U = gross velocity, fps
u = point velocity, fps
x = distance downstream from center of sphere, ft
x' = distance downstream from leading point of sphere, ft
Y_T = characteristic width of wake, ft
y = vertical distance from lower wall, ft
y_0 = separation between parallel walls, ft
z = horizontal distance from center of sphere, ft
Δ = difference operator
∂ = partial differential operator
ϵ_e = eddy conductivity, ft^2/sec
K = thermometric conductivity, ft^2/sec
σ = specific weight, lb/ft^3
Ω = electrical resistance, ohms

Subscripts

a = air stream
B = air boundary layer
Co = constantan
Cu = copper
f = free-stream value
n = node in analog circuit
s = surface of sphere
w = thermocouple wire

Introduction

Both theoretical and experimental studies have been made of the velocity and temperature distribution in the wake of a cylinder mounted transverse to an air stream. The theoretical studies (1, 2, 3, 4, 5)[5] were limited to low Reynolds numbers when based on the cylinder diameter. Experimental data in this region (6, 7) have shown satisfactory agreement with theory. In the region of high Reynolds numbers detailed measurements of velocity (8, 9, 10, 11, 12) and temperature (8, 10, 11, 13) are available. Additional measurements of the over-all thermal transfers have been reported by many investigators (6, 7, 14). Correlations of such measurements over a wide range of variables have been presented by McAdams (15) and Jakob (16). The detailed experimental data indicate rather complex behavior in the immediate vicinity of the cylinder (10) but the distributions of both speed and temperature in the wake 10 or more diameters downstream have been generalized (11, 17, 18, 19) with an accuracy adequate for most engineering purposes.

Studies of the temperature and velocity distributions in the wakes of spheres have not been as extensive as for cylinders. Stokes (4) was perhaps the first to predict the velocity distribution around a sphere and Lamb (3) reviewed the early analytical considerations. The drag of spheres was investigated analytically over a limited range of Reynolds numbers (20, 21, 22). Experimental measurements of Allen (23) and Arnold (24) indicate that the generalizations of Goldstein (22) describe the drag with accuracy for Reynolds numbers less than 2. Experimental measurements of drag are available throughout a wide range of flow rates and this work was summarized for subsonic conditions by Schiller (25) and presented by Goldstein (22) and Rouse (26). In contrast to the numerous investigations of drag coefficient of spherical objects detailed measurements of the velocity distribution in the wake of a sphere do not appear to be available. There is still need for further studies to determine the influence of surface roughness upon the transition from a laminar to a turbulent boundary layer.

In comparison with the rather copious data concerning the drag on both cylinders and spheres and abundant information as

[1] Engineer, Phillips Petroleum Company, Bartlesville, Okla.
[2] Chemical Engineer, The Texas Company, Montebello, Calif.
[3] Research Engineer, Stanolind Oil and Gas Company, Tulsa, Okla.
[4] Professor of Chemical Engineering, California Institute of Technology.

Contributed by the Applied Mechanics Division and presented at the Semi-Annual Meeting, Los Angeles, Calif., June 28–July 2, 1953, of THE AMERICAN SOCIETY OF MECHANICAL ENGINEERS.

Discussion of this paper should be addressed to the Secretary, ASME, 29 West 39th Street, New York, N. Y., and will be accepted until October 10, 1953, for publication at a later date. Discussion received after the closing date will be returned.

NOTE: Statements and opinions advanced in papers are to be understood as individual expressions of their authors and not those of the Society. Manuscript received by ASME Applied Mechanics Division, July 14, 1952. Paper No. 53—SA-2.

[5] Numbers in parentheses refer to the Bibliography at the end of the paper.

to the thermal transfer from cylinders, detailed experimental measurements of the temperature profiles in the wake of a heated sphere as well as the over-all thermal transfer from spheres are fewer. However, Kramers (27) and Johnstone (28) studied the over-all thermal transfer from spheres, and Kronig (29) developed a theoretical expression which agrees with the data of Kramers (27) for low Reynolds numbers.

The present study is concerned with the temperature distribution in the wake and the over-all thermal transfer from a sphere 0.5 in. diam mounted in a flow channel 0.70 in. in height. The total thermal transfer from the sphere was determined as a function of flow rate up to a maximum gross velocity of 90 fps whereas the temperature distribution in the wake was measured only at a gross velocity of 30 fps.

Apparatus

The apparatus employed for this investigation was described (10, 30) in some detail. In principle, it involves a recirculating air stream which passes through a rectangular channel 0.70 in. in height, 12 in. in width, and 13 ft in length. The upper and lower surfaces of the channel may be kept at any fixed temperatures between 70 and 160 F. The equipment was so arranged that the entire interior of the flow channel could be traversed. Air was circulated through the flow channel at gross velocities up to 90 fps. In the present instance a sphere was mounted in the channel as shown in Fig. 1.

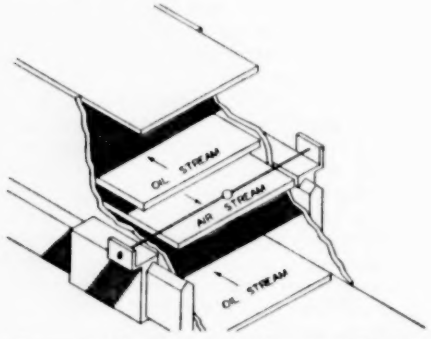

Fig. 1 Schematic Arrangement of Sphere in Flow Channel

The details of construction of this sphere are shown in the cutaway sectional view, Fig. 2. A small hardened steel wire A passes through the assembly and supports the sphere in the flow channel as indicated in Fig. 1. A stainless-steel tube B, 0.096 in. diam, is silver-soldered at C to the thin shell D which is constructed from silver and is 0.016 in. thick. The inner sphere E is composed of copper and is provided with a spiral groove 0.015 in. in width. A short piece of silk-insulated chromel wire was placed in this groove and secured with glyptal cement. The ends of this heater were connected to copper leads which were brought outside the sphere in the annular space between the stainless-steel tube B and the support wire A. In addition, four thermocouples were located around the sphere at points F, G, H, and J. The leads from the thermocouples were placed in the groove K of the silver shell and brought out through the tube B. Rotation of the sphere about the axis A-A permitted the determination of the surface temperature along four circular paths whose planes were normal to the supporting axis. In order to afford good thermal transfer between the inner sphere E and the shell D a soft solder was employed in assembly. The outer surface of the sphere was polished to a surface roughness of 15 microinches.

The temperature of the surface was determined from the indications of the copper-constantan thermocouples located at F, G, H, and J, Fig. 2. Electrical energy input was measured by determining the electromotive force applied to the heater and the electromotive force across the standard resistance connected in series with the heater leads. The electromotive force developed by the thermocouples was measured with a White double potentiometer having a range of 10,000 microvolts, whereas the energy measurements were made with a calibrated "type K" potentiometer. It is believed that the temperature of the surface of the sphere was known within 0.3 F relative to the international platinum scale, and the energy input was established with an uncertainty of not more than 0.1 per cent.

The temperature of the air stream in the wake of the sphere was determined with a 3-mil or in some instances a 10-mil copper-constantan thermocouple which was without enlargement at the junction and which was mounted upon a traversing mechanism (30), permitting controlled movement along any of the three coordinate axes. This thermocouple was calibrated in position by bringing both walls of the flow channel to each of a series of prescribed temperatures and determining the electromotive force of the thermocouple under quiescent conditions as a function of the temperature of the oil baths surrounding the channel. The thermocouples on the surface of the sphere were calibrated by the same procedure. There was little tendency for the calibration of thermocouples of either size to drift with time. The position of the sphere and of the traversing thermocouple relative to

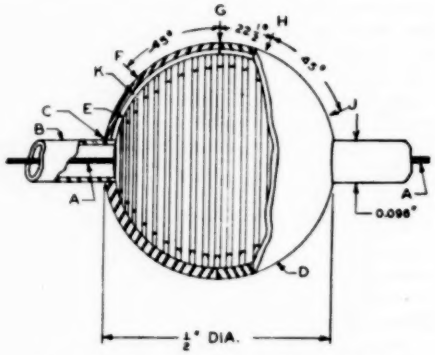

Fig. 2 Sectional View of Heated Sphere

the walls of the channel was determined by means of a cathetometer mounted upon the traversing gear (30). It is believed that their relative positions were established within 0.001 in. Some minor variations in the distance between the plates occurred in the course of the measurements. Differences of as much as 0.002 in. were encountered as a result of changes in room temperature. All measurements of position were made during flow in order to take into account minor distortions resulting from the dynamic forces acting on the sphere or on the traversing thermocouple.

Experimental Results

Experimental measurements of temperature were made during some 50 vertical traverses each of which involved approximately 15 positions. A period of approximately 30 min was required to obtain the points for a given traverse after the equipment had reached equilibrium. Fig. 3 shows in plan the location of the traverses relative to the vertical walls of the flow channel and to the sphere. In each case the traverses were taken vertically at the point shown in the figure and the numbers and letters correspond to the identification number assigned to each traverse. Fig. 4 presents three typical traverses identified as C-10, D-7, and G-8

in accordance with co-ordinates shown in Fig. 3. The standard deviation of the experimental points from the smooth curves relating apparent temperature to position in the wake was 0.07 F. This deviation assigns all the error to the temperature measurements and none to the determination of position.

All the traverses were made with the average surface air stream and the upper and lower plates at 100 F. The gross air velocity was 30 fps and the temperature of the sphere was 243.7 F. Under these conditions the gross thermal flux from the sphere was 0.006147 Btu per sec. The velocity as a function of vertical position in the unobstructed channel during these measurements is shown in Fig. 5 and recorded in Table 1. The corresponding values of the eddy conductivity (31) and of the total Prandtl number (32) are included in Table 1. The total Prandtl number, which is often known as the turbulent Prandtl number, is defined as the ratio of the sum of the eddy viscosity and kinematic viscosity to the sum of the eddy conductivity and thermometric conductivity.

Measurements of the divergence of the wake from a small wire in this channel at the same gross velocity established a value of the intensity of turbulence of 3.8 per cent (11) which compared favorably with preliminary measurements made with a hot-wire anemometer. The sphere was located 70 in. downstream from the end of the approach section and velocity measurements (30) indicate that the flow was uniform at this point in the channel. In a part of Table 1 are presented a limited number of values of velocity, eddy conductivity, and total Prandtl number for gross velocities of 60 and 90 fps (32). These measurements serve to establish the flow pattern in which the over-all thermal transfer from the sphere was determined.

With the exception of the temperature measurements made with the 3-mil thermocouple upstream from the trailing point of the sphere, all the apparent temperatures indicated by the thermocouple electromotive force were corrected to compensate for conduction along the thermocouple leads. This correction was established by means of the electrical analogy shown in Fig. 6. The electrical resistances R_B represent the local average resistance to thermal transfer through the boundary layer surrounding the thermocouple wire whereas R_{Ca} and R_{Cb} represent the total re-

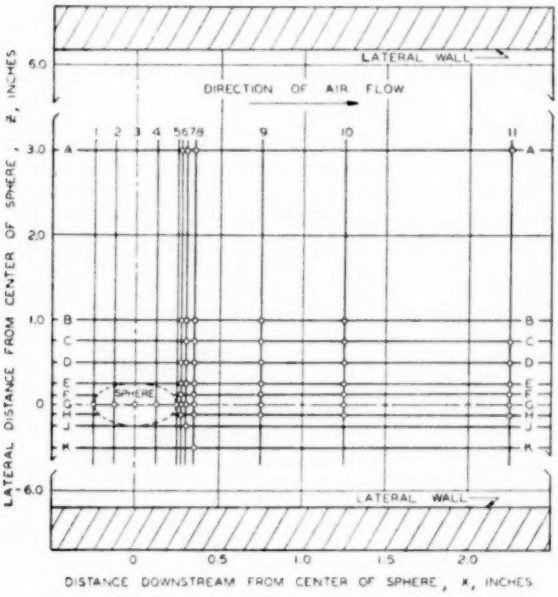
LATERAL WALL
DIRECTION OF AIR FLOW
SPHERE
LATERAL WALL
LATERAL DISTANCE FROM CENTER OF SPHERE, Z, INCHES
DISTANCE DOWNSTREAM FROM CENTER OF SPHERE, X, INCHES

Fig. 3 Plan View of Relative Position of Traverses

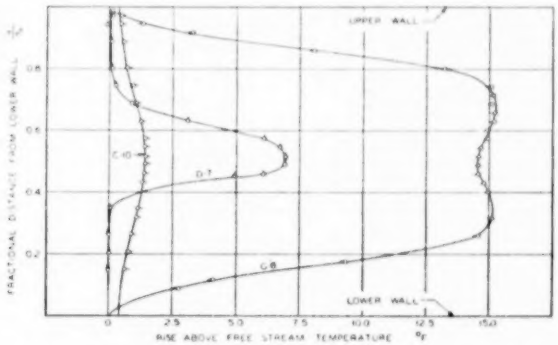

Fig. 4 Typical Temperature Traverses in Wake of Sphere

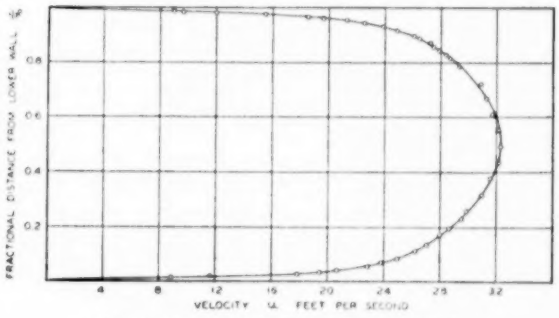

Fig. 5 Velocity Profile in Open Channel

TABLE 1 EFFECT OF POSITION UPON EDDY CONDUCTIVITY AND TOTAL PRANDTL NUMBER[a]

	Gross velocity, fps								
	30			60			90		
y/y_0	u	ϵ_c	Pr	u	ϵ_c	Pr	u	ϵ_c	Pr
0.00	0[b]	0[c]	0.712[d]	0[b]	0[c]	0.712[d]	0[b]	0[c]	0.712[d]
0.10	25.66	3.27	0.752	52.49	6.92	0.798	81.51	9.29	0.847
0.20	28.75	5.60	0.786	58.61	9.99	0.836	90.37	12.42	0.891
0.30	30.69	5.84	0.808	63.09	9.97	0.860	96.21	12.15	0.910
0.40	31.89	4.90	0.826	65.90	8.42	0.882	99.72	10.25	0.928
0.50	32.50	4.34	...	66.71	7.79	...	101.20	9.42	...
0.60	31.89	4.90	0.826	65.75	8.42	0.882	100.13	10.25	0.928
0.70	30.78	5.84	0.808	63.56	9.97	0.860	95.06	12.15	0.910
0.80	28.95	5.60	0.786	59.71	9.99	0.836	90.02	12.42	0.891
0.90	25.74	3.27	0.752	53.04	6.92	0.798	80.48	9.29	0.847
1.00	0	0	0.712	0	0	0.712	0	0	0.712

[a] Unobstructed channel.
[b] Point velocity expressed in ft per sec.
[c] Eddy conductivity expressed in sq ft per sec.
[d] Turbulent or total Prandtl number.

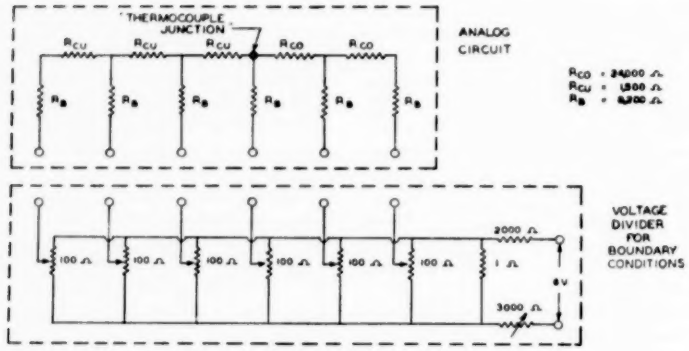

FIG. 6 SCHEMATIC ARRANGEMENT OF ELECTRIC ANALOG

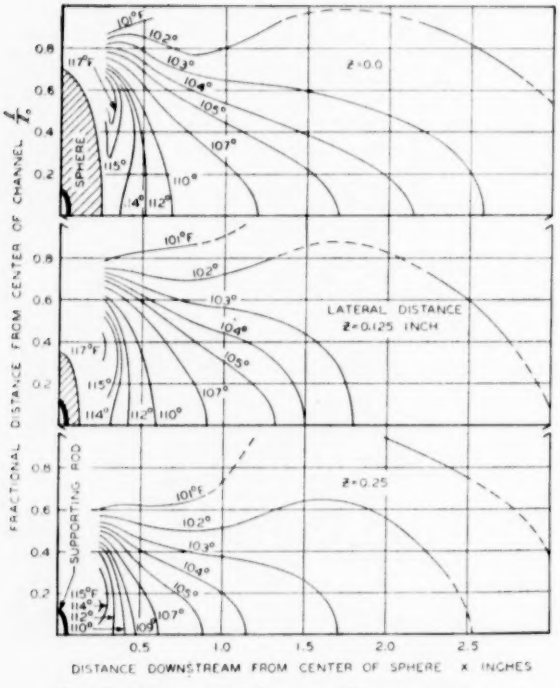

FIG. 7 TEMPERATURE FIELDS IN WAKE OF SPHERE

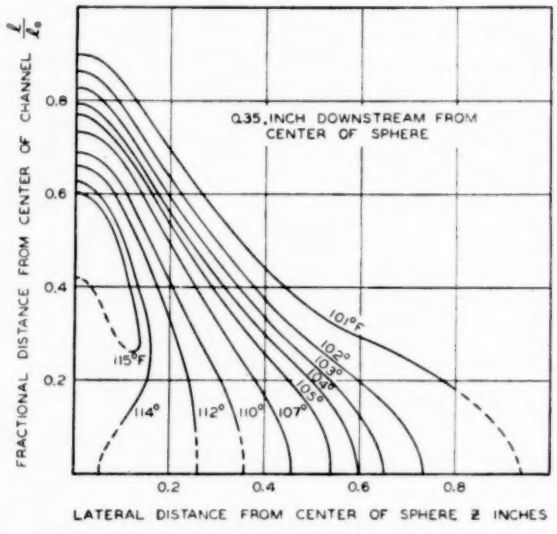
0.35 INCH DOWNSTREAM FROM CENTER OF SPHERE
FRACTIONAL DISTANCE FROM CENTER OF CHANNEL
LATERAL DISTANCE FROM CENTER OF SPHERE z INCHES

FIG. 8 TEMPERATURE FIELD IN PLANE NORMAL TO AXIS OF FLOW 0.35 IN. DOWNSTREAM FROM CENTER LINE OF SPHERE

sistances to thermal conduction along the copper and constantan wires. The analog provides a solution to the following differential equation and allows appropriate boundary conditions to be applied

$$t_a = t_w - \left(\frac{D_w k}{4h}\right)\frac{d^2 t_w}{dz^2} = t_{w,n} - \left(\frac{D_w k}{4h}\right)\frac{t_{w(n-1)} - 2t_{w,n} + t_{w(n+1)}}{\Delta z^2} \quad \ldots\ldots [1]$$

The ratio between R_B and R_{Cu} or R_{Co} must satisfy the following equation

$$\frac{R_B}{R_{Cu}} = \frac{D_w k_{Cu}}{4h\Delta z^2} \quad \ldots\ldots [2]$$

As a part of the boundary condition it was assumed that each of the needles supporting the thermocouple remained at the free-stream temperature of 100 F. The detailed measurements of the apparent temperatures as a function of position as well as the corrections corresponding to Equation [1] and the macroscopic thermal-transfer data are available (33).

In Fig. 7 are presented three sectional views of temperature contours in the wake. The upper diagram corresponds to a vertical plane through the center of the sphere and the two lower diagrams are for vertical planes 0.125 and 0.25 in. from the center of the sphere as shown by the lines F-F and E-E in Fig. 3. The data presented in Fig. 7 represent the average of the values obtained upon both sides of the center of the sphere. These data serve to show the marked changes in the wake that occur at different longitudinal positions. The supporting tube does not influence the wake greatly except near the point C adjacent to the sphere in Fig. 2. The magnitude of this effect may be estimated from Fig. 8 which presents the temperature field in a vertical plane normal to the direction of flow and located 0.35 in. downstream from the center of the sphere. The effect of the supporting tube may be seen, but the greater part of the axial asymmetry results from a combination of the velocity distribution shown in Fig. 5 with the flow about the sphere. The combined effects of the two types of symmetrical flow yield the asymmetric pattern shown in Fig. 8.

The values of temperature as a function of position in the wake obtained by smoothing the experimental data and applying the corrections obtained from Equation [1] have been made available (33). A sample of this tabular information constitutes Table 2.

TABLE 2 SAMPLE OF SMOOTHED TEMPERATURE DISTRIBUTION IN WAKE OF HEATED SPHERE

Position l/l_0	Lateral distance from center of sphere, z, in. 0.0	0.125	0.250	0.500	0.750
0.9	100.29[a]	100.00	100.00	100.01	100.00
0.8	103.05	100.28	100.00	99.99	100.00
0.7	111.45	104.38	100.00	99.97	100.00
0.6	116.80	111.23	101.13	99.98	100.06
0.5	116.35	115.56	104.67	100.05	100.13
0.4	115.60	117.35	111.03	100.23	100.20
0.3	115.20	117.13	114.05	100.89	100.54
0.2	114.96	115.90	115.36	104.35	101.43
0.1	114.87	114.65	114.51	108.04	102.73
0.0	114.81	114.03	113.27	108.31	103.22

[a] Air temperature, deg F.

The temperature distribution in the wake of cylinders has been correlated satisfactorily (11, 18). If the same considerations are applied to the wake of a sphere, it is possible to predict the temperature distribution with useful accuracy. If thermal transfer by conduction along the axis of flow is neglected and if average velocity vectors normal to the direction of flow are assumed to be everywhere zero, the basic differential expression describing the temperature distribution in the wake may be described as follows

$$\frac{\partial}{\partial z}(\epsilon_c + \mathrm{K})\frac{\partial t}{\partial z} + \frac{\partial}{\partial y}(\epsilon_c + \mathrm{K})\frac{\partial t}{\partial y} = u\frac{\partial t}{\partial x} \quad \ldots [3]$$

If the velocity and the sum of the eddy conductivity and the thermometric conductivity are assumed to be constant in the wake and if the sphere may be treated as a point source in an infinite stream, Equation [3] may be integrated to yield

$$\Delta t = \frac{\overset{\circ}{Q}}{4\pi C_p \sigma(\epsilon_c + \mathrm{K})x} e^{-\left(\frac{(l^2 + z^2)u}{4(\epsilon_c + \mathrm{K})x}\right)} \quad \ldots [4]$$

Along the plane of symmetry $l = 0$ it follows that

$$\Delta t = \Delta t_{max} = \frac{\overset{\circ}{Q}}{4\pi C_p \sigma(\epsilon_c + \mathrm{K})x} e^{-\frac{z^2 u}{4(\epsilon_c + \mathrm{K})x}} \quad \ldots [5]$$

A combination of Equations [4] and [5] gives the following ratio for the relative temperature at any point in the wake

$$\frac{t - t_f}{\Delta t_{max}} = e^{-\frac{l^2 u}{4(\epsilon_c + \mathrm{K})x}} \quad \ldots [6]$$

For convenience the characteristic width of a wake is defined as the distance between points in the same lateral section at which the temperature rise is one half the maximum for that section. Under these circumstances the characteristic width becomes

$$Y^2_T = \frac{4(\epsilon_c + \mathrm{K})x}{u} \ln 2 \quad \ldots [7]$$

A combination of Equations [6] and [7] yields

$$\frac{t - t_f}{\Delta t_{max}} = e^{-\left(\frac{}{Y_T}\right)^2 \ln 2} \quad \ldots [8]$$

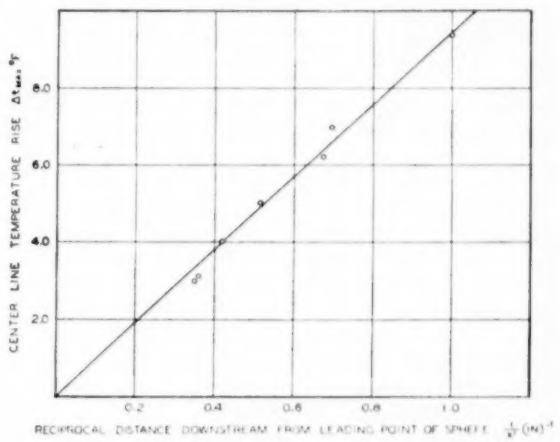

FIG. 9 MAXIMUM TEMPERATURE RISE IN WAKE AS FUNCTION OF RECIPROCAL OF DOWNSTREAM DISTANCE

The foregoing derivation involves little that is new since it applies conventional methods of analysis which have been used effectively for cylinders. Equation [4] indicates that the temperature along the center line of the channel should increase linearly with the reciprocal of the downstream distance. Fig. 9 presents the temperature change along the center line as a function of this variable. The origin has been shifted to the leading point of the sphere to compensate in part for the dispersed source of energy from the 0.5-in. sphere.

The agreement of the experimental data with the predictions of Equation [4] is satisfactory to within 1 in. of the leading point of the sphere, where the assumptions involved in the derivation are not applicable. In the case of a cylinder the temperature at the center line of the wake increases linearly with the reciprocal of the square root of the downstream distance.

Equation [6] may be employed to predict the temperature distribution in the wake. In Fig. 10 is presented the ratio of the actual temperature rise to the maximum temperature rise as a

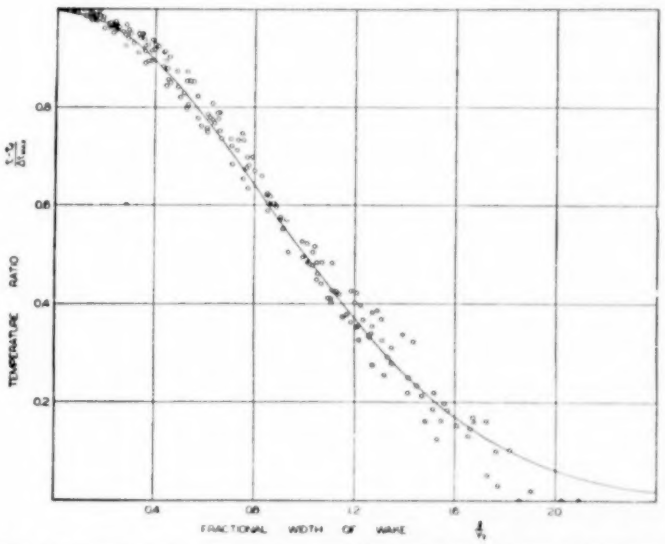

FIG. 10 COMPARISON OF PREDICTED AND MEASURED TEMPERATURE DISTRIBUTION IN WAKE OF SPHERE

function of the distance from the center line expressed as a fraction of the characteristic width. All experimental data corresponding to a downstream distance of more than 1 diam have been included. They indicate a standard deviation of 0.02 in. temperature ratio from the predictions if it is assumed that all of the error is in the prediction of the temperature with no uncertainty as to the position of the thermocouple. The primary error in the prediction of the temperature distribution results from the relative size of the sphere and the flow channel. The sphere is large enough to bring the wake in contact with the walls of the channel at a relatively small downstream distance. The standard deviation found here was larger than that encountered in a similar correlation of the temperature distribution in a wake of a cylinder (11). It is probable that the increased error resulted from the larger relative size of the sphere with respect to the channel.

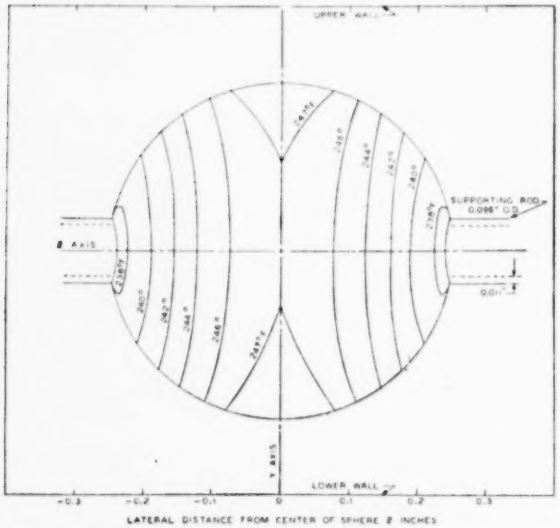

FIG. 11 TEMPERATURE DISTRIBUTION ON FRONT SURFACE OF SPHERE

As indicated in Fig. 2, thermocouples were located upon the surface of the sphere at azimuths of —45, 0, 22½, and 67½ deg from the lead point. Figs. 11 and 12 present the temperature distribution on the surface of the sphere as measured with these thermocouples. The measurements were obtained by rotating the sphere about the supporting tube under conditions of steady flow at a velocity of 30 fps. Table 3 presents the measurements of the surface temperature distribution of the heated sphere for this gross velocity. The character of the temperature distribution about a circle on the sphere normal to the axis of the supporting tubes is not greatly different from that found for cylinders. However, the high thermal conductivity of the silver shell minimizes the temperature variation over the spherical surface. Isothermal contours near the supporting axis indicate slightly lower temperatures resulting from the conduction along the stainless-steel supporting tube. Isotherms in the wake of the sphere in the plane $z = 0$ are included in Fig. 12 for the sake of completeness.

TABLE 3 TEMPERATURE DISTRIBUTION ON SURFACE OF HEATED SPHERE[a]

Angle of displacement,[b] deg	Azimuth[c] —45 deg	0 deg	22½ deg	67½ deg
45.....	241.32[d]	247.62	245.88	238.23
90.....	240.81	246.70	245.18	237.75
135.....	241.23	247.31	245.42	238.20
180.....	241.90	247.98	246.31	238.95
235.....	242.32	248.80	246.62	239.32
270.....	242.39	248.10	246.62	239.36
315.....	242.25	248.09	246.60	239.10
360.....	241.88	247.96	246.45	238.70

[a] Gross velocity of unobstructed air stream, 30 fps.
[b] Displacement measured from vertical about horizontal axis with top of sphere rotating into air stream.
[c] Locations of thermocouples depicted in Fig. 2. Azimuth measured from lead point of sphere.
[d] Air temperatures, deg F.

The gross thermal transfer from the sphere, expressed in terms of the total area and the average surface temperature, was measured at gross velocities of 10, 30, 60, and 90 fps. The average

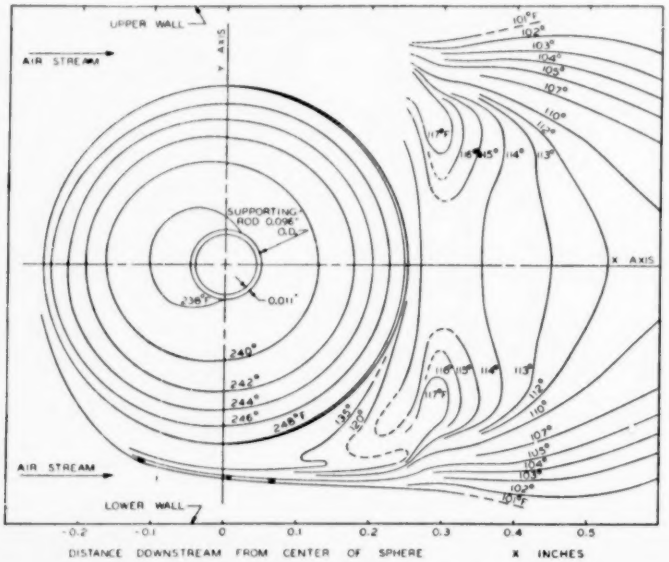

FIG. 12 TEMPERATURE DISTIBUTION ON SIDE SURFACE OF SPHERE

temperature was established from the following expression

$$T = \frac{\oint_0^A t_s dA}{A} = \frac{\oint_0^A t_s dA}{4\pi r_0^2} \quad \ldots\ldots [9]$$

For each condition of flow the average temperature of the surface of the sphere was determined as a function of energy dissipation. The results of this series of measurements are presented in Table 4 and shown in Fig. 13 for several values of Reynolds number.

TABLE 4 GROSS THERMAL TRANSFER FROM HEATED SPHERE

$\dot{Q}$	Temp, deg F	$\dot{Q}$	Temp, deg F
10 fps[a] Re = 2410[b]		30 fps[a] Re = 7010[b]	
...[c]	...[d]	0.006147[c]	243.7[d]
0.003069	206.6	0.003073	172.0
0.001456	149.9	0.001470	134.5
0.000765	125.5	0.000765	118.1
60 fps Re = 13,900		90 fps Re = 20,400	
0.006136	200.6	0.006143	181.2
0.003070	150.2	0.003073	140.3
0.001470	124.1	0.001470	119.4
0.000765	112.6	0.000821	110.0

[a] Gross velocity of unobstructed air stream.
[b] Reynolds number based on sphere diameter.
[c] Thermal flux expressed, Btu per sec.
[d] Average surface temperature.

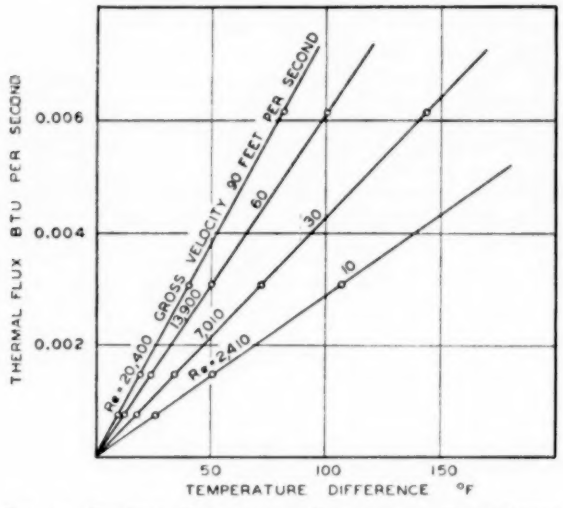

FIG. 13 THERMAL TRANSFER AS FUNCTION OF TEMPERATURE DIFFERENCE BETWEEN SPHERE AND FREE STREAM

based upon the diameter of the sphere. This number was calculated from the gross velocity in the unobstructed channel as defined by the following integral

$$U = \frac{\int_0^{y_0} u dy}{y_0} \quad \ldots\ldots [10]$$

The viscosity and specific weight of the fluid in the free stream, which was maintained at 100 F, were employed to establish the Reynolds number at each velocity indicated in Fig. 13. The results show a nearly linear relationship of the average surface temperature to the gross thermal transfer at a given Reynolds number. Fig. 14 presents the measurements of gross thermal transfer correlated by the method suggested by McAdams (15). The values of the dimensionless parameters have been computed in two ways. In one instance the thermal conductivity, specific

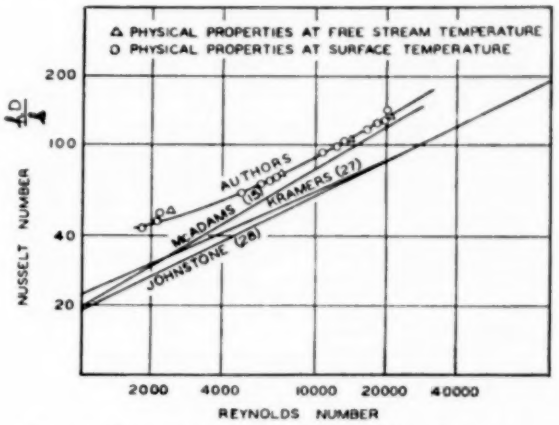

FIG. 14 VARIATION OF NUSSELT NUMBER WITH REYNOLDS NUMBER

weight, and viscosity were based on the free-stream temperature whereas the second set corresponds to the temperature of the surface of the sphere. Both sets of points form a single curve with somewhat higher coefficients of thermal transfer than recommended by McAdams (15). This increase in the thermal transfer coefficient probably results primarily from a higher level of turbulence generated within the present flow channel than was obtained from measurements on freely falling spheres. The measurements of Kramers (27) and the theoretical relation of Johnstone (28) have been included. The measurements and theory of Johnstone were based on spheres moving through quiescent media whereas the studies of Kramers were conducted under conditions approximating potential flow. The difference in these sets of data serves to show the magnitude of the effect of turbulence upon the thermal transfer.

ACKNOWLEDGMENT

This work was made possible by the financial support of the Fluor Corporation. D. H. Baer was the Peter E. Fluor Fellow for 1949–1950. The interest and co-operation of Ira Bechtold and Clyde Blohm, of the Fluor Corporation, contributed materially to the progress of this program. The assistance of H. H. Reamer, R. M. Sherwin, and Elwood Rogers in carrying out the measurements is acknowledged. Virginia Berry aided in the correlation of the results and the preparation of the figures. W. N. Lacey reviewed the manuscript.

BIBLIOGRAPHY

1 "The Two-Dimensional Slow Motion of Viscous Fluids," by L. Bairstow, B. M. Cave, and E. D. Lang, Proceedings of the Royal Society of London, series A, vol. 100, 1922, pp. 394–413.

2 "The Resistance of a Cylinder Moving in a Viscous Fluid," by L. Bairstow, B. M. Cave, and E. D. Lang, Philosophical Transactions of the Royal Society of London, series A, vol. 223, 1923, pp. 383–432.

3 "Hydrodynamics," by H. Lamb, Cambridge University Press, London, England, sixth edition, 1932.

4 "On the Effect of the Internal Friction of Fluids on the Motion of Pendulums," by Sir George G. Stokes, Transactions of the Cambridge Philosophical Society, vol. IX, part II, 1850, pp. 8–106.

5 "Mathematical Attacks on Forced Convection Problems: A Review," by T. B. Drew, Transactions AIChE, vol. 26, 1931, pp. 26–80.

6 "Die Warmeabgabe eines Drahtes oder Rohres an einen senkrecht zur Achse strömenden Gas oder Flüssigkeitsstrom," by J. Ulsamer, *Forschung auf dem Gebiete des Ingenieurwesens*, vol. 3, 1932, pp. 94–98.

7 "On the Convection of Heat From Small Cylinders in a Stream

of Fluid," by L. V. King, Philosophical Transactions of the Royal Society of London, series A, vol. 214, 1914, pp. 313–432.

8 "Notes on Experiments on the Temperature and Velocity in the Wake of a Heated Cylindrical Obstacle," by A. Fage and V. M. Falkner, Proceedings of the Royal Society of London, series A, vol. 135, 1932, pp. 702–705.

9 "Über das ebene Windschattenproblem," by H. Schlichting, *Ingenieur-Archiv*, December, 1930, pp. 533–571.

10 "Temperature and Velocity Profiles in Wake of a Heated Cylinder, Part I," by G. W. Billman, D. M. Mason, and B. H. Sage, *Chemical Engineering Progress*, vol. 46, 1950, pp. 625–634.

11 "Temperature and Velocity Distribution in the Wake of a Heated Cylinder," by V. J. Berry, D. M. Mason, and B. H. Sage, in "Heat Transfer," *Chemical Engineering Progress, Symposium*, series no. 5, vol. 49, 1953, pp. 1–9.

12 "Measurements in the Turbulent Wake of a Cylinder," by A. A. Townsend, Proceedings of the Royal Society of London, series A, vol. 190, 1947, pp. 551–561.

13 "The Fully Developed Wake of a Circular Cylinder," by A. A. Townsend, *Australian Journal of Scientific Research*, series A, vol. 2, 1949, pp. 451–468.

14 "Air Turbulence and Transfer Processes," by E. W. Comings, J. T. Clapp, and J. F. Taylor, *Industrial and Engineering Chemistry*, vol. 40, 1948, pp. 1076–1082.

15 "Heat Transmission," by W. H. McAdams, McGraw-Hill Book Company, New York, N. Y., 1942.

16 "Heat Transfer," by M. Jakob, John Wiley and Sons, Inc., New York, N. Y., vol. 1, 1949.

17 "The Transport of Vorticity and Heat Through Fluids in Turbulent Motion," by G. I. Taylor, Proceedings of the Royal Society of London, series A, vol. 135, 1932, pp. 685–705.

18 "Velocity and Temperature Distribution in Turbulent Wakes Behind an Infinite Cylinder and a Body of Revolution," by N. Hu, *Chinese Journal of Physics*, Peiping, China, vol. 5, 1944, pp. 1–48.

19 "Über die ausgebildete Turbulenz," by L. Prandtl, Verhandlungen des 2 internationalen Kongresses für Technische Mechanik, 1926, Orell Füssli Verlag, Zürich, Switzerland, und Leipzig, Germany, 1927.

20 "Neure Methoden und Ergebnisse in der Hydrodynamik," by C. W. Oseen, Akademische Verlagsgesellschaft, Leipzig, Germany, 1927.

21 "On the Uniform Motion of a Sphere Through a Viscous Fluid," by H. Lamb, *Philosophical Magazine*, series 6, vol. 21, 1911, pp. 112–121.

22 "The Steady Flow of Viscous Fluid Past a Fixed Spherical Obstacle at Small Reynolds Numbers," by S. Goldstein, Proceedings of the Royal Society of London, series A, vol. 123, 1929, pp. 225–235.

23 "The Motion of a Sphere in a Viscous Fluid," by H. S. Allen, *Philosophical Magazine*, series 5, vol. 50, 1900, pp. 323–338.

24 "Limitations Imposed by Slip and Inertia Terms Upon Stokes' Law for the Motion of Spheres Through Liquids," by H. D. Arnold, *Philosophical Magazine*, series 6, vol. 22, 1911, pp. 755–775.

25 "Handbuch der Experimental Physik," by L. Schiller, Akademische Verlagsgesellschaft, Leipzig, Germany, 1932.

26 "Fluid Mechanics for Hydraulic Engineers," by Hunter Rouse, McGraw-Hill Book Company, Inc., New York, N. Y., 1935.

27 "Heat Transfer From Spheres to Flowing Media," by H. Kramers, *Physica*, vol. 12, 1946, pp. 61–80.

28 "Heat Transfer to Clouds of Falling Particles," by H. F. Johnstone, R. L. Pigford, and J. H. Chapin, Transactions AIChE, vol. 37, 1941, pp. 95–133.

29 "On the Theory of Heat and Mass Transfer From a Sphere in a Flowing Medium at Low Values of Reynolds Number," by R. Kronig and J. Bruijsten, *Applied Science Research*, series A, vol. 2, 1951, pp. 439–446.

30 "Temperature Gradients in Turbulent Gas Streams. Methods and Apparatus for Flow Between Parallel Plates," by W. H. Corcoran, F. Page, Jr., W. G. Schlinger, and B. H. Sage, *Industrial and Engineering Chemistry*, vol. 44, 1952, pp. 410–419.

31 "The Analogy Between Fluid Friction and Heat Transfer," by Th. von Kármán, Trans. ASME, vol. 61, 1939, pp. 705–710.

32 "Temperature Gradients in Turbulent Gas Streams. Point Values of Eddy Conductivity and Viscosity in Uniform Flow Between Parallel Plates," by F. Page, Jr., W. G. Schlinger, D. K. Breaux, and B. H. Sage, *Industrial and Engineering Chemistry*, vol. 44, 1952, pp. 424–430.

33 "Measurements of Temperature Distribution in the Wake of a Heated Sphere," by D. H. Baer, W. G. Schlinger, V. J. Berry, and B. H. Sage, Document No. 3664, American Documentation Institute, Library of Congress, Washington, D. C., 1952. For material supplementary to this article order Document 3664 from American Documentation Institute, Library of Congress, Washington 25, D. C., remitting $1.00 for microfilm or $3.60 for photocopies.

Skin Friction and Heat Transfer for Laminar Boundary-Layer Flow With Variable Properties and Variable Free-Stream Velocity[1]

By S. LEVY[2] and R. A. SEBAN,[3] BERKELEY, CALIF.

Numerical solutions of the momentum and energy equations are presented for particular types of laminar boundary-layer flow analogous to the Hartree "wedge flows." Variation of the viscosity and of the thermal conductivity is considered under the circumstances of no dissipation, favorable pressure gradient, and the product of conductivity and density a constant. The solution is based on approximate representations of the velocity and temperature profiles in the boundary layer and these are of such character that the labor of calculation is minimized and the accuracy of the results preserved. The differential equations are reduced to two algebraic equations which rapidly yield the skin friction and the heat transfer in terms of the wall to free-stream temperature ratio for the desired value of Prandtl number. Numerical results are given for a range of wedge flows with gases of Prandtl number 0.70 and 1.0. These results reveal that when the free-stream velocity is variable the temperature difference between the wall and the free stream exerts a substantial effect on the velocity distribution in the boundary layer and on the skin-friction coefficient. Alternatively, the heat-transfer coefficient is not affected radically. A calculation method is presented for the determination of the heat transfer and skin friction for a flow with an arbitrary variation of velocity over an isothermal surface. This method utilizes the results of the present analysis for the variable property wedge flows.

Nomenclature

The following nomenclature is used in the paper:

A, B, C, D = constants appearing in Equation [9]
a, b, c, d = constants appearing in Equation [8]
c_p = specific heat at constant pressure, Btu/lb deg F
D = significant dimension of the body, ft
F = function appearing in Equation [41]
f = function of the independent variable η
g = temperature ratio, T/T_1
h = heat-transfer coefficient, Btu/hr sq ft deg F
K = constant equivalent to $1-T_w/T_1$
k = thermal conductivity, Btu/hr sq ft deg F/ft
m = exponent appearing in Equation [43]
p = pressure in boundary layer, psf
r = constant appearing in Equation [43]
s = function of x defined by $ds = \mu_1\rho_1 u_1 dx$
T = temperature in boundary layer, deg R
T_1 = temperature at edge of the boundary layer, deg R
T_w = wall temperature, deg R
u = velocity component of flow in x-direction, fps
u_a = arbitrarily selected constant velocity, fps
u_1 = velocity at edge of boundary layer, fps
v = velocity perpendicular to body surface, fps
x = distance along body surface, ft
y = distance normal to body surface, ft
z^* = nondimensional displacement thickness
z_t = nondimensional momentum thickness
β = velocity distribution parameter
γ = constant defined by Equation [28]
$\bar{\gamma}$ = constant defined by Equation [29]
γ' = constant defined by Equation [35]
η = independent variable defined by Equation [4]
λ = exponent determining effect of Prandtl number
μ = absolute viscosity, lb sec/ft^2
ν = kinematic viscosity, ft^2/sec
ρ = density of the flowing fluid, lb sec^2/ft^4
σ = Prandtl number, $\mu c_p/k$ nondimensional
τ = shear stress, psf
ϕ = error integral

Subscripts:

1 = conditions at edge of the boundary layer
w = conditions at surface of the body

Introduction

Because of the dependence of the thermal conductivity and viscosity of a gas upon the temperature, the variation of these properties must be accounted for in the calculation of the skin friction of, and heat transfer to, a boundary layer when the difference between the wall temperature and the free-stream temperature is large. Inclusion of the variation of these physical properties in the analysis leading to the desired quantities substantially increases the complexity of the analysis; but the importance of the evaluation of the effect of property variation has directed much attention to the problem and has produced numerous results for the case of flow with constant free-stream velocity. With variable free-stream velocities, the differential equations have been set up by Illingworth (1)[4] for the case of wedge flows.

For flat-plate flows (u_1 = const), with a laminar boundary layer, the assumption that the product of the thermal con-

[1] This paper comprises a part of the research on Heat Transfer to Boundary Layers sponsored by the Flight Research Laboratory, Wright Air Development Center, on Contract 33(038)-12941. The authors are grateful for this support.

[2] Research Engineer, Institute of Engineering Research, University of California.

[3] Associate Professor of Mechanical Engineering, University of California. Mem. ASME.

Contributed by the Applied Mechanics Division and presented at the Semi-Annual Meeting, Los Angeles, Calif., June 28–July 2, 1953, of The American Society of Mechanical Engineers.

Discussion of this paper should be addressed to the Secretary, ASME, 29 West 39th Street, New York, N. Y., and will be accepted until October 10, 1953, for publication at a later date. Discussion received after the closing date will be returned.

Note: Statements and opinions advanced in papers are to be understood as individual expressions of their authors and not those of the Society. Manuscript received by ASME Applied Mechanics Division, September 6, 1952. Paper No. 53—SA-3.

[4] Numbers in parentheses refer to the Bibliography at the end of the paper.

ductivity and the density is a constant ($\rho\mu$ = const),[5] simplifies the problem considerably. Chapman and Rubesin (2) have presented the most complete solution on this basis, accounting for the effects of frictional heating and allowing a power-function variation of the wall temperature, for a gas having a Prandtl number of 0.70. When the product, $\mu\rho$, is not a constant the difficulty of solution is magnified. Crocco (3), postulating viscosity variation with temperature according to Sutherland's equation, has given results for a gas with a Prandtl number of 0.725, including dissipation, and assuming the wall to be isothermal. Johnson and Rubesin (4) have formulated equations defining the appropriate temperature for property evaluations so that, with properties evaluated at this temperature, the correct skin friction and heat transfer can be calculated from the results for constant property flow.

For the circumstances in which the free-stream velocity is variable, some solutions are available for cases restricted to a Prandtl number of unity, the product $\mu\rho$ a constant, and no heat transfer at the wall. Weil (5) and Low (6) have presented such solutions based on the Kármán-Pohlhausen integral method. Ferrari (7) has indicated a more general method which involves solutions of the external and internal regions of the boundary layer for the particular case where the free-stream velocity can be expressed as a power series of the distance measured along the body. The calculations needed to arrive at numerical results appear to be laborious because of the successive approximations required.

When the wall is not insulated and the free-stream velocity is variable, ordinary differential equations can be obtained for the momentum and energy equations for particular types of flow (analogous to the Hartree wedge flows) if the effect of frictional heating is neglected. Illingworth gave these equations and, by a method of successive approximations, arrived at a result for one particular case. Numerical solutions have also been obtained by Brown and Donoughe (13) for a range of cases. A large amount of labor would be required to obtain solutions covering a large range of possible conditions. These can be obtained easily if the product $\mu\rho$ is taken as constant and an approximate method is employed. This approximate method, here presented, requires the assumption of velocity distributions and temperature distributions in the manner already used by Ringleb (8) for the approximate solution of the laminar boundary layer with suction. Certain definite types of flows are considered quite exactly by this method, which, in the second part of this paper, is extended more approximately to the more general case of flow about an arbitrary body.

Laminar Flow With Variable Properties and With Power-Function Free-Stream Velocity

Analysis. The boundary-layer forms of the continuity, momentum, and energy equations for the two-dimensional flow, over a surface of large curvature, of a gas with constant Prandtl number and specific heat, are

$$\frac{\partial}{\partial x}(\rho u) + \frac{\partial}{\partial y}(\rho v) = 0 \quad \ldots\ldots [1]$$

$$\rho\left(u\frac{\partial u}{\partial x} + v\frac{\partial u}{\partial y}\right) = \frac{\partial}{\partial y}\left(\mu\frac{\partial u}{\partial y}\right) - \frac{dp}{dx} \quad \ldots\ldots [2]$$

$$\rho c_p\left(u\frac{\partial T}{\partial x} + v\frac{\partial T}{\partial y}\right) - u\frac{dp}{dx} = \frac{c_p}{\sigma}\frac{\partial}{\partial y}\left(\mu\frac{\partial T}{\partial y}\right) + \mu\left(\frac{\partial u}{\partial y}\right)^2 \quad \ldots [3]$$

The boundary conditions considered are

$y = 0$	$u = 0$	$v = 0$	$T = T_w$
$y \to \infty$	$u = u_1$		$T = T_1$

Taking $u/u_1 = f'$ (prime indicates order of differentiation with respect to η) in such a way as to satisfy the continuity equation, defining $g = T/T_1$, neglecting the dissipation term in the energy equation, and transforming the independent variables (x, y) to (s, η) as

$$s = \int_0^x \mu_1\rho_1 u_1 dx \qquad \int_0^\eta \frac{T}{T_1}d\eta = \frac{u_1\rho_1 y}{(2s)^{1/2}} \quad \ldots\ldots [4]$$

yields for the momentum and energy equations the forms

$$f''' + ff'' + \left(2\frac{s}{u_1}\frac{du_1}{ds}\right)(g - f'^2) = 0 \quad \ldots\ldots [5]$$

$$g'' + \sigma fg' = 0 \quad \ldots\ldots [6]$$

with the transformed boundary conditions

$$\left.\begin{array}{lll} f(s,0) = f'(s,0) = 0 & g(s,0) = 1 - K; & \left(K = \dfrac{T_1 - T_w}{T_1}\right) \\ f'(s,\infty) = 1 & g(s,\infty) = 1 & \end{array}\right\} \quad \ldots [7]$$

If

$$\beta = 2\frac{s}{u_1}\frac{du_1}{ds}$$

is a constant Equations [5] and [6] become ordinary differential equations, and they were derived in this form by Illingworth through similar transformations.

The present method involves the assumption of β = const and of solutions of the form

$$\frac{u}{u_1} = f' = 1 - e^{a\eta + \frac{b}{2!}\eta^2 + \frac{c}{3!}\eta^3 + \frac{d}{4!}\eta^4} \quad \ldots\ldots [8]$$

$$\frac{T}{T_1} = g = 1 - Ke^{A\eta + \frac{B}{2!}\eta^2 + \frac{C}{3!}\eta^3 + \frac{D}{4!}\eta^4} \quad \ldots\ldots [9]$$

With these solutions, all boundary conditions at $\eta \to \infty$ are satisfied if the coefficient of the highest power of η is negative. Also, the conditions $f'(0) = 0$ and $g(0) = 1 - K$ are satisfied.

With

$$\beta = 2\frac{s}{u_1}\frac{du_1}{ds}$$

the velocity distribution over the body is of the form $u_1 = Px^{\beta/(2-\beta)}$; this corresponds to the wedge flows considered by Hartree, the parameter β being identical in the present equations and in Hartree's solutions.

The unknown constants a, b, c, d and A, B, C, D can be determined by satisfying the boundary-layer Equations [5] and [6] along $\eta = 0$ (i.e., $y = 0$) as far as practicable. Differentiation of Equations [5] and [6] three times with respect to η yields for $\eta = 0$ the following eight equations

$$\left.\begin{array}{l} f'''(0) + \beta g(0) = 0 \\ f^{IV}(0) + \beta g'(0) = 0 \\ f^{V}(0) + f''^2(0) - 2\beta f''^2(0) + \beta g''(0) = 0 \\ f^{VI}(0) + 4f''(0)f'''(0) - 6\beta f''(0)f'''(0) + \beta g'''(0) = 0 \\ g''(0) = 0 \\ g'''(0) = 0 \\ g^{IV}(0) + \sigma f''(0)g'(0) = 0 \\ g^{V}(0) + \sigma f'''(0)g'(0) = 0 \end{array}\right\} \quad \ldots [10]$$

The derivatives that appear in these equations have to be calculated from Equations [8] and [9] for $\eta = 0$. Substitution

[5] If the Prandtl number and specific heat are constants, $k\rho$ = constant means $\mu\rho$ = constant.

of these derivatives gives eight simultaneous algebraic equations for the terms a, b, c, d, A, B, C, and D

$$\left.\begin{aligned}
&-(b + a^2) + \beta(1 - K) = 0\\
&-(c + 3ba + a^3) - \beta KA = 0\\
&-(d + 4ac + 3b^2 + 6a^2b + a^4) + a^2 - 2\beta a^2 = 0\\
&-(5da + 10bc + 10ca^2 + 15b^2a + 10ba^3 + a^5)\\
&\qquad +4a(b + a^2) - 6\beta a(b + a^2) = 0\\
&-K(B + A^2) = 0\\
&-K(C + 3BA + A^3) = 0\\
&-K(D + 4AC + 3B^2 + 6A^2B + A^4)\\
&\qquad + \sigma KaA = 0\\
&-K(5DA + 10BC + 10CA^2 + 15B^2A\\
&\qquad + 10BA^3 + A^5) + \sigma KA(b + a^2) = 0
\end{aligned}\right\} \quad \ldots [11]$$

The first three of these equations determine b, c, d in terms of a and A, while the fifth, sixth, and seventh of these equations yield B, C, D in terms of a and A. Thus

$$\left.\begin{aligned}
b &= \beta(1 - K) - a^2\\
c &= 2a^3 - 3\beta(1 - K)a - \beta KA\\
d &= -6a^4 + 12\beta(1 - K)a^2 - 2\beta a^2 + 4\beta KAa + a^2\\
&\qquad - 3\beta^2(1 - K)^2\\
B &= -A^2\\
C &= 2A^3\\
D &= -6A^4 + \sigma aA
\end{aligned}\right\} \quad \ldots [12]$$

Substitution of Equations [12] into the fourth and the last equation of the System [11] gives the equations

$$\left.\begin{aligned}
&10\beta KA(2a^2 - \beta) = 24a^5 - 5a^3[12\beta(1 - K) - 2\beta\\
&+ 1] + 2\beta a[15\beta(1 - K)^2 - 2(1 - K) - 3\beta(1 - K)]\\
&24A^5 - 5\sigma aA^2 = -\sigma\beta(1 - K)A
\end{aligned}\right\} \quad \ldots [13]$$

Thus the system of two simultaneous differential equations is reduced to a system of two algebraic equations. The solution to these equations is obtained by trial and error for fixed values of β, σ, and K. Two real values of quantities a and A are obtained, the desired solutions being those which yield the smaller value of quantities d and D. With quantities a and A determined, all quantities associated with the velocity and temperature profiles are given by Equations [12]. The skin-friction coefficient and the heat-transfer coefficient are determined by quantities a and A alone. The shear stress and heat rate at the wall are

$$\tau_w = \mu_w \left.\frac{\partial u}{\partial y}\right|_{y=0} = \mu_w \frac{T_1}{T_w}\frac{u_1^2\rho_1}{(2s)^{1/2}} f''(0)$$

$$= -\frac{a}{\sqrt{2 - \beta}}\sqrt{\frac{\mu_w}{u_1 x \rho_w}}\,\rho_w u_1^2 \quad \ldots [14]$$

$$q_w = -k_w \left.\frac{\partial T}{\partial y}\right|_{y=0} = -k_w \frac{T_1^2}{T_w}\frac{u_1\rho_1}{(2s)^{1/2}} g'(0)$$

$$= -\frac{A}{\sqrt{2 - \beta}}\sqrt{\frac{u_1 x \rho_w}{\mu_w}}\,(T_w - T_1)\frac{k_w}{x} \quad \ldots [15]$$

The local skin-friction and heat-transfer coefficients are

$$\frac{\tau_w}{\rho_1 u_1^2}\sqrt{\frac{u_1 x \rho_1}{\mu_1}} = \frac{\tau_w}{\rho_w u_1^2}\sqrt{\frac{u_1 x \rho_w}{\mu_w}} = -\frac{a}{\sqrt{2 - \beta}} \quad \ldots [16]$$

$$\frac{hx/k_1}{\sqrt{\frac{u_1 x \rho_1}{\mu_1}}} = \frac{hx/k_w}{\sqrt{\frac{u_1 x \rho_w}{\mu_w}}} = -\frac{A}{\sqrt{2 - \beta}} \quad \ldots [17]$$

A measure of the accuracy of the solutions so obtained consists in the comparison of them with exact solutions for the momentum and energy equations as given by Hartree (9) and by Eckert (10) for constant property flows. For this case Equation [13] becomes

$$24a^4 - 5a^2(10\beta + 1) + 2\beta(12\beta + 2) = 0 \quad \ldots [18]$$

$$24A^4 - 5\sigma aA + \sigma\beta = 0 \quad \ldots [19]$$

Quantity a is given by Equation [18] as

$$a = -\sqrt{\frac{5(10\beta + 1) + \sqrt{196\beta^2 + 116\beta + 25}}{48}} \quad \ldots [20]$$

The comparison is made in terms of the equivalent values of quantities a and A for the exact solutions, and is indicated in Table 1. Acceptable correspondence in the values of a exists

TABLE 1. SKIN FRICTION AND HEAT TRANSFER FOR CONSTANT-PROPERTY WEDGE FLOW FOR $\sigma = 1.0$

	$\sqrt{2 - \beta}\,\frac{\tau_w}{\rho_1 u_1^2}\sqrt{\frac{u_1 x \rho_1}{\mu_1}}$		$\sqrt{2 - \beta}\,\frac{hx}{k_1}\Big/\sqrt{\frac{u_1 x \rho_1}{\mu_1}}$	
β	Predicted	Exact	Predicted	Exact
1.6	1.526	1.521	0.590	0.594
1.0	1.236	1.233	0.569	0.570
0.5	0.930	0.928	0.537	0.539
0.2	0.684	0.687	0.501	0.507
0	0.456	0.470	0.456	0.470

in the range of accelerated flows for which exact results are available, $0 < \beta < 1.6$, with the maximum error, at $\beta = 0$, of $2^1/_2$ per cent. With decelerating flows, $\beta < 0$, the error increases. Zero shear ($a = 0$) is indicated at $\beta = -0.167$, a value substantially less than that of $\beta = -0.20$ obtained by Hartree. Table 1 contains quantity A calculated for a fluid with a Prandtl number of unity. These also agree well with the results of Eckert.

Fig. 3 reveals the effect of changes in the Prandtl number on quantity A. The nearly straight lines obtained indicate the effect can be represented as a factor σ^λ, with $\lambda \to 1/2$ for large β, $\lambda = 1/2$ for $\beta = 0$, and $\lambda = 1/4$ for separation flow. This dependence is that previously predicted by Eckert (10) and Tifford (11).

These results indicate the approximate method to be satisfactory for accelerating flows, and solutions have been obtained for variable properties for various values of K.

The calculations as made yielded negative values of quantity d except for large values of T_w/T_1. In these cases only the smaller of the positive values would lead to a finite displacement thickness and the smaller value was chosen. When d becomes positive the outer boundary condition Equation [7] no longer is satisfied, although termination of the exponential series with either c or a fifth coefficient e, which remained negative, will do so. This tendency of the signs in the series

$$\left(a\eta + \frac{b}{2!}\eta^2 + \frac{c}{3!}\eta^3 \ldots\right)$$

to alternate, combined with the small arithmetical differences involved in the calculation of the exponents d, e, and so on, terminates the usefulness of this approximation. System characteristics for which $\partial^2 u/\partial y^2$ does not decrease monotonically from the wall value to zero at large distances from the wall lead to these conditions. Thus discrepancies are expected for large values of T_w/T_1 which are similar to those experienced for $\beta < 0$ in the case of constant property flows.

Results. Calculations have been carried out for a sufficient number of cases to describe the combined effect of variable properties and variable free-stream velocity. The calculations were performed for Prandtl numbers of 0.70 and 1.0.

TABLE 2 $\dfrac{\tau_w}{\rho_1 u_1^2}\sqrt{\dfrac{u_1 x \rho_1}{\mu_1}}$ FOR VARIABLE PROPERTIES WEDGE FLOW; FOR $\sigma = 1.0$ AND $\sigma = 0.7$

	$\beta = 1.6$		$\beta = 1.0$		$\beta = 0.5$		$\beta = 0.2$		$\beta = 0$	
T_w/T_1 / σ	0.7	1.0	0.7	1.0	0.7	1.0	0.7	1.0	0.7	1.0
0.6	1.828	1.850	0.972	0.983	0.662	0.667	0.456	0.459	0.323	0.323
0.8	2.152	2.163	1.117	1.122	0.700	0.703	0.484	0.486	0.323	0.323
Constant property	2.413	2.413	1.236	1.236	0.759	0.759	0.510	0.510	0.323	0.323
1.5	2.960	2.936	1.491	1.478	0.922	0.915	0.567	0.563	0.323	0.323
2.0	3.441	3.397	1.714	1.690	1.052	1.039	0.618	0.607	0.323	0.323
3.0	...	...	2.113	2.074	1.204	1.172	0.710	0.681	0.323	0.323

TABLE 3 $\dfrac{hx}{k_1}\Big/\sqrt{\dfrac{u_1 x \rho_1}{\mu_1}}$ FOR VARIABLE PROPERTIES WEDGE FLOW; FOR $\sigma = 0.7$ AND $\sigma = 1.0$

	$\beta = 1.6$		$\beta = 1.0$		$\beta = 0.5$		$\beta = 0.2$		$\beta = 0$	
T_w/T_1 / σ	0.7	1.0	0.7	1.0	0.7	1.0	0.7	1.0	0.7	1.0
0.6	0.757	0.879	0.471	0.541	0.378	0.430	0.323	0.366	0.286	0.323
0.8	0.787	0.914	0.486	0.558	0.379	0.432	0.326	0.370	0.286	0.323
Constant property	0.803	0.933	0.495	0.569	0.385	0.438	0.330	0.373	0.286	0.323
1.5	0.816	0.957	0.508	0.586	0.403	0.459	0.336	0.380	0.286	0.323
2.0	0.813	0.972	0.516	0.597	0.403	0.472	0.341	0.385	0.286	0.323
3.0	...	...	0.518	0.610	0.412	0.470	0.347	0.389	0.286	0.323

The most important results, the skin-friction and heat-transfer coefficient, are presented for all cases in Tables 2 and 3 and also in Figs. 1 and 2. The following cases are indicated in the tabulation

$$\beta = 1.6,\ 1.0,\ 0.5,\ 0.2,\ 0$$
$$K = 0.4,\ 0.2,\ 0,\ -0.5,\ -1.0,\ -2.0$$
$$\sigma = 0.70 \text{ and } 1.0$$

Discussion. Examination of Fig. 1 reveals that the skin friction increases considerably as the difference between the wall and free-stream temperatures becomes large. This effect becomes even more pronounced as the Prandtl number is reduced from 1.0 to 0.70. For instance, for stagnation flow and a wall temperature 3 times larger than the free-stream temperature the skin friction is 70 per cent higher than for the corresponding constant-property case. The effect of variable properties decreases as β decreases until no effect is observed for flat-plate flow ($\beta = 0$), which verifies the classic result for this case. The present results indicate that no grounds exist for the use of the incompressible skin-friction relation in solving the momentum equation about an arbitrary body with high or very low surface temperatures.

Fig. 2 reveals that the heat-transfer coefficient is not affected radically by variable properties. Thus for $\beta = 1$ and $T_w/T_1 = 3.0$ the heat-transfer coefficient is only 6 per cent higher than the corresponding constant-property value.

Illingworth arrived at the same conclusions from his numerical calculations for the particular case $\beta = 1.0$, $T_w/T_1 = 0.8$, $\sigma = 0.725$, and he obtained

$$\frac{\tau_w}{\rho_1 u_1^2}\Big/\sqrt{\frac{u_1 x \rho_1}{\mu}} = 1.084 \text{ and } \frac{hx}{k_1}\sqrt{\frac{u_1 x \rho_1}{\mu_1}} = 0.502$$

which compare favorably with the values of 1.117 and 0.486 computed from the present analysis for $\sigma = 0.7$.

Further checking on the accuracy of the present results is possible by comparison with the computations of Brown and Donoughe. Their values are shown in Figs. 1 and 2. For $0.5 < T_w/T_1 < 2.0$ the skin friction and heat transfer compare favorably. As the ratio of wall to free-stream temperature becomes increasingly larger, discrepancies are observed for the momentum thickness. The deficiency of the present method in that range has been noted already, but further investigation of the negative values of the momentum thickness obtained by Brown and Donoughe may be of interest.

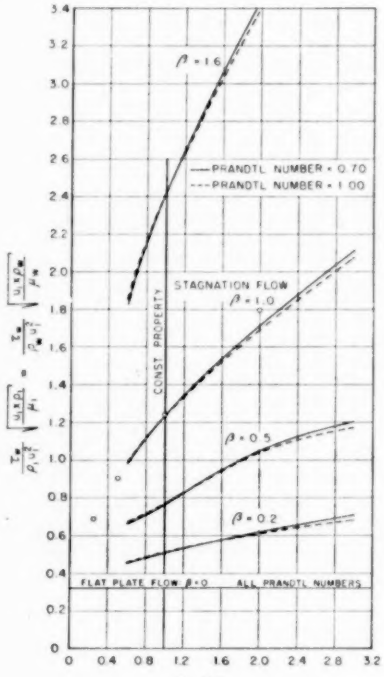

FIG. 1 SKIN FRICTION FOR VARIABLE PROPERTIES WEDGE FLOWS (○—Brown-Donoughe for $\beta = 1.0$, $\sigma = 0.7$.)

LAMINAR FLOW WITH VARIABLE PROPERTIES AND VARIABLE FREE-STREAM VELOCITY

Calculation of the Momentum and Displacement Thickness for a Power Function Free-Stream Velocity. The momentum integral equation for flow about an arbitrary body is

$$2u_1\rho_1\theta\frac{du_1}{dx} + u_1^2\frac{d}{dx}(\rho_1\theta) + \rho_1 u_1\delta^*\frac{du_1}{dx} = \tau_0 \quad \ldots\ldots [21]$$

where the displacement thickness δ^* and the momentum thickness θ are defined as

$$\delta^* = \int_0^\infty \left(1 - \frac{\rho}{\rho_1}\frac{u}{u_1}\right) dy \quad \ldots\ldots [22]$$

$$\theta = \int_0^\infty \frac{\rho u}{\rho_1 u_1}\left(1 - \frac{u}{u_1}\right) dy \quad \ldots\ldots [23]$$

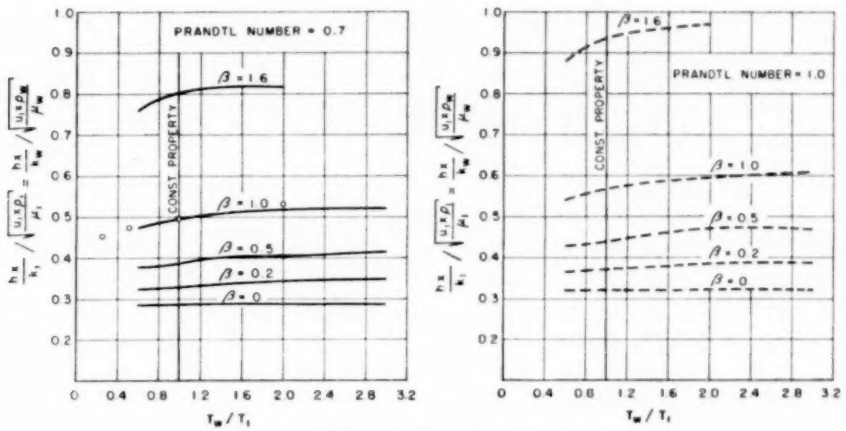

FIG. 2 HEAT TRANSFER FOR VARIABLE PROPERTIES WEDGE FLOWS
(○—Brown-Donoughe for $\beta = 1.0$.)

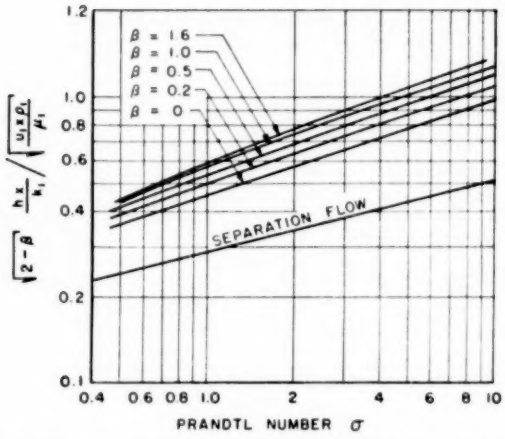

FIG. 3 EFFECT OF PRANDTL NUMBER UPON HEAT TRANSFER FOR CONSTANT PROPERTIES WEDGE FLOWS

Introduction of the variable η into Equations [22] and [23] yields

$$z_4 = \frac{\theta}{(2s)^{1/2}} u_1 \rho_1 = \int_0^\infty f'(1 - f')d\eta \quad [24]$$

$$z^* = \frac{\delta^*}{(2s)^{1/2}} u_1 \rho_1 = \int_0^\infty (1 - f')d\eta - \int_0^\infty (1 - g)d\eta \quad [25]$$

For a power function of free-stream velocity the calculated constants a and A enable the computations from Equations [12] of the function f' and g, i.e., the Integrals [24] and [25]. However, the calculations of the nondimensional displacement and momentum thickness are simplified considerably by approximating the velocity, and temperature profiles by a Gauss curve of the form

$$f' = \frac{u}{u_1} = 1 - e^{a\eta + \gamma\eta^2} \quad [26]$$

$$g = \frac{T}{T_1} = 1 - Ke^{A\eta + \bar{\gamma}\eta^2} \quad [27]$$

where γ and $\bar{\gamma}$ are constants determined by ascertaining that Equations [26] and [27] pass through the same point for $\eta = 1/a$ as Equations [8] and [9]. Thus

$$\gamma = \frac{b}{2} - \frac{c}{6a} + \frac{d}{24a^2} \quad [28]$$

$$\bar{\gamma} = \frac{B}{2} - \frac{C}{6A} + \frac{D}{24A^2} \quad [29]$$

Equations [24] and [25] can be written through Equations [26] and [27]

$$z_4 = \int_0^\infty e^{a\eta + \gamma\eta^2} d\eta - \int_0^\infty e^{2a\eta + 2\gamma\eta^2} d\eta \quad [30]$$

$$z^* = \int_0^\infty e^{a\eta + \gamma\eta^2} d\eta - K \int_0^\infty e^{A\eta + \bar{\gamma}\eta^2} d\eta \quad [31]$$

Ringleb indicated that these integrations can be simplified through the use of the error integral $\phi(z)$

$$\phi(z) = \frac{2}{\sqrt{\pi}} \int_0^z e^{-z^2} dz \quad [32]$$

$$z_4 = \frac{\sqrt{\pi}}{2} \left\{ \frac{e^{-\frac{a^2}{4\gamma}}}{\sqrt{-\gamma}} \left[1 - \phi\left(\frac{a}{2\sqrt{-\gamma}} \right) \right] - \frac{e^{-\frac{a^2}{\gamma'}}}{\sqrt{-\gamma'}} \left[1 - \phi\left(\frac{a}{\sqrt{-\gamma'}} \right) \right] \right\} \quad [33]$$

$$z^* = \frac{\sqrt{\pi}}{2} \left\{ \frac{e^{-\frac{a}{4\gamma}}}{\sqrt{-\gamma}} \left[1 - \phi\left(\frac{a}{2\sqrt{-\gamma}} \right) \right] - K \frac{e^{-\frac{A^2}{4\bar{\gamma}}}}{\sqrt{-\bar{\gamma}}} \left[1 - \phi\left(\frac{A}{2\sqrt{-\bar{\gamma}}} \right) \right] \right\} \quad [34]$$

where

$$\gamma' = b - \frac{c}{6a} + \frac{d}{48a^2} \quad [35]$$

Calculations for z_4 and z^* have been carried out for the following cases:

TABLE 4 DISPLACEMENT THICKNESS z^* FOR VARIABLE PROPERTIES WEDGE FLOW; FOR $\sigma = 0.7$ AND $\sigma = 1.0$

	$\beta = 1.0$		$\beta = 0.5$		$\beta = 0.2$		$\beta = 0$	
$T_w/T_1/\sigma$	0.7	1.0	0.7	1.0	0.7	1.0	0.7	1.0
0.8	0.476	0.502	0.620	0.642	0.772	0.805	0.959	0.990
Constant property	0.647	0.647	0.811	0.811	1.002	1.002	1.238	1.238
1.5	1.217	1.050	1.247	1.195	1.569	1.516	1.936	1.857
2.0	1.630	1.474	1.770	1.597	2.167	2.042	2.634	2.476
Constant property exact	0.648	0.648	0.804	0.804	0.984	0.984	1.217	1.217

TABLE 5 MOMENTUM THICKNESS z_i FOR VARIABLE PROPERTIES WEDGE FLOW; FOR $\sigma = 0.7$ AND $\sigma = 1.0$

	$\beta = 1.0$		$\beta = 0.5$		$\beta = 0.2$		$\beta = 0$	
$T_w/T_1/\sigma$	0.7	1.0	0.7	1.0	0.7	1.0	0.7	1.0
0.8	0.325	0.320	0.377	0.371	0.422	0.425	0.453	0.453
Constant property	0.292	0.292	0.354	0.354	0.414	0.414	0.453	0.453
1.5	0.244	0.250	0.285	0.290	0.390	0.406	0.453	0.453
2.0	0.213	0.220	0.251	0.258	0.390	0.406	0.453	0.453
Constant property exact	0.292	0.292	0.350	0.350	0.408	0.408	0.470	0.470

$\beta = 1.0, 0.5, 0.2, 0$
$K = 0.2, 0, -0.5, -1.0$
$\sigma = 0.7, 1.0$

The results are presented in Tables 4 and 5 and also in Fig. 4,

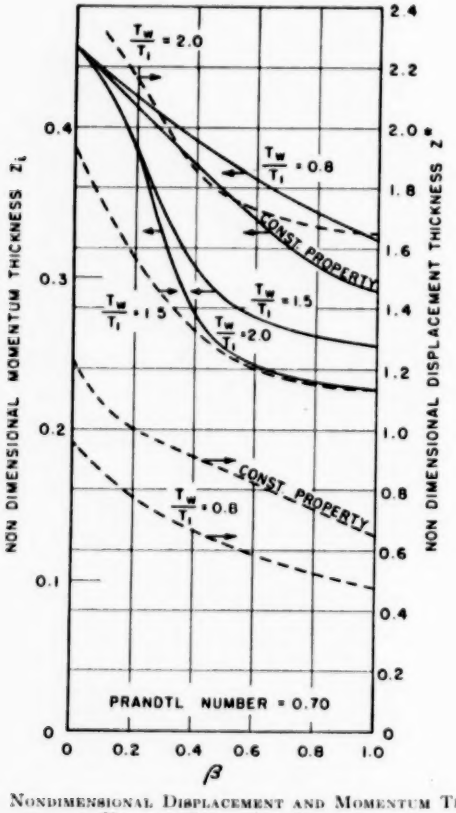
NON DIMENSIONAL MOMENTUM THICKNESS z_i
NON DIMENSIONAL DISPLACEMENT THICKNESS z^*
$\frac{T_w}{T_1} = 2.0$
$\frac{T_w}{T_1} = 0.8$
CONST PROPERTY
$\frac{T_w}{T_1} = 1.5$
$\frac{T_w}{T_1} = 2.0$
$\frac{T_w}{T_1} = 1.5$
CONST PROPERTY
$\frac{T_w}{T_1} = 0.8$
PRANDTL NUMBER = 0.70
β
0 0.2 0.4 0.6 0.8 1.0
0 0.1 0.2 0.3 0.4
0 0.2 0.4 0.6 0.8 1.0 1.2 1.4 1.6 1.8 2.0 2.2 2.4

FIG. 4 NONDIMENSIONAL DISPLACEMENT AND MOMENTUM THICKNESS FOR VARIABLE PROPERTIES WEDGE FLOWS

for a Prandtl number of 0.70. The accuracy of the results is again very good as indicated by the close check between the predicted values and the exact values in the case of constant property flow.

Extension of Results to Arbitrary Body. The method of solution is based on the assumptionthat the velocity profiles about an arbitrary body are defined by a single parameter β. Under such conditions the skin friction, the nondimensional momentum thickness z_i, and the nondimensional displacement thickness z^* are assumed identical for the wedge flows and for the arbitrary body for the same value of the parameter β.[6] This parameter is related to the momentum thickness θ, from the condition at the wall

$$\frac{\partial}{\partial y}\left[\left(\mu\frac{\partial u}{\partial y}\right)\right]_{y=0} = -\rho_1 u_1 \frac{du_1}{dx} \quad [36]$$

Introduction of the variable η yields

$$\frac{T_1}{T_w}\frac{\mu_1\rho_1 u_1^2}{2s} f'''(0) = -\frac{du_1}{dx} \quad [37]$$

From the first of Equations [10]

$$f'''(0) = -\beta g(0) = -\beta\frac{T_w}{T_1} \quad [38]$$

Substituting for $2s$ the value

$$\frac{\theta^2 u_1^2 \rho_1^2}{z_i^2}$$

as derived from Equation [24] gives

$$\beta z_i^2 = \frac{\theta^2}{\nu_1}\frac{du_1}{dx} \quad [39]$$

The integral momentum equation, Equation [21], yields through Equations [39], [24], and [14]

$$\beta z_i^2\left(2 + \frac{z^*}{z_i}\right) + \frac{\rho_1\theta u_1}{\rho_1\mu_1}\frac{d}{dx}(\rho_1\theta) = -az_i \quad [40]$$

Equation [40] can be written

$$u_1\frac{d}{dx}\left(\frac{\theta^2}{\nu_1}\right) = 2\left[-az_i - \beta z_i^2\left(2 + \frac{z^*}{z_i}\right)\right] = F(\beta z_i^2) \quad [41]$$

Equations [39] and [41] together with the known velocity distribution specify the boundary-layer growth. Estimates of θ^2/ν_1 yield values of βz_i^2 from Equation [39] and thus determine

$$\frac{d}{dx}\left(\frac{\theta^2}{\nu_1}\right)$$

from Equation [41]. This solution may be more rapidly obtained

[6] Details of the calculation method can be found in reference (12).

by direct integration of Equation [41] through the approximate linearity of the function $F(\beta z_i^2)$. As evaluated from Fig. 5

$$F(\beta z_i^2) = -m\beta z_i^2 - r = -m\frac{\theta^2}{\nu_1}\frac{du_1}{dx} - r \quad [42]$$

where $r = 0.43$ and m is given by

T_w/T_1	0.8	1.0	1.5	2.0
m	4.32	4.71	7.25	11.5

Equation [40] can be integrated to give

$$\left(\frac{\theta}{D}\sqrt{\frac{u_a D}{\nu_1}}\right)^2 = r\left(\frac{u_a}{u_1}\right)^m \int_0^{x/D}\left(\frac{u_1}{u_a}\right)^{m-1} d(x/D) \quad [43]$$

Here D is some significant dimension of the body and u_a an arbitrarily selected, constant velocity. At the stagnation point

$$\left(\frac{x}{D} = 0\right), \quad \frac{\theta}{D}\sqrt{\frac{u_a D}{\nu_1}}$$

is obtained directly from Equation [24] for $\beta = 1.0$.

The local value of the skin friction and heat-transfer coefficient can be determined from the available results. Thus from Equations [14] and [15]

$$\frac{\tau_w}{{}^1/_2\rho_1 u_1^2} = -2a\frac{z_i}{u_1\theta/\nu_1} \quad [44]$$

$$\frac{hD}{k_1} = -\frac{Az_i D}{\theta} \quad [45]$$

Discussion. The equations determining the momentum thickness, skin friction, and heat-transfer coefficient are identical to the equations derived by Seban (12) for constant-property flow over an arbitrary body. The only change in Equation [43] is the variation of the exponent m with the ratio T_w/T_1. To determine the exact effect of this variation the calculation method was applied to flow over the forward portion of a right circular cylinder over which the flow accelerates. The quantity T_w/T_1 was taken as 1.5 and the results were compared with the constant-property solution. Both

$$\frac{\theta}{D}\sqrt{\frac{u_a D}{\nu_1}}$$

and z_i decreased for the case $T_w/T_1 = 1.5$. Their effect tends to cancel out so that the local heat-transfer coefficient expressed as

$$\frac{hD/k_1}{\sqrt{\frac{u_a D}{\nu_1}}}$$

varies very little. The large increase in the value of the term a gave greater values of the skin friction in particular over the forward part of the cylinder.

The present method accounts for any possible variation of the properties across the boundary layer, but it is restricted to isothermal surface systems in low-speed flow, i.e., constant free-stream temperature. Most practical cases involve a variation of surface temperature and frictional heating. Accounting for a variable wall temperature does not appear possible as the superposition method used for the constant-property flows is no longer valid.

Conclusions

1 The present method of calculation accounts for the variation of the properties across a laminar boundary layer allowing the determination of the skin friction and heat transfer from an isothermal surface for a variable free-stream velocity. It is restricted to $\beta > 0$ and T_w/T_1 not too large, so that many features of an arbitrary flow, such as separation, cannot be considered.

2 The results of this analysis reveal that the skin friction is considerably affected by large or small ratios of wall to free-stream temperature; alternatively, the heat transfer as obtained from the energy equation without dissipation remains practically unchanged.

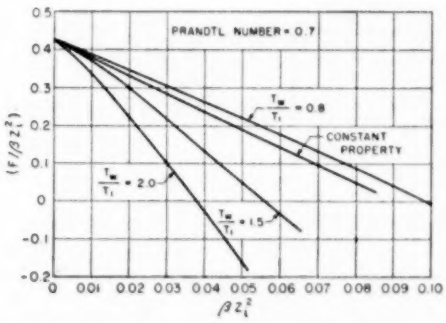

Fig. 5 Function $F(\beta z_i^2)$ in Terms of Flow Parameter βz_i^2

Bibliography

1 "Steady Flow in the Laminar Boundary Layer of a Gas," by C. R. Illingworth, Proceedings of the Royal Society, London, England, series A, vol. 199, 1949, pp. 533–558.

2 "Temperature and Velocity Profiles in the Compressible Laminar Boundary Layer With Arbitrary Distribution of Surface Temperature," by D. R. Chapman and M. W. Rubesin, *Journal of the Aeronautical Sciences*, vol. 16, 1949, pp. 547–565.

3 "The Laminar Boundary Layer in Gases (Translation)," by L. Crocco, APL/NAA/CF-1038, 1948.

4 "Aerodynamic Heating and Convective Heat Transfer—Summary of Literature Survey," by H. A. Johnson and M. W. Rubesin, Trans. ASME, vol. 71, 1949, pp. 447–456.

5 "Effects of Pressure Gradient on Stability and Skin Friction in Laminar Boundary Layers in Compressible Fluids," by H. Weil, *Journal of the Aeronautical Sciences*, vol. 18, 1951, pp. 311–318.

6 "Simplified Method for Calculation of Compressible Laminar Boundary Layer With Arbitrary Free-Stream Pressure Gradient," by G. M. Low, U. S. National Advisory Committee for Aeronautics, Technical Note No. 2531, 1951.

7 "Velocity and Temperature Distribution Through the Laminar Boundary Layer in Supersonic Flow," by G. Ferrari, *Journal of the Aeronautical Sciences*, vol. 19, January, 1952, pp. 39–47 and 65.

8 "Computation of the Laminar Boundary Layer With Suction," by F. O. Ringleb, *Journal of the Aeronautical Sciences*, vol. 19, January, 1952, pp. 48–54.

9 "On an Equation Occurring in Falkner and Skan's Approximate Treatment of the Equations of the Boundary Layer," by D. R. Hartree, Proceedings of the Cambridge Philosophical Society, Cambridge, England, vol. 33, 1937, pp. 223–239.

10 "The Computation of the Heat Transfer in the Laminar Boundary Layer of Bodies in Flow," by E. Eckert, *Vereines deutscher Ingenieure Forschungsheft* No. 416, 1942.

11 "Some Prandtl Number Effects on the Transfer of Heat," by A. N. Tifford, Engineering Experiment Station News, Ohio State University, vol. 22, February, 1950, pp. 11–12 and 30–34.

12 "Calculation Method for Two-Dimensional Laminar Boundary Layers With Arbitrary Free Stream Velocity Variation and Arbitrary Wall Temperature Variation," by R. A. Seban, Institute of Engineering Research, Report 12, series 2, University of California, Berkeley, Calif., 1950.

13 "Tables of Exact Laminary-Boundary-Layer Solutions When the Wall Is Porous and Fluid Properties Are Variable," by W. B. Brown and P. L. Donoughe, U. S. NACA TN 2479, 1951.

The Measurement of Acceleration Pulses With the Multifrequency Reed Gage

By HENRY SHAPIRO[1] and D. E. HUDSON[2]

It is shown that the data recorded by a multifrequency reed gage can be used to derive information concerning the time history of the exciting motion. If the general shape of an exciting acceleration-time pulse is known approximately, then reed-gage data alone will permit calculations of peak acceleration, time duration of pulse, and time to peak acceleration. A study of response curves for typical pulses will give design data on the proper frequencies, frequency distributions, and damping for the individual elements of the gage. Response curves for a series of typical pulse shapes are determined by electric-analog-computer methods, and are presented in dimensionless form.

IT has been recognized generally that while it might be desirable to have a complete magnitude versus time record of a shock motion so that the effect of the shock on a structure could be computed accurately, the complexity of the measuring apparatus required often makes it impractical to obtain such a record. In an attempt to simplify such instrumentation, much work has been done on the development of various peak-reading accelerometers. The difficulty of obtaining any time-duration information from such peak-reading instruments, however, has limited severely their usefulness.

The multifrequency reed gage stands midway in complexity between the seismic-type time-recording instrument, and the simplest forms of peak-reading devices. It consists of a series of single-degree-of-freedom systems of various frequencies so arranged that the maximum displacements of each mass can be recorded. The name is derived from the fact that the elements usually take the form of cantilever beams, or reeds, with concentrated end masses. Since the maximum displacements only are recorded, no time-recording mechanism needs to be incorporated into the instrument, and this not only simplifies the design considerably, but eliminates the need for a power supply.

Several practical versions of such multifrequency reed gages have been built and tested (1, 2, 3).[3] Most of the difficulties which have been encountered with these instruments are due to various specific mechanical design features which it is believed could be improved in future designs. Such work has shown that the basic principle of the instrument is a sound one and that there are certain types of shock-measuring problems where the particular characteristics of the reed gage can be used to advantage.

There are two ways in which the data from a multifrequency reed gage can be used to obtain information as to the effect of mechanical shocks on structures. The first point of view conceives of the reed gage as a dynamic model, in which the various modes of vibration of an actual structure are represented by the various reeds of the instrument. The response of the instrument to a given shock thus indicates the behavior of the modes of the structure, from which, by superposition, an over-all pattern of the structural response can be constructed. Closely related to this view is the concept which regards the data from the reed gage as defining the "shock spectrum" of the exciting motion. Knowing the natural frequency or frequencies of any structure which is subjected to this same shock spectrum, the response of the structure can be determined immediately.

The second point of view regards the reed-gage record as data from which to compute as many features of the exciting motion as is possible. Once this exciting motion is determined, the effects of this motion on structures having known characteristics can be computed. In general, it will not be possible to determine from a reed-gage record alone the complete motion-time picture of complex exciting motions. For some simple motions such a complete picture can be obtained, and for almost any motion at least some of the important time parameters can be derived.

It is considered generally that for most work in the dynamics of shock excitation a knowledge of the effects of the shock on a structure is more important than a description of the shock itself. Even if the exciting motion is known precisely, the calculation of the response of complicated structures to the motion may be a difficult problem which can be solved only approximately. It is probable that the first point of view represents the most generally useful way of employing the reed gage. There are, however, some applications for which a knowledge of the exciting motion itself is desired, as, for example, in testing work in which the degree to which exciting shocks are duplicated may be important. It is this use of the reed-gage record to define the exciting motion which shall be considered in the present paper.

The response of the reed gage to exciting motions having the forms of step velocities and accelerations, rectangular pulses of velocity and acceleration, a half-sine pulse of acceleration, and suddenly applied simple harmonic motion, and a consideration of the methods of determining these exciting motions from the reed-gage record itself, have been treated in a paper by Davidson and Adams (4). The present paper considers other types of exciting pulses and shows how relatively complete information concerning the pulse can be derived from a detailed study of the reed-gage data.

Response of a Reed Gage to Exciting Pulses

The exciting motions to be considered all have the form of a single acceleration pulse which starts with a positive slope which decreases steadily through zero to a final negative slope, as shown in Fig. 1(*a*). The actual shapes are composed either of segments of sine waves or of straight lines, as defined in Fig. 1(*b*). The initial portions of the pulses up to the peak acceleration are in all cases identical quarter-sine waves.

[1] Engineer, Propulsion Research Corporation, Inglewood, Calif.

[2] Division of Engineering, California Institute of Technology, Pasadena, Calif. Mem. ASME.

[3] Numbers in parentheses refer to the Bibliography at the end of the paper.

Contributed by the Applied Mechanics Division and presented at the Semi-Annual Meeting, Los Angeles, Calif., June 28–July 2, 1953, of The American Society of Mechanical Engineers.

Discussion of this paper should be addressed to the Secretary, ASME, 29 West 39th Street, New York, N. Y., and will be accepted until October 10, 1953, for publication at a later date. Discussion received after the closing date will be returned.

Note: Statements and opinions advanced in papers are to be understood as individual expressions of their authors and not those of the Society. Manuscript received by ASME Applied Mechanics Division, March 3, 1953. Paper No. 53—SA-8.

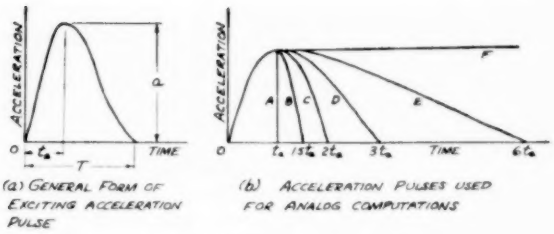

FIG. 1 EXCITING-PULSE SHAPES

The parameters which define such a pulse for most practical purposes are as follows:

(*a*) Maximum acceleration, a.

(*b*) Time to maximum acceleration, t_a.

(*c*) Total time duration, T.

(*d*) Total area of pulse (impulse applied to system).

The response of a typical reed-gage element to pulses having characteristic ranges of values of these major parameters will be determined first and then it will be shown how conversely the reed-gage responses could be used to derive values of these parameters.

The data which are obtained from the reed gage consist of the maximum excursion χ_{max}, on either side of the equilibrium position of the single-degree-of-freedom mass of each reed. The characteristics of the reeds which must be known are the natural frequency ω_n and an approximate value of the damping. In the following work, positive and negative-response magnitudes versus frequency for various values of damping will be plotted, so that the results also will indicate something of the design problem involved in selecting the number of reeds, their frequencies, and their damping for the optimum design of the instrument.

The responses of the damped single-degree-of-freedom systems representing the reeds were obtained using the electric-analog computer of the California Institute of Technology (5). In this computer the mechanical reed is simulated by its electrical equivalent, consisting of an inductance, a capacitance, and a resistance in series. The pulse shapes in Fig. 1(*b*) were reproduced in the form of a variable width trace on a circular transparent film, which was rotated between a light source and a photoelectric cell. In this way a voltage proportional to the acceleration pulse was produced which then could be applied to the electric circuit.

For various values of the circuit parameters, the desired maximum and minimum responses of the system to a particular pulse could be read directly from a cathode ray-oscilloscope trace. Fig. 2 shows typical results observed on the oscillograph tube. The lower trace is the exciting pulse, and the upper trace is the response to this pulse of an element having a known frequency and damping. It will be noted that this method of computation amounts, in effect, to an experimental determination of system response. The accuracy to be expected from this electric-analog computation may be estimated from Fig. 4 where the experimental points are shown along with an analytically determined curve, which readily may be obtained for the undamped one-half sine-wave pulse.

Some typical results of these electric-analog solutions are summarized in Figs. 3, 4, and 5. The abscissa in these figures is twice the rise time of the pulse divided by the natural period of the reed τ. The ordinate is the maximum reed deflection divided by the equivalent static deflection, which is the deflection which would be caused by a gradually applied acceleration of a magnitude equal to the maximum pulse acceleration. This ordinate is

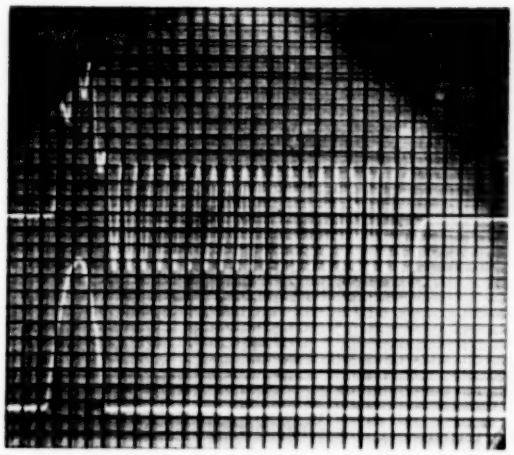

FIG. 2 TYPICAL CATHODE-RAY OSCILLOSCOPE TRACES FOR ELECTRIC-ANALOG COMPUTER

also equal to the equivalent static acceleration divided by the maximum pulse acceleration, where the equivalent static acceleration is defined as the gradually applied acceleration which would produce the same maximum displacement as a given acceleration pulse. The equivalence of these two dimensionless parameters may be shown as

$$\chi_{max} = \frac{(\text{mass})\,(\text{equivalent static acceleration})}{(\text{spring constant})}$$

so

$$\text{equivalent static acceleration, } a_{st} = \frac{\chi_{max}\, k}{m} = \chi_{max}\, \omega_n^2$$

The static deflection corresponding to a particular peak acceleration is

$$\chi_{st} = \frac{ma}{k} = \frac{a}{\omega_n^2}$$

therefore

$$\frac{a_{st}}{a} = \frac{\chi_{max}\, \omega_n^2}{a} = \frac{\chi_{max}}{\dfrac{a}{\omega_n^2}} = \frac{\chi_{max}}{\chi_{st}}$$

The data from the reed gage can be plotted as the reed frequency versus the equivalent static acceleration of the reed. The co-ordinates used for the response curves in Figs. 3, 4, and 5 are dimensionless forms of those used for the reed-gage data; hence the shapes of the dimensionless response curves will be the same as those plotted from reed-gage data.

ANALYSIS OF THE RESPONSE CURVES

The problem of determining from response curves, derived from the reed-gage data, the maximum amount of information concerning the exciting acceleration pulse is considered. Used as co-ordinates for the reed gage-response curves are the frequencies of the individual reed plotted versus the equivalent static accelerations of the reed, as computed from the measured maximum displacements and the known single-degree-of-freedom mass. As mentioned previously, the response curves plotted in these co-ordinates will have the same shape as the dimensionless curves in Figs. 3, 4, and 5.

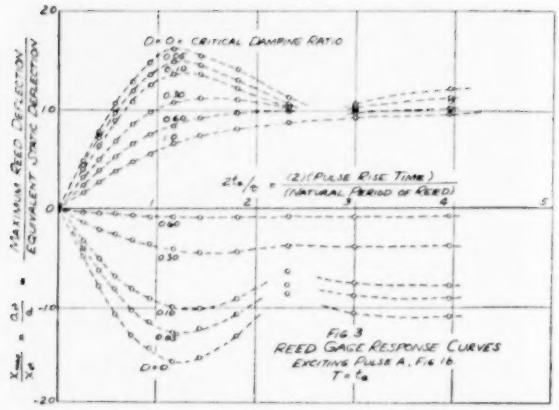

FIG. 3 REED-GAGE RESPONSE CURVES, EXCITING PULSE *A*, FIG. 1(*b*),
$T = 1t_a$

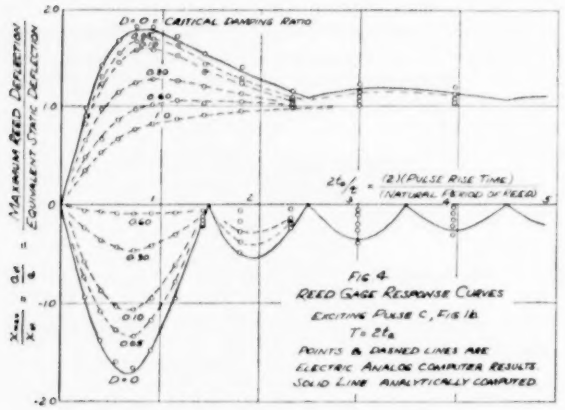
D=0 = CRITICAL DAMPING RATIO
FIG 4
REED GAGE RESPONSE CURVES
EXCITING PULSE C, FIG 1b
T = 2t_a
POINTS & DASHED LINES ARE ELECTRIC ANALOG COMPUTER RESULTS
SOLID LINE ANALYTICALLY COMPUTED

FIG. 4 REED-GAGE RESPONSE CURVES, EXCITING PULSE *C*, FIG. 1(*b*),
$T = 2t_a$

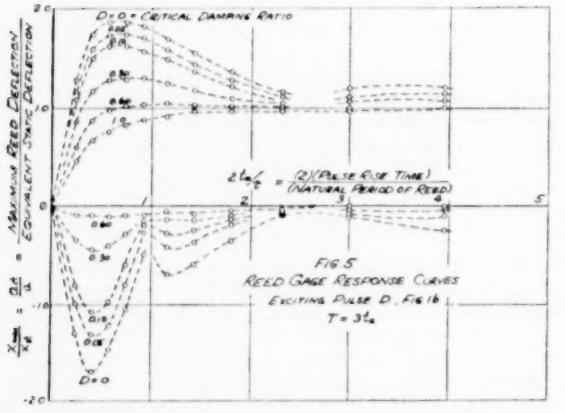

FIG. 5 REED-GAGE RESPONSE CURVES, EXCITING PULSE *D*, FIG. 1(*b*),
$T = 3t_a$

In Fig. 6 is shown a typical response curve as constructed from the reed-gage data, with an indication of some of the characteristic features to be used in the analysis. It is supposed that the instrument contains a large enough number of elements properly spaced in frequency so that the following general features, as marked in Fig. 6, can be distinguished:

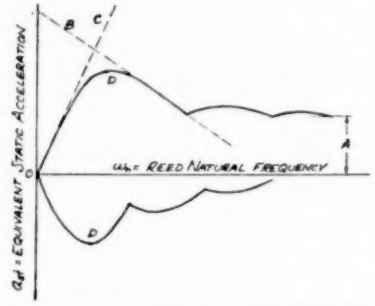

FIG. 6 TYPICAL RESPONSE CURVES CONSTRUCTED FROM REED-GAGE DATA

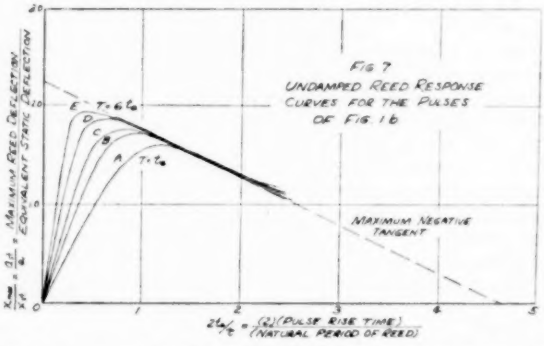

FIG. 7 UNDAMPED REED RESPONSE CURVES FOR PULSES IN FIG. 1(*b*)

(*a*) The value of the equivalent static acceleration indicated by the high-frequency elements, i.e., for these elements for which the response is essentially independent of the reed frequency.

(*b*) The slope of the maximum negative tangent to the response curve.

(*c*) The slope of the initial maximum positive tangent to the response curve.

(*d*) The maximum indicated responses, in the positive and negative directions.

Each of these items will be considered in turn.

(*a*) *High-Frequency Response.* It will be evident from Figs. 3, 4, and 5 that for values of $(2t_a/\tau)$ greater than 3, the reed responses rapidly approach a value of unity. In order to find the maximum acceleration of the exciting pulse it is theoretically necessary only to record the response of a reed which has a sufficiently high natural frequency to give the required accuracy. In practice, however, it may happen that the amplitudes of the reeds, which are of sufficiently high frequency for this purpose, are so small that accurate readings cannot be obtained (6). In this event the peak acceleration probably can be determined more accurately from the maximum negative tangent, as is discussed in the text following.

(*b*) *Maximum Negative Tangent.* In Fig. 7 the first portion of the zero damping curves for the pulses in Fig. 1(*b*) have been

plotted. It will be seen that the slopes and locations of maximum negative tangents for all of the pulses are approximately equal. Since all of the pulses are identical from zero time to the maximum acceleration, it appears that this maximum negative tangent defines this similarity of the pulses. A determination of slope and intercept of this line therefore will permit a calculation of two of the pulse parameters. Since there are only two pulse parameters involved in this first portion of the pulse, the peak acceleration and the time to the peak, both of these parameters can be determined uniquely. This slope line can be located with fair accuracy if two or three reeds lie in the frequency range where the maximum negative tangent and the response curves approximately coincide. This indicates one criterion for the frequency-distribution design of a reed gage for pulses of this type.

(*c*) *Initial Maximum Positive Tangent.* The initial maximum positive tangent, i.e., the slope of the response curve at $(2t_a/\tau) = 0$, is determined by the velocity change involved in the motion, and hence measures the impulse applied to the system. For an acceleration pulse having a time duration which is small compared to the natural period of all of the reeds, the reed-response curve would be a straight line through the origin having a slope proportional to the initial velocity imparted to the system by the pulse. It will be observed in Fig. 7 that for all of the pulses the area of the pulse is proportional to the slope of the tangent at the origin. A determination of this initial slope from the reed-gage record thus will give another parameter of the exciting motion. If, in addition to this total pulse area, the peak acceleration and the time to the peak can be determined from the maximum negative tangent as discussed in the preceding section, the total time duration of the pulse could be also computed.

For zero damping, the initial negative slope for the negative portion of the response curves is equal in magnitude to the initial positive slope. If the damping is not zero, it will be noted from Figs. 3, 4, and 5 that the slopes of the initial tangents of the negative responses are smaller than those of the corresponding positive responses. For small damping, the ratios of the positive and negative slopes at the origin can be shown to be approximately $e^{\pi D}$, where D is the critical damping ratio.

(*d*) *Maximum Positive and Negative Responses.* Additional information concerning the pulse shape as measured by the ratio of time to peak acceleration to total pulse time can be obtained by comparing the frequencies at which the maximum positive and the maximum negative reed amplitudes are reached. In Fig. 8

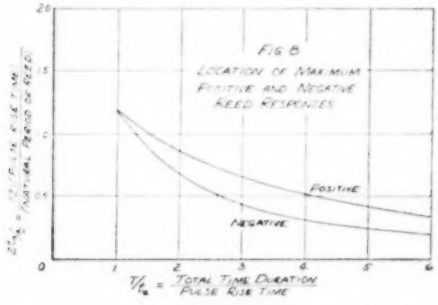

FIG. 8 LOCATION OF MAXIMUM POSITIVE AND NEGATIVE REED RESPONSES

are shown values of the frequency parameter $(2\ t_a/\tau)$ at which these extreme values are attained for various values of the ratio of time to peak to total time duration.

Other Pulse Shapes. It can be shown that a comparison of the positive and negative portions of the response curves will yield additional information as to the shape of the exciting pulse (7). The extent to which other pulse shapes can be defined will require the determination of more response curves and additional analysis of the type presented in the foregoing.

Effects of Damping. The curves in Figs. 3, 4, and 5 will indicate the effects of reed damping on the behavior of the reed gage. It will be seen that the response at high reed frequencies approaches unity more rapidly with larger values of damping; and hence, that the peak accelerations can be determined more accurately if some damping is present in the reeds. On the other hand, if the damping exceeds approximately 30 per cent of critical damping, many of the essential features of the response curves become less clearly defined and it is unlikely that much information could be obtained. For most purposes it appears that if the reed damping is of the order of 10 per cent or less of critical damping, its actual value is of minor importance, provided that it is known and that it stays reasonably constant.

Conclusions

As a summary of the foregoing discussion, reference may be made to Fig. 9 in which are shown several typical reed gage-response curves. Fig. 9(*a*) is characteristic of a very short time-duration acceleration pulse for which the motion is purely impulsive. The slope of the straight-line response curve would be proportional to the velocity change associated with the acceleration pulse, and from this velocity change the complete motion could be computed. For reeds having small damping, the positive and negative slopes of the two lines would be approximately equal in magnitude. The motion represented in Fig. 9(*b*) is not purely impulsive, since at the high-frequency end the equivalent static accelerations depart from linearity with reed frequency. From such a curve a very rough estimate of the location and slope of the maximum negative tangent could be made, and approximate values of the peak pulse acceleration and of rise time could be calculated. By combining this information with the total pulse area, as determined from the initial positive tangent, an approximate value of the total pulse-duration time could be obtained.

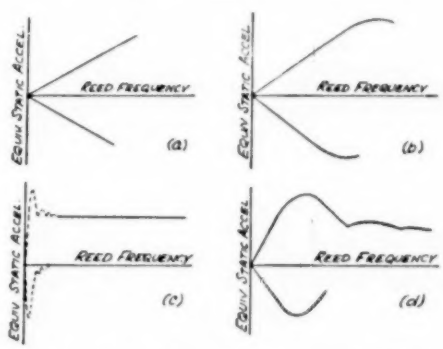

FIG. 9 TYPICAL REED-GAGE RESPONSE CURVES

Fig. 9(*c*) illustrates the case where all of the reeds have the same equivalent static accelerations, which indicates that the acceleration pulse must be applied relatively slowly; i.e., the applied acceleration is equivalent to a static inertia force. From such a record, only the peak acceleration can be determined, which, however, is sufficient to describe completely such a gradual loading. In Fig. 9(*d*) is shown the type of record which would be obtained from a reed gage which was designed correctly to measure a given pulse. From such a record, all of the important pulse parameters could be determined.

The question must be raised as to whether such reed-gage response curves will determine uniquely the exciting-pulse shape, or whether other quite different pulse shapes might give similar reed-gage patterns. Although this question has been answered partially by the work already done, more studies will have to be made before the extent to which the reed gage can distinguish between simple pulse shapes and more complex ones involving slope reversals, negative values, and so on, can be determined conclusively. It is believed that the electric-analog-computer technique just described is particularly well suited for studies of this kind.

It is hoped that the relatively simple situations discussed in this paper at least will serve to indicate a point of view which may enable the reed-gage principle to be extended, and which will encourage the exploitation of its special advantages in transient instrumentation problems.

Acknowledgment

The authors wish to express their appreciation to Prof. G. D. McCann and to the staff of Analysis Laboratory of the California Institute of Technology, particularly Profs. C. H. Wilts and R. H. MacNeal, for making available the electric-analog computer for this work, and for their assistance and advice.

Bibliography

1 "Experimental Investigation of the Type-2 Multifrequency Reed Gage for Recording Shock Motion," by B. J. W. Grier, TMB Report 603, September, 1949.

2 "Evaluation of Selected Shock Instruments," by T. A. Pers and H. L. Rich, TMB Report 720, February, 1951.

3 "Design of a Multifrequency Reed-Type Shock Gage With an Inertia-Operated Trigger," by M. Martin and P. Golovato, TMB Report 654, May, 1949.

4 "A Theoretical Study of the Multifrequency Reed Gage for Measuring Shock Motion," by S. Davidson and E. J. Adams, TMB Report 613, July, 1949.

5 "A New Device for the Solution of Transient-Vibration Problems by the Method of Electrical-Mechanical Analogy," by H. E. Criner, G. D. McCann, and C. E. Warren, Journal of Applied Mechanics, Trans. ASME, vol. 67, 1945, p. A-135.

6 "The Equivalent Static Accelerations of Shock Motions," by J. P. Walsh and R. E. Blake, NRL Report no. F-3302, June 21, 1948 (also, slightly abridged in Proceedings of SESA, vol. 6, no. 2).

7 "Transient Response of a Multifrequency Reed-Gage," by H. Shapiro, ME thesis, California Institute of Technology, Pasadena Calif., 1952

An Experimental Study of the Propagation of Transient Longitudinal Deformations in Elastoplastic Media[1]

By E. J. STERNGLASS[2] and D. A. STUART[3]

The propagation process of longitudinal plastic pulses in prestrained bars has been studied to test the validity of the Donnell-Taylor-von Kármán theory of plastic waves. The results obtained for the propagation velocity and wave-shape changes indicate that the theory fails to describe the dynamic process by its neglect of strain-rate and creep effects.

Introduction

THE problem of the propagation of plastic strains in bars has been studied intensively only in comparatively recent times. Following the first brief suggestions of Donnell (1)[4] in 1930, more detailed theoretical descriptions were developed by Taylor (2) and von Kármán (3) in 1942. A different approach, which considers the effect of the rate of strain, in contrast to the investigators mentioned, has been attempted during the last few years by Shanley (4) and Malvern (5). However, sufficient experimental evidence has not been available on the transient phenomena during the impact to make the development of more exact theories possible.

The experimental work to test the theory in the form developed by von Kármán so far has been concerned only with testing its predictions as to the form of the permanent deformation produced in bars by an impact (6, 7, 8). Since the permanent deformation measured subsequent to the whole propagation process only tests the validity of the theory in the limit of "infinite time," it seemed desirable to obtain information on the transient phenomena directly. The present paper is a report on such an investigation of the propagation of plastic deformations in prestressed metal bars. The results obtained lead to the conclusion that the existing theory is not adequate to describe the "dynamic" processes involved in the formation of plastic deformations under impact loading.

Description of Experimental Work

Plan of Investigation. The plan of the present investigation was to produce a short duration, longitudinal impact pulse of sufficient magnitude to result in permanent deformation and to observe the propagation velocity and change in shape of the pulse as it travels along the specimen. By comparing the actual behavior of such a pulse with that required by the von Kármán theory, it is possible to test its validity for transient conditions in a direct and unambiguous manner. The main questions to be answered are as follows:

1 For a material prestressed into the "plastic" region, does a very small plastic deformation pulse travel with a velocity given by the tangent modulus at that point on the curve; i.e., is

$$C_\epsilon = \left(\frac{d\sigma/d\epsilon}{\rho}\right)^{1/2}$$

where C_ϵ is the velocity of propagation of a strain with amplitude ϵ, $(d\sigma)/(d\epsilon)$ is the slope of the "engineering" or "nominal" stress-strain curve, and ρ is the density of the material?

2 Is the apparent velocity of propagation determined only by strain level and amplitude of pulse or is width or effective frequency of the pulse also important?

3 Is the maximum strain introduced into a prestressed bar given by

$$v = \int_{\epsilon_1}^{\epsilon_2} \left(\frac{d\sigma/d\epsilon}{\rho}\right)^{1/2} d\epsilon$$

Here v is the striking velocity, ϵ_1 is the strain to which the rod has been prestressed, and ϵ_2 is the maximum strain introduced by the impact.

In addition, it was desired to obtain a direct test of the view that a plastic deformation travels as a pulse of constant width and with a maximum amplitude which remains unchanged for a definite distance from the point of initiation, beyond which it decays rapidly (1, 3).

Finally, it was desired to obtain a measure of Poisson's ratio for dynamic or transient strains. It is well known, and widely used, that in static tests Poisson's ratio is one half for plastic strains. However, to the authors' knowledge, whether this is also true for transients has never been determined.

Description of Experimental Method and Apparatus. After various experimental methods of producing longitudinal pulses were tried in preliminary studies, the following simple scheme was found to be the most satisfactory. Flat strips of the material to be tested ($^1/_2$ in. $\times$ $^1/_4$ in.) are mounted in a standard testing machine (200,000 lb Olsen Universal) so that they can be prestressed by any desired amount. Resistance-wire strain gages (Baldwin SR-4, Type A-11 or C-8) were mounted on two sides of the strip and so connected either to cancel out the effects of any bending waves that might be produced, thus isolating the longitudinal wave, or to cancel the longitudinal wave, thus isolating the bending wave. The strips were made to be of the greatest possible length (about 120 in.) in order to avoid complications in the interpretation of the pulse shapes caused by reflections from the ends. In order to be able to use such long specimens, heavy extension tubes were mounted above the upper or fixed head and

[1] This work was supported by the Applied Physics Laboratory, Johns Hopkins University, under Contract No. 33031–2.

[2] Research Associate, Department of Engineering Materials, Cornell University, Ithaca, N. Y.; now at Westinghouse Research Laboratory, Pittsburgh, Pa.

[3] Associate Professor, Department of Engineering Materials, Cornell University, Ithaca, N. Y.

[4] Numbers in parentheses refer to the Bibliography at the end of the paper.

Contributed by the Applied Mechanics Division and presented at the Annual Meeting, New York, N. Y., November 30–December 5, 1952, of The American Society of Mechanical Engineers.

Discussion of this paper should be addressed to the Secretary, ASME, 29 West 39th Street, New York, N. Y., and will be accepted until October 10, 1953, for publication at a later date. Discussion received after the closing date will be returned.

Note: Statements and opinions advanced in papers are to be understood as individual expressions of their authors and not those of the Society. Manuscript received by ASME Applied Mechanics Division, July 30, 1952.

below the lower or movable head of the testing machine through which the strip was passed as shown in the test setup, Fig. 1. The impact is produced by means of a roller-bearing-mounted pendulum hammer falling freely under the influence of gravity and striking a platform clamped to the strip at some distance from the lower end as also indicated in Fig. 1.

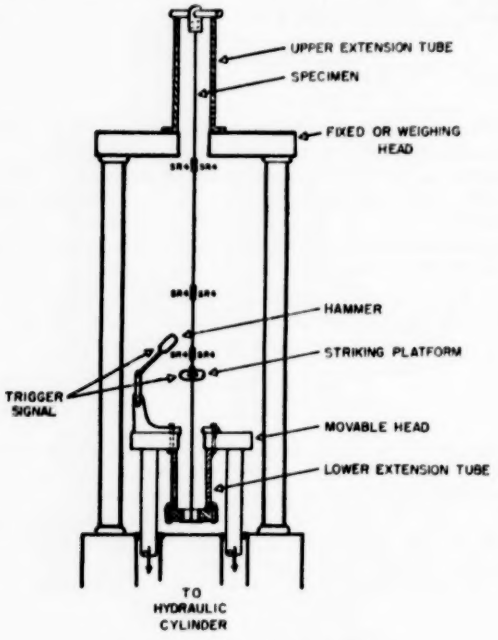

FIG. 1 SKETCH OF TEST SETUP

Fig. 2 shows the hammer and one of the striking platforms used in this series of experiments. The hammer has a length of 22 3/4 in. from the axis of rotation to the striking point. The head is made of aluminum, weighing 1.86 lb, and is electrically isolated from the hammer arm. Provisions are made for mounting on the hammer head a possible total of 5 lead plates, each weighing about 1.4 lb, two of which are shown mounted in Fig. 2. The hammer is held in its initial position by an electromagnet which serves to provide a means of uniform and positive release.

Two different types of striking platforms are used, a heavy steel one, which is shown, and a light aluminum one. The heavy platform weighs 3.25 lb and is constructed in the form of two concentric frames, the outer frame being free to rotate about the heavy bolts which exert the pressure against the strip. This platform is designed to prevent any application of a bending moment to the specimen, and to give automatic adjustment to unevenness in the wear of the impact-receiving screws. The light platform is a simple split ring, weighing 0.57 lb and secured by machine screws. Positive fastening of the platforms to the strip is obtained by the use of small pieces of file between the pressure-exerting screws and the specimen. Without these file pieces, the platforms gradually slip under repeated impacts, and premature rupture of the sample results when the screws are tightened to avoid further slipping. With either platform, the pulses obtained are remarkably reproducible both in width and height as well as in shape, provided two-point contact between hammer and platform is maintained.

For recording the wave forms of the pulses at the different gage stations along the strip, separate cathode-ray oscilloscopes, (Dumont model 304-H) are used with their sweeps synchronized and adjusted to give a single sweep, triggered by the contact of hammer and platform. A block diagram of the final arrangement of the equipment is shown in Fig. 3. The leads from each pair of strain gages are brought out in shielded 4-conductor cables to individual d-c bridges specially constructed to provide a means of measuring permanent deformations at the gage stations without necessitating any switching of gages and without interfering with the dynamic measurements. A Leeds and Northrup potentiometer is used to measure the unbalanced voltage in each bridge.

Three identical preamplifiers are provided to step up the signal level and to suppress undesirable noise. This latter function is accomplished by adjustment of the frequency response of the two-stage preamplifiers to pass only those frequencies required for faithful reproduction of the actual pulses encountered, roughly from 600 to 12,000 cycles per second (cps). By this means troublesome 60-cycle pickup, tube microphonics, and radio-frequency noise are eliminated almost entirely. The signals are then brought to the y-axis amplifiers of the three oscilloscopes.

The signal level at the gages is of the order of 1 mv for a peak strain of 180 μ-in/in. With a preamplifier gain of about 30, this signal results in a peak deflection of the order of 1 in. on the face of the scope. The sweeps are photographed using DuMont type 296 oscillograph record cameras whose shutters are actuated manually before the hammer is released.

Triggering of the sweep is accomplished by the closing of an electrical circuit when the insulated hammer head strikes the platform. This causes a previously charged condenser to discharge through a low resistance, and the resulting voltage spike actuates the sweep-triggering circuit in the first scope. The other two scopes have their x-deflection plates connected

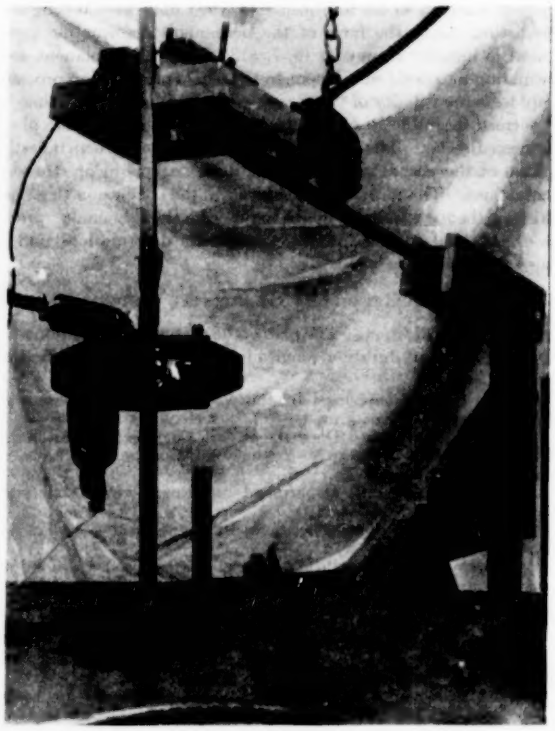

FIG. 2 VIEW OF HAMMER AND STRIKING PLATFORM

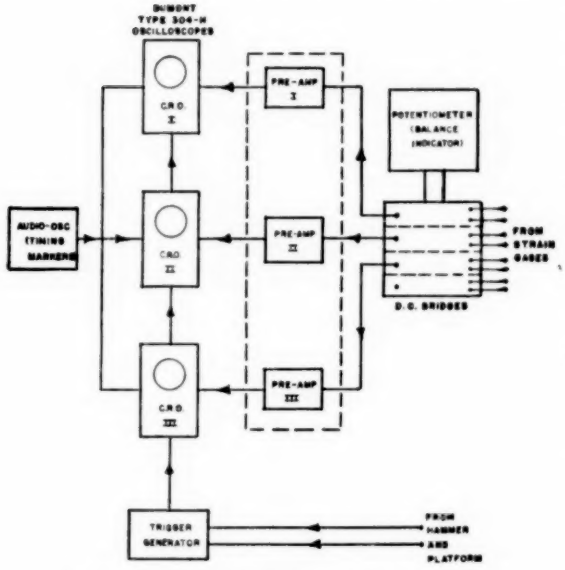

FIG. 3 BLOCK DIAGRAM OF RECORDING EQUIPMENT

in parallel with the first—hence all sweep in unison. Such an indirect triggering method is necessitated by the occurrence of multiple contacts between hammer and platform, each of which ordinarily would trigger a new sweep. However, by the use of the condenser discharge, multiple traces are avoided by setting the sync control to operate only on the first or largest pulse.

In order to obtain an absolute calibration of the time axes on the scopes, independent of small differences in their deflection sensitivity, timing markers are applied to the beam-intensity control. A sine wave of 50 kc from a Hewlett-Packard Model 200 D audio oscillator was found to give sufficiently satisfactory markers to make more elaborate pulse-shaping circuits unnecessary.

Adjustment of Equipment. Before each run, the amplification is adjusted and the frequency response checked so as to be the same for all three gages, preamplifiers, and oscilloscopes. Two methods are employed each time. The scope amplification is set to result in equal amplitude signals on all three scopes at the fundamental frequency of the pulses to be observed, about 1000 cps. Thereupon the frequency response is checked throughout the spectral range amplified by the system. Finally, the three amplifier inputs are connected in parallel and a single pulse is amplified and photographed on all three scopes as a standard of comparison. In this way any small differences in response characteristics that otherwise might lead to an apparent difference in pulse shape from station to station can be corrected for in the analysis of the resulting pictures.

Calibration of the system is accomplished by feeding a sine wave of known amplitude through the amplifiers and noting the deflections on the scopes in terms of millivolts per inch. The gage-battery voltages are recorded and from the known gage factors, gage resistances, and resistances in the bridge, the sensitivity in millivolts per unit strain is calculated.

Preliminary Experiments. The first experiments carried out were designed primarily to determine whether the velocity of wave propagation of pulses produced when the test specimen was brought into the nonlinear region of the stress-strain curve was determined by the tangent modulus at that point. These early experiments were carried out on cold-rolled copper, cold-rolled steel, and brass rods of $^1/_2$ in. diam and 75 in. length. A single gage was used and the time elapsed between initiation of the impact and the arrival of the pulse measured from the photographic record. Knowing the distance from the impact point to the gage allowed a calculation of the velocity. In every case the velocity of the wave front was found to be that of the ordinary elastic longitudinal wave within the experimental accuracy of this method, or about ± 10 per cent. The same result was obtained whether or not loading of the specimen was continued or stopped during the impact, so that it could not be explained by any possible unloading due to creep before the blow occurred.[5] The same result was also obtained independently by Bell (9), and it has since then been confirmed in more detailed investigations as will be described.

As a result of these first experiments the need became apparent for greater reproducibility and an understanding of the factors determining the shape of the pulses. Inasmuch as the amplitude and width were recognized as the fundamental variables that would have to be controlled in order to obtain significant tests of the existing theory, it was decided to devote a whole series of experiments to a study of this problem.

Investigation of Factors Determining Pulse Shapes

In an effort to obtain greater reproducibility of the pulse shapes, the equipment was reconstructed as described previously. Flat strips were substituted for the rods, the hammer construction was made more rigid, the gimbal arrangement was built, and the amplifiers modified to eliminate noise.

If the distance from the point of striking to the lower end of the strip is greater than $^1/_2$ the distance traveled by the pulse during the impact duration, the reflected wave does not return before the end of the pulse. In this case, the width of the pulse is determined only by the mass of the hammer and the mass of the striking platform. The impact velocity, in the velocity range investigated, has no apparent effect on pulse width, either in the elastic or the plastic region. Neither does the length of the hammer arm play a determining role. A plot of width at the base of the pulse versus hammer weight is shown in Fig. 4. It is seen that a linear relation seems to hold between hammer weight and width of the pulse. This can be shown theoretically

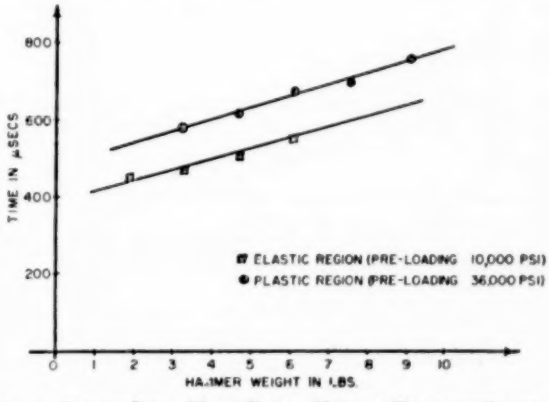

FIG. 4 PLOT OF PULSE WIDTH VERSUS HAMMER WEIGHT IN ELASTIC AND PLASTIC REGION

(Height of drop 8 in.; 3.25 lb striking platform; $^1/_8$-in. × $^1/_8$-in. cold-rolled copper specimen.)

[5] This phase of the early experimental work was suggested by Professor Riparbelli of the Graduate School of Aeronautical Engineering, and carried out by Mr. Chang S. Hahn, Department of Engineering Mechanics, Cornell University, Ithaca, N. Y.

by setting the strain energy, using the relation $\epsilon = v/c$, equal to the kinetic energy of hammer and platform. This leads to the conclusion that the width of the pulse in the elastic region is determined only by the ratio of hammer plus platform mass to the mass per unit length of the strip.

The manner in which the weight of the platform influences the width of the pulse is demonstrated in Fig. 5. It is seen that the rate of rise of the strain is strongly influenced by the mass of the platform which receives and transmits the impact. Since the time required to accelerate the platform to the final velocity must be expected to differ greatly in the two cases, the observed effect is not surprising. Interesting to note is the fact that the time between the beginning of the sweep and the beginning of the pulse increases with increasing mass and complexity of the platform. In the elastic region (not shown) the height of the pulse with the heavier platform is always less than that for the lighter one. This is due to the fact that for the same hammer momentum, the velocity attained by the heavier clamp will be much less than for the lighter one. This effect of platform mass can be compensated for by considering the impact of the hammer on the platform to be an inelastic impact and using the equations of conservation of momentum.

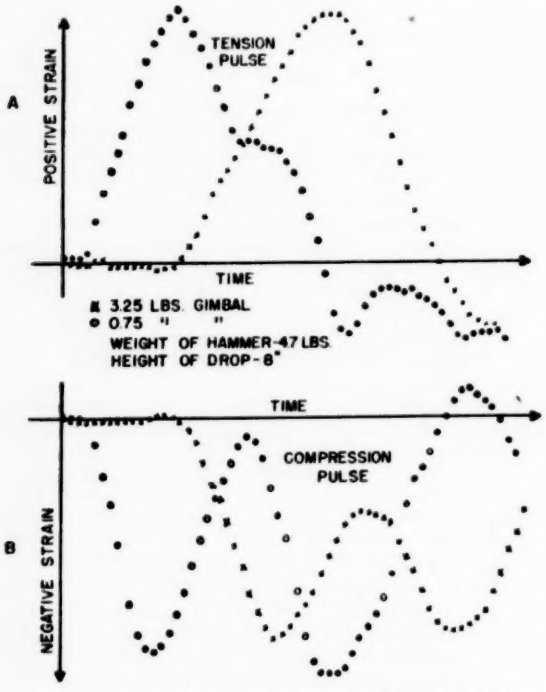

FIG. 5 TENSION AND COMPRESSION PULSE TO ILLUSTRATE PLASTIC DEFORMATION

(A, Tension pulses obtained at point 2 in. above impact point. B, Compression pulses obtained at point 2 in. below impact point. 1/8-in. × 1/2-in. cold-rolled copper specimen; 50-kc timing markers; prestress 36,000 psi.)

In the elastic region, the strain returns to its initial value if the reflection occurs late enough. On the other hand, when a plastic deformation is produced it is recognizable by the fact that the strain does not return to its initial value after the tension pulse has passed. However, irrespective of the amount of prestressing, a compression pulse, such as occurs below the striking platform, should show complete recovery since it represents unloading along an elastic line. That these two phenomena are actually observable is demonstrated in Fig. 5 where tension and compression pulses produced simultaneously are shown. In the case of the pulse produced with the light platform, the permanent tensile deformation is clearly visible as a short plateau following the pulse, and only the return of the reflection from the lower end brings the material back through zero strain into compression. At the same time, the compression pulse for the light platform shows nearly complete recovery which is prevented from becoming perfect only by the return of the reflected pulse. Unfortunately, the impact duration with the heavy platform is too great to observe these phenomena.

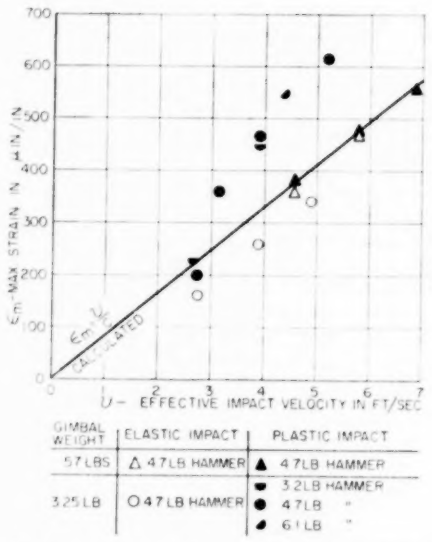

FIG. 6 PLOT OF MAXIMUM STRAIN VERSUS EFFECTIVE IMPACT VELOCITY

[1/8 × 1/2 in. cold-rolled copper specimen. Data taken 1.5 in. above impact point. Specimen prestressed into elastic region (10,000 psi, open symbols) and plastic region (36,000 psi, solid symbols) using 0.57 lb and 3.25 lb gimbal.]

For the short and quickly rising pulse, the amplitudes are the same (2 in. from striking point) for the tension and compression wave and, furthermore, equal to those obtained in the elastic region. On the other hand, for the slowly rising wide pulses produced with the heavy platform, the amplitude of the plastic tension pulse is nearly twice as large and much wider than in the elastic case, whereas the compression pulse remains practically unchanged in "amplitude and width." These results would seem to indicate that for sufficiently long pulses creep takes place, resulting in a strain above that calculated on the basis of an elastic velocity, but that for very short pulses, the behavior is nearly elastic even when the material is prestressed far into the plastic region.

A plot of the data on the maximum strain versus the calculated effective striking velocity obtained under different conditions of impact is shown in Fig. 6. It is seen that for the short pulses produced with the lightweight platform, the strain measured is always nearly equal to the value calculated using the elastic velocity under all conditions of prestressing. On the other hand, a deviation toward higher strains is found for the slowly rising pulses produced with the heavy platform. This is to be expected since the conditions where Donnell's and von Kármán's hypothesis applies are more nearly approached by the long than by the short pulses.

However, a calculation of the strain according to von Kármán's theory using the slope of the stress-strain curve at the

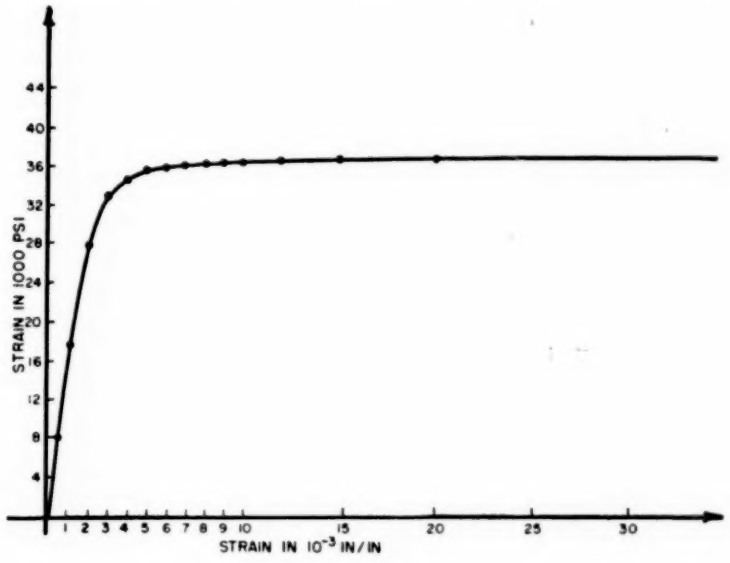

FIG. 7 TYPICAL STRESS-STRAIN CURVE FOR NEW COPPER SPECIMEN (1/8-in. × 1/4-in. copper strip.)

point to which the samples were preloaded leads to values many times larger than the ones observed even for the broadest pulses used in the present investigation (approximately 0.8 millisec in duration).

MAIN EXPERIMENTS ON PULSE PROPAGATION

With the factors determining the pulse shape at the point of impact established, it is possible to study in detail the effects of varying the amplitude and width on the propagation in the plastic region. These experiments were all performed on cold-rolled copper strips 1/8 in. × 1/2 in. in cross section. A representative stress-strain curve for a new copper specimen is shown in Fig. 7.

Two types of experiments were carried out to this end. In the first type, two or three sets of gages spaced along the bar were left permanently connected to their respective amplifiers and scopes throughout the run. In the second type of experiment, one of two scopes used is connected to successively more distant gages for each of a series of identical impacts, while the other scope always remains connected to the gage nearest the striking platform. In this manner the decay in amplitude and the changes in shape can be observed for a larger number of stations than there are scopes available. This method also eliminates some errors due to possible slight differences in the amplifiers since only a single amplifier is used for all the gage stations except the first.

In a typical run, gages were fastened along the strip at distances of 2, 12, 27, and 47 in. above the center of the striking platform, which was placed 29 in. from the lower end of the strip whose over-all length was 120 in. With this choice of spacing and the usual pulse width of 400 to 800 μ-sec, the reflected wave from the upper end cannot return to the lower three gages before the complete pulse is recorded. A reflection from the lower end, on the other hand, has no other effect than to shorten the pulse width slightly and, therefore, offered no difficulty in the present experiments.

All four gages were brought to the multiple bridge for static readings and two or three of them were connected to the scopes. After the various adjustments just described had been made, the load was increased gradually and photographs were taken at intervals of about 3200 to 6400 psi up to the "knee" of the stress-strain curve.

Owing to its construction, the machine unloads itself to an extent roughly proportional to the amount of permanent deformation measured as a result of the impact. For a hammer weight of 4.68 lb, a drop height of 8 in. and using the heavy striking platform, the maximum unloading amounted to 3200 psi. This corresponds to a change in average strain of 200 μ in. per in. as calculated on the basis of elastic unloading, an amount actually closely equal to the average plastic strain measured. After each impact in the plastic region the bar was reloaded to or beyond the value of stress before the impact. If the material is strained "far" beyond the knee of the original curve, this process can be repeated many times without noticeable changes in pulse shape so that the specimen is usable until the total strain exceeds that permitted by the type of gage used, approximately 3 to 5 per cent. Each time readings were taken on the d-c bridges before and after the impact and after reloading to the same stress value so that the permanent deformation could be compared with the dynamic strains recorded.

Using these methods, a number of photographs have been obtained. In Fig. 8 the pulse as it appears at two gage stations 35 inches apart has been replotted to the same time scale and superimposed for both elastic and plastic preloading of the bar. It is seen that whereas the pulse travels unchanged in shape in the elastic region, it undergoes decay as well as broadening or dispersion in the plastic region. Furthermore, as is evident from the unchanged distance between the beginning of the sweep and the beginning of the pulse in the two cases, the front of the pulse travels at the elastic velocity. Even the top of the plastic pulse, for instance the point where unloading begins, travels at an instantaneous velocity close to the elastic one and very much larger than that predicted by the slope of the static stress-strain curve according to the existing theory. However, as is evident from Fig. 9, where photographs of a typical pulse obtained at three successive stations have been replotted and superimposed, the broadening of the pulse is very much larger from station No. 1 to No. 2 than from No. 2 to No. 3 despite the larger distance from No. 2 to No. 3.

A number of other interesting features also are revealed by

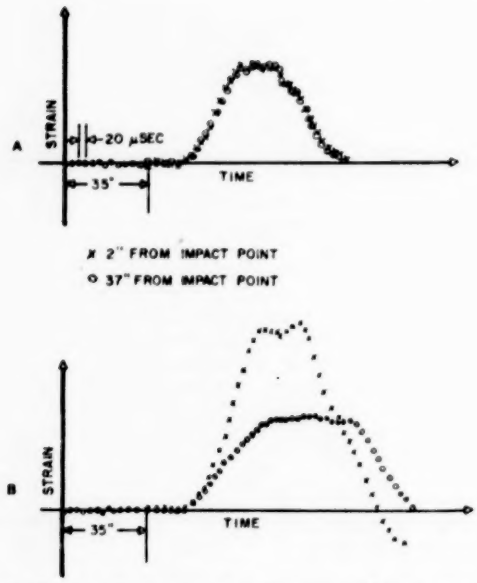

FIG. 8 TYPICAL PULSES AT TWO SUCCESSIVE STATIONS FOR (A) ELASTIC 9250-PSI AND (B) PLASTIC 36,300-PSI PRELOADING

(Distance between stations 35 in.; 50-kc timing markers; 1/8-in. × 1/2-in. cold-rolled copper specimen; hammer weight 6.1 lb, 3.25 lb striking platform; hammer-drop height 8 in. Traces shifted to coincide at beginning of pulse.)

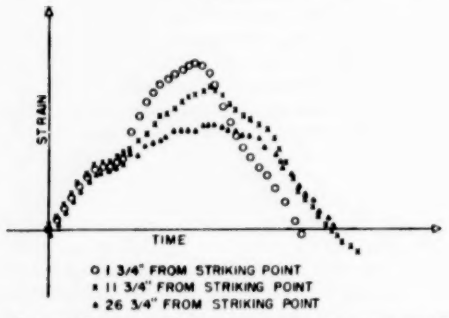

FIG. 9 TYPICAL PULSE AT THREE SUCCESSIVE STATIONS FOR PLASTIC PRELOADING

(Traces shifted to coincide at beginning of pulse at each station. 3.25 lb striking platform; 1/8-in. × 1/2-in. cold-rolled copper specimen; 50-kc timing markers.)

these traces. The lower parts of the loading and unloading slopes are seen to be closely parallel at each station, indicating an apparent elastic behavior for a certain time interval. This interval seems to be roughly equal to the duration of the very short pulses which were found to lead to strains given by an elastic law even in the plastic region. This lower portion of the pulse is always found to travel unchanged in shape once the plastic strain has been dissipated. The amplitude of this "residual elastic portion" of the pulse was observed to be largely independent of impact velocity or hammer weight, and it is not yet certain what factors determine it. By varying the mass of the hammer, the relative amount of broadening as a function of original pulse width at the base was found to increase with increasing width. A plot of this relation is shown in Fig. 10, and it would seem to suggest that a frequency-dependent dispersion holds for the propagation of plastic pulses, in disagreement with the prediction of the von Kármán theory.

On the other hand, a plot of the width of the pulse at two successive stations as a function of pulse amplitude, Fig. 11, does not reveal any functional dependence between relative broadening and initial amplitude over the range investigated. This again is not in agreement with the theory, though it is clear that the investigation would have to be extended to much larger strain amplitudes before any more general conclusions can be drawn. It also must be pointed out that this definition of the width of the pulse is made somewhat uncertain by the fact that it requires the presence of a reflected wave of opposite sign to bring the strain back to its value before the impact. It is important to note that the effect of the reflected wave would be such as to shorten and not to widen the pulse even if it were an important factor in determining the pulse width.

The decay in pulse amplitude was measured both statically, by measuring the permanent strain, and dynamically, by measuring pulse amplitudes. In both cases strain did not decrease linearly with distance from the point of impact. Fig. 12 shows the data on the dynamic pulse amplitudes under different impact conditions. It is seen that the rate of decay increases with the initial amplitude but that for all impact conditions the plastic deformations are practically confined to a distance of 30 in. from the impact point. The points are not inconsistent with an exponential type of absorption law, but further studies would be required to establish the exact functional form. The permanent deformations measured decay in the same manner as the total pulse amplitude, as illustrated in Fig. 13. The general form of these plots and the length of specimen in which a permanent strain is observed agree roughly with the tails of the curves obtained for

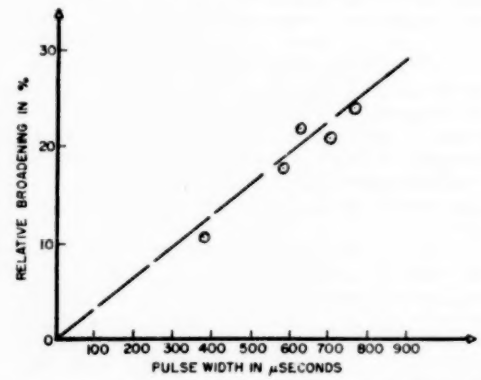

FIG. 10 RELATIVE BROADENING AS A FUNCTION OF PULSE WIDTH AT STATION 2 IN. FROM IMPACT POINT; 36,500-PSI PRELOADING

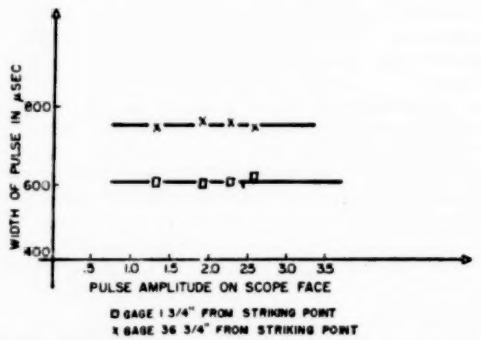
WIDTH OF PULSE IN μSEC
400
600
800
.5 1.0 1.5 2.0 2.5 3.0 3.5
PULSE AMPLITUDE ON SCOPE FACE
□ GAGE 1 3/4" FROM STRIKING POINT
X GAGE 36 3/4" FROM STRIKING POINT

FIG. 11 WIDTH OF PULSES AT TWO STATIONS AS FUNCTION OF AMPLITUDE AT STATION 2 IN. FROM IMPACT POINT

(Weight of hammer 4.7 lb; weight of striking platform 3.25 lb; 1/8-in. × 1/2-in. cold-rolled copper strip; 36,000 psi.)

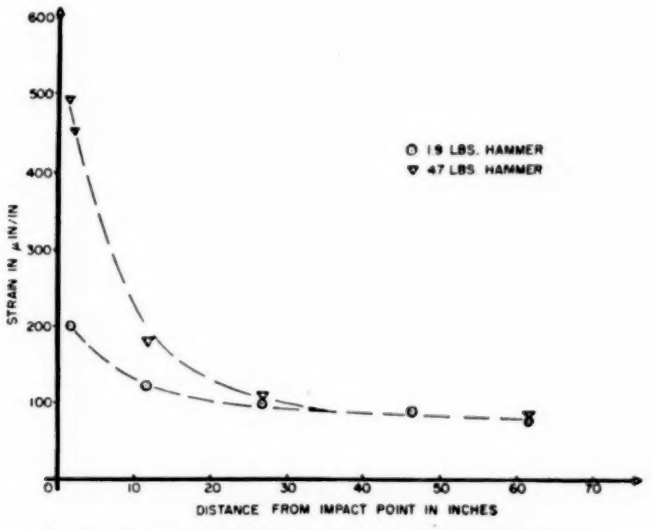

FIG. 12 DECREASE IN PULSE AMPLITUDE WITH DISTANCE, DYNAMIC
(1/8-in. × 1/2-in. cold-rolled copper strip prestressed to 36,000 psi; 3.25-lb striking platform.)

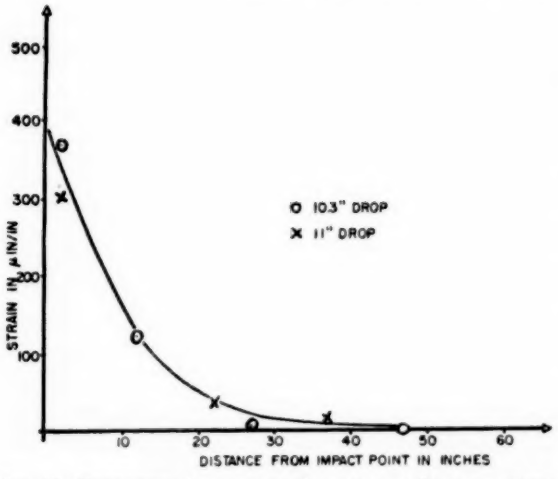

FIG. 13 PERMANENT STRAIN AS A FUNCTION OF DISTANCE FROM IMPACT POINT, STATIC MEASUREMENT
(1/8-in. × 1/2-in. cold-rolled copper strip, prestressed to 36,500 psi. 4.7-lb hammer, 3.25-lb striking platform.)

copper wires by the California group for impacts of similar duration (3, 6), although there is here no evidence for any portions of the strip showing constant strain.

To determine the dynamic value of Poisson's ratio, two sets of SR-4 type C-8 resistance-wire strain gages were cemented on the strip—one set longitudinal and one transverse. Tension pulses of varying widths and amplitudes were generated as previously noted at different distances from the gages. The ratio of the signal from the transverse gages to that from the longitudinal gages give directly the value of Poisson's ratio. In no case was Poisson's ratio found to be 1/2 but rather it seemed to be independent of amplitude and to increase with pulse width from the elastic value to a maximum value of 0.29 for the widest pulse.

SUMMARY OF EXPERIMENTAL RESULTS

The principal results obtained by the present investigation as to the propagation of plastic strains are summarized below: It must, however, be emphasized that these results were obtained with short (< 1 millisec), small amplitude (< 10^3 μ in./in.) pulses in a prestressed strip and as such are strictly applicable only to pulses of this general type.

1 The velocity of propagation of the wave front is that of the elastic wave.

2 The velocity of propagation of any part of the pulse is much greater than that given by the tangent modulus at the point of the stress-strain curve to which the material has been prestressed.

3 Dispersion or broadening exists for pulses obtained when the material has been prestressed into the plastic range.

4 The dispersion appears to be frequency-dependent such that it increases with decreasing effective frequency (or increasing width) of the pulse.

5 For a given pulse width, the total per cent broadening of the pulse does not appear to depend on the initial amplitude.

6 The rate of broadening decreases rapidly with increasing distance from the point of impact.

7 The amplitude of a plastic strain does not decay linearly with distance. The decay would seem to be approximately exponential.

8 The rate of decrease of amplitude with distance appears to be an increasing function of the amplitude of the strain at the point of impact.

9 The maximum amplitude of the strain exceeds that calculated on the basis of a propagation velocity equal to the normal elastic value only for the broadest pulses. Consequently, the maximum strain is, in general, not given by the relation

$$v = \int_{\epsilon_1}^{\epsilon_2} \left(\frac{d\sigma/d\epsilon}{\rho} \right)^{1/2} d\epsilon$$

10 The width of a pulse in the plastic as well as in the elastic region increases linearly with the mass of the body producing the impact and is essentially independent of the impact velocity.

11 Poisson's ratio appears to increase with increasing pulse width. For very short pulses the value is approximately the elastic value.

Discussion of Results

The experimental evidence summarized by results 1, 2, 4, 5, and 9, indicates that in so far as the transient phenomenon is concerned, the existing theory neglecting strain-rate effects cannot describe the propagation of plastic strain satisfactorily. The assumption that the ordinary engineering stress-strain curve can be used to describe the dynamic aspects of plastic wave propagation does not seem tenable in the light of the observed propagation velocity and the apparent absence of a dependence of dispersion upon amplitude. Thus the assumption that the instantaneous tangent modulus is only a function of the strain and not the strain rate cannot be maintained if transient phenomena are to be described. This same conclusion has been reached independently by Riparbelli and his co-workers.

Such a dependence upon strain rate pointing toward the influence of creep actually has been anticipated by Malvern (5) and Shanley (4). The latter emphasized that for so-called "zero time" or instantaneous loading, the elastic line of modulus E is followed, and that creep during the deformation accounts for the deviation of the static curve from the straight line. Malvern advanced the hypothesis that the material is brought initially into a condition of "incipient flow" and that this flow requires a definite amount of time in which to become appreciable. From this hypothesis he predicted that the front of the wave always would travel at the elastic velocity, and this seems now to have been confirmed by direct experiment.

It should be pointed out that von Kármán himself realized the limitations of his theory imposed by the need to neglect the strain rate in order to obtain a simple analytical solution. Certain discrepancies between the predictions of the theory and the experimental results obtained by him and his co-workers actually were attributed to the influence of the rate of strain (3). However, the type of experiment carried out so far was not well suited to a study of strain rate effects.

A number of important consequences follow from the inadequacy of the Donnell-Taylor-von Kármán theory in accounting for the dynamic behavior. Perhaps the most important of these is that all detailed analyses of the interactions of plastic waves based on the assumption that each strain increment travels at its own characteristic velocity must be revised. Furthermore, it appears that there is now no longer any basis for assuming the existence of so-called "shock waves" at velocities less than those of sound in solids, since the experiments do not show any "catching up" of the unloading front with a more slowly traveling plastic front (10). Such a phenomenon requires the presence of a physically distinct "unloading front" moving at the same velocity as the elastic leading edge of the pulse, which therefore would leave the pulse width constant (1). The data clearly show, however, that the whole process of change in shape of the pulses is quite different from that to be anticipated by such a view. On the other hand, results 4 and 5 would seem to indicate that a linear model for describing the behavior of a material like copper may be adequate to give an analytical description of the transient phenomenon of plastic-wave propagation.

Acknowledgments

Many individuals have contributed to this paper. In particular, the authors wish to express their appreciation to Prof. Carlo Riparbelli of the Cornell Graduate School of Aeronautical Engineering for originally suggesting the experiments leading to this investigation, and for his numerous valuable suggestions and many fruitful discussions with the authors. They also want to thank Mr. Hu-Nan Chu for his assistance in the experimental work, and Mr. Herbert F. Spirer for his aid in planning and executing the instrumentation. The authors are indebted to the Applied Physics Laboratory for sponsoring this investigation which was carried out at Cornell University under Contract No. 33031-2.

BIBLIOGRAPHY

1 "Longitudinal Wave Transmission and Impact," by L. H. Donnell, Trans. ASME, vol. 52, 1930, p. 153.

2 "The Plastic Wave in a Wire Extended by an Impact Load," by G. I. Taylor, British Official Report RC 329, 1942.

3 "On the Propagation of Plastic Deformation in Solids," by Th. von Kármán, NDRC A-29, OSRD 365, January, 1942. See also the summary by von Kármán and P. Duwez in the *Journal of Applied Physics*, vol. 21, 1950, pp. 987–994.

4 "Analysis of Stress-Strain-Time Relations From the Engineering Viewpoint," by F. R. Shanley, presented at the Second Symposium on Plasticity, Brown University, Providence, R. I., April, 1949, revised, September, 1951.

5 "The Propagation of Longitudinal Waves of Plastic Deformation in a Bar of Material Exhibiting a Strain-Rate Effect," by L. E. Malvern, Journal of Applied Mechanics, Trans. ASME, vol. 73, 1951, pp. 203–207.

6 "On the Propagation of Plastic Strains in Solids," by Th. von Kármán and P. E. Duwez, presented at the Sixth International Congress of Applied Mechanics, Paris, France, September, 1946.

7 "The Propagation of Plastic Strain in Tension," by P. E. Duwez, D. S. Wood, and D. S. Clark, NDRC Report No. A-99 (OSRD No. 931), 1942.

8 "An Experimental Study of the Propagation of Plastic Deformation Under Conditions of Longitudinal Impact," by P. E. Duwez and D. S. Clark, Proceedings of the American Society for Testing Materials, vol. 47, 1947, pp. 502–532.

9 "Propagation of Plastic Waves in Pre-Stressed Bars," by J. F. Bell, Technical Report No. 5, Navy Contract N6-ONR-243, Task Order VIII, Johns Hopkins University, June, 1951.

10 "On the Impact Behavior of a Material With a Yield Point," by M. P. White, Trans. ASME, vol. 71, 1949, p. 39.

Design Data and Methods

It is important that the data contained in technical papers be made readily available to designing engineers. In order to satisfy these needs of industry, this section of the Journal includes a concise presentation of data and information drawn chiefly from papers previously published by the Applied Mechanics Division of The American Society of Mechanical Engineers.

Design of Helical and Leaf Springs for Minimum Weight

By M. F. SPOTTS,[1] EVANSTON, ILL.

This paper presents equations for the direct determination of the proportions of a helical spring which will contain the least possible amount of material. In general, it is possible by this method to effect considerable economies over a spring whose dimensions have been selected arbitrarily. The advantages are illustrated by numerical examples. The method also has been applied to leaf springs and design equations are presented.

General Problem of Spring Design

THE multiplicity of symbols in the equations for the stress and deflection of a closely coiled helical spring makes the general problem of spring design largely one of trial and error. However, there is one type of problem whose recurrence is sufficiently frequent to deserve special consideration. For this case the spring must satisfy the following requirements:

1 In its least compressed position, the spring must be capable of exerting a force of specified value P_1.

2 After the spring has been compressed an additional amount from the operation of the mechanism, the maximum shearing stress must not exceed a specified value τ_2.

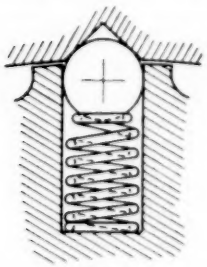

Fig. 1

A large percentage of springs with static or infrequently applied load cycles is employed in the foregoing manner. A typical example is the indexing mechanism shown in Fig. 1. When the ball is in the detent, the important factor is the holding ability of the mechanism as determined by the force exerted by the spring. When the lower number rotates and the ball is out of the detent, the controlling factor is the shearing stress in the spring material.

The disadvantage of a trial-and-error solution to the problem is that the resulting spring usually contains more material than necessary. We will now show how to overcome this difficulty and proportion the spring so that the least possible amount of material is consumed.

Helical Springs

Standard equations for the stress and deflection are as follows

$$\tau = \frac{16\,PR}{\pi d^3} \qquad [1]$$

$$\delta = \frac{64\,PR^3n}{dG} \qquad [2]$$

where τ is the shearing stress, P the axial load, R the mean radius of helix, d the diameter of wire, δ the deflection, n the number of active coils, and G the modulus of elasticity in shear.

The volume V of the material in the spring is equal to the cross-sectional area of the wire $\pi d^2/4$ times the length $2\pi Rn$, or

$$V = \frac{1}{2}\pi^2 d^2 Rn \qquad [3]$$

The equation for V can be written in another form as follows: Let P_2 and P_1 be the loads on the spring at its most and least compressed conditions, respectively. Let Δ be the difference between δ_2 and δ_1, the respective deflections for loads P_2 and P_1. Then by Equation [2]

$$\Delta = \frac{64\,(P_2 - P_1)R^3n}{dG} \qquad [4]$$

The value of P_2 from this equation is

$$P_2 = P_1 + \frac{\Delta\, dG}{64\,R^3n}$$

By Equation [1], stress τ_2, when load P_2 is acting, is $16\,P_2R/\pi d^3$. When the value of P_2 from this equation is substituted, the following result is obtained

$$\tau_2 = \frac{16\,R}{\pi d^3}\left(P_1 + \frac{\Delta dG}{64\,R^3n}\right)$$

This equation should be solved for Rn and the result substituted into Equation [3]. The desired expression for V is obtained

$$V = \frac{\pi^2 \Delta d^2 G}{8(\pi d^3\tau_2 R - 16\,P_1R^3)} \qquad [5]$$

$$= \frac{\pi^2 \Delta R G}{c^3(\pi R^2\tau_2 - 2\,P_1c^2)} \qquad [6]$$

where spring index c is equal to $2R/d$.

[1] Professor of Mechanical Engineering, Technological Institute, Northwestern University. Mem. ASME.

Discussion of this paper should be addressed to the Secretary, ASME, 29 West 39th Street, New York, N. Y., and will be accepted until October 10, 1953, for publication at a later date. Discussion received after the closing date will be returned.

Note: Statements and opinions advanced in papers are to be understood as individual expressions of their authors and not those of the Society. Manuscript received by ASME Applied Mechanics Division, January 2, 1953.

In general, the approximate value for the spring index c can be specified in advance. All terms on the right side in Equation [6] are thus known except helix radius R. When Equation [6] is differentiated partially with respect to R and the result placed equal to zero, the resulting expression gives the relationship between the variables for the spring of least possible volume. The result is

$$R^2 = \frac{4\,P_1c^3}{\pi\tau_2}$$

or

$$d^2 = \frac{16\,P_1c}{\pi\tau_2} \qquad [7]$$

Equation [7] can be used for finding diameter d corresponding to the tentative value of spring index c. The final value of d then can be taken as a nearby standard diameter spring wire.

Substitution for c in Equation [7] gives

$$\tau_2 = \frac{32\,P_1R}{\pi d^3} \qquad [8]$$

or

$$\tau_2 = 2\,\tau_1 \qquad [9]$$

Then

$$P_2 = 2\,P_1 \qquad [10]$$

and

$$\delta_2 = 2\,\delta_1 \qquad [11]$$

As the foregoing equations indicate, whenever the maximum load, stress, or deflection is double the minimum load, stress, or deflection, respectively, the spring will contain the minimum amount of material.

Substitution of Equations [1] and [10] into Equation [4] gives an expression for the number of active coils n

$$n = \frac{\Delta d^4G}{64\,P_1R^3} = \frac{\Delta dG}{2\,\pi R^2\tau_2} \qquad [12]$$

An equation for the amount of material in the spring of minimum volume can be found by the substitution of R from Equation [8] and n from Equation [12] into Equation [3]. Thus

$$V_{\min} = \frac{8\,\Delta P_1G}{\tau_2^2} \qquad [13]$$

The relationship between the volume of a spring of arbitrarily selected dimensions and the spring of minimum volume can be found by dividing Equation [5] by Equation [13]. The quotient can be reduced to

$$\frac{V}{V_{\min}} = \frac{1}{4\left[\frac{P_1}{P_2} - \left(\frac{P_1}{P_2}\right)^2\right]} \qquad [14]$$

$$= \frac{1}{4\left[\frac{\tau_1}{\tau_2} - \left(\frac{\tau_1}{\tau_2}\right)^2\right]} \qquad [15] \qquad = \frac{1}{4\left[\frac{\delta_1}{\delta_2} - \left(\frac{\delta_1}{\delta_2}\right)^2\right]} \qquad [16]$$

A plot of these equations is given in Fig. 2.

The effect of stress concentration can be taken care of by adjustment of the value of stress τ_2.

Example 1. Suppose a spring must be capable of exerting a force of 20 lb in its most extended position. After being compressed an additional 0.625 in. the shearing stress is to be 75,000 psi. The spring index is to have a value approximately equal to 8. $G = 11{,}500{,}000$ psi.

(*a*) Find the nearest standard-size wire for the spring of minimum volume. Find the mean radius of helix and the required number of active coils.

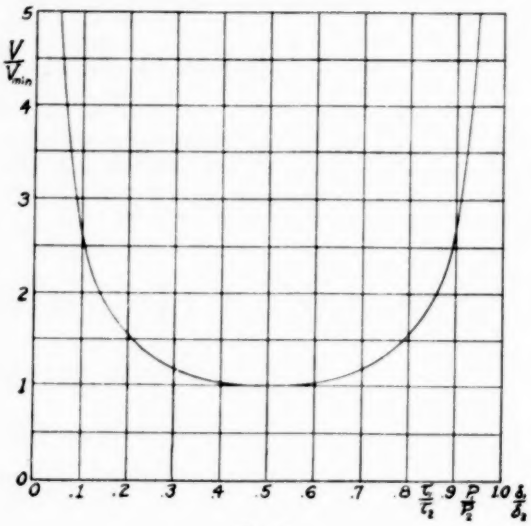

FIG. 2

(*b*) Suppose the spring is wound from No. 11 wire with an arbitrarily selected radius of helix of 0.35 in. How does the amount of material for this spring compare with that of the minimum spring?

Solution (*a*). By Equation [7]

$$d^2 = \frac{16\,P_1c}{\pi\tau_2} = \frac{16 \times 20 \times 8}{\pi\ 75{,}000} = 0.010865$$

$$d = 0.1042 \text{ in.}$$

Use No. 12 wire $\quad d = 0.1055$ in.

By Equation [8] $R = \dfrac{\pi d^3\tau_2}{32\,P_1} = \dfrac{\pi\,0.1055^3 \times 75{,}000}{32 \times 20} = 0.4323$ in.

By Equation [12]

$$n = \frac{\Delta dG}{2\,\pi R^2\tau_2} = \frac{0.625 \times 0.1055 \times 11{,}500{,}000}{2\,\pi\,0.4323^2 \times 75{,}000} = 8.61 \text{ coils}$$

Solution (*b*) For No. 11 wire, $d = 0.1205$ in. By Equation [1]

$$P_2 = \frac{\pi d^3\tau_2}{16R} = \frac{\pi\,0.1205^3 \times 75{,}000}{16 \times 0.35} = 73.62 \text{ lb}$$

By Equation [14]

$$\frac{V}{V_{\min}} = \frac{1}{4\left[\frac{P_1}{P_2} - \left(\frac{P_1}{P_2}\right)^2\right]} = \frac{1}{4\left[\frac{20}{73.62} - \left(\frac{20}{73.62}\right)^2\right]} = 1.263$$

The spring of part (*b*) contains 26 per cent more material than necessary.

LEAF SPRINGS

Equations corresponding to the foregoing can be derived for leaf springs. Fig. 3 shows a cantilever spring of rectangular cross section with a load on the end. Equations for the stress at the support and deflection at the end are as follows

$$s = \frac{6\,Pl}{bh^2} \qquad [17]$$

$$\delta = \frac{(1 - \mu^2)Pl^3}{3\,EI} = \frac{4(1 - \mu^2)Pl^3}{Ebh^3} \qquad [18]$$

where s is the bending stress, P is the load at the end, l is the length, b is the width of cross section, h is the depth of cross section, δ is the deflection at the end, μ is Poisson's ratio, E is the modulus of elasticity, and $I = bh^3/12$, the moment of inertia of the cross section.

FIG. 3

Term $(1 - \mu^2)$ should be used for wide beams where b is at least 8 or 10 times the value of h. For narrow beams this parenthetical term should be replaced by unity. Now

$$\Delta = \frac{4(1 - \mu^2)\, l^3(P_2 - P_1)}{Ebh^3}$$

This equation should be solved for P_1, and the value $s_2bh^2/6l$ for P_2 substituted

$$P_1 = \frac{bh}{2l}\left[\frac{s_2h}{3} - \frac{\Delta Eh^2}{2(1 - \mu^2)l^2}\right] \quad [19]$$

The square bracket is reduced to a common denominator, and the entire equation multiplied by l. It is then solved for bhl or V

$$V = \frac{12\, P_1(1 - \mu^2)l^4}{2(1 - \mu^2)s_2hl^2 - 3\,\Delta Eh^2} \quad [20]$$

If thickness of stock h is chosen, all factors on the right side of this equation are known except length l. The equation should be differentiated partially with respect to l and the result set equal to zero to give

$$l^2 = \frac{3\Delta Eh}{(1 - \mu^2)s_2} \quad [21]$$

When l is determined by means of this equation, the spring of minimum volume results.

Substitution of the value of h from Equation [21] into Equation [19] gives the following expression for b

$$b = \frac{108\, P_1\Delta^2E^2}{(1 - \mu^2)^2 s_2^3 l^3} \quad [22]$$

Equations [9], [10], and [11] apply equally well to leaf springs with bending stress s substituted for shearing stress τ. This can be shown in the following manner: The value of s_2 from Equation [21] is set equal to $6\, P_2l/bh^2$ and the result solved for P_2. The value of s_2 from Equation [21] is substituted into Equation [19]. The resulting value of P_1 is one half as great as the value of P_2.

An equation for the minimum volume is obtained by substituting the value of h from Equation [21] into Equation [20]. The result is

$$V_{\min} = \frac{36\, P_1\Delta E}{(1 - \mu^2)s_2^2} \quad [23]$$

Since $V_{\min} = bhl$, a simpler form of equation for b is

$$b = \frac{V_{\min}}{hl} = \frac{36\, P_1\Delta E}{(1 - \mu^2)s_2^2hl} \quad [24]$$

The quotient $V/V_{\min}$ yields equations identical with those for helical springs so that Equations [14], [15], and [16] apply also to leaf springs.

Example 2. A leaf spring like Fig. 3 is to exert a force of 20 lb at its least deflected position. After undergoing an additional deflection of 0.5 in. the stress is not to exceed 90,000 psi. E = 30,000,000 psi; $\mu = 0.3$.

(*a*) For $h = 0.1$ in. find the values of b and l for the spring of minimum volume.

(*b*) Find the value of b if h is taken as 0.125 in. and l is taken as 6.5 in. By what percentage is this spring larger than the one of part (*a*)?

Solution (*a*). By Equation [21]

$$l^2 = \frac{3\,\Delta Eh}{(1 - \mu^2)s_2} = \frac{3 \times 0.5 \times 30{,}000{,}000 \times 0.1}{(1 - 0.3^2) \times 90{,}000} = 54.945$$

$l = 7.412$ in.

By Equation [23]

$$V_{\min} = \frac{36\, P_1\Delta E}{(1 - \mu^2)s_2^2} = \frac{36 \times 20 \times 0.5 \times 30{,}000{,}000}{0.91 \times 90{,}000^2} = 1.4652 \text{ cu in}$$

By Equation [24] $\quad b = \dfrac{V_{\min}}{hl} = \dfrac{1.4652}{0.1 \times 7.412} = 1.977$ in.

Solution (*b*). In Equation [19]

$$20 = \frac{0.125\, b}{2 \times 6.5}\left[\frac{90{,}000 \times 0.1250}{3} - \frac{0.5 \times 30{,}000{,}000 \times 0.125^2}{2 \times 0.91 \times 6.5^2}\right]$$

$b = 2.963$ in.

$V = bhl = 2.963 \times 0.125 \times 6.5 = 2.4074$ cu in.

$$\frac{V}{V_{\min}} = \frac{2.4074}{1.4652} = 1.643$$

The spring of part (*b*) contains 64 per cent more material than necessary.

Fig. 4 shows a simply supported leaf spring with concentrated load at the center of the span. Equations for proportioning the spring of minimum volume can be derived by the methods used previously.

$$l^2 = \frac{12\,\Delta Eh}{(1 - \mu^2)s_2} \quad [25] \qquad b = \frac{36\, P_1\Delta E}{(1 - \mu^2)s_2^2hl} \quad [26]$$

$$V_{\min} = \frac{36\, P_1\Delta\, E}{(1 - \mu^2)s_2^2} \quad [27]$$

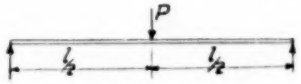

FIG. 4

Equations [9], [10], and [11] apply to the spring of Fig. 4 as well as Equations [14], [15], and [16].

When springs are used in quantities, the saving in material by means of the foregoing equations is considerable.

The question of optimum design has been discussed by J. Jennings, reference (1). The remaining references pertain to the analogous problem of finding the energy per unit volume of space occupied by the coiled spring.

REFERENCES

1 "Springs of Minimum Weight," by J. Jennings, *Machinery*, London, England, vol. 52, 1938, p. 707.

2 "Combining Maximum Spring Deflection With Minimum Space," by A. M. Wahl, *Machine Design*, vol. 14, January, 1942, p. 57; discussion, March, 1942, p. 84.

3 "Maximum Capacity of Helical Springs," by J. Jennings, *Machinery*, London, England, vol. 51, 1937, p. 109.

4 "Springs for Maximum Resilience," by J. Jennings, *Engineering*, vol. 152, 1941, p. 134.

5 "Maximum Performance of Helical Springs," by E. J. Sholbert, JOURNAL OF APPLIED MECHANICS, Trans. ASME, vol. 69, 1947, p. A-53.

6 "Design of Helical Springs for Minimum Over-All Dimensions," by V. Tarinov, *Machinery*, London, England, vol. 74, 1949, p. 39.

Discussion

Nonlinear Distribution of Bending Stresses[1]

LYNDON CRAWFORD.[2] The author has performed an excellent piece of work. The discusser has lived with this superstructure problem for some time, dating back to the President Wilson data which we analyzed.

Reed Research, Inc., under contract to the Ship Structure Committee of the Government, has performed certain experimental work in order to corroborate the author's theory. This Society may be interested in certain of the early findings from this work.

A 20-ft box model is used, Fig. 1, the material for which, except for end plates, is all unclad aluminum 24 ST and 14 ST. Fasteners are highly torqued steel bolts. This has permitted testing of various superstructure houses, one of which is shown in place in this figure. Loading is accomplished by screw jack through equalizers that create constant bending moment in the superstructure area.

The trend of results is shown in Fig. 2. These are only trends observed at the midship station and neglect a certain amount of shear-lag effect at the step. Test Nos. 1 and 11 are bare hull tests. Three houses have been tested:

1 A long low house was tested first, represented by the test Nos. 2, 3, and 4.

(*a*) In test No. 2 the support for the house was furnished by simulated deck beams only. The dotted line represents the theoretical value predicted by the author's method. (Assuming deck beams acting alone as beams.) The solid line represents the trend of tests. The expected stress reduction occurred.

FIG. 1 TWENTY-FOOT BOX MODEL FOR TESTING

(*b*) Test No. 3 duplicated the previous one with outsize deck

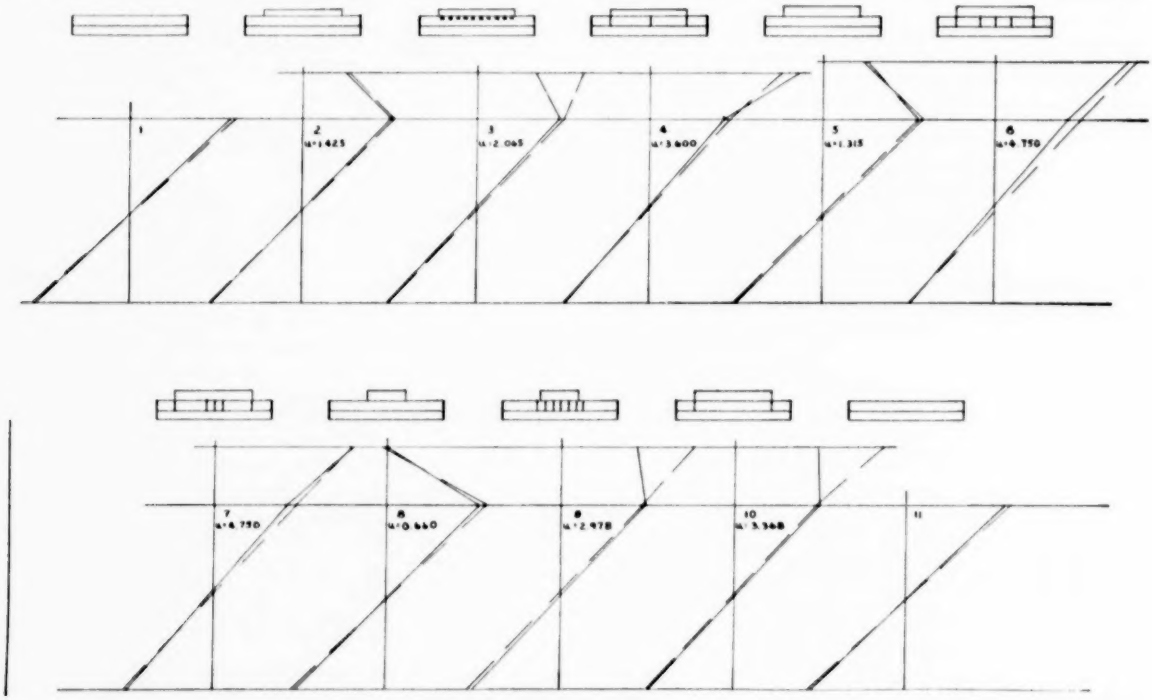

FIG. 2 TREND OF TEST RESULTS

———— Experiment — — — — — Theory

[1] By H. H. Bleich, published in the March, 1953, issue of the JOURNAL OF APPLIED MECHANICS, Trans. ASME, vol. 75, pp. 95–104.

[2] Chief, Analytical Engineering Department, Reed Research, Inc., Washington, D. C.

beams fitted at every seventh frame space. The agreement of theory and experiment is less convincing.

(*c*) In test No. 4 the outside deck beams were replaced by three rather rigid bulkheads. The trend again is followed. The difference shown is being studied at the present time, possibly being due to singularity effects.

2 A higher house of the same length was tested under four conditions represented by test Nos. 5, 6, 7, and 10.

(*a*) No. 5 again shows normal deck beams only with similar results as No. 2.

(*b*) No. 6 was a configuration of five equally spaced bulkhead supports and shows rather fair correlation.

(*c*) Test No. 7 presents a configuration with irregularly bunched bulkheads, but by arithmetic mean the same value of u and hence Φ (of the paper) as test No. 6. Here the actual stress built up at the midship section is in excess of test No. 6 and the theory.

(*d*) Test No. 10 is not a fair test of the present theory. Since bulkheads were placed at the ends only, this was performed to show a limiting case that might be experienced on shipboard.

3 Two short house tests have been run to date.

(*a*) Test No. 8 without bulkheads conforms to theory extremely well.

(*b*) However, test No. 9, tested with seven bulkheads, shows an inability to meet the theoretical conditions. This very likely signifies that the house chosen was too short and stubby to avoid biaxial stress conditions and a general breakdown of double-beam theory.

The test work to date is currently being evaluated thoroughly which accounts for the sketchiness of this discussion. No conclusion can be given at this time. The author is to be congratulated on his excellent presentation.

Author's Closure

The author is very glad that the results of the tests reported by Mr. Crawford were available in time for this discussion, and give an opportunity for comparison.

When making this comparison it is necessary to keep in mind that the paper analyzes the case of uniformly distributed stiffness of the deck beams, while the tests include a number of cases having several distinct deck beams for which the theory is not applicable. In these cases the discusser has compared the test results with the theoretical ones by averaging the deck-beam stiffness over the length of the deck house, which is reasonable in some cases but not in others.

It will be noticed that in the three cases, Nos. 2, 5, and 8, where the stiffness is uniformly distributed, really good agreement is obtained.

Of the three cases giving poor agreement, Nos. 9 and 10 do not belong in the scope of the author's analysis, for reasons outlined in the discussion. It is worth stating that it is possible to obtain a theoretical result for case No. 10 from the author's basic differential equations with appropriate boundary conditions.

The large difference in case No. 3 is more serious and will require closer study. In the remaining cases the differences are not large, and are presumably due to the nonuniform distribution of deck-beam stiffness.

The New Approach to Shell Theory: Circular Cylinders[1]

E. Reissner.[2] The difficulties inherent in Professor Epstein's approach to the theory of thin shells are well brought out by the present author. Briefly, application of series in powers of the thickness co-ordinate as indicated in the paper leads to two-dimensional approximate differential equations of successively higher order as more terms in the power series are taken into account. Unless it is possible to determine rationally at the same time the nature of the boundary conditions which correspond to the order of the chosen system of differential equations, the differential equations themselves cannot well be utilized with confidence. The present paper should be welcomed for having clarified and further developed the application of series in powers of the thickness co-ordinate to the problem of the form of the differential equations of the theory of thin shells. It may be that *combination* of the variational method with the method of the present paper is what is needed for further progress in this field.

Author's Closure

A peculiar problem undoubtedly exists in that the order of the differential Equations [12] is excessively high in relation to the possible number of the boundary conditions, and this discrepancy would become worse if the approximation were pushed to higher powers of the thickness h. It is surmised that this difficulty can be entirely removed by restricting consideration to those solutions of the differential equations that vary sufficiently slowly with x and s to make valid the method of approximation used in deducing the equations. This was proved in the paper, however, only for a simple degenerate case, Equation [15].

Analogue to High-Velocity Combustion[1]

E. V. Laitone.[2] This paper is one of the few that emphasize the proper perspective in the application of the hydraulic analogy to compressible flow problems. The author understands the fact that the hydraulic analogy is not a model test or a similarity study but is strictly a device for studying the behavior or nature of a solution for certain sets of equations and boundary conditions. He also notes that the energy equation itself has no place in the analogy.

In this particular application, the author has devised an ingenious water-channel analogue which is governed by a set of equations and boundary conditions that are related to those used in describing the one-dimensional propagation of a combustion front. He then shows that this type of dynamic boundary condition leads to a double discontinuity system that must be considered in determining the stability of the system. The most interesting conclusion from observation of the water channel is that the combustion zone must move at the local velocity of sound with respect to the burned gases it leaves behind.

The writer would like to point out that the entire basis of the hydraulic analogy rests entirely on the assumption that the water motion is the same at all depths. This condition is never exactly fulfilled, because of the friction boundary layer at the channel walls and the turbulent motion in large hydraulic jumps, which explains most of the discrepancies found in the experimental values.

Generally the most deleterious effect, producing a nonuniform motion at varying depth, is the relation among the group velocity, wave velocity, and the water depth. However, this effect is not important when only one-dimensional normal hydraulic jumps are involved, as in the author's application, but

[1] By E. H. Kennard, published in the March, 1953, issue of the Journal of Applied Mechanics, Trans. ASME, vol. 75, pp. 33–40.

[2] Massachusetts Institute of Technology, Cambridge, Mass.

[1] By A. K. Oppenheim, published in the March, 1953, issue of the Journal of Applied Mechanics, Trans. ASME, vol. 75, pp. 115–121.

[2] Associate Professor of Mechanical Engineering, University of California, Berkeley, Calif.

it is very important when the two-dimensional analogy is considered. For this application a note of warning should be added for future users of the hydraulic analogy, as pointed out previously by the writer.[3] It must be remembered that the group velocity of water-wave propagation will not be constant unless the water is 1/4 in. deep. The group velocity is the actual rate of propagation of the energy of the wave and is the only analogy to the speed of sound in a gas. The group velocity is less than the so-called wave velocity which has no analogy to the speed of sound unless the water is 1/4 in. deep so the wave velocity becomes independent of wave length and equal to the group velocity. Therefore we must restrict ourselves to 1/4 in. water depths and weak hydraulic jumps in order to obtain equations that are comparable to those corresponding to a two-dimensional perfect gas flow with a specific heat ratio of 2.

Author's Closure

The author agrees with Professor Laitone's comments on the principles of the hydraulic analogy to compressible flow. The main virtue of this analogy is the fact that the behavior of the two analogous systems is governed by a similar set of nonlinear equations of motion, the nonlinearity resulting in the transition from an elliptic to a hyperbolic type. The physical implication of this property is the creation of discontinuities appearing in the form of bores in the hydraulic system and of shock waves in the compressible flow. The electrical field does not exhibit this property and consequently the electrical system cannot be used for this purpose. On the other hand, the details of the processes such as the velocity profiles, viscosities, and so on, are not the same, and in particular, the energy conditions are quite different. Hence the analogy can only yield information on the "behavior or nature of the solution," as Professor Laitone rightly pointed out, and any attempts to utilize it as a basis for an analog computer, similarly as it is usually done with electrical analogies, are deemed to be futile.

An Electrical Method for Determining Journal-Bearing Characteristics[1]

A. A. Raimondi.[2] By suitable transformations, the author has succeeded for the case of journal bearings in reducing Reynolds equation to the form[3]

$$\frac{\partial^2 u}{\partial \xi^2} + \left(\frac{m}{n}\frac{B}{L}\right)^2 \frac{\partial^2 u}{\partial \zeta^2} - f(\xi)u + g(\xi) = 0 \ldots\ldots [1]$$

The partial derivatives in Equation [1] can be approximated by finite-difference equations with the result that it becomes

$$(u_1 + u_2 - 2u_0) + \left(\frac{m}{n}\frac{B}{L}\right)^2 (u_3 + u_4 - 2u_0) - f(\xi_0)u_0 + g(\xi_0) = 0 \ldots\ldots [2]$$

which can now be solved for u by applying Southwell's[4] "relaxation" method. However, the author has substituted for the manual relaxation process an electrical method which is analogous to applying the relaxation technique automatically and instantaneously at every node on the bearing surface. The question arises as to the accuracy of the solutions obtained using this electrical method. The author answers this question for the case of a journal bearing of infinite length. However, it is desirable to know what results this method would give when applied to bearings of finite length.

In order to obtain such results and to determine what difficulties, if any, would be encountered in applying this resistance-network method to the more difficult finite-bearing problems, the apparatus, shown in Fig. 1 of this discussion, was built. With this device it is possible to obtain the pressure distributions for bearings having an L/B ratio equal to 1 (L = length perpendicular to direction of motion, B = length in direction of motion). As precision resistors were not available, plain 1/2-watt carbon-type resistors were used throughout the apparatus. The commercial tolerance of the network resistors (located in Fig. 1 approximately on the center of the board between the two banks of switches and rheostats) was given as ±5 per cent. However, measurement of the individual resistors showed that they did not deviate more than 2 per cent from each other. This deviation was not considered serious for Liebman[5] has shown that because of the averaging properties of resistance networks it is possible to obtain solutions ranging in accuracy from one part in 10^3 to one part in 10^4 (depending upon the geometry and scale of the network) when precision resistors accurate to ±1 per cent were used.

In the tests conducted it was thought desirable to obtain values of the pressure at ten different points along the bearing surface in the direction of motion and at ten different points across the bearing surface, perpendicular to the direction of motion. However, advantage was taken of the symmetry of the pressure distributions which necessitated the determination of the pressures at only five different points across the bearing surface and thus reduced the size of the required network by a factor of 2. Hence the network, rectangular in shape, was made of $10 \times 5 = 50$ resistors and consisted of $11 \times 6 = 66$ nodes. An average value of R_1 (i.e., the resistors which lie along the center line of the bearing) was 1020 ohms; R_2 (all other resistors in network) averaged 515 ohms. These values were made very low in comparison to the resistances used for regulating the input currents I_0, for the reason set forth by the author. The bank of switches and rheostats shown at the left in Fig. 1 were used to regulate the input currents I_0, while the bank of switches and rheostats at the right were used to set the leak resistances r_L, to their proper values. A precision-type potentiometer and a sensitive galvanometer were used for accurately setting the input currents, leak resistors, and for measuring the node voltages.

Early in the tests it was discovered that when a 135-volt B-battery was used for supplying the input currents it was not possible to check the node-voltage readings any closer than 4 per cent in some cases, depending upon the amount of time the battery was delivering current. A more satisfactory stable voltage supply was obtained by using the circuit shown in Fig. 2, herewith. With this arrangement it was possible to repeat node-voltage readings to better than 0.5 per cent accuracy.

The first pressure distribution obtained with this apparatus was that of a 120-deg journal bearing with Type I boundary condition having an $\epsilon = 0.2$, $\theta_A = 67.4$ deg, and $L/B = 1$. In this problem it was required to simulate four negative leak resistors near the entering edge of the bearing along a line of nodes perpendicular to the direction of motion. This condition was handled with little difficulty by the method given by the

[3] "A Study of Transonic Gas Dynamics by the Hydraulic Analogy," by E. V. Laitone, *Journal of the Aeronautical Sciences*, vol. 19, April, 1952, pp. 265–272.

[1] By D. S. Carter, published in the March, 1952, issue of the Journal of Applied Mechanics, Trans. ASME, vol. 74, pp. 114–118.

[2] Research Engineer, Mechanics Department, Westinghouse Electric Corporation, East Pittsburgh, Pa. Jun. ASME.

[3] The nomenclature used in this discussion is the same as that used in the paper.

[4] "Relaxation Methods in Engineering Science," by R. V. Southwell, Clarendon Press, Oxford, England, 1940.

[5] "Solution of Partial Differential Equations With a Resistance Network Analogue," by G. Liebman, *British Journal of Applied Physics*, vol. 1, 1950, pp. 92–103.

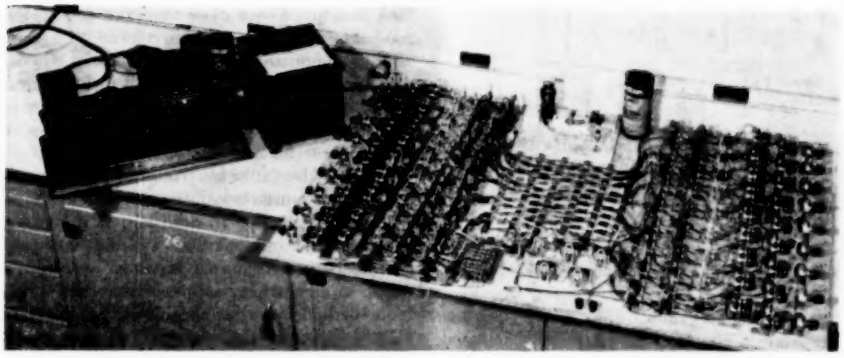

FIG. 1 RESISTANCE-NETWORK APPARATUS

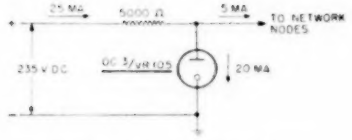

FIG. 2 VOLTAGE-SUPPLY CIRCUIT

author. Needs[6] also had obtained the pressure distribution for this same bearing by using the electrolytic-tank method developed by Kingsbury.[7] Thus it was possible to compare the pressure distributions obtained by two different experimental methods. Fig. 3 of this discussion shows this comparison, the circles being the test results and the full curves graphical interpolations from the data of Needs. It is evident that the two methods give pressure values which agree quite closely.

The load-carrying capacity of this bearing was obtained using graphical integration methods and was found to be

$$W = 0.316 \frac{\mu U R^2 L}{C^2}, \text{ (resistance network)}$$

If this is compared to the load given by Needs for the same bearing

$$W = 0.319 \frac{\mu U R^2 L}{C^2}, \text{ (Needs)}$$

it will be seen that the two values agree within 1 per cent.

The resistance-network method is not restricted to journal bearings but is equally applicable to slider bearings and, indeed, bearings having odd film shapes resulting from distortion, misalignment, and so on. In order to set up these problems on the resistance network, it is necessary to introduce the proper equation for the film shape into the general equations developed by the author. For example, for a slider bearing, the film thickness at any point, x, along the bearing is expressed by

$$h = h_2 \left[a - \frac{x}{B} (a - 1) \right] \quad [3][8]$$

where

$$a = h_1/h_2 \quad [3a]$$

[6] "Effects of Side Leakage in 120-Degree Centrally Supported Journal Bearings," by S. J. Needs, Trans. ASME, vol. 56, 1934, pp. 721–732.

[7] "On Problems in the Theory of Fluid Film Lubrication, With an Experimental Method of Solution," by A. Kingsbury, Trans. ASME, vol. 53, 1931, pp. 59–75.

[8] See Fig. 4 for illustration.

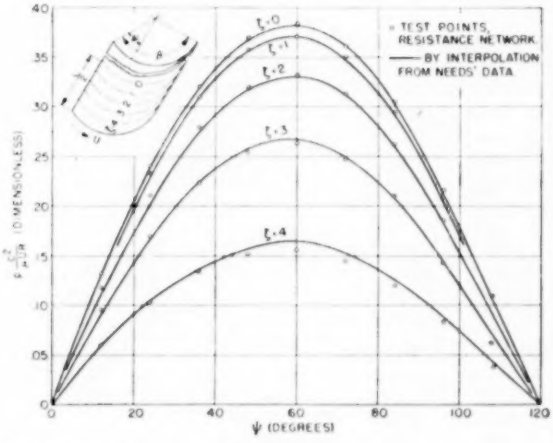

FIG. 3 COMPARISON OF PRESSURE-DISTRIBUTION METHODS BY THE AUTHOR AND BY NEEDS

Then

$$h' = \frac{\partial h}{\partial \xi} = \frac{\partial h}{\partial x} \frac{\partial x}{\partial \xi} = -\frac{h_2}{n} (a - 1) \quad [4a]$$

and since

$$H = h^{3/2} = h_2^{3/2} \left[a - \frac{x}{B} (a - 1) \right]^{3/2} \quad [4b]$$

then

$$H'' = \frac{3}{4} \frac{h_2^{3/2}}{n^2} (a - 1)^2 \left[a - \frac{x}{B} (a - 1) \right]^{-1/2} \quad [4c]$$

Substituting the foregoing into the author's Equation [5], dividing by $Bh_2^{-1/2}$ and setting q proportional to the new function u

$$q = Bh_2^{-1/2} u \quad [5]$$

the following equation is obtained

$$\frac{\partial^2 u}{\partial \xi^2} + \left(\frac{m}{n} \frac{B}{L} \right)^2 \frac{\partial^2 u}{\partial \zeta^2} - f(\xi) u + g(\xi) = 0 \quad [6]$$

which although it is identical to the author's Equation [9] is different in that the functions $f(\xi)$, $g(\xi)$ now have the form

$$f(\xi) = \frac{3}{4}\frac{(a-1)^2}{a^2}\left[a - \frac{x}{B}(a-1)\right]^{-2} \quad \ldots\ldots [7a]$$

$$g(\xi) = \frac{(a-1)}{a^2}\left[a - \frac{x}{B}(a-1)\right]^{-5/2} \quad \ldots\ldots [7b]$$

Substituting Equations [3] and [5] of this discussion into Equation [2] of the author, and solving for p yields

$$p = \frac{6\mu UB}{h_2^2}\left[a - \frac{x}{B}(a-1)\right]^{-5/2} u \quad \ldots\ldots [8]$$

which is the equation for the pressure at any point on the bearing surface.

Having obtained the functions $f(\xi)$ and $g(\xi)$ for a slider bearing, the leak resistances and input currents may be calculated through use of Equations [21*a*, *b*] given by the author and readily adjusted to their proper values in the apparatus shown in Fig. 1, herewith. The node voltages then may be measured and converted to pressure values through use of the author's Equation [22] and Equation [8] of this discussion.

The foregoing procedure was followed for a slider bearing having a ratio of entrance to exit film thickness equal to 2, (i.e., $h_1/h_2 = 2$) and $L/B = 1$. This particular bearing was chosen in order to compare the test data with the data calculated by Michell[9] for the same bearing. Pressure values obtained using the electrical network method are shown plotted as circles in Fig. 4, herewith. These values may be compared with those

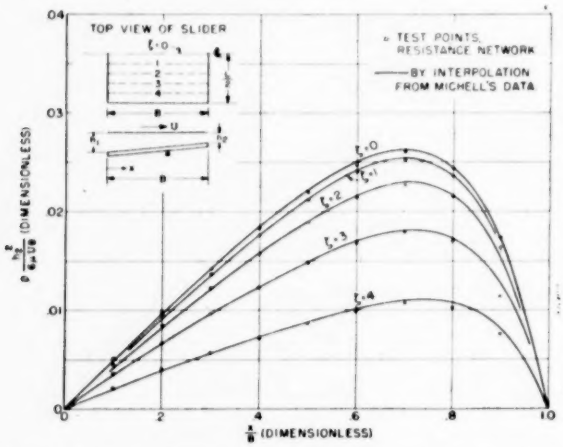

FIG. 4 PRESSURE VALUES OBTAINED BY ELECTRICAL NETWORK METHOD AND BY CALCULATION

given by the full curves which were obtained by graphical interpolation from the results of Michell's calculations. In general, the agreement is quite good.

The respective load-carrying capacities, obtained by employing graphical integration methods on the curves and circles in Fig. 4 yield the following equations

$$W = 0.06895\,\frac{\mu UB^2L}{h_2^2}, \text{ (Michell)}$$

$$W = 0.06871\,\frac{\mu UB^2L}{h_2^2}, \text{ (resistance network)}$$

which agree within 1 per cent. Kingsbury,[7] using his electrolytic-tank analogy, also worked this same problem and obtained very good agreement with Michell.

Thus there are two experimental methods for determining bearing characteristics which will yield solutions in satisfactory agreement with analytical methods. The resistance-network method has the advantage that it is less tedious than the electrolytic-tank method in that the number of voltage readings which must be extracted from the respective apparatus in order to plot a pressure distribution is much less in the former than in the latter method. In addition, it may be possible that the resistance-network method will be applicable for obtaining characteristics of journal bearings operating in the important region of eccentricity ratios greater than 0.8. The electrolytic-tank method is not applicable in this region owing to the difficulty of wetting the model representing the film shape and the fact that the minimum bath depth becomes very small.

[9] "The Lubrication of Plane Surfaces," by A. G. M. Michell, *Zeitschrift für Mathematik und Physik*, vol. 52, 1905, pp. 123–137.

On Asymmetric Flow in an Axial-Flow Compressor Stage[1]

W. D. RANNIE.[2] The unsteady flow that arises in the stalled region of operation of turbomachines has been observed and has become of interest comparatively recently. Perhaps a description of typical behavior of compressor flow in the stalled region is the best way of indicating the difficulties of providing an adequate theory. Hot-wire measurements have been made by one of the writer's students on an axial-flow compressor project supported by the Office of Naval Research at the California Institute of Technology. The compressor blading was designed for vortex flow with prerotation in the direction of the wheel speed and a design axial velocity of 45 per cent of the tip speed. The hub ratio was 0.6 and the blade solidity averaged about unity for rotor and stator with nearly constant chord for the rotor. There were three complete stages with 30 blades in the rotor and 32 in the stator.

On throttling the flow rate below design value a narrow region of low velocity (i.e., stall) extending over the inner half of the blades was observed to rotate in space in the direction of the rotor with 37 per cent of the rotor speed. There is one such region circumferentially. As the flow rate is decreased this region broadens, then breaks up into two regions eventually 180 deg apart. Further throttling causes a splitting into three regions eventually 120 deg apart. The multiple stalled regions traveled at the same speed as the single region and did not extend beyond mid-radius. All of these patterns were observed within a rather narrow band of flow rates and their appearances and disappearances occurred at slightly different flow rates depending on whether the throttle was opened or closed.

At flow rates smaller than the foregoing a single stalled region appeared, but this one involved the entire blade height. It rotated with a speed of 26 per cent of the rotor speed, again in the same direction. This pattern appeared to persist down to completely closed throttle although the hot-wire response became very irregular near shutoff. All of the patterns observed occurred throughout the length of the compressor behind the entrance vanes. The stator blades were certainly involved in the flow but whether this is the cause or the effect is not yet definitely known.

The writer believes that the author's theory is the first important contribution to an analysis of stalling phenomena. There are several obvious limitations to his simplified model; it cannot

[1] By W. R. Sears, published in the March, 1953, issue of the JOURNAL OF APPLIED MECHANICS, Trans. ASME, vol. 75, pp. 57–62.

[2] Professor of Mechanical Engineering, California Institute of Technology, Pasadena, Calif.

describe multiple stall and it involves only one blade row. Nevertheless, it represents a start at an extremely complex problem.

F. E. Marble.[3] It is a privilege to be able to congratulate the author upon his penetrating and simple analysis of a problem which is of vital importance to turbomachine technology through its relation to the problem of "rotating stall," experimental observations of which have been discussed by Professor Rannie. The interest in the phenomenon arises not only because it may lead to some understanding of the onset of stall, but also because of its association with mechanical blade failure. The author's work seems to be the first in which the mechanism is stated clearly and its relation shown to the fluid mechanics of turbomachines. Prof. H. S. Tsien and the writer were led, after recalling the same suggestion of Dr. von Kármán from 13 years ago, to the identical mechanism and a very similar model.

The author treats a single blade row which may be either stationary or rotating. However, as has been pointed out by Professor Rannie, it is usual that the entire machine exhibit a rotating stall pattern which is similar for all blade rows, stationary or rotating. Consequently, although the propagation mechanism is as the author indicates, there is certainly an important influence associated with the fact that the stall propagates at the same absolute rate in adjacent rotors and stators. It is possible that the observed stall propagation is more nearly described by an analysis which treats two adjacent blade rows in relative rotation.

Finally, there is the interesting problem of the manner in which the turbomachine approaches the condition of asymmetric flow. According to the analysis of Tsien and the present writer, there exist the alternate theoretical possibilities of symmetric and asymmetric flow. At very low angles of attack the amplitude of the asymmetric flow is excessively large and the mean pressure rise in the blade row is small or possibly negative. Therefore it is extremely unlikely that the asymmetric flow would be observed. As the angle of attack is increased, the amplitude of the asymmetry becomes smaller and the mean pressure rise, under asymmetric flow conditions, increases. Thus it seems possible to observe a propagating stall under these conditions; the question is the manner of transition from one to the other. The experimental observations are made by holding the constant (or nearly constant) rotation speed and adjusting an external throttling device. Therefore, when deciding whether asymmetric flow may occur, the symmetric and asymmetric flows, and associated pressure rises, which correspond to the same external throttling conditions and same rotative speed must be compared.

J. M. Stephenson.[4] In most high pressure-ratio axial-flow compressors the first stage passes through stall at quite high compressor speeds, so one of the most important problems in design is to insure that this stalling is not violent. The writer does not believe that the problem can be tackled usefully by considering different shapes of the force-incidence curve of cascade blades; for there is no evidence that this curve can be altered at will by redesign of cascade geometry. Except for sections with surface inflection, or with slots and flaps, all the practical shapes have similar lift curves.

It is possible, however, to change the violence of the stall by another method. Usually, the blade sections at different radii are set to give the maximum efficiency at the same flow. This implies that, as the flow is reduced, the outer radius stalls first

[3] Assistant Professor, Daniel and Florence Guggenheim Jet Propulsion Center, California Institute of Technology, Pasadena, Calif.

[4] Research Associate, Division of Engineering, Brown University, Providence, R. I.

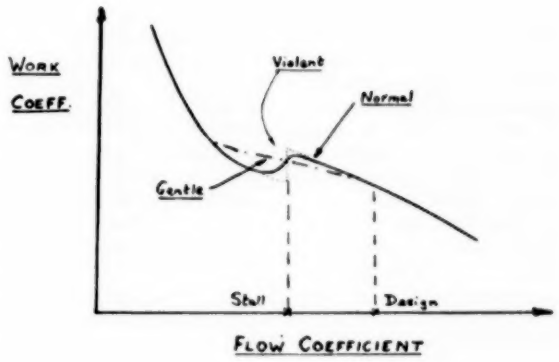

Fig. 1

(at least if the blades are designed with constant circulation). By altering the settings of sections other than at the mean radius, and thus altering the flows at which they stall, single-stage work characteristics can be obtained with normal, more violent, or gentle transition to surge, as shown in Fig. 1, herewith.

Influence Coefficients of Tapered Cantilever Beams Computed on SEAC[1]

F. S. Shaw.[2] In relation to the application of digital computers for obtaining numerical solutions of problems by using specific numerical procedures, the question is often asked whether or not the relaxation technique can be carried over and handled directly by such high-speed machines. The writer believes that while it is very likely possible for an electronic digital computer to be so instructed that it could perform the routine implied by the relaxation technique, it would be an unnecessary refinement to attempt to do so.

An important part of the relaxation process is the judgment and experience built up over a period of time by the relaxer, and it is just these attributes which enable the relaxer to speed up his computation. A considerable amount of art or, if it is preferred, low cunning is involved. Such devices as over-relaxation, use of block operators, and the like are the stock-in-hand of the successful relaxer, and, where the relaxer is doing his task by hand, such tricks are essential if he is to accomplish his task in finite time.

Use of the devices just mentioned are not essential for the success of the relaxation method, but are related solely to the time that will be involved in obtaining a solution.

In addition, the relaxer is usually called on to solve but one problem of its kind at a time. To ask a machine to solve but one problem of a particular class would be a waste of its value.

Since the high-speed electronic digital computer carries out each operation so fantastically quickly, such short-cut time-saving devices as those just mentioned are not necessary, or even desirable for such a machine. It would be much better to obtain a solution by having the machine perform a relatively simple operation many times over, rather than ask it to use selective judgment and apply special tricks whenever they could be applied. With-

[1] By Samuel Levy, published in the March, 1953, issue of the Journal of Applied Mechanics, Trans. ASME, vol. 75, pp. 131–133.

[2] Associate Professor, Polytechnic Institute of Brooklyn, Department of Aeronautical Engineering and Applied Mechanics, Brooklyn, N. Y.

out the use of special tricks, the machine will still solve the problem with sufficient rapidity as to give rise to no complaints.

A good example of this can be found in solving Laplace's or Poisson's equation. For this differential equation at least two excellent techniques exist: (1) the relaxation procedure, (2) the Liebmann process. In the hands of a suitably skilled computer the former method can be used to obtain answers quite rapidly; on the other hand, the latter method goes much more slowly. However, the Liebmann process is an extremely simple one, and consists essentially of one simple operation endlessly repeated. To my mind the Liebmann process is the one an electronic digital computer should be coded to use.

In a word, the writer does not believe that electronic digital computers should be asked to apply the relaxation technique as it is understood by the relaxer.

C. C. Wan.[3] The application of high-speed computing devices to engineering problems is fairly recent. Therefore the author's presentation of the calculation of influence coefficients on SEAC is a timely contribution to the techniques available for applied sciences. The primary advantage of the high-speed computing device and its immediate effect on applied problems may fall in one of two broad categories:

It makes possible reduction of complicated problems into a series of simple problems, which may be solved readily by precoded machine processes. Inasmuch as the speed of computation will be high, the solution of the entire problem may be obtained in a small fraction of time and cost when compared with the more familiar manual computing processes.

Problems that heretofore were too unwieldy for rigorous mathematical solutions may be treated by suitable iteration process. This point is significant in applied sciences, since the number of restrictive assumptions usually introduced to facilitate rigorous mathematical treatment may be reduced. Furthermore, the fatigue characteristic of high-speed computing machines are considerably better than that of human calculators.

Author's Closure

The author wishes to thank the discussers for presenting additional information regarding the fields of most useful application of high-speed electronic digital computers. As Professor Shaw points out, relaxation may well be one type of computation for which the machines are not best suited. Dr. Wan indicates the saving in time and cost that is possible if the more complicated problems encountered in engineering are reduced to a series of simple problems for which the machine codes are available; this use of the electronic computer in some of our work has been found very effective. As he points out, a broad field of applied problems can now be solved which were previously too unwieldy or long to consider. The author believes that high-speed electronic digital computers such as SEAC are not a panacea, but should be used primarily in their field of greatest efficiency, that is, where long, repetitive, and tedious computations must be carried out.

Stresses in Curved Beams—A Tabular Method of Solution Based on Winkler's Theory[1]

W. E. Black.[2] The method presented in the paper should be of considerable interest to engineers in the design of curved members, particularly because of its speed and simplicity. This method, however, does not escape one of the chief difficulties associated with the analysis of curved members, namely, the evaluation of the integral

$$\int \frac{y}{R_0 + y}\, dA$$

or its equivalent. If evaluation of this integral is attempted by numerical summation, as the author has done, approximately the same number of positive and negative terms are obtained, and the summation reduces to the difference between two quantities of nearly the same magnitude. Thus accuracy suffers, and it generally will be found necessary to maintain a high degree of accuracy (four or five significant figures) in the initial computations and to use a large number of strips in order to insure a reasonable degree of accuracy in the final result.

Some of this difficulty may be avoided by the use of an alternative form[3] of the integral referred to in the preceding paragraph. The Winkler equation for stress may be written in the following form

$$S_y = \frac{M}{AR_0}\left(1 + \frac{1}{Z}\frac{y}{R_0 + y}\right)$$

in which Z is a property of the cross-sectional area and may be expressed in either of two forms, as follows

$$Z = -\frac{1}{A}\int \frac{y}{R_0 + y}\, dA = \frac{1}{AR_0}\int \frac{y^2}{R_0 + y}\, dA$$

Use of the first form for the Z-function results in a solution almost identical to that advanced by the author, and subject to the same difficulties with respect to accuracy. If, however, the alternative form

$$Z = \frac{1}{AR_0}\int \frac{y^2}{R_0 + y}\, dA$$

is used, the summation involves positive quantities only, and results obtained by this method have been found to be consistently more reliable than by other methods. Using this method, a lesser degree of initial accuracy is required, and fewer strips are needed in the analysis of irregular sections such as the crane-hook section. Slide-rule accuracy generally is satisfactory for all of the computations.

The paper also states that the proposed method "is applicable to all shapes of cross section." In this connection it should be pointed out that serious errors may result from the application of the Winkler theory, using the author's method or any other, to curved members with I-shaped, T-shaped, tubular, or other similar types of cross sections. It has been well established by Bleich[4] and by Anderson[5] that the cross sections of curved members of this type tend to distort under load, resulting in greater stresses and displacements than those predicted by the Winkler theory. Such shapes are used extensively for curved members in punch-press frames, trailer goosenecks, airframes, and the like, so that the problem is of some importance. Unfortunately, this limitation of the Winkler theory frequently has been disregarded

[2] Project Engineer, Chance Vought Aircraft, Dallas, Tex.

[1] By W. Wright, published in the March, 1953, issue of the Journal of Applied Mechanics, Trans. ASME, vol. 75, pp. 138–139.

[3] Associate Professor of Theoretical and Applied Mechanics, College of Engineering, University of Illinois, Urbana, Ill.

[3] "Advanced Mechanics of Materials," by F. B. Seely and J. O. Smith, John Wiley and Sons, Inc., New York, N. Y., 1952, pp. 669–672.

[4] "Die Spannungsverteilung in den Gurtungen gekrümmter Stabe mit T- und I-formigen Querschnitt," by H. Bleich, *Beilage zur Zeitschrift, Die Bautechnik*, vol. 6, January 6, 1933, pp. 3–6.

[5] "Flexural Stresses in Curved Beams of I- and Box Sections," by C. G. Anderson, Proceedings of The Institution of Mechanical Engineers, vol. 163, 1950, pp. 295–306.

in the literature, and it behooved the writer to call attention to it here, even though the scope of the original paper obviously was not intended to encompass this phase of the problem.

Author's Closure

The author wishes to thank Dr. Black for his most interesting and welcome comments, particularly with regard to the use of the alternative form of integral involving y^2.

A solution can be found by the tabular method based on the alternative form of integral quite simply if the moment is completed directly by numerical summation instead of indirectly from the load W. In other words we compute the value of $\int S_y y dA(M)$ instead of $\int S_y dA(W)$.

The slight increase in labor necessitated by this procedure would be a small price to pay for the gain in accuracy to be expected.

The author wishes to thank Dr. Black for calling attention to the fact that Winkler's theory is strictly applicable only to cross sections which do not distort under load.

Turbulent Mixing of Two Parallel Streams[1]

W. R. Sears.[2] The writer wishes to disagree with certain statements of the introduction to this paper. The transformation to the independent variable used by Tollmien and by Kuethe does not involve any "loss of generality" and is not "restrictive." Rather, the similarity of profiles and the straight boundary lines are "exact" consequences of the equations of motion for the particular problems studied by these authors.

To be sure, the present authors may feel that the classical mixing problems of Tollmien, Kuethe, and Görtler are academic, since initial boundary layers are ignored. Nevertheless, as we know, their solutions have proved extremely useful for many years, their accuracy in relation to real physical setups depending (among other things) upon the size of the boundary layers present, relative to other dimensions. Rather than being in error, as the authors' remarks suggest, they are correct solutions for the idealized case without boundary layers.

When initial boundary layers are considered, the similarity disappears and the boundaries become curved, as is well known. The authors should not say, as they do, that the linear variation of width is "not necessary," but rather that it is not possible in this case. The authors' present attack on this much more difficult problem is a valuable one. But it is to be noted that they have not in fact solved the problem analogous to Tollmien's, but a much simpler one—at least in the present paper.

Authors' Closure

The authors appreciate Dr. W. R. Sears' discussion of their paper, the more so since it brought out the fact that misunderstandings of some of their statements might occur in spite of the care they have taken in discussing previous work.

Nowhere has it been stated or even implied that Tollmien's and Kuethe's work, or Görtler's work was in error, as Dr. Sears suggests. The authors are fully aware of the excellent work done by Tollmien and in particular by Kuethe, and also by Görtler. Also, there has been no doubt that their results are exact consequences of the equations of motion under the restrictive assumptions of no boundary layers along the separating plate and the a priori prescribed straight-line boundaries of the mixing zone. However, no physical case of mixing of streams exists without developed boundary layers along the plate separating the streams before mixing starts (unless these boundary layers are sucked away which is a special case and which has not been considered either by the previous workers or by the present authors). Neither are the boundaries of the mixing zone straight lines in any physical case. That analyses without consideration of the boundary layers give reasonable approximate results in special cases of mixing is also well known to the present authors, but this does not detract from the restricted applicability of previous work.

The authors' statement that it is not necessary to assume (and not simply "not necessary" as Dr. Sears has quoted) straight boundaries if a sufficient number of equations are used is still valid. Previous analyses had to assume the shape of the boundaries because it was not possible to determine two variables (the shape of the boundaries of the mixing zone and the velocity distribution in it) from one equation. Naturally it is not "possible" to obtain straight-line boundaries in any analysis, if the correct physical case is considered, as has been done in the paper discussed.

The authors fail to understand the last sentence of Dr. Sears' discussion: "But it is to be noted that they (the present authors) have not in fact solved the problem analogous to Tollmien's, but a much simpler one—at least in the present paper." In his previous sentence, Dr. Sears implies that the problem of accounting for the upstream boundary layers is much more difficult than the analysis of mixing without the influence of boundary layers. Also, the authors have solved the case for $m = 1$ (the ratio of the velocities of the two streams, U_1 and U_2, is denoted by $m = U_2/U_1$) and Tollmien solved the case for $m = 0$. No claim has been made by the authors to have solved a problem analogous to Tollmien's. In subsequent work by the senior author and some of his co-workers, Tollmien's problem ($m = 0$) has been solved as a special case. This work will be published at a future date. It is shown there that Tollmien's case is just as "simple" to solve as the case presented in the discussed paper.

On Turbulent Flow Between Parallel Plates[1]

A. M. Kuethe.[2] The paper represents an important advance in the theory of turbulent shear flows. The accurate representation of both the complete velocity distribution and the distribution of turbulent shearing stress by a straightforward application of the Reynolds equations is a real feat, even though the solution does involve two empirical factors. It is noteworthy that one of these factors has a definite physical interpretation.

The representation of the mean velocity profile by Equation [45] of the paper merits some discussion. One has only a limited number of boundary conditions to which definite values can be assigned and it is not feasible to determine more than two parameters empirically.

These are the limiting features of the problem and the author has made a fortunate choice of the form of the solution, but the writer cannot justify his statement ". . . . the power series can contain only three terms . . . ." on any basis except that the results agree with experiment.

[1] By T. P. Torda, W. O. Ackermann, and H. R. Burnett, published in the March, 1953, issue of the Journal of Applied Mechanics, Trans. ASME, vol. 75, pp. 63–71.

[2] Director, Graduate School of Aeronautical Engineering, College of Engineering, Cornell University, Ithaca, N. Y.

[1] By S. I. Pai, published in the March, 1953, issue of the Journal of Applied Mechanics, Trans. ASME, vol. 75, pp. 109–114.

[2] University of Michigan, Aeronautical Engineering Department, Ann Arbor, Mich.

WILLIAM SQUIRE.[3] The velocity distribution for turbulent flow obtained by the author can be derived very simply without any appeal to Reynolds equations.

We have three boundary conditions which are independent of Reynolds equations

$$V = \frac{U_m}{U^*} \quad \text{at} \quad \eta = 0 \qquad [1]$$

$$V = 0 \qquad \text{at} \quad \eta = 1 \qquad [2]$$

$$\frac{dV}{d\eta} = -R^* \quad \text{at} \quad \eta = 1 \qquad [3]$$

The symmetry argument is a simple way of taking the boundary conditions at $\eta = -1$ into account.

Using these boundary conditions enables three constants to be determined. For example

$$V = \frac{U_m}{U^*} [1 + (S - 1)\eta^2 + (1 - S)\eta^4]$$

can be obtained. The author seeks to improve this by using an additional constant determined empirically and selects the exponent of the last term. However, he then obtains a value for the exponent (Equation [50] of the paper) which contradicts his assumption that it is an even integer and has not shown that the result obtained is superior to simply adding a fourth term to the power series. The assertion under Equation [45] that the series can have only three terms does not seem correct.

Until the shear stress is defined in terms of the flow variables Reynolds equation gives very little information. A function may satisfy Reynolds equations, the boundary conditions, and reduce to the laminar-flow solution and still be a very poor velocity distribution. An example is

$$V = \frac{U_m}{U^*}\left(1 - \frac{\alpha}{1 - 2\alpha} + \frac{\alpha}{1 - 2\alpha}\cos \pi\eta\right)$$

$$\alpha = \frac{1}{2}\frac{S - 1}{S}$$

$$\tau = \frac{\pi\alpha}{2}\sin \pi\eta$$

The derivation of the logarithmic velocity distribution seems basically similar to that given by von Mises[4] who used the von Kármán similarity law

$$\frac{U_m - U}{U^*} = f(\eta)$$

instead of the Stanton law which is an obvious consequence, and obtained the drag law as well as the velocity distribution.

AUTHOR'S CLOSURE

Professor Kuethe and Mr. Squire's objection to Equation [45] of the author's paper is based on the uniqueness of the solution of the Reynolds equations. However, there is no *unique* solution for Reynolds equations if only the boundary conditions are considered since from experiments it is known that the velocity profiles change with Reynolds number for given boundary conditions. What was done was to find one parameter family of profiles which would closely represent the true velocity distributions for various Reynolds number and shear stress parameter S as obtained from experiments. In order to find such solution, the author started with the power series and found that three terms are enough to satisfy the boundary conditions. Since the profile should tend to be the laminar one as $S = 1$, the profile as given in the paper, was chosen. The third term may be *any one* of those terms in the power series as $n \geq 2$, depending on the parameter Reynolds number. Experimental results were checked and the agreement found quite satisfactory. It is believed that one might improve the solution by finding some complicated function depending on Reynolds number, but as yet no such solution has been found which is better than that given in the paper.

[3] Kenmore, N. Y.

[4] "Some Remarks on the Laws of Turbulent Motion in Tubes," by R. von Mises, Th. von Kármán Anniversary Volume, California Institute of Technology, Pasadena, Calif.

Some Problems of Orthotropic Plane Stress[1]

A. E. GREEN.[2] Equations used by the author are not the most general equations for an orthotropic plate, and, although they may be approximately correct for some materials, they cannot be used, for example, for highly orthotropic materials such as spruce wood.

Most of the problems considered by the author have been solved by the writer[3] for a general orthotropic plate, and some numerical results were given for spruce. Problems of stress distributions in a semi-infinite body, however, can be solved best by complex variable methods.[4] More powerful techniques due to Muschelisvili also can be used for these problems and for the more difficult mixed-boundary value problems associated with a half plane.

AUTHOR'S CLOSURE

The author greatly regrets that the extensive researches of Professor Green did not come to his attention until after the publication of his papers. Some duplication occurred as a consequence of this, and the author would like to express his apologies.

As Professor Green has stated, a more general expression for the differential equation is

$$\left(\frac{\partial^2}{\partial x^2} + k_1^2\frac{\partial^2}{\partial y^2}\right)\left(\frac{\partial^2}{\partial x^2} + k_2^2\frac{\partial^2}{\partial y^2}\right)\phi = 0$$

but the method of the papers may still be applied to the solution, of this equation. It is interesting to estimate the degree of approximation involved by writing k_2^2 equal to unity in one cases and this is conveniently done by means of an example discussed in one of Professor Green's papers.[5]

In this paper, the case of a circular hole of radius a in an infinite orthotropic plate is treated, the periphery of the hole being subjected to uniform radial pressure p. Calculations and plots of the circumferential stress around the hole are given for both oak

[1] By H. D. Conway, published in the March, 1953, issue of the JOURNAL OF APPLIED MECHANICS, Trans. ASME, vol. 75, pp. 72–76. Discussion applies also to the paper "The Stress Distributions Induced by Concentrated Loads Acting in Isotropic and Orthotropic Half Planes," ibid., pp. 82–86.

[2] Department of Mathematics, King's College, Newcastle upon Tyne 2, England.

[3] "Stress Systems in Aeolotropic Plates," by A. E. Green and G. I. Taylor, Proceedings of the Royal Society of London, England, vol. 173, part 1, 1939, pp. 162–172; ibid., by A. E. Green, part 2, pp. 173–192.

[4] "A Note on Certain Stress Distribution in Isotropic and Aeolotropic Materials," by A. E. Green, Proceedings of the Cambridge Philosophical Society, Cambridge, England, vol. 41, 1945, pp. 224–231.

[5] "Stress Systems in Aeolotropic Plates—IV," by A. E. Green, Proceedings of the Royal Society, London, England, series A, vol. 180, 1942, p. 173.

and spruce plates. If the plate is isotropic, the appropriate stress function is

$$\phi = -pa^2 \log r$$

and this is seen to be harmonic as well as biharmonic. Thus, if it is a good assumption to write $k_2^2 = 1$ in the above differential equation, the stresses in the isotropic case will be very nearly the same as those in the orthotropic, and this is seen to be true for the quite highly orthotropic oak which has a moduli ratio of nearly 6. However, the comparison is poor for the very highly orthotropic spruce with moduli ratio of about 26.

From the author's point of view, the most interesting result of the investigations was that the pressure distribution under a rigid punch applied to a half plane is the same whether the latter is isotropic or orthotropic. It should be mentioned that this is also true if the more general differential equation is used.

Brief Notes*

On the recommendations of the Executive Committee of the ASME Applied Mechanics Division, it has been decided to initiate a section devoted to brief notes on technical matters in mechanics. These notes must not be longer than 750 words (about 2½ double-spaced typewritten pages, including figures) and will be subject to the usual review procedure prior to publication. After approval such notes will be published in the next issue of the Journal. The notes should be submitted to the Secretary of the ASME Applied Mechanics Division.

A Strain-Energy Expression for Thin Cylindrical Shells[1]

By H. H. BLEICH[2] AND F. DIMAGGIO,[3] NEW YORK, N. Y.

Nomenclature

The following nomenclature is used in the paper:
Co-ordinates: r, z, θ, (see Fig. 1)

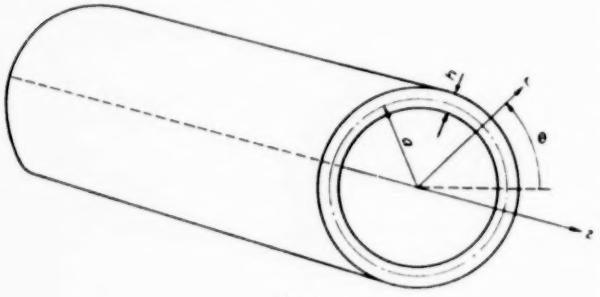

Fig. 1

a = mean radius of shell
h = shell thickness
u = longitudinal displacement (positive in direction of z-axis)
v = tangential displacement (positive in direction of positive θ)
w = radial displacement (positive inward)
$u_z, u_\theta \ldots, w_{zz}, \ldots$ derivatives of u, v, w with respect to subscripts
E, ν = Young's modulus, Poisson's ratio
ϵ_z, ϵ_θ, $\gamma_{z\theta}$ = strains in shell

DIFFERENTIAL equations for the determination of the displacements of thin shells, and an expression for the strain energy in terms of the displacements were first derived by Love (1).[4] However, Love already realized and stated that his expression for the strain energy was not sufficiently accurate, and only applicable if the bending part of the strain energy was small compared with the membrane-stress part. That there is a discrepancy between the differential equations and the strain-energy expression becomes evident if an extremum principle is used to derive a set of differential equations for the displacements which are then found to differ from the differential equations derived directly.

Subsequently, further objections were raised even against the differential equations, the principal one being that these equations lack certain symmetries. These objections are discussed in detail in recent papers by Osgood and Joseph (2), Langhaar (3), and Vlasov (4).

Approaching the problem on a higher level, Vlasov's paper starts with the general equations of elasticity and derives a new set of differential equations for thin shells of any shape. He gives also a simplified set for cylindrical shells, showing the necessary symmetries. It is interesting to note that Vlasov's equations agree with the differential equations for cylindrical shells derived in a direct and fairly elementary manner by Flügge (5). It appears, therefore, that Flügge's approach is sufficient to treat the case of cylindrical shells.

For many engineering applications it would be advantageous to know the strain-energy expression, which was not derived by Flügge or Vlasov. A more accurate strain-energy expression than the one given by Love was derived recently by Langhaar (3). When this expression is used to obtain the differential equations for the cylindrical shell it is found that they disagree with those derived by Flügge and Vlasov.

The differential equations for the cylindrical shell given by Flügge and confirmed by Vlasov are in general use and may be presumed correct up to terms of the order $(h/a)^2$. As none of the strain-energy expressions is consistent with these equations, the authors have used Flügge's approach to obtain a strain-energy expression which is consistent with his differential equations.

Flügge's book contains expressions for the strains[5] from which the strain energy can be computed by integration over the volume of the shell in an obvious manner. The strain energy for plane stress is

$$U = \frac{E}{2(1-\nu^2)} \int\int\int \left[\epsilon_z^2 + \epsilon_\theta^2 + \frac{1-\nu}{2} \gamma_{z\theta}^2 + 2\nu \epsilon_z \epsilon_\theta \right] dr\, dz\, rd\theta \quad \ldots\ldots [1]$$

where the term $rd\theta$ (not $ad\theta$) is used, allowing for the different length of circumferential fibers through the thickness of the shell.

The strains are

$$\epsilon_z = u_z + (r-a) w_{zz}$$

$$\epsilon_\theta = \frac{v_\theta}{a} + \frac{r-a}{a} \frac{w_{\theta\theta}}{r} - \frac{w}{r}$$

$$\gamma_{z\theta} = \frac{u_\theta}{r} + \frac{r}{a} v_z + w_{z\theta} \left(\frac{r-a}{a} + \frac{r-a}{r} \right) \quad \ldots\ldots [2]$$

where the signs differ from Flügge's because of the change in direction of positive deflections w. After integration with respect to r from $a - h/2$ to $a + h/2$ the strain energy becomes finally

---

[1] This note is a result of investigations sponsored by the Office of Naval Research under Contract Nonr-266(08).

[2] Professor of Civil Engineering, Columbia University. Mem. ASME.

[3] Instructor in Civil Engineering, Columbia University.

Note: Statements and opinions advanced in papers are to be understood as individual expressions of their authors and not those of the Society. Manuscript received by ASME Applied Mechanics Division, February 20, 1953.

* Discussion of papers in Brief Notes should be addressed to the Secretary, ASME, 29 West 39th Street, New York, N. Y., and will be accepted until October 10, 1953, for publication at a later date. Discussion received after the closing date will be returned.

[4] Numbers in parentheses refer to the Bibliography at the end of the paper.

[5] Equations [68], reference (5), p. 115.

$$U = \frac{E}{2(1-\nu^2)}\frac{h}{a}\int\int\left[a^2u_s^2 + (v_\theta - w)^2 + 2a\nu u_s(v_\theta - w) + \frac{1-\nu}{2}(u_\theta + av_s)^2\right]dz\,d\theta + \frac{E}{24(1-\nu^2)}\frac{h^3}{a^3}\int\int\left[a^4w_{ss}^2 + (w_{\theta\theta} + w)^2 + \frac{1-\nu}{2}(aw_{,\theta} - u_\theta)^2 + \frac{3(1-\nu)}{2}a^2(v_s + w_{,\theta})^2 + 2\nu a^2w_{ss}(w_{\theta\theta} + v_\theta) + 2a^3u_sw_{ss}\right]dz\,d\theta \quad [3]$$

Logarithmic terms occurring in the integration leading to Equation [3] were approximated by expanding in series of ascending powers of h/a and neglecting terms above the cubic one.

The first term of Equation [3], proportional to h/a, is identical with the strain energy of the membrane stresses given by Love and all other authors. The second term, proportional to h^3/a^3, differs from the respective expressions of Love

$$\frac{E}{24(1-\nu^2)}\frac{h^3}{a^3}\int\int[a^4w_{ss}^2 + (w_{\theta\theta} + v_\theta)^2 + 2\nu a^2w_{ss}(w_{\theta\theta} + v_\theta) + 2(1-\nu)a^2(w_{s\theta} + v_s)^2]dz\,d\theta \quad [4]$$

and of Langhaar

$$\frac{E}{24(1-\nu^2)}\frac{h^3}{a^3}\int\int[a^4w_{ss}^2 + (w_{\theta\theta} + w)^2 + 2\nu a^2w_{ss}(w_{\theta\theta} + w) + 2(1-\nu)a^2(w_{,\theta} + v_s)(w_{,\theta} - u_\theta)]dz\,d\theta \quad [5]$$

It should be emphasized that the numerical differences between the three expressions are quite small if compared to the total strain energy. On the other hand, if the terms proportional to h^3/a^3 only are compared, the differences may be substantial. However, these terms in themselves are quite small compared to the membrane strain energy, unless the state of deformations considered is inextensional, or nearly so. In the inextensional case, the decisive h^3/a^3 term in Equation [3] and the corresponding terms listed in Equations [4] and [5] become entirely identical, and in a close to inextensional case the differences are not large. In this respect the reader is referred to the discussion of Langhaar's paper by Koiter (6).

It appears therefore that the difference in the value of U found from Equation [3] and the other expressions considered is presumably not very important. The advantage of Equation [3] lies essentially in the fact that the principle of stationary potential energy when used with the Expression [3] actually furnishes the accepted differential equations.

As Langhaar's expression has been derived on a fundamentally strict, geometrical basis, the source of the difference between Equations [3] and [5] deserves examination. One cause for the difference is the fact that Langhaar neglects certain terms which correspond to the nonlinearity in the stress distribution, stating that their effect is quite small. That this is a contributory cause can be verified by comparing the expressions for the strains which are found to agree only up to the linear terms in $(r - a)$. A second cause is the fact that in Equation [1] Flügge uses the expression $rd\theta$ for the length of a circumferential fiber, while Langhaar uses the approximate value $ad\theta$ in the expression for the element of volume.

In closing it is noted that an expression identical with Equation [3] was used by Pflüger (7) in the solution of a problem of shell buckling.

BIBLIOGRAPHY

1 "Mathematical Theory of Elasticity," by A. E. H. Love, Cambridge University Press, London, England, 1927.

2 "On the General Theory of Thin Shells," by W. R. Osgood and J. A. Joseph, JOURNAL OF APPLIED MECHANICS, Trans. ASME, vol. 72, 1950, pp. 396–398.

3 "A Strain-Energy Expression for Thin Elastic Shells," by H. L. Langhaar, JOURNAL OF APPLIED MECHANICS, Trans. ASME, vol. 71, 1949, pp. 183–189.

4 "Basic Differential Equations in General Theory of Elastic Shells," by V. S. Vlasov, NACA TM 1241, February, 1951.

5 "Statik und Dynamik der Schalen," by W. Flügge, Edwards Brothers, Inc., Ann Arbor, Mich., 1943.

6 "A Strain-Energy Expression for Thin Elastic Shells—Discussion," by W. T. Koiter, JOURNAL OF APPLIED MECHANICS, Trans. ASME, vol. 72, 1950, p. 107.

7 "Stabilitätsprobleme der Elastostatik," by A. Pflüger, J. Springer, Berlin, Germany, 1950, p. 130.

Angle and Strain Relations in Flat-Plate Lüders' Bands

By G. R. IRWIN,[1] WASHINGTON, D. C.

CERTAIN major features of flat-plate Lüders' bands are explicable on a simple and primarily kinematic basis. The discussions by Nadai[2] and Hill[3] are not clear as to what features of their results must be true independent of the usual formalisms, simplifications, and flow-stress laws of theoretical plasticity.

Experimentally, one knows these bands of extra thickness reduction, often observed in mild steel and 248-T aluminum, have the following features. The length of each band is large compared with its width; the width is several times the plate thickness; the band is straight if formed in a straight-sided test section; and the thickness reduction in the band can be increased by decreasing the stiffness of the loading arrangement.

Consider a thin flat tensile specimen is being pulled so that its test-section length is extending gradually. Assume x, y, z-axes in the width, length, and thickness directions, respectively. It is convenient to have a second set of axes x', y', z obtained by rotating the original axes about z through some angle θ, so that x' is parallel to the deformation band. Only the additional deformations in the band over those in the adjacent material need be considered. Also, only the averages through the plate thickness of these additional strains are considered. Let u, v be the "thickness averaged" particle displacements corresponding to the added strain in the x, y-directions and let u', v' be the components of these displacements referred to the x', y'-directions. Because of the uniform and relatively narrow width of the deformation band it is clear that these added strain displacements are not functions of the co-ordinate x'. Suppose now that at some stage of extension, a deformation band occurs. The additional strains therein must be such that

$$\frac{\partial u'}{\partial x'} = \frac{\partial u}{\partial x}\cos^2\theta + \frac{\partial v}{\partial y}\sin^2\theta + \left(\frac{\partial u}{\partial y} + \frac{\partial v}{\partial x}\right)\sin\theta\cos\theta = 0 \quad [1]$$

$$\frac{\partial v'}{\partial x'} = \left(\frac{\partial v}{\partial y} - \frac{\partial u}{\partial x}\right)\sin\theta\cos\theta - \frac{\partial u}{\partial y}\sin^2\theta + \frac{\partial v}{\partial x}\cos^2\theta = 0 \quad [2]$$

[1] Superintendent, Mechanics Division, Naval Research Laboratory.

[2] "Theory of Flow and Fracture of Solids," by A. Nadai, McGraw-Hill Book Company, Inc., New York, N. Y., 1950, pp. 320–324.

[3] "On Discontinuous Plastic States, With Special Reference to Localized Necking in Thin Sheets," by R. Hill, *Journal of Mechanics and Physics of Solids*, vol. 1, 1952, pp. 19–30.

Manuscript received by ASME Applied Mechanics Division, January 29, 1953.

There is no reason to assume the added strains occur in any way other than that which would contribute maximum strain-energy release in a clamped-grip experiment. Thus the y-direction must be a maximum extensional strain direction throughout the Lüders' band, whence

$$\frac{\partial u}{\partial y} + \frac{\partial v}{\partial x} = 0 \qquad [3]$$

One also may assume the added strains do not alter appreciably the density of the material so that

$$\frac{\partial u}{\partial x} + \frac{\partial v}{\partial y} + \epsilon = \frac{\partial v'}{\partial y'} + \epsilon = 0 \qquad [4]$$

where ϵ is the added thickness-reduction strain.

Using Equations [3] and [4] with Equation [2]

$$\tan^2 \theta = -\frac{\partial u}{\partial x} \Big/ \frac{\partial v}{\partial y} = \frac{\partial u}{\partial x} \Big/ \left(\frac{\partial u}{\partial x} + \epsilon \right) \qquad [5]$$

Now, although the ratio of strains which determines θ need not be the same for the added strains in the deformation band as for the plastic strains in the adjacent material, at least it should be nearly the same. For example, it may be observed that θ approaches 35 deg, corresponding to equal strains in the x and z-directions, when the test piece is long, and can be reduced to less than 15 deg by shortening the relative length of the test section in the direction of greatest tension. In the latter experiment one must take care that the gripped ends of the specimen are sufficiently oversize to avoid plastic deformation. Actually, the observed angles, θ, are usually a little under those which one would expect from the ratio of plastic strains outside the deformation band as if the narrowness of the band applied some additional constraint to strain in the x-direction inside the band.

Some variation of thickness reduction is obvious when one inspects a deformation band carefully along the y-direction. The fact that θ, from Equation [5], must be the same throughout the band places a limitation on the variation of these plastic strains except near the sides of the test section where the shape of the deformation band is not independent of x' as was assumed earlier. Within deformation band rotations about the z-axis are given by

$$\frac{\partial u'}{\partial y'} = 2\,\frac{\partial u}{\partial y} = -2\,\frac{\partial v}{\partial x} = \epsilon \tan (2\theta) \qquad [6]$$

If the test piece has lightly scribed lines or photogrid lines in the x and y-directions, Equation [3] infers that the intersections of these lines will remain right angles within the deformation band. Equation [6] shows how the magnitude of the small rotations of these intersections is related to the added strains in the deformation band.

Note on Oil Whip

By OSCAR PINKUS,[1] LYNN, MASS.

OIL whip, which is a resonant form of vibration in journal bearings, is being investigated to establish (a) its characteristic behavior, and (b) the effect of the many operating variables on whip.

A fundamentally new feature found in the oil-whip phenomenon is that oil whip stops at speeds slightly exceeding 3 times the first critical frequency. This has been observed consistently on a great number of tests with various bearings and conflicts with

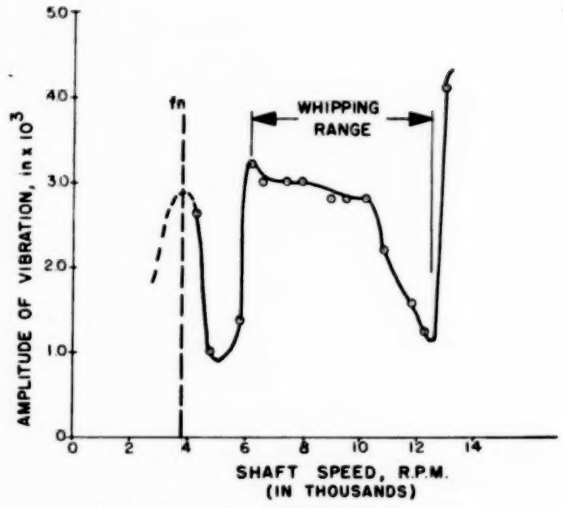

FIG. 1 DIAMETRAL AMPLITUDE OF VIBRATION VERSUS SHAFT SPEED

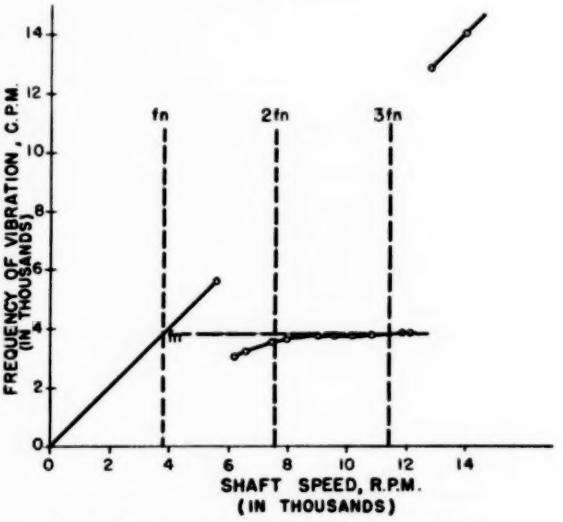

FIG. 2 FREQUENCY OF VIBRATION VERSUS SHAFT SPEED

previous statements[2] that oil whip, once started, persists at all speeds exceeding twice the value of the first critical. In most cases the amplitudes of vibration, which rise with the onset of whip, begin to drop at speeds equal to 3 times the first critical which is the upper limit of oil whip.

Figs. 1 and 2 show a set of typical whip curves obtained on cylindrical bearings 2 in. long, 2 in. diam with a diametral clearance of 0.005 in. All operating conditions except speed were kept constant throughout this run and were as follows: Loading, 23.5 psi; inlet oil temperature, 60 C with a viscosity of 12 centipoises; and inlet oil pressure, 25 psi. The Sommerfeld numbers at the beginning and at the end of whip are 1.2 and 2.4, respectively. It should be noted in Fig. 2 that the frequency of whipping is near the natural frequency throughout the whipping range.

[1] Thomson Laboratory, General Electric Company. Jun. ASME.

Manuscript received by ASME Applied Mechanics Division, January 8, 1953.

[2] "Shaft Whipping Due to Oil Action in Journal Bearings," by B. L. Newkirk, *General Electric Review*, vol. 28, 1925, p. 559.

The effect of oil-inlet temperature on oil whip also was investigated in greater detail. Some of the test bearings whipped at high inlet-oil temperatures had a narrow whipping range at intermediate temperatures, and did not whip at all on cold oil. This apparently contradicts some recent attempts to delineate whip as a function of shaft eccentricity. According to this theory high eccentricities tend to eliminate whip, an example of this being high loading at which whip rarely occurs. However, the present tests with variable oil-inlet temperature appear to indicate a trend opposite to the one mentioned, as higher oil-inlet temperatures tend to give higher eccentricities. Also, the fact that whip stopped at higher speeds, when lower eccentricities occurred, disagrees with the hypothesis that eccentricity is the sole criterion of shaft stability.

The test apparatus used in the present tests consists of a 200-lb shaft with a rotor in the middle driven by a 200-hp motor through two sets of gears. Details of the machine are given by Wilcock.[3] The motion of the shaft center is picked up by a series of magnetic gages which in combination with an amylifier and an oscilloscope trace the locus of the shaft center and measure the amplitudes of vibration.

[3] "Turbulence in High-Speed Journal Bearings," by D. F. Wilcock, Trans. ASME, vol. 72, 1950, p. 825.

Book Reviews

Foundation Engineering

FOUNDATION ENGINEERING. By Ralph B. Peck, Walter E. Hanson, and Thomas H. Thornburn. John Wiley & Sons, Inc., New York, N. Y., 1953. Cloth, 6 × 9 in., xix and 410 pp., illus., index, $6.75.

REVIEWED BY ALBERT G. H. DIETZ[1]

THIS is a first course in soil mechanics and foundation engineering, designed for the student or engineer who has no broad background in the subject, but is familiar with the principles of mechanics and structural engineering.

The authors emphasize the engineering design aspects of foundations and draw upon the principles of soil mechanics to the extent necessary to provide the basis of the engineering development. The book begins with a discussion of the properties and identification of soils and rocks, subsurface explorations, and the character of natural deposits. This opening section is followed by descriptions of types of foundations and methods of construction including underpinning and bracing. The final section is devoted to the selection of foundation types and to their design. Here the material is illustrated with a number of design examples of such items as combined footings, bridge piers, and others.

A feature of the book is a series of brief biographies of outstanding engineers who have contributed to foundation engineering and to soil mechanics.

Turbulence

THE THEORY OF HOMOGENEOUS TURBULENCE. By G. K. Batchelor. Cambridge University Press, New York, N. Y. 1953. Cloth, 8½ × 5½ in., xi and 197 pp., fig., bibliography, $5.

REVIEWED BY HIROSHI SATO[2]

THE author has recently published many papers on the detailed structure of turbulence. This book, written with the intention of being an introduction for new-comers, consists mostly of his own work. The contents of the text are restricted to fundamental considerations omitting diffusion or transfer theories. Consequently, neither over-all view nor practical applications are found. Apparently, the author tries to organize and rearrange the existing theories on homogeneous turbulence, preparing a next step of development. Many pages are devoted to clarifying the basic concept of turbulence, a concept which sometimes causes confusion because of its vague definition. In the course of the discussion, the author frequently cites experimental results to give physical insight into the complicated mathematics. He succeeds in distinguishing the ambiguous assumptions and treatments of present theories from the established facts, thus making it easy to realize what is important and what is not important.

In chapter 1, a brief historical sketch of this subject is presented together with the fundamentals of turbulent motion. Chapters 2 and 3 are devoted to a mathematical formulation of the homogeneous turbulent field using the correlation and spectrum tensors. Chapter 4 deals with some examples of linear problems. The Navier-Stokes equation appears in chapter 5, from which important formulas are derived in a generalized form. A solution to the problem of turbulent motion in the final period of decay is also presented in this chapter. Chapters 6 and 7 discuss the most essential point of turbulence—the inertia term, which is difficult to treat mathematically. The hypothesis of statistical equilibrium is introduced and every phase of the problem is sharply criticized. In chapter 8, the probability density of velocity fluctuation is dealt with principally from the experimental point of view. The mathematical treatment of pressure fluctuation is also taken into consideration here. The book is concluded by a complete bibliography of some 200 published papers.

It is difficult to write this kind of book, because there are many theories in progress and most of them cannot be said to be well established. The author's efforts are successful in selecting materials, in making physical concepts clear, and in giving suggestions for the future advancement of the theory of homogeneous turbulence.

British Engine Report

Technical Report, New Series, vol. 1, November, 1952, British Engine Boiler & Electrical Insurance Co. Ltd., Manchester, England. Paper 6¾ × 9½ in., figs., tables, bibliography, 212 pp., 12s, 6d.

REVIEWED BY J. M. LESSELLS[3]

THE engineer usually profits by a study of the causes of service failures. Unfortunately, the particulars of such failures are,

[1] Professor, Structural Engineering, Massachusetts Institute of Technology, Cambridge, Mass. Mem. ASME.

[2] Research Fellow, Department of Aeronautical Engineering and Applied Mechanics, Polytechnic Institute of Brooklyn, Brooklyn, New York.

[3] Associate Professor of Mechanical Engineering, Massachusetts Institute of Technology, Cambridge, Mass. Hon. Mem. ASME.

for commercial reasons, usually restricted. Because of the lack of such information, the practice adopted by the British Engine Boiler and Electrical Insurance Company of issuing technical reports covering characteristic failures, and which practice was continued until 1938, provided useful means of disseminating knowledge on the causes of failure. By the appearance of the present report it is gratifying to learn that the former practice regarding these publications will be continued, not on an annual basis as heretofore, but whenever sufficient material has been accumulated.

The present report, following the previous practice, has a broad coverage and discusses many different types of failures. In each case an explanation is given, in so far as possible, of the underlying causes.

Fractures by caustic cracking are given considerable attention and other interesting instances of failures of such parts as a crankshaft, a turbine shaft, turbine blades, an eyebolt, and a crane hook come under review.

In view of the importance and significance of brittle behavior of ductile steel the article on the notched-bar-testing technique appears to be timely.

This company is to be congratulated on its policy of making such information available to engineers.

Statistics

STATISTICAL THEORY WITH ENGINEERING APPLICATIONS. By A. Hald. John Wiley and Sons, Inc., New York, N. Y.; Chapman and Hall, Ltd., London, England, 1952. Cloth, 6¼ × 10 in., tables, figs., author index, index of symbols and formulas, subject index, xii and 783 pp., $9.

STATISTICAL TABLES AND FORMULAS (Wiley Publications in Statistics). By A. Hald. John Wiley and Sons, Inc., New York, N. Y.; Chapman and Hall, Ltd., London, England, 1952. Paper, 8½ × 11 in., 98 pp., $2.50.

REVIEWED BY A. E. HOERL[4] AND J. T. RANSOM[4]

As the author states in the preface, this book has been strongly influenced in the choice of statistical methods by the English school of Fisher and by Shewhart in statistical quality control.

As a whole this well-printed book is highly recommended, not only from the standpoint of having a wealth of material and examples, but also because enough mathematical theory is introduced to keep it semirigorous without weighting it down for the nonmathematician. However, contrary to the author's statement, it is doubtful that a knowledge of only standard differential and integral calculus is sufficient to completely follow all proofs and derivations. On the other hand, for much of the material the lack of a thorough knowledge of integral calculus is offset if the reader is fairly adept with mathematical symbols and equations. Also, due to the general development of the mathematical theory underlying the statistical derivations it is difficult to use the material in a given section without having read or carefully skimmed the preceding sections first.

Unfortunately, several fundamental concepts are introduced rather abruptly and are thus likely to leave the nonstatistician, for whom the book is written, somewhat confused. Most notable of these are the concepts associated with degrees of freedom, especially in calculating s^2 with $(n - 1)$, and interaction. In addition, while the author has been careful in stating mathematical conditions underlying the statistical distributions and tests, there are still a few instances where they are not explicitly stated for the casual user, e.g., the requirement of linearity of the relation between variables for the correlation coefficient to be a meaningful measure of association.

There is a certain confusion on the reader's part in regard to the substitution of equality for the approximately-equal-to symbol, $\simeq$, in successive lines, such as, for example

$$P(y) \simeq \int_{x_1}^{x_2} g(y, x)dx$$
$$= h(y)$$

The most notable of these occur on the following pages: 69 (X), 301 (C^2 [c]), 611 ($\bar{Z}$), 679 ($P[x_1 \leq x \leq x_2]$), etc. Also, there are several misprints such as occur on pages 710 ($P = 0.0401$ instead of 0.401), 294 ($k = 3$ not f), etc. Due to the voluminous quantity of material it was not possible to check all the computations for the examples. However, no errors were found in the supplementary edition "Statistical Tables and Formula."

All in all, this book with its wealth of material would be an excellent addition to any engineer's or statistician's library.

Applied Mechanics

ANNIVERSARY VOLUME ON APPLIED MECHANICS, dedicated to C. B. Biezeno, by some of his friends and former students on his sixty-fifth birthday, March 2, 1953. H. Stam, Haarlem, The Netherlands, 1953. Cloth, 6 × 9 in., figs., bibliography, tables, 328 pp., Hfl. 20.

REVIEWED BY J. P. DEN HARTOG[5]

Professor Biezeno of the Technical Institute in Delft Holland, is one of the great names in applied mechanics in the world. His contributions are laid down in some seventy-five papers and in the great book, "Technical Dynamics," written in collaboration with Grammel, of which an English translation will soon be available. Also, he has become widely known as the organizer of the First International Congress of Applied Mechanics, Delft, 1924, which was the first of a series of such congresses (the eighth was just held in Istanbul in 1952) and which have had a large influence on the development of our science.

This anniversary volume is a collection of nineteen papers, fifteen of which are in English, three in French, and one in German, the majority being of considerable actual interest. Two papers, one by von Kármán and Millan, the other by J. M. Burgers, deal with the theory of flame propagation or 'deflagration.' A paper by Koning deals with the interaction of propellers and airplane bodies and the interference of each on the flow pattern caused by the other. Southwell and Vaisey contribute a relaxation solution of the warping function in St. Venant's torsion of a rectangular section, showing a curious effect. Grammel gives a theory of the longitudinal and flexural vibrations of a bar with a nonlinear law of elasticity $\sigma/E = \epsilon + \lambda\epsilon^3$, showing diagrams of natural frequencies as functions of the amplitude. Koiter brings a new theory of the plasticity problem of thick cylinders with internal pressure and compares it to the several other theories, based on different assumptions.

Other papers deal with the buckling of sandwich plates and structures made up of flat plates, with the shimmy motion of railway cars on a track; with the stresses and deformations in corrugated and flat diaphragms and in coil springs of various cross sections; with the local stress distribution in flat reinforced concrete floors in the vicinity of the supporting columns; and finally with the stresses and deformations of the steel frame and glass center of steel windows under various loadings.

The book is well printed, illustrated, and bound, and is a worthy tribute to an eminent scientist and a beloved teacher.

[4] Engineering Research Laboratory, Engineering Department, E. I. du Pont de Nemours and Company, Inc., Wilmington, Del.

[5] Professor, Mechanical Engineering, Massachusetts Institute of Technology, Cambridge, Mass. Mem. ASME.

AN ASME PAPER

Its Preparation, Submission and Publication, and Presentation

To a large degree the papers prepared and presented under the ASME sponsorship are evidence by which its professional standing and leadership are judged. It follows, therefore, that to qualify for ASME sponsorship, a paper must not only present suitable subject matter, but it must be well written and conform to recognized standards of good English and literary style.

The pamphlet on "AN ASME PAPER" is designed to aid authors in meeting these requirements and to acquaint them with rules of the Society relating to the preparation and submission of manuscripts and accompanying illustrations. It also includes suggestions for the presentation of papers before Society meetings.

CONTENTS

PREPARATION OF A PAPER—

General Information—Style, Preferred Spelling, Length Limitation, Approvals and Clearances.

Contents of the Paper—Title, Author's Name, Abstract, Body of Paper, Appendixes, Acknowledgments, Bibliographies, Tables, Captions, Photographs, Other Illustrations.

Writing the Paper—Outline Tabulations, Tables, Graphs, Charts for Computation, Drawings, Mathematics, Accuracy, Headings and Numbering, Lantern Slides, Motion Pictures, Typing, Number of Copies.

SUBMISSION AND PUBLICATION OF A PAPER—

Intention to Submit Paper Required in Advance, Meeting Dates, Due Dates for Manuscript, Discussers, Review and Acceptance, Proofs, Advance Copies and Reprints, Discussion and Closure, Publication by Others.

PRESENTATION OF A PAPER—

Time Limit, Addressing Your Audience, Public Address Systems, Use of Slides.

REFERENCES—

References on Writing and Speaking, Engineering Standards.

Price 40¢. No discount allowed. ***A remittance must accompany all orders for $5.00 or less. U. S. Postage Stamps are acceptable.***

THE AMERICAN SOCIETY OF MECHANICAL ENGINEERS

29 West 39th Street, New York 18, N. Y.